Modeling and Simulations of Defect-free Collagen Film Formation Process and Biological Plywood Morphology Analysis.

Oscar Felipe Aguilar Gutiérrez

Doctor of Philosophy

Department of Chemical Engineering

McGill University

Montreal, Quebec

June, 2017

A thesis submitted to McGill University in partial fulfillment of the requirements of the degree of Doctor of Philosophy

DEDICATION

This thesis is dedicated to my wife Karla and to my parents Elia and Felipe.

To the memory of Don Roberto and Rosa Enna.

CONTRIBUTIONS OF THE AUTHOR

The author chooses the manuscript-based thesis option following the guidelines stipulated by the Faculty of Graduate and Postdoctoral Studies:

http://www.mcgill.ca/gps/thesis/thesis-guidelines/preparation

The contents of Chapters 2 – 6 of the present thesis are adopted from articles published in (chapters 2, 4 – 6) or to be submitted (chapter 3) to scientific journals under the normal supervision of my research supervisor, Prof. Alejandro D. Rey who is also co-author. All computations, data analysis and articles included are the work of the author.

Acknowledgements

I would like to express my gratitude to my supervisor Dr. Alejandro D. Rey for his guidance, support, mentorship, encouragement and patience throughout these years. I was honoured of being part of his research group and learn from his example. Special thanks to Barbara for her kindness and enthusiasm in our group meetings and celebrations.

I am also grateful for the financial support of CONACyT (Government of Mexico scholarship number 313480) and McGill University for the GEF (Graduate Excellence Fellowship).

Thank you to my research group colleagues Pardis, Zeina, Estela, Hang, Sebastian, Thomas, Sina, Alireza, Matus and Emilio for their advice, comments and recommendations during our weekly meetings and providing a warm and peaceful workplace.

Thank you to my friends who have become over the past years in an extended family, Norma, Charlie, Paulina, Matus, Chava, Mario, Vero, Beto, Laura, Abraham, for the encouragement, support and the shared moments that made the course of these years much easier.

I am deeply grateful to my parents, Elia and Felipe, to whom I owe everything, thank you for your unconditional support and continuous encouragement. I am grateful to my siblings, Sergio and Carina, for being there for me despite the distances. Thank you to my mother-in-law Lupita for being so caring.

And I am most especially thankful to my wife Karlita for her unconditional love and support. There are no words that can express how grateful I am with you. During these years we've been through good and bad times, but no matter what we've always managed to get ahead and that is because we have each other. ¡Gracias mi amor!

ABSTRACT

This thesis uses multiscale computational modeling, scaling and analysis to characterize the steps of a multistage process used to produce a defect-free cholesteric collagen film and to characterize the resulting chiral biological plywood microstructure, found throughout Nature.

The process makes use of a complex flow deposition of a liquid film of a dilute collagen solution on a substrate which is later converted to a chiral biological plywood by exposure to an airflow of filtered air. During the flow deposition analysis and simulations, two crucial material properties are estimated: the rheological shape parameter β and the rotational diffusivity D_r; the former is then used to obtain the reactive parameter λ of collagen which is of crucial importance in film flow-control. These material properties are then used to describe the dynamic behavior of dilute collagen solutions by means of a spatially homogeneous Landau – de Gennes **Q** tensor model under the influence of the kinematics of a four roll mill apparatus which allows to explore a wide variety of flow types and intensities with unequal contributions of strain and vorticity rates relevant to film flow-processing. The kinematic conditions required to obtain the appropriate para-nematic phase in terms of orientation and order are also provided. The transformation of a dilute flow-aligned non-equilibrium para-nematic phase into a cholesteric film is simulated by integrating the nematodynamics of collagen solutions with dehydration mass transfer as water leaves the film. The microstructure controlling dimensionless parameter in given in terms of the geometry of length L and the ratio of collagen rotational diffusivity to water mass diffusion. The integrated microstructure-mass transfer with moving boundaries is carefully simulated and the resulting microstructural modes are classified into three modes: monodomain-cellular, monodomain, and

polydomain. The conditions that lead to the sought-after defect free monodomain plywood architectures are found and the synchronization mechanism that yield perfect uniform chirality is revealed.

Finally, computational geometry is used to determine the architecture of collagen films as formed in the film dehydration process as well as others found in Nature, such as cornea-like tissues. Inverse problems of 3D reconstructions from 2D planar sectioning observations that usually lead to ill-defined processes are resolved by introducing intrinsic geometric features (arcs and herringbones) of these fibrous composites. By including the curvature of the arcs or the aperture angle for the herringbones, a unique value of the chiral pitch can be obtained which lead to a proposed characterization methodology which is used to predict the chiral pitch profile of the "aurigans scarab" beetle via in silico cross sections and the cell wall thickness of the "eremosphera viridis" algae species.

ABREGÉ

Cette thèse utilise la modélisation numérique et l'analyse multi-échelle pour explorer les étapes d'un processus conçu pour la fabrication d'une pellicule sans défauts et la morphologie résultant des pellicules qui est omniprésent dans des matériaux naturelles ayant une organisation dénommée TPA (pour ses sigles en anglais), structure très répandu chez les matériaux naturelles.

Le processus est composé d'un écoulement complexe où un substrat est enrobé par une pellicule d'une dissolution diluée à base de collagène et ensuite transformée en un plywood biologique ayant une microstructure nématique chirale en l'exposant à un écoulement d'air filtré. Premièrement, dans l'analyse et simulations concernant au découlement complexe deux propriétés physiques sont calculées: le paramètre rhéologique de forme β et la diffusivité rotationnelle D_r, dont le premier permet d'obtenir le paramètre réactif (λ), propriété fondamentale dans le contrôle d'écoulement des pellicules. Ensuite, les propriétés sont utilisées pour décrire le comportement dynamique et formation de la phase para-nématique utilisant un modèle du tenseur Q de Landau – de Gennes spatialement homogène imposant la cinématique de l'appareil à quatre rouleaux de Taylor. Cette cinématique permet explorer une vaste variété et intensités d'écoulements qui ont contributions inégales de déformations contre celles de tourbillons. Les conditions cinématiques auxquelles les dissolutions diluées de collagène doivent être soumises sont fournies en termes d'orientation et ordre. La transformation de la phase para-nématique instable en cholestérique est modélisée par en accouplant le modèle nématodynamique et une équation de transfert de masse du dissolvant sortant le système binaire. Le paramètre qui permet de contrôler la microstructure final est donné en fonction de la longueur caractéristique et le quotient de la diffusivité rotationnelle du mesogène

et la diffusivité translationnelle du dissolvant. Le modèle avec frontières mobiles est simulé soigneusement et fourni trois modes : mono-domaine-cellulaire, mono-domaine et multi-domaine. La synchronisation des processus simultanés présents fournis la microstructure recherchée.

Finalement, la morphologie des matériaux obtenus et d'autres trouvés dans la nature, telle que les tissus ayant microstructure comme la cornée, est explorée par un modèle géométrique. Des problèmes inverses de reconstruction 3D à partir des sections 2D, qui sont normalement des problèmes mal-définis, sont résolus en introduisant des caractéristiques géométriques (motifs d'arches et de chevrons) qui sont observés dans ces types des matériaux. L'inclusion des variables géométriques fournis une description unique du pas cholésterique et est utilisée pour une méthodologie de caractérisation pour prédire le profil du pas cholésterique trouvé dans la cuticule de l'insecte « aurigans scarab » grace a des sections obliques in silico et la détermination de la paroi cellulaire de l'algue « eremosphera viridis ».

TABLE OF CONTENTS

LIST OF FIGURES

Figure

List of Tables

1 General Introduction

1.1 Thesis Motivation

Nature has always been a source of inspiration for science and technology development due to its capability in assembling complex material architectures using building blocks composed mostly of C, H, O, N, and S. This assembly process results in multi-functional materials with characteristics such as self-healing, adaptation to changes in the environment, and optimized properties. The microstructure of these materials is usually responsible for those properties, and in particular the liquid crystalline state and organization is widely present throughout the plant and animal kingdoms [1, 2]. The synthesis of materials in controlled laboratory conditions with the morphology present in their natural counterpart [3 – 8] (which is the ultimate goal for certain areas such as tissue engineering [4, 9 – 11] and biomimicry) has driven efforts in the development of bio-inspired materials using some of Nature's building blocks such as collagen, cellulose and chitin. Even when some processes have been reported [5, 12 – 14], the underlying principles are still not fully understood since the full processing-structure-property relationships are still under development. It is therefore of great importance the development of theoretical/simulation work to elucidate the principles behind the self-assembly of biomacromolecules through non-equilibrium flow and mass transfer processes. A particular microstructure that forms the central theme of this work is the "biological helical plywood" widely found in most fibrous composites and is a molecular analogue of man-made plywoods. The theoretical and computational work presented in this thesis explores a multi-step flow-dehydration process whose ultimate goal is to

achieve a defect free liquid crystalline collagen film. This structure presenting the perfect microstructure of a chiral nematic phase (also known as cholesteric and/or helical plywood) can be detected and characterized when observing cross-sectional arc-patterns of these solid-like materials. The periodicity of these arcs along with other characteristics of the patterns can provide quantitative information about the plywoods and can be used as an additional characterization tool which is also presented in this work.

1.2 Liquid Crystals

Liquid crystals are viscoelastic anisotropic materials that show positional/orientation order through several length-scales [15 – 17]. These materials flow when submitted to relatively low stress, but also display the properties of an anisotropic crystal at rest [18]. One essential requirement to display liquid crystallinity is a large aspect ratio such as an elongated rod or a flat disc, and the interesting properties they display are known to be present in a well-defined range of temperature or concentration depending on the type of liquid crystallinity [15]. Materials that respond to changes in temperature are known as thermotropic liquid crystals. These are pure substances that show a cloudy state when cooling down from the liquid towards the solid state. This "cloudy-state" was firstly observed by Reinitzer who was intrigued by this anomalous behaviour observed when melting pure low molecular weight organic substances with molecules presenting large aspect ratios. On the other hand, materials that are affected by changes in concentration are denominated lyotropic liquid crystals where phase transitions are governed by excluded volume interactions [19]. In these materials a solvent is required and the crowding of high aspect ratio mesogens reduce

drastically the rotational motion, hence an oriented material is obtained. Chromonics are an additional classification of liquid crystals where both concentration and temperature induce ordering and phase transitions in the material [20].

Liquid crystallinity can be observed in different types of molecules ranging from low molecular weight molecules [15, 17], to larger molecules such as surfactants, known as amphiphilic mesogens [21], up to high molecular weight polymers, that can display liquid crystallinity in both the main chain or ramifications of the polymeric structure [16, 18]. It was also recently recognized that even in natural materials [2] as long the corresponding building block has a large aspect ratio. These materials can organize into different types of mesophases such as the nematic, smectic and cholesteric phases [22, 23] where the latter is the most common arrangement present in nature due to the intrinsic chirality in structural materials such as collagen [24, 25], chitin [26, 27] and cellulose [28 – 30]. The characteristics of each phase are described as follows and depicted schematically in figure (1.1).

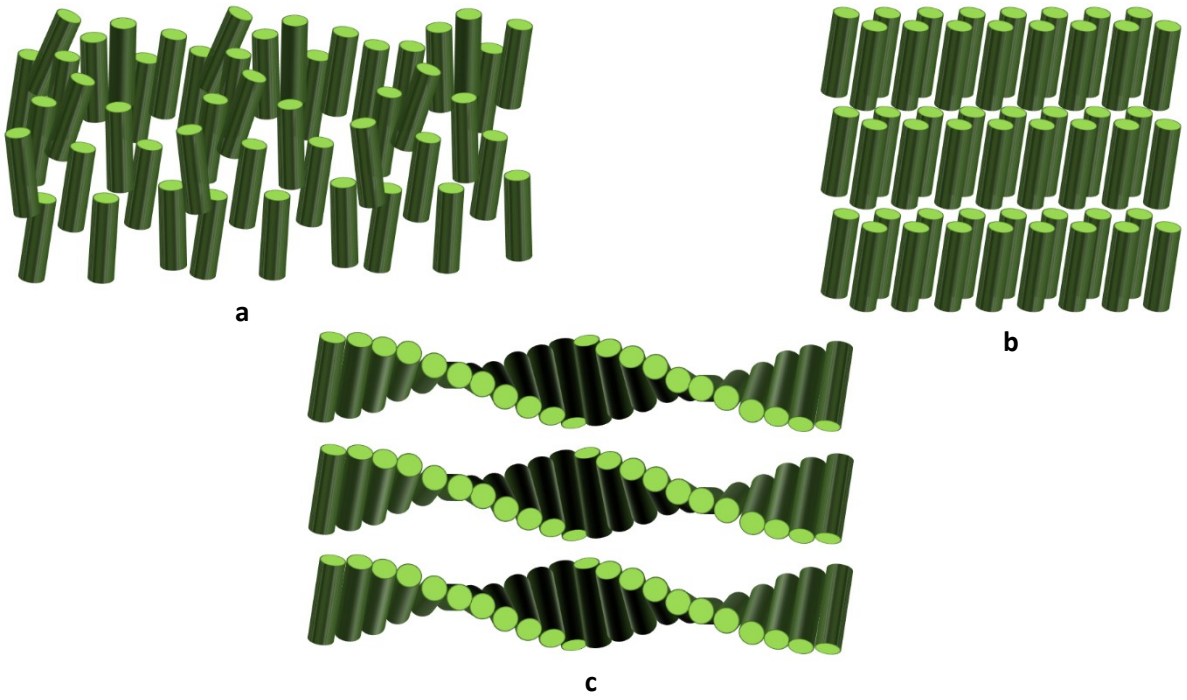

Figure 1.1 Schematic representation of the nematic (a) with orientational order only, smectic (b) with orientational and positional order present, and chiral nematic or cholesteric phase (c) with the characteristic helical axis and characteristic length-scale for a 2π rotation of the director p_o.

The nematic phase is the simplest phase where only orientational order is found, i.e. the mesogens' centers of mass undergo free motion but the rotational motion is restricted and in average remains constant. Thus, the molecules composing the phase are pointing in average to one preferred orientation which defines the director field **n**. The Smectic phase is the most ordered and viscous mesophase. Additionally to the orientation, positional order is also found in these materials. The material is ordered in a layered fashion and the molecules' center of mass is allowed to move freely within its respective layer. Finally, the cholesteric phase is observed when chirality is present in the mesogen. This phase is also known as the chiral nematic whose characteristic is the presence of a twist in the preferred direction and has a characteristic length-scale associated to it which is called the pitch (p_o), defined as the distance required for the director to undergo a full 2π rotation.

This phase can also be conceived as a collection of nematic planes showing a twist between adjacent planes and the achiral nematic phase can thus be though as a cholesteric with an infinite pitch p_o.

1.3 Biological Liquid Crystals

Liquid crystallinity is widely present in natural materials, evidence of it includes the manifestation of arced patterns through oblique incisions of certain solidified materials composed of structural compounds such as cellulose [28], chitin [2], collagen [3] and other molecules like DNA [31] which indicate the building blocks undergo rotations about a common axis. Moreover, the aforementioned compounds have been extracted and studied in vitro where liquid crystalline behavior is present in such solutions above a critical concentration [32]. In vivo [1] and in vitro [1,13,33] observations have also pointed out the presence of defects that have been observed in conventional liquid crystals denominated elsewhere as faults [1, 34 – 37].

The characteristics of nature building blocks in addition to the large aspect ratio are the presence of charged functional groups or residues. The main chain conformation is affected when surrounded by a charged medium and can affect the effective geometry of the molecule [38]. For the particular case of collagen, it is usually considered to be a semi-flexible biopolymer with a persistence length ranging from 57 to 250 nm [33, 39] and effective diameters up to approximately 4 nm [33].

Biological liquid crystals are formed through a multi-scale hierarchical self-assembly process from the molecular level up to fiber formation. This self-assembly over several length-scales impart the

multi-functionality to BLCs. It is commonly observed for these materials to manifest adaptation to the surrounding medium such as stresses and humidity content [23], capability of self-healing [1] while at the same time displaying high mechanical resistance and interesting optical properties or even thermal regulation as hypothesized in beetles [40]. It is worth noting that the most widely observed mesophase in biological materials is the chiral nematic [2], however, other arrangements such as the nematic or even orthogonal can be observed where the latter layers composing the material show abrupt 90º changes in between layers. Interestingly, the same building block can exhibit different arrangements such as in vitro collagen where changes ionic content of the precursor solution lead to a cholesteric organization for pH of 2.5 and an orthogonal organization for pH of 3.5 [12].

Biological liquid crystals have been classified intro three different analogous phases [41]:

1. Solid Analogues: These are solid state materials displaying a frozen liquid crystalline organization. They were first identified and investigated by Bouligand [2] in samples of crab cuticle. Other examples include plant cell walls [28], exoskeletons of insects [34], cuticle of some crustaceans [2] and even bone osteons [3]. The optimized set of multi-functionality of the plywoods vary depending on the intended application and any additional reinforcing material and their particular arrangement of the building blocks. For instance, the mechanical requirements for cornea differ drastically from those in bones despite being made of the same mesogen: collagen. In the former case, the optical properties and shape preservation [1] are crucial providing its transparency whereas in the latter case tough composites are required in these cholesteric arrangements, made possible with mineral inclusion, specifically of hydroxyapatite as reinforcement [3].

2. In vitro: This type of analogue include solutions of extracted biomacromolecules which can be dilute or concentrated. The former have been reported to display liquid crystallinity under the influence of external fields or forces while presenting isotropic behavior at rest while [33] the latter display such behavior above a characteristic threshold [42, 43].

3. In vivo: In these analogues, the liquid crystalline behavior is displayed in natural conditions with the remarkable examples of spider silk and biological membranes [1, 44].

1.4 Biological Plywoods: Morphology and Structure Relationships with Characteristic Patterns

The path that Nature follows for the synthesis and fabrication of biological plywoods is complex and has not been fully understood. This is due to the multi-component nature of the plywood and simultaneous phenomena and synthesis of such components occurring in different places. It is also important to notice two steps have been reported for the control of fiber orientations which are denominated as primary and secondary fiber orientation control [1]. The former is the initial fiber orientation which is mainly controlled by two non-exclusive mechanisms:

i) Self-assembly where intermolecular forces are the main driving force through an efficient entropy-driven process resulting from the fibrillary shape, effective geometry due to electrostatic interactions between residues and ionic content of the surrounding medium, chemical and geometric chirality which are generally manifested to higher

levels of the hierarchical architecture with the example of the frozen chiral nematic phases observed in plywoods where the pitch (p_o) can also be identified.

ii) Directed assembly where other cellular mechanisms or the presence of other components affect the fiber orientation such as microtubules that have been linked to the orientation of cellulose microfibrils in plant cell walls.

Once the fibers are laid down to a given orientation during the primary fiber orientation, additional physiological processes occur moving the fibers to a new position such as growth, contraction, body forces among others in the secondary fiber orientation [1, 45].

Characteristic patterns are associated to a specific arrangement of the building blocks can be observed in oblique cross sections of biological plywoods. For plywoods exhibiting chiral nematic organization the associated pattern correspond to nested arcs where the periodicity of the arcs are correlated to the pitch [1, 2, 28, 46]. Orthogonal plywoods, on the other hand, are associated with herringbone patterns and the periodicity of such patterns is similarly related to the pitch and the thickness of each layer composing the plywood [1]. The case of nematic plywood is not associated to any characteristic pattern. Figure 1.2 depicts schematically the three cases with its respective oblique sections where the characteristic patterns are visible. In vivo [28] and in silico [47] characteristic patterns are shown in figure 1.3.

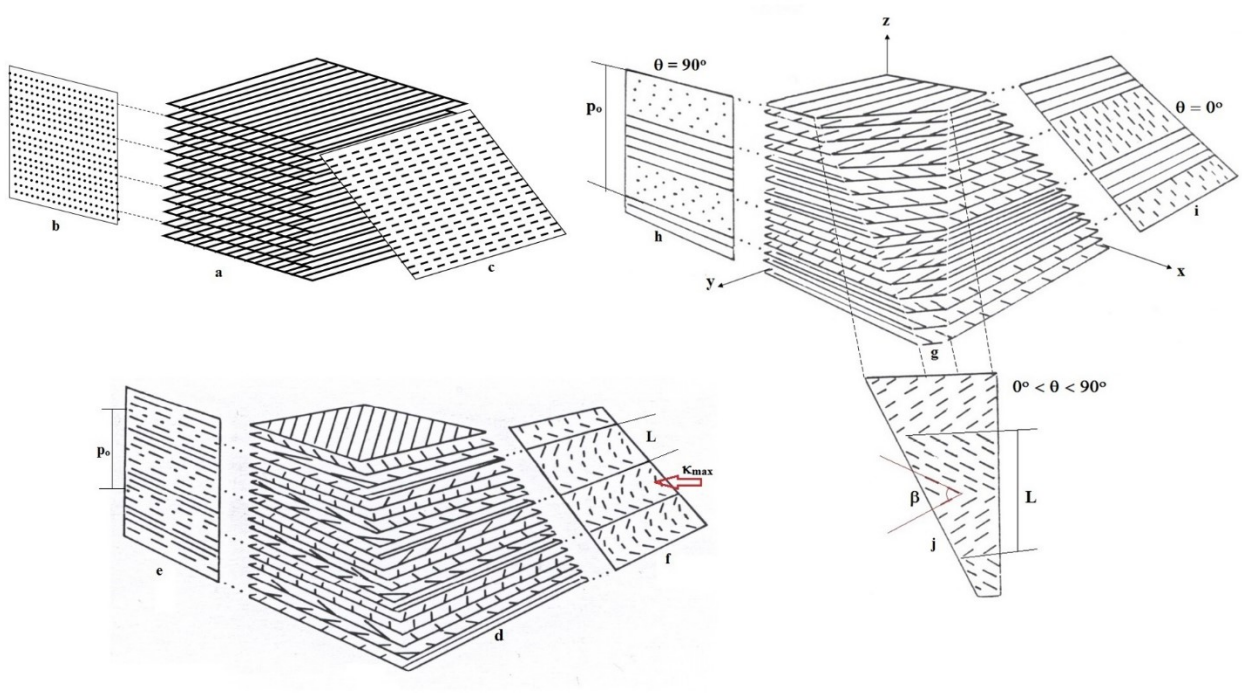

Figure 1.2. Nematic (a-c), cholesteric (d-f), and orthogonal (g-j) plywood organizations with their respective cross sections where the arced patterns are projected for the cholesteric and herringbones are observed in the orthogonal plywoods.

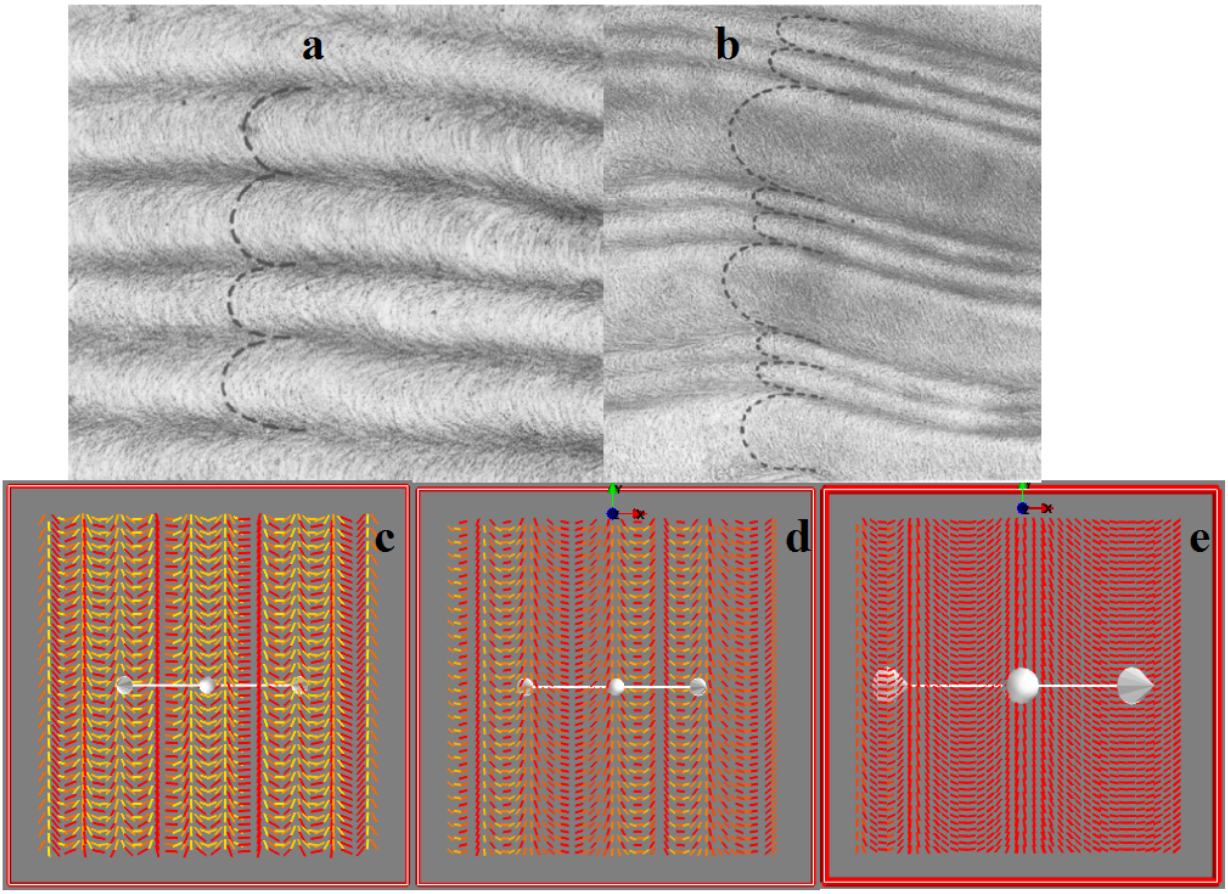

Figure 1.3. Experimental observations (a-b) of biological plywoods where the arced patterns are visible with homogeneous (a) and bimodal (b) arcs (adapted from [28]) with in silico visualizations of constant p_o (c), double pitch (d) and graded pitch (e).

Ideal plywoods correspond to an architecture where a linear relationship between the twist angle and the spatial coordinate is found where the constant slope of such relationship is a function of the cholesteric pitch and homogeneous arcs are projected. Deviations from such linear relationships are quite common in Nature [47]. These types of arrangements have been denominated as non-ideal helicoids or plywoods where some examples of non-idealities include graded plywoods as observed in the Aurigans Scarab [26] cuticle showing a complex non-monotonic graded pitch with an increase of the pitch followed by a steep decrease with a later

quasi-constant pitch region which is followed by a less steep increase. Another example is encountered in the endocarps of fruits like plums, peaches, among others where a double-pitch system is identified and oblique sections project one large arc followed by two smaller arcs where 180^{o} rotation is encountered in the former and a full 360^{o} in the latter [28] , which can be regarded as an ideal plywood in a piecewise manner. Ideal and non-ideal plywoods are schematically depicted in figure 1.4 in terms of the twist angle and the pitch profile. The former example leads to inhomogeneous arcs and the latter to intercalated arcs with different periodicity.

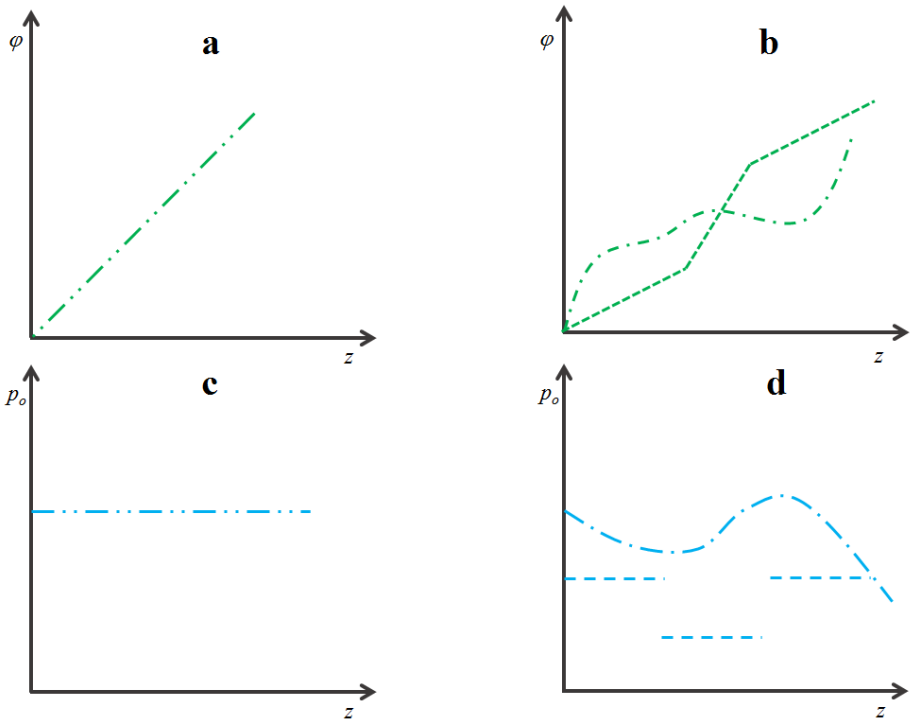

Figure 1.4 Schematic representation of ideal plywoods (a & c) with a linear relationship between the twist angle and the spatial coordinate z leading to a constant pitch throughout z and non-ideal plywoods (b & d) where a nonlinear relationship between the twist angle and z lead to a graded pitch.

Deviations to orthogonal plywoods have been classified as quasi-orthogonal plywoods where angles of 45^{o} can be encountered and also what might seem to be a linear combination of ideal TPA and orthogonal plywood have been reported where two lagged phase helices are interweaved and is manisfested as interleaved arced patterns [1]. Table 1 shows examples of natural biological plywoods along constitutive mesogen and the displayed arrangement.

Table 1.1. Biological plywoods and their respective building block.

Nematic Plywood	TPA (Ideal and non-ideal)	Orthogonal Plywood
Intermediate layer in beetle cuticle (chitin) [40]	Crab cutible [2]	Eremosphera viridis cell wall (cellulose) [29]
Nails (keratin) [45]	Endocarp of plums prunus sativum (cellulose) [28]	Paralvinella grasslei (annelid) cuticle (collagen) [48]
Tendon fibrils (collagen) [49]	Aerenchyma cell wall (cellulose) [28]	Pagrus major scales (collagen) [25]
	Stone cells in pears pyrus malus (cellulose) [28]	Oryctes rhinoceros eggshell (chitin) [50]
	Bone osteons (collagen) [23]	Bird cornea (several species) (collagen) [1]

In spite of being a 2D projection of the full 3D organization of a plywood, these patterns include information regarding the helical axis and the cholesteric pitch, however they have not been quantified or described completely given the fact the observed characteristics of the patterns is a matter of perspective, therefore two plywoods with different pitch might give rise to similar periodic structures as analyzed in goniometric studies where arcs even seem to disappear [51], phenomenon which was denominated as “trompe à l’oeil”. An additional variable is then required to differentiate the plywoods in such cases and remove the apparent degree of freedom and the full description can be used as a characterization technique that do not rely on optical properties [52], which could be a drawback for certain biological plywoods.

The scope of the work presented here is on solid and in vitro analogues, specifically the transformation of in vitro analogues to a biological plywood through a multi-stage process to be detailed in section 1.5 where defect-free collagen films presenting the frozen cholesteric structure are obtained from acidic dilute solutions. Moreover, the aim is also to fully describe the projected patterns for ideal, non-ideal and orthogonal plywoods, where the arced patterns can be observed in oblique incisions of the obtained collagenous films. This description is used to propose a characterization procedure for biological plywoods based on the relationships of the characteristics of the arced or herringbone patterns with the material properties such as the pitch.

1.5 Film Formation Processes

There is a great interest in the development of defect-free thin film materials for the aforementioned reasons and applications, however experimental evidence has shown this task is far from trivial. Some experimental efforts have indeed achieved the formation of such materials where the application of external fields are used, such fields are known for modifying the orientation of the building blocks and can be used to induce specific orientations depending on the magnitude and direction of such field [53, 54] and provide a control of the helical axis and the cholesteric pitch [14, 55]. For the particular case of collagen, several approaches have been used in the thin film formation process for controlling the helical axis such as electrochemical induced alignment [6, 56], magnetic field alignment [57, 58, 59], flow induced alignment [6, 13, 60, 61] and light irradiation [55].

Hydrodynamic forces are a relatively simple approach since an additional field is not required like a magnetic field for instance, making it a more attractive and practical for large-scale production. Typically, a collagen solution is deposited on a substrate where uneven contributions of shear and extensional components are encountered. Dilute [13] and concentrated [6] solutions have been used for the purpose. It is worth noting the resulting microstructure was reported to strongly depend on the rheological type of the precursor, i.e. whether the precursor presents a viscous-like or a gel behavior [10] which also impacts its ease of manipulation. In terms of liquid crystalline rheology, a crucial aspect is to determine whether the material aligns with the direction of the flow or presents time dependent behavior such as wagging or tumbling. On the one hand, dilute collagen solutions are characterized for being isotropic at rest but show flow-birefringency. Rheo-SAXS experiments report a flow aligning behavior where the scalar order parameter is a function of the shear rate, the higher the shear rate, the sharper the scattering intensity distribution. Once the flow ceases, the isotropic state is recovered [33]. On the other hand, concentrated solutions exhibit banded textures, which are characteristic of a tumbling behavior, and irreversible out-of-plane orientations are observed after flow cessation. Figure 1.5 presents the aforementioned dynamic behavior through scattering intensities and the observed textures in capillary suction of concentrated solutions. Hence, experimental and theoretical predictions regarding its dynamic behavior place dilute solutions as better suited precursors [33, 41] for the formation of defect-free collagen films. However the cost to be paid is the incorporation of an additional process to remove the solvent in order to observe the phase transition i.e. cross the threshold depicted as the grey line shown in the partial phase diagram presented in figure 1.6. For building blocks like collagen where the chemical stability of the helix can be compromised through temperature variations [3, 23], such process

should be isothermal, i.e. the driving force must be based on changes in concentration of the solvent to be removed from the deposited film.

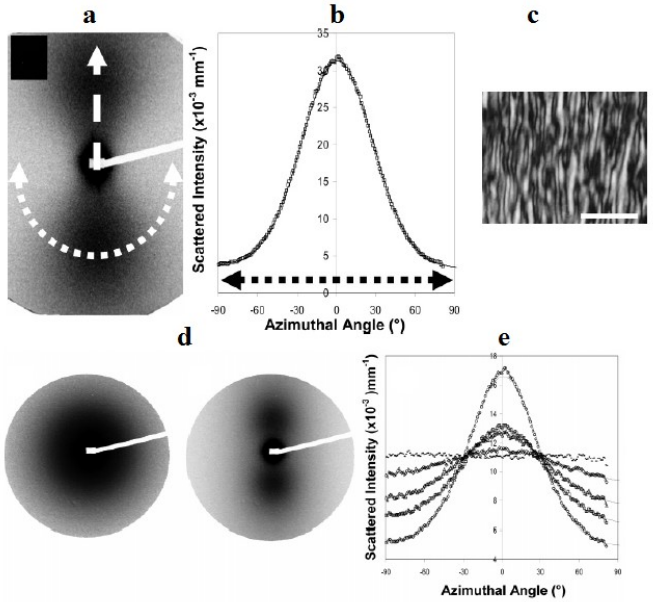

Figure 1.5 Experimental SAXS profiles for concentrated solutions (a-c) with the SAXS patterns (a), the extracted scattering profile (b) and the observed texture through capillary suction (c) and for dilute solutions (d-e) with the SAXS patterns at rest and under shear (d) and the scattering profile whose peak is sharper with increasing shear rate (e). (Adapted from [33])

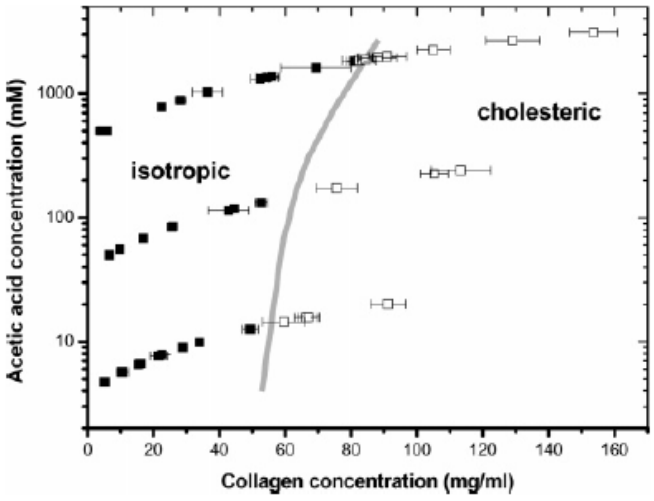

Figure 1.6 Partial phase diagram dividing the isotropic and the cholesteric regions given in terms of acetic acid and collagen concentration in mM for the former and mg/ml for the latter (adapted from [33]).

In the process reported by Kirkwood and Fuller [13], shown in figure 1.7, a dilute collagen I solution is deposited on a substrate by a modified blade coating technique, where the substrate and an injecting device move in opposite directions which creates an extensional contribution that strongly aligns the mesogens in the direction of the flow while the stresses developed inside the injecting device provides the shear contribution. After the flow deposition, the film is exposed to a filtered airflow in a laminar flow hood at constant temperature whose objective is to transport the solvent out the film. As the solvent evaporates, the concentration of collagen increases and eventually a para-nematic-to-cholesteric phase transition can be observed, as the state of the mixture crosses the binodal line shown in Fig.1.6; the para-nematic phase is the flow-aligned dilute collagen solution obtained from the flow process. The sought after results shown in Fig. 1.7 (c) is a perfectly aligned homogeneous helix of direction h everywhere.

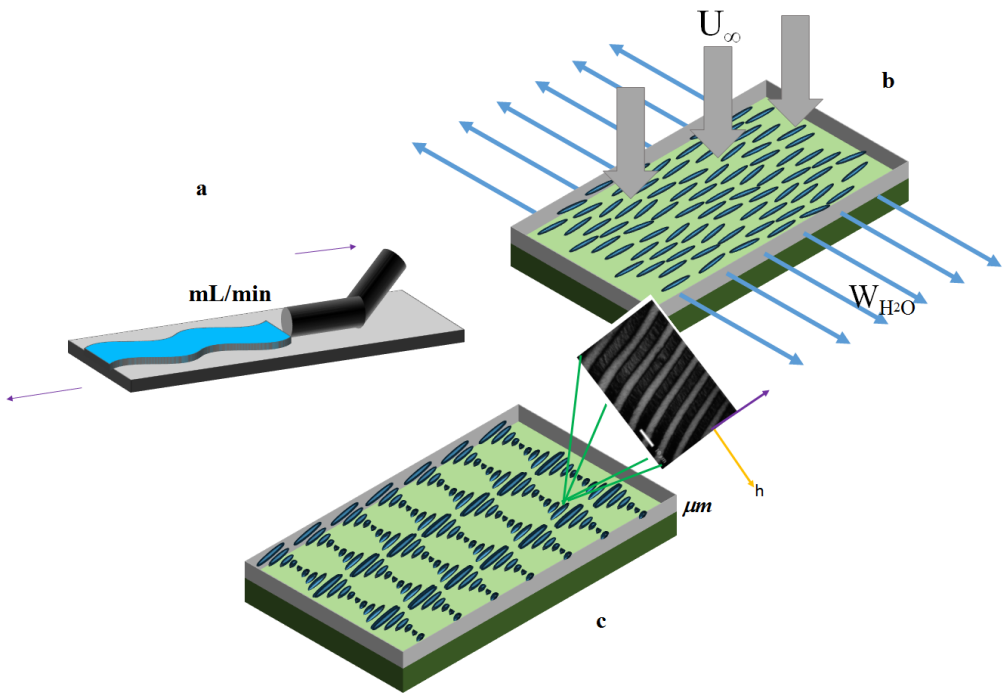

Figure 1.7 Schematic representation of the process reported by Kirkwood and Fuller [13] where the flow deposition kinematics (a) present a combination of shear and extensional contributions followed by the drying of the deposited film (b) with an airflow of filtered air with a constant far-field velocity and the resulting film (c) showing a lying helix perpendicular to the flow deposition with constant pitch and homogeneous helical axis (Adapted from [13]).

The phase transition was reported to begin at the edges of the substrate where the contact line is assumed to be pinned and proceeds to the central region of the film. Some results indicate three different regions can be present in the collagen stripes, two cholesteric regions close to both edges of the substrate separated by the central region where the para-nematic phase relaxed to isotropic [13]. This clearly indicates the mass transfer process is responsible for the resulting formed mesophase but this effect has not been analyzed yet.

Even when previous work [13] reports the formation of defect-free films successfully, several aspects regarding the kinematic conditions of the pre-aligned phase and the correlation between the phase transition driving forces and the resulting microstructure of the film have not been evaluated. The description and knowledge of these complex phenomena occurring in the formation of the collagen films is of great importance to provide insights and feedback to current strategies leading to an improvement in the development of these materials which forms part of the present work and will be detailed in sections 1.7 through 1.9.

1.6 Theoretical Modeling Background

The modeling and computational engineering used here is composed of a three stage sequence: (1) rheology and fluid mechanics based on Landau-deGennes, (2) film formation by phase ordering-dehydration based on Landau-de Gennes and diffusion mass transfer, and (3) film microstructure characterization by computational geometry and visualization, summarized below.

1.6.1 Landau – de Gennes Mesoscopic Theory

A complete description of liquid crystals in general is achieved through the use of the Landau – de Gennes Q tensor mesoscopic theory where the definition of **Q** is the second moment of an orientation distribution function $\rho(\mathbf{u})$ (ODF). This tensor has the properties of being symmetric and traceless and includes information regarding the preferred directions through the director orthonormal triad **n**, **m** & **l** and the degree of alignment with respect to **n** & **m** through the uniaxial and biaxial scalar order parameters S & P as expressed in eqn. (1.1 a-d). As any other order parameter, S & P vanish in the disordered state and the maximum value indicates a perfect alignment state. The ODF and uniaxial order parameter are schematically depicted in figure 1.8. Other theories have been used for describing liquid crystals mainly the Leslie – Ericksen [62, 63] but lacks to describe changes of S and describes the dynamics of **n** only [64 – 66].

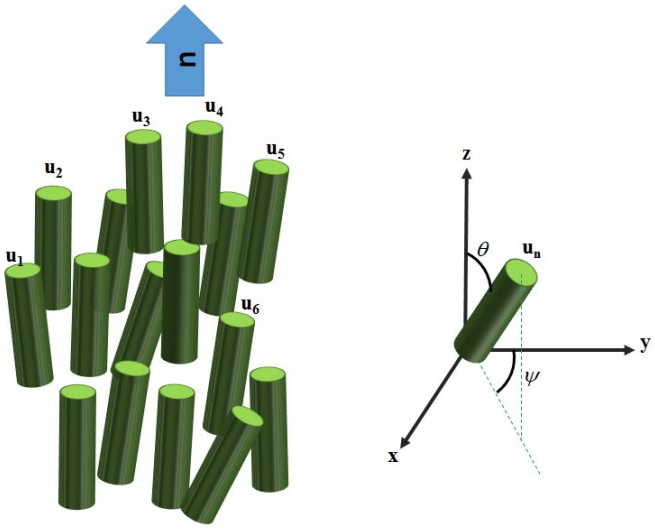

Figure 1.8 Schematic representation of the concept of the ODF where a collection of elongated objects each with a particular orientation $\mathbf{u}_i$ which averaged leads to the director **n** and the Eulerian angles θ and ψ in a coordinate system where the z direction points in the same direction as the director.

$$\mathbf{Q}=\int\left(\mathbf{uu}-\mathbf{I}/3\right)\rho(\mathbf{u})d^2\mathbf{u};\;\;\mathbf{Q}=\mathbf{Q}^T;\;tr(\mathbf{Q})=0;\mathbf{Q}=S\left(\mathbf{nn}-\frac{\mathbf{I}}{3}\right)+\frac{P}{3}\left(\mathbf{mm}-\mathbf{ll}\right)$$
$$-1/2\le S\le 1;-3/2\le P\le 3/2 \qquad (1.1\text{ a-d})$$

Liquid crystalline phases are known to be affected by external fields and forces. The focus in the present work is in flow processes where flow induced alignment (FIA) is observed. The coupling between the Q tensor and the applied field have been described through the Landau – de Gennes theory [15]. The phenomenological equation is derived from a linear relationship between the relevant fluxes and driving forces resulting in eqn. (1.2) which is derived in Chapter 2 and Appendix B [44, 67 – 69]:

$$\hat{\mathbf{Q}}=-6\overline{D}_r\mathbf{H}\left[\mathbf{Q},\nabla\mathbf{Q}\right]+\mathbf{F}\left[\beta,\mathbf{Q},\mathbf{A}\right];\hat{\mathbf{Q}}=\frac{D\mathbf{Q}}{Dt}+\mathbf{W}\cdot\mathbf{Q}-\mathbf{Q}\cdot\mathbf{W};\nabla\mathbf{v}=\mathbf{A}+\mathbf{W} \qquad (1.2)$$

where **v** is the velocity, **A** and **W** are the rate of strain and vorticity tensors. This nematodynamics model represents a balance between two terms: on the one hand, the so-called molecular field $\mathbf{H}\left[\mathbf{Q},\nabla\mathbf{Q}\right]$ which is the contribution driving the system to its equilibrium configuration and on the other hand the flow contribution $\mathbf{F}\left[\beta,\mathbf{Q},\mathbf{A}\right]$ which provides the coupling between the macroscopic kinematics to the order and orientation of the material. The former is related to the Brownian motion, particularly to the process of maintaining or restoring the orientation distribution of the mesophase and the crucial physical property is the rotational diffusion constant D_r [70, 71]. Moreover, the molecular field is the functional derivative of the total free energy, given in Appendices B and D, with respect to **Q** where the free energy is given by the sum of two terms:

$$F=\int f dV;f=f_h+f_{el};f_h=f_h\left(U=\frac{\varphi}{3\varphi^*},\mathbf{Q}\right);f_{el}=f_{el}\left(L_i,\mathbf{Q},\nabla\mathbf{Q}\right) \qquad (1.3)$$

The homogeneous contribution is proportional to the nematic potential, a dimensionless mesogen concentration with respect to the critical value to observe a phase transition, and a Landau expansion of invariants of **Q**. For low mesogen concentration, the isotropic is the stable state and as the concentration increases the cholesteric becomes the stable thermodynamic state as depicted in figure 1.9. The inhomogeneous contribution contains information regarding elastic deformation that might arise and is a function of gradients of **Q**. For cholesterics [41, 72, 73], two elastic constants have been used to describe the system: L_1 associated to the helical axis and the pitch, and L_2 englobing other modes of deformation as schematically depicted in figure 1.10.

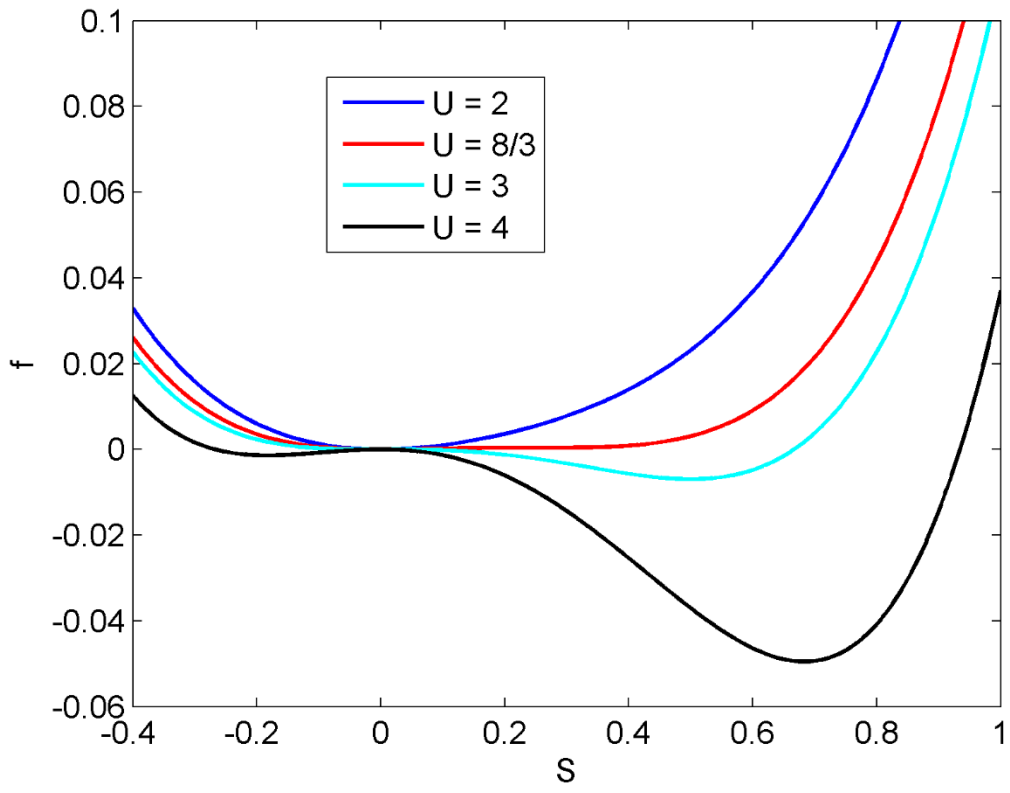

Figure 1.9 Homogeneous free energy as a function of S for increasing mesogen concentration where the blue curve represents the isotropic as stable state and the black curve the cholesteric is the minimum energy configuration and intermediate values are metastable.

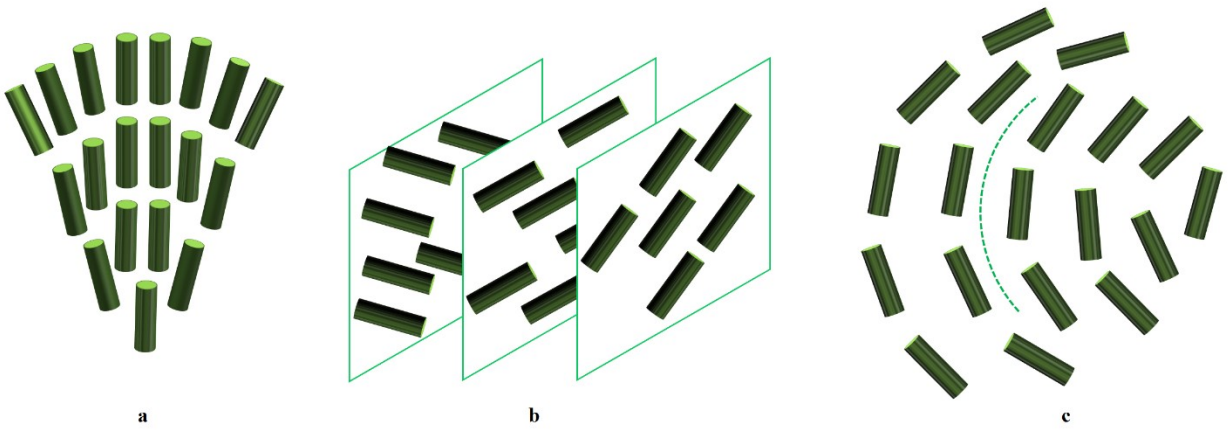

Figure 1.10 Schematic representation of the elastic deformation modes present in liquid crystals with splay (a), twist (b) and bend (c). (Adapted from [15])

The flow contribution **F** is a function of appropriate tensor products of **Q** and **A**, the symmetric part of the velocity gradient and is modulated by the rheological shape parameter β that ranges between 0 and 1 for rod-like mesogens. This parameter is a function of the aspect ratio and tends to 1 as the aspect ratio increases.

The full description of a material depends on determining the crucial properties such as D_r and β. The latter allows to obtain the reactive parameter curve defined as $\lambda = \frac{\beta\left(4+2S-S^2\right)}{6S}$ which determines for which values the material presents flow aligning ($\lambda > 1$) or tumbling behavior ($\lambda < 1$) under simple shear flow. Finally, appropriate kinematic conditions should be imposed according to the objective of the analysis. In the present case, a wide variety of kinematic conditions are to be explored to assess the microstructure change under such conditions. The four roll mill apparatus, which was invented by G.I. Taylor is known for being capable of producing different types of 2D flow and varying the intensities which is schematically depicted in figure 1.11. The sample is loaded in the central region and is surrounded by four rolls which can rotate

independently and produce a wide variety of flow types and intensities by varying the directions of rotation and the angular velocities. The expression for the velocity gradient is expressed in eqn. (1.4) where two parameters are introduced κ and E where changes in the former lead to changes in the flow type and the latter impact the intensity of the flow. The kinematic parameter κ ranges within [-1, 1] where the lower limit leads to pure rotational flow and the higher to pure planar extensional flow and the case of simple shear flow is $\kappa = 0$.

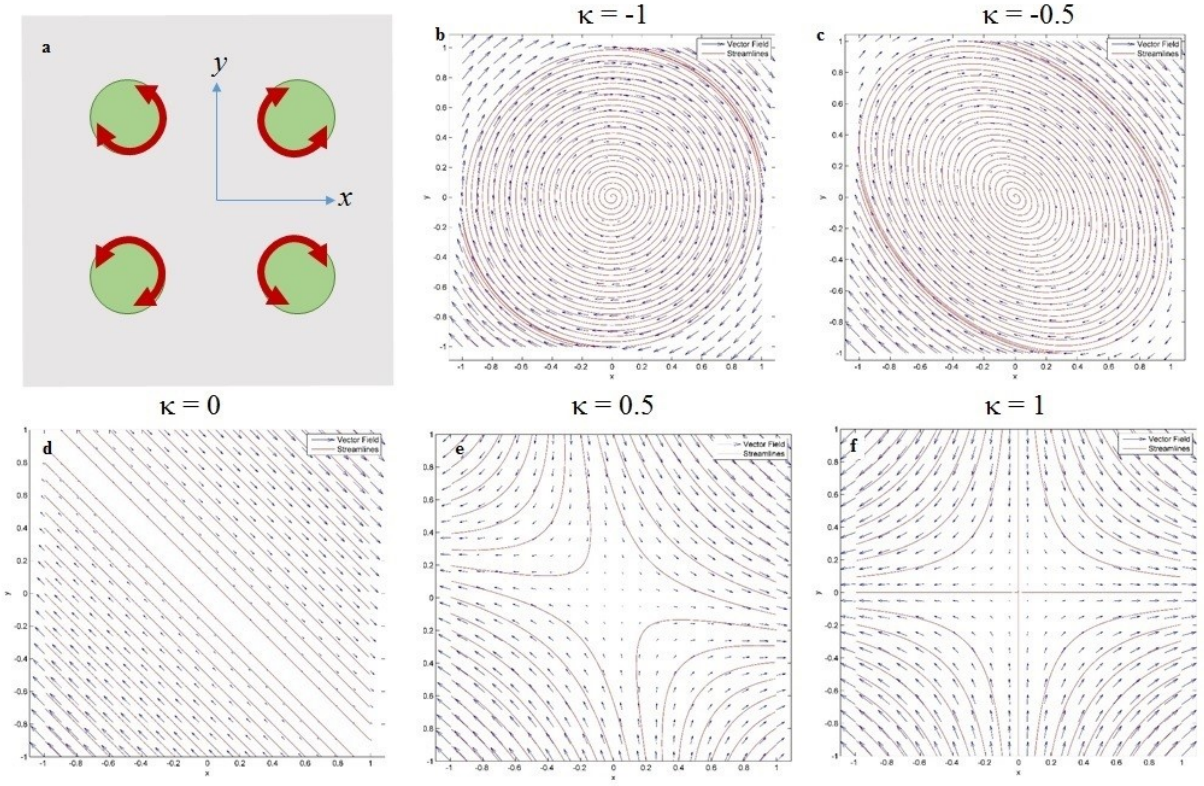

Figure 1.11 Schematic representation of the four roll mill kinematics (a) and some of the flow types that can be create by changing the value of the kinematic parameter (b-f).

$$\nabla \mathbf{v} = \frac{E}{2}\begin{pmatrix} 1+\kappa & -(1-\kappa) & 0 \\ 1-\kappa & -(1+\kappa) & 0 \\ 0 & 0 & 0 \end{pmatrix}; \mathbf{A} = \frac{E}{2}\begin{pmatrix} 1+\kappa & 0 & 0 \\ 0 & -(1+\kappa) & 0 \\ 0 & 0 & 0 \end{pmatrix}; \mathbf{W} = \frac{E}{2}\begin{pmatrix} 0 & -(1-\kappa) & 0 \\ 1-\kappa & 0 & 0 \\ 0 & 0 & 0 \end{pmatrix} \qquad (1.4)$$

When no external fields are applied to the material, the flow contribution **F** from eqn. (1.2) vanishes and the time derivative of **Q** is proportional to the molecular field only. In order to account for the mesogen increasing concentration during evaporation, we assume a binary system composed of the mesogen and the solvent where the relationship $\varphi_c + \varphi_w = 1$ is always valid. A transient mass transfer conservative equation is used in terms of an anisotropic mass flux coupling **Q** with gradients of the solvent concentration expressed in eqn. (1.5) [74]. The full model is derived in chapter 3 and Appendix D.

$$\frac{\partial c_w}{\partial t} = -\nabla \cdot \mathbf{j}_w ; \mathbf{j}_w = -\left(D_{iso} \nabla c_w + D_{ani} \mathbf{Q} \cdot \nabla c_w \right)$$
$$D_{iso} = \frac{D_{\parallel} + 2D_{\perp}}{3} ; D_{ani} = D_{\parallel} - D_{\perp} \qquad \text{(1.5 a-c)}$$

This information is introduced in the nematic potential U and is now a function of time and space. Therefore, the single minimum of the initial para-nematic is transformed into the double minima where the cholesteric is the stable state as shown in figure 1.9. To ensure mass conservation, as the solvent leaves the system the film experiences a volume reduction. The height decrease of the film is derived from the mesogens' mass conservation and is proportional to the flux leaving the film and the respective cross section.

1.6.2 Microstructure Geometric Description

The arced patterns shown in Fig.1.2 are accessible only through oblique incisions to a cholesteric helix normal to the x – y plane. Since the pitch and the incision angle are unknown the periodicity of the patterns is insufficient to determine the pitch. To find the missing equation, we use the information contained in the actual geometry of the patterns. To describe these patterns we take the projection of the director field to a hypothetic x – s plane that simulates the cross section which

allows us transform the director field **n** into the projected field **u** as depicted in figure 1.12. The components of the projected director field can be used in a streamline approach to obtain the trajectories of the arced patterns by means of the boundary value problem stated in eqn. 1.6.

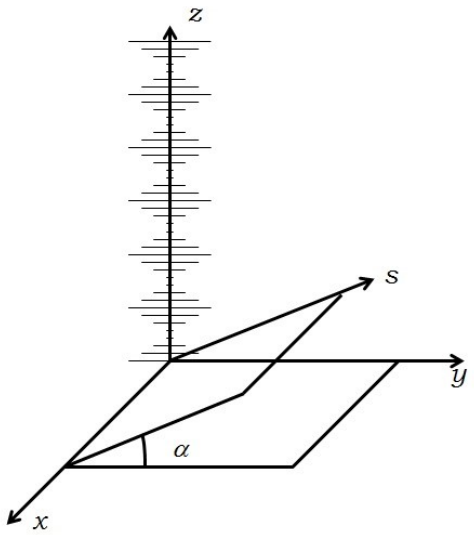

Figure 1.12. Schematic representation of a director field lying in the plane x – y where the helical axis is parallel to the z direction and the incision plane where the arced patterns are visible in the plane x – s.

$$\frac{dx}{ds} = f\left(\alpha, p_o, s\right); x(s=0) = x_o \tag{1.6}$$

The curvature of the periodic structures observed can be calculated by the conventional definition expressed in eqn.(1.7) and will be helpful to remove an apparent degree of freedom and provide a unique calculated value of the pitch with one pair of periodicity and curvature values.

$$\kappa(s, L, \alpha) = \frac{\dfrac{d^2x}{ds^2}}{\left(1+\left(\dfrac{dx}{ds}\right)^2\right)^{3/2}} \tag{1.7}$$

Due to the geometric similarity of the herringbone patterns seen in cornea and algae, similar expressions are obtained for the periodicity of the herringbones and an expression for the aperture angle instead of the curvature is required. The dot product of the projection of two orthonormal vector provide a measure to determine the angle herringbone angle where the projection is parameterized by a unit normal vector **k**, expressed in eqn. 1.8:

$$\boldsymbol{\delta}_i^p = \left(\mathbf{I} - \hat{\mathbf{k}}\hat{\mathbf{k}}\right)\cdot\hat{\boldsymbol{\delta}}_i ; \boldsymbol{\delta}_x^p \cdot \boldsymbol{\delta}_y^p = f(\beta,\alpha) \tag{1.8}$$

In summary, the geometric modeling developed in this work provides a direct 3D microstructure reconstruction from 2D slices

.

1.7 Need and Opportunity for Computational Modelling

The underlying principles in non-equilibrium self-assembly processes remain still obscure, presenting an opportunity for simulation work to explore the stages involved in the film formation process [13] in order to control and design optimal processing conditions.

Specifically, the understanding on the response of the microstructure in a general type of kinematics would allow to predict which combination of flow type and intensity of deformation should be applied to a dilute collagen solution to obtain a properly pre-aligned and ordered structure that precedes solvent evaporation and helical axis formation.

Through modelling and simulations it is also possible to explore the conditions for the helical axis formation through water removal without the need of expensive and complex experiments and narrowing the process variables. Moreover, the evaluation and correlation between the driving

forces and the resulting microstructure can also be obtained through numerical experiments. Visualization of the resulting material submitted to a set of process conditions can evaluate and determine whether the material possesses the required morphology or not.

These visualization techniques where the arced patterns are visible can also be applied to materials encountered in Nature and provide additional tools for characterising and understanding the morphology of these materials. Given the fact that each arrangement has its particular pattern projected to an incision plane and that characteristics of these patterns are a function of the pitch and the helical axis, this can be used as a complementary characterization tool that allow to understand the material's morphology and being capable of reconstruct the full 3D structure based on the cross sections.

1.8 Thesis Objectives

The main objective of this thesis is to model and simulate the stages involved in the formation of defect-free collagen I films through the non-equilibrium multi-step self-assembly process and explore the microstructure of the resulting material through geometric modelling and develop a characterization procedure based on the characteristic projected patterns to oblique incisions of the full 3D structure.

The specific objectives are the following:

1. Model and simulate the flow induced orientation of dilute solutions representing the initial stage of the film formation process using a general type of kinematics to understand the response of such solutions under several kinematic conditions.

1.1 Estimate crucial effective geometry dependent material properties consistent with experimental shear induced alignment.

1.2 Explore the influence of diverse kinematic conditions to the microstructure and ordering of the system that allows understanding the full state of orientation of the precursors.

1.3 Determine the kinematic conditions to which the dilute collagen solutions should be submitted in order to become appropriate precursors for later solvent evaporation.

2. Model and simulate the transformation of the deposited para-nematic phase into the cholesteric phase through evaporation.

2.1 Develop a self-assembly model coupled with mass transfer to take into account the solvent evaporation at constant temperature.

2.2 Understand the formation of the helical axis from a para-nematic phase and the microstructure of the resulting plywood under diverse mass transfer resistances.

2.3 Determine the parametric conditions that allow the formation of defect-free films from the dynamically aligned para-nematic phase.

3. Model and understand the projected 2D patterns of the ideal and non-ideal twisted plywood architecture obtained from oblique slices.

3.1 Relate the characteristic projected 2D patterns to each type of plywood.

3.2 Explore through geometric modelling and 3D visualization tools the influence of the characteristics of the projected pattern characteristics.

4. Develop a characterization procedure for the explored plywoods based on characteristic patterns.

4.1 Propose a robust characterization procedure that allow understand and reconstruct the full 3D structure.

4.2 Test and validate the proposed characterization procedure with in vivo and in silico samples.

4.3 Provide recommendations and best practices to be adopted in the use of the characterization methodology.

1.9 Thesis Organization

Chapters 2 and 3 focus on the flow deposition and drying stages respectively of the process reported by Kirkwood and Fuller [13]. Chapters 4 – 6 are focused on the geometric modeling and characterization procedure for biological plywoods. A more detailed organization of the thesis is given in the flowchart shown in figure 1.13.

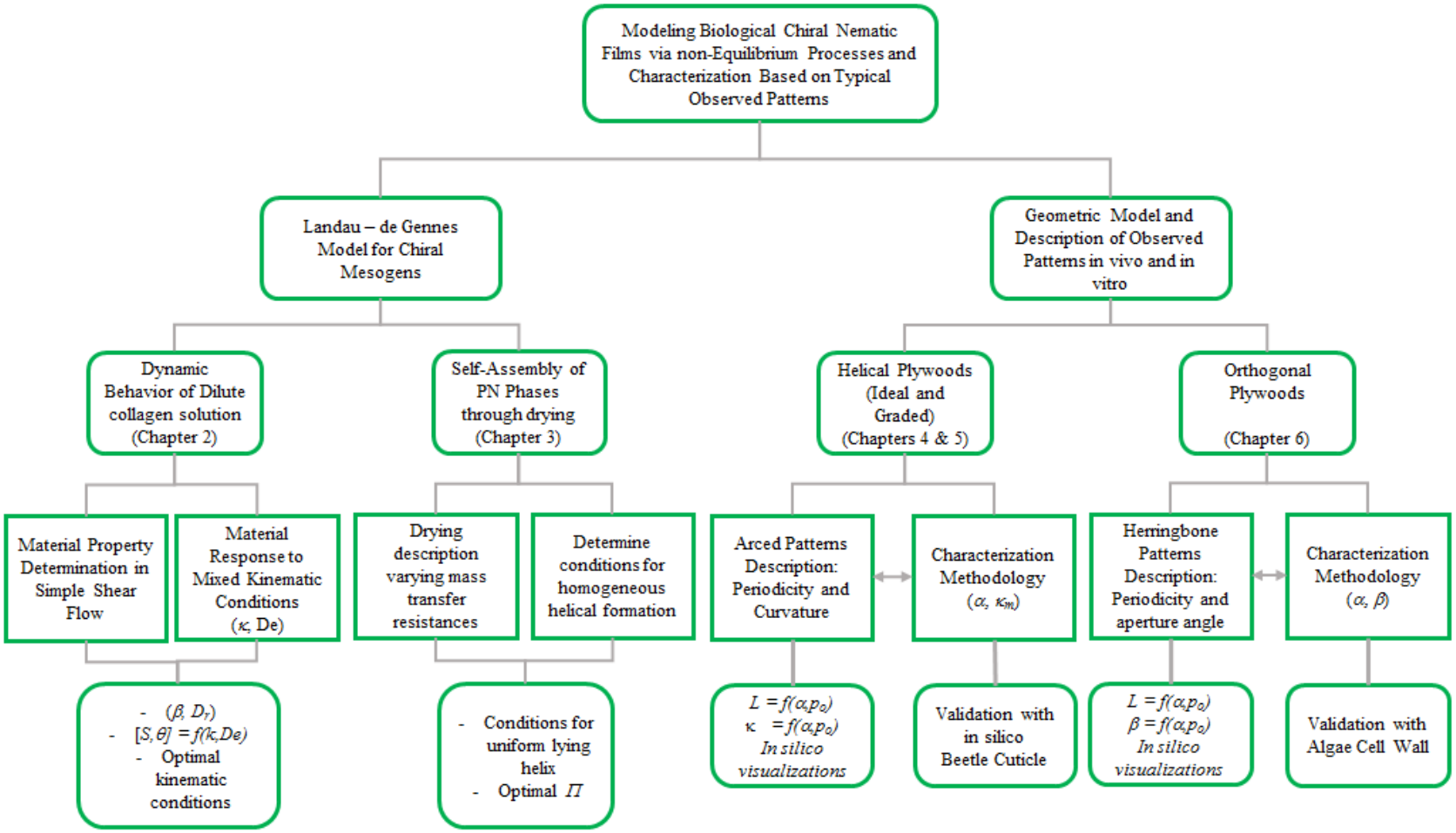

Figure 1.13. Thesis organization flowchart divided by chapter and the objectives are shown in the rectangles.

The following is a brief summary of each of the chapters composing this thesis:

Chapter 2. Theory and Simulation of Cholesteric Film Formation Flows of Dilute Collagen Solutions.

This chapter provides the material property determination of dilute collagen solutions used in non-equilibrium film formation processes such as the one reported by Kirkwood and Fuller [13] and the microstructure response of such solutions under a wide variety of kinematic conditions. The experimentally guided property determination allowed the estimation of effective shape dependent physical properties like the rotational diffusivity constant and rheological shape parameter. Such properties were used as inputs to a general nematodynamics model using the four roll mill kinematics, allowing to obtain the microstructure response of the dilute solutions under conditions that include as limit cases the well-known: 1) planar extensional flow, 2) simple shear flow, and 3) pure rotational flow and also unequal contributions of the aforementioned limit cases, as expected in real polymer processing operations, depending on the value of a kinematic parameter. The kinematic conditions to which these precursors should be submitted in order to promote a homogeneous lying helix rather than a non-uniform helix are given in a phase-space expressed in terms of the alignment angle and the scalar order parameter. The resulting structure are used as initial condition in Chapter 3, where the para-nematic phase is converted into the chiral nematic with changes in the nematic potential as driving force.

Chapter 3. Biological Plywood Formation from Dilute Para-nematic Liquid Crystalline Phases

This chapter provides the modeling and simulations of the resulting dynamically aligned para-nematic phase obtained through the kinematic conditions specified in Chapter 2 submitted to water

removal. A 2D Landau – de Gennes model is developed with a time dependent concentration profile used in the nematic potential to simulate the increase of the mesogen concentration. The model is coupled with a mass transfer equation for the solvent considering anisotropic diffusion and the volume reduction is derived from the mesogen mass conservation. The initial condition is the para-nematic state in all the simulations. The phase transition is induced from the edges and depending on the mass transfer resistance accounted by the dimensionless number Π, three regimes are observed: i) homogeneous helical axis, ii) polydomain helical axis, and iii) polygonal texture found in the central region of the film. The second and third indicate the helical axis formation time is not synchronized with the solvent diffusion, which is the crucial aspect and key point in the control of helix formation processes.

Chapter 4. Structure Characterisation Method for Ideal and non-Ideal Twisted Plywoods.

The resulting material from Chapter 3 is expected to have a helical axis present that when completely dried will lead to a biological plywood. Regardless of the origin of the plywood (man-made or present in Nature) the chiral ordering manifests into arced patterns when an oblique incision is made in the material. These projections depend on the incision angle and the magnitude of the helical pitch. Characteristic measurements as the periodicity of the arcs and the maximum curvature are used to characterize the material when the pitch is unknown leading to a unique prediction of the pitch. In silico visualizations are used to explore the effect of the pitch and the incision angle on the observed arc and a characterisation methodology is proposed in samples where these characteristic patterns are visible.

Chapter 5. Chiral Graded Structure in Biological Plywoods and in the Beetle Cuticle.

This chapter implements the proposed methodology from chapter 4 to the case of the beetle cuticle by means of in silico cross sections. These artificially created incisions were necessary due to the lack of experimental visualizations of the arced patterns which were created since the graded pitch profile was reported recently. Further analysis of the model furnished a phase plane of the observed patterns is given in terms of the periodicity and the reciprocal maximum curvature where constant pitch hyperbolas appear. Interestingly, the regions of the hyperbolas approaching the asymptotes correspond to the low angle incisions leading to ill-conditioning. Hence, incisions at higher angles are recommended to improve accuracy and being capable of characterizing a wider region of the graded pitch structure.

Chapter 6. Geometric Reconstruction of Biological Orthogonal Plywoods

Herringbone patterns are found from slices of orthogonal plywoods that presents abrupt changes in the orientation of approximately 90^{o} in a layer-like fashion. Analogously to the arced patterns, the herringbones' characteristic measurements as the periodicity and aperture angle are used in the characterization and geometric reconstruction of orthogonal plywoods where the methodology is capable of predicting the layer thickness. To validate the methodology, in silico orthogonal plywoods are created and validated with experimental results of a typical algae.

Chapter 7. Conclusions and Original Contributions to Knowledge

Finally, the key findings of the project are listed along with the original contributions to knowledge.

References (Chapter 1)

[1] Neville, A.C. *Biology of Fibrous Composites*. Cambridge University Press, London, 1993.

[2] Boulingand, Y. *Tissue and Cell*, 1972, **4**, 189-217

[3] Giraud-Guille, M.M.; Besseau, L.; Martin, R. *Journal of Biomechanics*. 2003, **36**, 1571-1579

[4] Giraud Guille, M.M.; Mosser, G.; Helary, C.; Eglin, D. *Micron*, 2005, **36**, 602.

[5] Price, J.C.; Roach, P.; El Haj, A.J. *ACS Biomater. Sci. Eng*. 2016 ***2***, 625-633.

[6] Paten, J.A.; Siadat, M.E.; Susilo, S.M.; Ismail, E.N.; Stoner, J.L.; Rothstein, J.P.; Ruberti, J.W. *ACS Nano*, 2016, ***10***, 5027-5040.

[7] Eglin, D.; Mosser, G.; Giraud-Guille, M.M.; Livage, J.; Coradin, T. *Soft Matter*, 2005, **1**, 129-131

[8] Zhang, Y.; Chodavarapu, V.; Andrews, M.P. *Proc SPIE 8258 Organic Photonic Materials and Devices XIV*, p 825808, 2012

[9] Albu, M.G.; Titorencu, I.; Ghica, M.V. *Collagen-Based Druge Delivery Systems for Tissue Engineering, Biomaterials Applications for Nanomedicine*. Intech, 2011

[10] Giraud-Guille, M.M; Nassif, N.N.; Fernandes, F.M.; Collagen-based materials for tissue repair, from bio-inspired to biomimetic. In: Materials Design Inspires by Nature: Function through Inner Architecture. Ed. Fratzl, P.; Dunlop, J.W.C.; Weinkamer, R. RSC. 2013. 107-127

[11] Wilson, S.L.; El Haj, A.J.; Yang, Y. Journal of Functional Biomaterials, 2012, **3**, 642.

[12] De Sa Peixoto, P.; Deniset-Besseau, A.; Schmutz, M.; Anglo, A.; Illoul, C.; Schanne-Klein, M.C.; Mosser, G. Soft Matter, 2013, **9**, 11241.

[13] Kirkwood, J.E.; Fuller, G.G. *Langmuir*, 2009, ***25***, 3200-3206.

[14] Park, J.; Noh, J; Salazar-Alvarez, G.; Scalia, G.; Bergstrom, L.; Lagerwell, J. *ChemPhysChem,* 2014, **15**, 1477-1484

[15] de Gennes, P.G.; Prost, J. *The Physics of Liquid Crystals*. Oxford University Press, 1993

[16] Donald, A.; Winder, A; Hanna, S. *Liquid Crystalline Polymers*.2nd Edition, Cambridge University Press, London, 1992.

[17] Oswald, P.; Pieranski, P. *Nematic and Cholesteric Liquid Crystals*. Taylor and Francis CRC Press, 2005.

[18] Larson, R.G. *The Structure and Rheology of Complex Fluids*, Oxford University Press, 1999.

[19] Livolant, F. *Journal de Physique,* 1986, **47**, 1813-1827

[20] Lydon, J. *Handbook of Liquid Crystals*, 2014, **14**, 1-45.

[21] Rey, A.D.; Herrera-Valencia. "Rheological Theory and Simulation of Surfactand Nematic Liquid Crystals," in *Self-Assembled Supramolecular Architectures*, Hoboken, John Wiley & Sons, 2012, pp. 21-77.

[22] Fratzl, P.; Giraud-Guille, M.M. *Progress in Materials Science.* 2007, **52**, 1263-1334

[23] Fratzl, P.; Giraud-Guille, M.M.: *Hierarchy in Natural Materials.* Wiley-VCH Verlag

[24] Giraud Guille, M.M. *Calcified Tissue International*, 1988, 42, 167.

[25] Ikoma, T.; Kobayashi, H.; Tanaka, J.; Walsh, D.; Mann, S. *Journal of Structural Biology*, 2003, **142**, 327.

[26] Libby, E.; Azofeifa, D E.; Hernández-Jiménez, M; Barboza-Aguilar, C.; Solís, A.; García-Aguilar, I.; Arce-Marenco, L.; Hernández, A.; Vargas, W E. *J. Opt.* 2014, **16**, 082001

[27] Sharma, V.; Crne, M.; Park, J.O.; Srinivasarao, M. *Science*, 2009, **325**, 449-451.

[28] Roland, J.C.; Reis, D.; Vian, B.; Satiat-Jeunemaitre B.; Mosiniak, M. *Protoplasma*, 1987, **140**, 75-91.

[29] Weidinger, M.; Ruppel, H. *Protoplasma*, 1985, **124**, 184-187

[30] Roland, J.C.: *Cell Walls '81: Proceedings of the Second Cell Wall Meeting* (D.G. Robinson and H. Quader, ed.). Wissenschaftliche Verlagsgesellschaft, 1981.

[31] Livolant, F.; Leforestier, A. *Progress in Polymer Science,* 1996, **21**, 1115-1164

[32] Giraud-Guille, M.M. *Biology of the Cell*, 1989, **67**, 97-101

[33] Gobeaux, F. ; Belamie, E.; Mosser, G.; Davidson, P.; Panine, P.; Giraud-Guille, M.M. *Langmuir*, 2007, ***23***, 6411-6417.

[34] Neville, A.C. *Biology of the arthropode cuticle*, Sprinter-Verlag, 1975

[35] Bouligand, Y. *Handbook of liquid Crystals,* Wiley-VCH, 1998

[36] Kleman, M.; Lavrentovich, O. *Soft Matter Physics: An Introduction*, Springer-Verlag, 2003

[37] Kleman, M.; Friedel, J. *Reviews of Modern Physics*, 2008, **80**, 61-115

[38] Lovelady, H.; Shashidhara, S.; Matthews, W. *Biopolymers*, 2013, **101**, 329-335

[39] Gauteri, A.; Russo, A.; Vesentini, S.; Redaelli, A.; Buehler, M. *Journal of Chemical Theory and Computation*, 2010, **6**, 1210-1218

[40] Allahverdyan, K.; Galstian, T.; Gevorgyan, A.; Hakobyan, R. *Optics and Photonics Journal* 2013, **3**, 17-22

[41] Rey, A.D. *Soft Matter*, 2010, ***6***, 3402-3429.

[42] Yasuda, K.; Saito, M.; Kaide, K. *Polymer International*, 1993, **30**, 393-400

[43] Navard, P.; Haudin, J. *Journal of Applied Pokymer Sciences*, 1986, **32**, 5829-5839

[44] Rey, A.D.; Herrera-Valencia, E.E. *Biopolymers*, 2012, **97**, 374-396

[45] B. Forslind and M. Lindberg, *Skin, Hair and Nails*, Taylor and Francis, 2005.

[46] Y. Bouligand, *Le Journal de Physique,*1969, **30**, 90-103.

[47] Aguilar Gutierrez, O.F.; Rey, A.D. *Journal of Renewable Materials,* 2016, **4**, 241-250

[48] L. Lepecheux, "Spatial organization of collagen in annelid cuticle: order and defects," *Biology of the Cell,* 1988, **62**, 11-31.

[49] Belamie, E.; Mosser, G.; Gobeaux, F.; Giraud-Guille, M.M. *J. Phys.: Condens. Matter*, 2006, **18**, S115-S129

[50] Furneaux, P.J.S.; Mackay, A.L.: *The insect Integument* (H.R. Hepburn, ed.). Elsevier, 1976.

[51] Livolant, F.; Giraud-Guille, M.M.; Bouligand, Y. *Biology of the Cell*, 1978, **31**, 159

[52] Baessler, H.; Labes, M. *Mol. Cryst. Liq. Cryst.* 1969, **6**, 419-422

[53] McKay, G. *Journal of Engineering Mathematics,* 2014, **87**, 19-28

[54] Kedney, P.; Stewart, I. *Letters in Mathematical Physics*, 1994, **31**, 261-269

[55] Zheng, Z.; Li, Y.; Bisoyi, H.K.; Wang, L.; Bunning, T.J.; Li, Q. *Nature*, 2016, **531**, 352-356.

[56] Cheng, X.; Gurkan, U.A.; Dehen, C.J.; Tate, M.P.; Hillhouse, H.W.; Simpson, G.J.; Akkus, O. *Biomaterials*, 2008, **29**, 3278-3288

[57] Torbet, J.; Malbouyres, M.; Builles, N.; Justin, V; Roulet, M; Damour, O; Oldberg, A; Ruggeiro, F; Hulmes, D.J. *Biomaterials*, 2007, **29**, 4268-4276

[58] Torbet, J.; Ronziere, M. *Biochemical Journal*, 1984, **219**, 1057-1059

[59] Andman-Passig, M; Shefi, O. *Nano Letters*, 2016, **16**, 2567-2573

[60] M. Paukshto, H. McMurtry, G. Fuller, Y. Bobrov and J. Kirkwood, "Collagen Materials, Films and Methods of Making Same". US Patent 0151563A1, 23 June 2011.

[61] Lee, P.; Lin, R.; Moon, J.; Lee, L. *Biomedical Devices*, 2006, **8**, 35-41

[62] Barbero, G.; Evangelista, L. *An Elementary Course on the Continuum Theory for Nematic Liquid Crystals*, Singapore: World Scientific, 2001.

[63] Stewart, I. *The Static and Dynamic Continuum Theory of Liquid Crystals*, London, UK: Taylor & Francis, 2004.

[64] Rey, A.D. *Journal of Rheology*, 2000, **44**, 855-869

[65] Rey, A.D. *Phys. Rev. E*, 1996, **53**, 4198

[66] Rey, A.D. *Journal of Chemical Physics*, 1996, **44**, 855-869.

[67] Tsuji, T.; Rey, A.D. *J. Non-Newt. Fluid. Mech.* 1997, **73**, 127-152.

[68] Grecov, D.; Rey, A.D. *Mol. Cryst. Liq. Cryst.* 2003, **391**, 57-94

[69] Singh, A.; Rey, A.D. *Rheologica Acta*, 1998, **37**, 30-45.

[70] Doi , M.; Edwards, S. *The Theory of Polymer Dynamics*, Oxford Science Publication, 1988.

[71] Doi, M. *Soft Matter Physics*, Oxford, UK: Oxford University Press, 2013.

[72] de Luca G.; Rey, A. D. *Phys. Rev. E,* 2004*, **69***, 011706

[73] de Luca G.; Rey, A. D. *Eur. Phys. J. E,* 2003*, **293***, 291-302

[74] Rey, A.D. *Mol. Cryst. Liq. Cryst.* 1997, **293**, 87-109

Chapter 2

2 Theory and Simulation of Cholesteric Film Formation Flows of Dilute Collagen Solutions

2.1 Preface

This chapter focuses on the the dynamic behavior of dilute collagen solutions. A material property determination is performed the results are consistent with previous experimental data. The nematodynamics model based on the Landau – de Gennes theory is derived and solved by imposing the four roll mill kinematics. The relationships between the type of flow and intensity with the order and orientation are established for the dilute mesogens. This chapter is reproduced from a published paper titled: "Theory and Simulation of Cholesteric Film Formation Flows of Dilute Collagen Solutions" co-authored with Prof. Alejandro D. Rey; Langmuir, 2016, 32, 11799. The results are the basis for the simulations performed on Chapter 3.

2.2 Summary

Dilute isotropic collagen solutions are usually flow processed into mono-domain chiral nematic thin films for obtaining highly ordered materials by a multi-step process that starts with complex inhomogeneous flow kinematics. Here we present rigorous theory and simulation of the initial precursors during flow steps in cholesteric collagen film formation. We first extract the molecular shape parameter and rotational diffusivity from previously reported simple shear data of dilute collagen solutions, where the former leads the reactive parameter (tumbling function) which determines the net effect of vorticity and strain rate on the average orientation and where the latter establishes the intensity of strain required for flow-birefringence, both crucial quantities for controlled film formation flow. We find that

the tumbling function is similar to those of rod-like lyotropic liquid crystalline polymers and hence it is predicted that they would tumble in the ordered high concentration state leading to flow-induced texturing. The previously reported experimental data is well fitted with rotational diffusivities whose order of magnitude is consistent to those of other biomacromolecules. We then investigate the response of the tensor order parameter to complex flow kinematics, ranging from pure vorticity, through simple shear, to extensional flow, as may arise in typical flow casting and film flows. The chosen control variable to produce precursor cholesteric films is the director or average orientation, since the nematic order is set close to typical values found in concentrated cholesteric type I collagen solutions. Using the efficient four-roll mill kinematics, we summarize the para-nematic structure-flow process diagram in terms of the director orientation and flow type. Using analysis and computation we provide a parametric envelope that are necessary to eventually produce well-aligned cholesteric films. We conclude that extensional flow is an essential ingredient of well-ordered film precursors with required Deborah numbers of the order of the unity.

2.3 Introduction

Collagen is the most abundant structural protein present in the human body exhibiting a hierarchical organization from the molecular to the macroscopic level [1 – 4]. Certain sufficiently concentrated collagenous solutions are biological liquid crystalline polymers [5, 6] where partial orientational and positional order is present due to the large molecular aspect ratio (L_p/D); here L_p is the persistence length and D the effective diameter [7, 8]. It has been long recognized collagenous based materials undergo self-assembly in vivo [2-4, 6, 9-11] and in vitro [9, 12-16]. Due to the ubiquity of collagen in vertebrates, this structural protein possesses the key ingredients

for applications that include drug delivery systems [18], tissue engineering scaffolds [12, 18, 19], and wound-healing biomaterials [19, 20] among others. The ability of controlling the order and orientation using collagen as building block could be really advantageous in the production, design and development of microstructurally ordered materials, however this is far from a trivial task. Some complications arise due to the difficulty of manipulating collagen solutions specially in concentrated solutions, moreover some of the resulting material properties strongly depend on the rheological type of precursor, whether the material was produced using a precursor with a viscous fluid-like character solution than a gel [19]. Several strategies to achieve ordered collagen macrostructures have been used, including electrochemical induced alignment (EIA) [14, 21], electrospinning (ES) [22] , magnetic alignment [23-26], flow-induced alignment (FIA) [14, 27-31], and light irradiation [32]. Coating flow-based processes are relatively simple processes where the combined effects of shear and extensional deformations and torques are capable of creating highly ordered phases. Additionally, these two processes do not require the application of external fields as an electric field in electrospinning or magnetic field induced alignment, making them more practical for larger-scale production and commercialization purposes. A remarkable example of coating-flow based process is the one reported by Kirkwood and Fuller [27-29] (to be detailed in section 2.3.1) whose first stage is a modified blade coating process of a dilute collagen solution, however the exact nature of all the operating principles remain unclear and not completely understood. Aspects such as reproducibility or precise control over the collagen orientation are crucial in these structured and organized materials. For processes making use of flow fields to pre-align the precursor solutions, one needs to assess the impact of the kinematic variables on the organization of the casted material, since the ultimate goal is to obtain relatively large volumes of uniform defect-free twisted plywood with specified helix axis. The twisted plywood is the

analogue of a cholesteric liquid crystals characterized by a helical axis vector **h** and a pitch p_o (or distance for 2π rotations) of the collagen triple helices about **h**.

Film formation using various transport phenomena can be classified as non-equilibrium self-assembly processes, having the advantage over equilibrium self-assembly processes, described theoretically in [33], of producing the resulting materials in less time and having the possibility of a systematic control of the helix **h** spatial distribution. Particularly, for processes that use FIA to create chiral film precursors, which is the main focus of the present work, typically a substrate is coated with a thin collagen solution by means of a complex flow involving shear and extensional deformation. This allows a non-equilibrium aligned phase, usually denoted as the para-nematic (PN) phase, to be formed [11, 14, 27-29]; we note that the PN phase of collagen and other biopolymer solutions is achiral with the macromolecules partially aligned along a common direction or director **n** which is essentially constant within the initial film. To decrease the mobility of the deposited collagen molecules several techniques have been used such as cross-linking [34] or solvent evaporation [27, 35, 36]. In the latter, by proper dehydration rates, the transformation of the mobile para-nematic PN phase into a solid helical plywood (cholesteric) is effected.

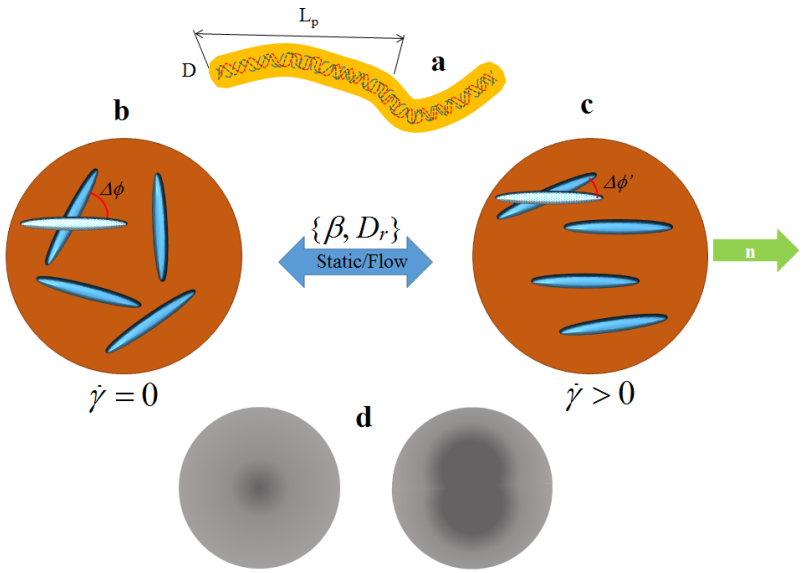

Figure 2.1. Schematic of the shear-induced alignment (flow birefringence) of typical semi-flexible biopolymers and relevant material properties. (a) Semi-flexible molecule with persistence length (L_p) and effective diameter (D) in dilute isotropic solution at rest (b) undergoing free Brownian rotational motion with rotational diffusivity D_r changing its orientation by $\Delta\phi$, and (c) para-nematic phase with restricted rotational motion, due to flow with smaller changes in orientation given by $\Delta\phi$', where the non-affine motion is quantified by the molecular shape parameter $\beta=\beta(L_p/D)$; the PN phase has molecular order around an average orientation **n** represented by the green arrow. (d) Flow birefringence schematics adapted from [19] indicating the isotropic and anisotropic optical properties at rest and under shear, respectively. The molecular order parameter S is zero under no shear but finite under shear.

Previous experimental results indicate that dilute collagen solutions are well-suited precursors with isotropic behavior at rest but showing flow-birefringence, as schematically depicted in figure 2.1d, for the formation of defect-free collagen films through a multi-step formation processes [27, 28] that essentially consists of melting the chirality through dilution (a), flow-processing into well aligned para-nematic (PN) phase (b), with a final solvent evaporation to form solid plywoods. However, to have a systematic control of the helix, to improve strategies and design new processes that allow fabrication of biomimetic materials, the full state of orientation of the precursor solutions must be quantified in terms of the deformation variables involved during the initial flow processing. This currently lacking ability can be improved by accurate theory and simulation

informed and guided [37] by existing experimental results [27, 28, 36]. In particular, it was demonstrated in [36], that acidic collagen solutions display rheological properties similar to those of synthetic liquid crystalline polymers, including flow-birefringence in dilute solutions, and banded textures after cessation of shear in concentrated solutions, where the latter is an indication of tumbling under shear.

The specific objectives of this chapter are to model and simulate the dynamic behavior of dilute collagen solutions, precursors of the aforementioned defect-free collagen films, and to assess the microstructure changes under different kinematic conditions relevant to experimental film formation flows. This will allow us predict under what conditions an ordering in the system resembling the one obtained from equilibrium self-assembly can obtained by means of flow-induced orientation. In order to achieve this objective we (a) first perform an experimentally-guided parameter determination and then (b) nematodynamic simulations, as follows:

(a) We first carry out a parameter estimation of the molecular shape parameter β and the rotation diffusion constant D_r, for molecular collagen in solution. We use previously reported experimental values of the effective molecular geometry pair (L_p, D) [36, 38-40] and calculate β and D_r from well-established expressions for these dynamic properties [41 – 43]. These latter pair is used as input to our model to carry out our nematodynamic simulations where the specific objective is to seek consistent behavior between the theoretical predictions we provide here for the scalar order parameter as a function of the shear rate for simple shear flow and previously reported small angle X-ray scattering profiles from flow birefringence experiments [36]. Further analysis of our model allows us to predict the maximum achievable order under simple shear flow conditions which we will show is a function of the effective aspect ratio, and interestingly has a higher value compared to the achiral synthetic liquid crystalline polymers

where values of about $S_\infty \approx 0.53$ have been reported [44]. This upper limit has not been previously reported or estimated due to instrumental limitations in the applicable stresses [36], and possibly from high shear rate-associated phenomena such as the appearance of edge instabilities in cone and plate geometries or important viscous dissipation in capillary rheometry. To fully characterize the collagen solutions under analysis we provide the reactive/tumbling parameter function that depends on β and S and provides quantitative information on the collagen solution conditions that lead to alignment or tumbling under simple shear flow.

(b) Once the material parameters β and D_r are determined, we then compute the microstructure evolution to simulate other kinematic conditions that resemble actual processing conditions by using the general flows included in the four roll mill process. The ultimate goal is to develop a master plot that indicates the complete state of orientation for diverse flow types and flow strengths. Additionally we provide an analysis of some limiting cases and finally based on experimental information [32, 36] and the process conditions reported by Kirkwood and Fuller [27, 28] we indicate what kinematic conditions are required for achieving order in film formation processes that use FIA of dilute collagen solutions as a first step.

The scope of this chapter is to carry out the simulations that allow for the experimentally informed parameter estimation for dilute acidic collagen solutions and to use such information to explore with further simulations other kinematic conditions that can be encountered in real processing conditions, by using the rich four roll mill kinematics. This computational platform is specific to collagen acidic solutions rather than a generalized scheme for other bio-macromolecules since it is crucially dependent on specific material properties such as the effective molecular shape anisotropy, orientational diffusivity, and the specific response to shear. The subsequent

transformation of the PN state into a cholesteric liquid crystal through evaporation is not simulated here and is outside the scope of this chapter.

The organization of this chapter is as follows: the required experimental background regarding alignment under simple shear flow and processes used to create collagen films are described in section 2.3.1. Section 2.3.2 introduces the kinematics of the four roll mill and an analysis of the principal axis of deformation which will be used as a reference to analyze the flow aligning nature of the solutions. The model, scaling, methodology and simulation conditions are presented in sections 2.4.1 and 2.4.2, respectively. The results are presented and discussed in two parts: section 2.5.1 presents the parameter estimation and section 2.5.2 provides the microstructure description for the applied kinematics and the kinematic conditions to create the thin film precursors is provided with the appropriate order and orientation. Finally, a summary of key findings and conclusions are given in section 2.6. Three appendices are associated to this chapter and can be found at the end of this thesis. Appendix A contains mathematical details on flow hydrodynamics such as the invariance of the eigenvectors of the strain tensor and helpful relations between the kinematic parameter κ and the invariants of the strain and vorticity tensors, Appendix B contains a brief background of the theoretical description of flow processes of chiral systems and the mathematical details on the derivation of the model, finally Appendix C contains mathematical details on the uniaxial approach used to analyze the limit cases of the scalar order parameter and director angle for given kinematic parameter κ. The first part of this modeling and simulation work extends in significant ways previous work reported in [7, 8] where an essential quantity such as the rotational diffusion constant was not estimated and left the molecular geometry as a free parameter. Here we adopt a rigorous property determination procedure applied to dilute acidic collagen solutions using a simulation-experiments [36] loop whose convergence yields values for

all parameters whose value are exclusive of such precursor solutions. Part two of this work, dedicated to the structural response of model collagen solutions to four roll kinematics, scans the parametric processing space to identify the degree of shear and extensional rates and the flow intensity required to produce a para-nematic state that is best suited for the formation of defect free cholesteric films reported in [27, 28].

2.3.1 Experimental Background of Collagen Solutions and Film Formation Process

Microstructure changes in dilute and concentrated collagen acidic solutions under the influence of a controlled flow have been characterized [36]. Previous experimental work on the dynamic properties of collagen solutions in a cylindrical shear cell showed that concentrated solutions display a complex non-reversible and out of plane orientational behavior at low shear rates of ~8 s^{-1}, while dilute solutions exhibit a uniform flow alignment for shear rates up 600 s^{-1} [36]. These rheological experimental results provide a measure of how the scalar order parameter (defined in eqn. (2.2b)), depends on the shear rate through SAXS [36]. The birefringent behavior (Figure 2.1c) disappears in the dilute regime after flow cessation and the isotropic pre-shear state (Figure 2.1b) is recovered. However, this dynamic behavior not only depends on how the material is deformed but also is highly sensitive to the aspect ratio of the molecule. As depicted in figure 2.1, crucial material properties such as the rotational diffusivity D_r and the rheological shape parameter β depend on the persistence length (L_p) and the aspect ratio of the molecule ($p = L_p/D$). The former has been reported elsewhere to vary from 57 nm up to 250 nm in both experimental and theoretical works [36, 38-40] (and references therein) and the effective diameter D of collagen has been reported from its actual molecular diameter estimated to be 1.36 nm up to about 4 nm [36, 39]. These effective molecular geometry variables depend on the electrostatic interactions of the chiral

rods and the surrounding medium [38]. For the particular case of the acidic collagen solutions used in these plywood formation processes the actual values of the geometry have not been reported. These observations suggest collagen solutions present a behavior similar to liquid crystalline polymers [5], that show flow alignment in the isotropic regime and also at concentrations/temperatures (depending on the nature of the material) close to the transition value and a complex shear rate dependency of the flow alignment/tumbling behavior for concentrated solutions [5, 44].

The uniform flow alignment behavior in the dilute region was used and patented by Kirkwood and Fuller [27, 28] to produce a defect-free collagen film through a multi-step process; as above-mentioned the initial step is the coating of a substrate with the precursor solution through complex kinematics that involve shear and extensional deformations. The deposition of the collagen solution is carried out by injecting the precursor through a capillary to coat a substrate that undergoes translational motion in the opposite direction of the flow inside the capillary creating a PN phase on the substrate. Further steps involve the drying of such film at room temperature with an external flow field of filtered air, where the helical axis is obtained and reported to be perpendicular to the flow direction [27] as depicted in figure 2.2a where we show the difference between the para-nematic and cholesteric phases. Such alignment is more likely to occur as the ratio H/p_o decreases where H is the thickness of the film [32].

The challenge and the need for precise knowledge of the microstructure response of the dilute collagen solutions precursors in different types of flow is the multiple time-scales associated to the process: the flow induced alignment, relaxation of the structure, helix formation and evaporation rate. These time-scales must be well synchronized to obtain the desired material, otherwise several scenarios might be observed. For instance, if the order is not uniform in the deposited fluid this

could lead to gradients in the helical axis as depicted in figure 2.2b, however if the order is uniform but the evaporation rate is too high one might expect to obtain a frozen FIA plywood which might resemble a nematic structure and finally, if the evaporation is too slow, the deposited film will relax to the isotropic state.

Although no extensive studies relating the director angle of the PN phase with the amount of defects in the solid films are available, one would expect the more parallel the collagen molecules with respect to the deposition direction (i.e. $\theta \rightarrow 0^{o}$) the more homogeneously the helix will be reconstructed, which has been observed in helical axis control experiments by light irradiation where low angles ($< 20^{o}$) lead to little to no defects [32]. On the other hand, for a sufficiently tilted orientation with poor alignment with the substrate, different formation directions associated with different time scales would not produce uniform homogeneous films. In addition to the average orientation, the molecular order S along the average orientation needs to be flow-controlled. Flows that yield low S, will require faster evaporation rates which may lead to instabilities. On the other hand, flows that yield S values close to final equilibrium values of a stable cholesteric phase at a particular concentration leave the transport processes (solvent evaporation) responsible only for creating the helix, and hence allowing for a more systematic control over the helix formation, as opposed to a scenario where the evaporation would be responsible for both creating order and the helical axis. This criteria will be used below when evaluating different flow kinematics.

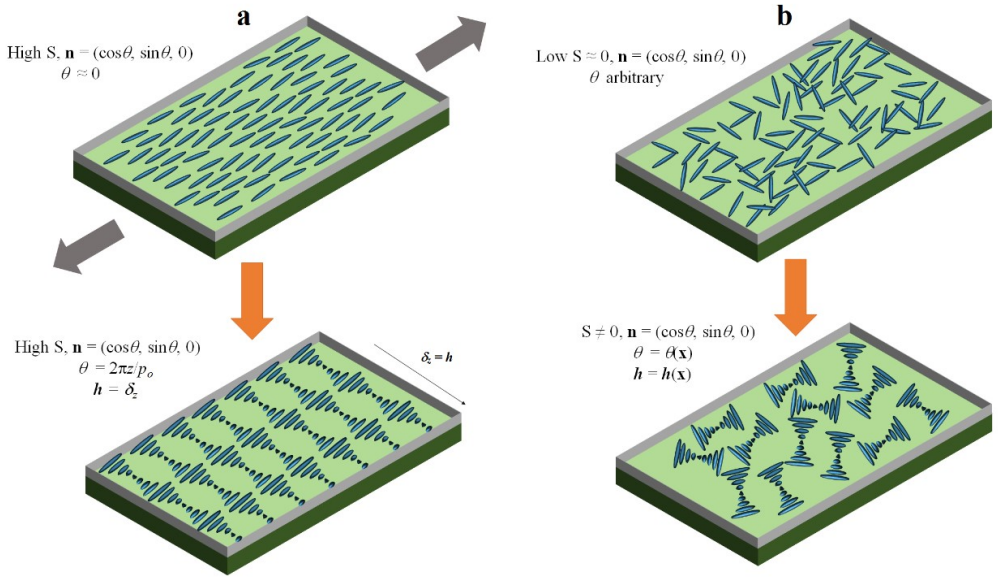

Figure 2.2. Schematic of para-nematic phases (the two top frames) with high (a) and low (b) scalar order parameter S. In the upper left frame the gray arrows indicates the deposition direction and leads upon evaporation, to a mono-domain lying helix in the "z" direction represented by the black thin arrow having the same direction of the unit vector $\boldsymbol{\delta}_z$. The disordered state depicted in the upper right frame leads, upon evaporation, to poly-domain structures with space dependent S = S(**x**) and graded director **n** angles and multiple helical axes. The uniform sough-after film reported by Kirwkood and Fuller [27, 28] are schematically represented by the upper and lower (a) frames.

An additional feature of flow configurations such as that in the work of Kirkwood and Fuller is the inhomogeneity of the flow presenting a combined effect of shear and extensional deformations and non-uniform gradients in the velocity field. This feature is present in both confined and free-surface flows [45]. A widely known example of the former is the flow in a pipe whose cross-section changes in the longitudinal direction, used to simulate important technological processes [5, 45, 46]. Examples of the latter include the drawing of a fluid from a reservoir [45] or with a capillary where inhomogeneous extension is encountered [14] where regions of recirculation (i.e. more vortex-like flows) can be found. Due to the complexity of these flows, even when mathematical treatments have been reported in the literature, many assumptions have to be considered and only weak non-homogeneities can be analyzed [46]. Besides, inhomogeneous flow

often cannot be assessed from combining the study of homogeneous flows in shear and extensional conditions independently. The approach adopted here is the use of a versatile flow such as the four roll mill (invented by G.I. Taylor [47]) where a wide variety of 2D flows can be created, including pure rotational, shear and extensional flow by changing a kinematic parameter in the velocity gradient tensor associated to the rotation of the rolls [47-49]. By imposing such kinematics the microstructure of the solution is expected to be drastically affected, creating a perfectly aligned phase under the upper limit of pure extensional flow, and a disordered in the lower limit of a rotational flow. Based on the relative contribution of strain over rotation, similar conditions to real processing conditions are expected to be present. The microstructure changes are also expected to change to variations of the flow strength, which is quantified by the pre-factor of the velocity gradient tensor to be explained in detail in Section 2.3.2.

2.3.2 Kinematics of the Four Roll Mill

The four roll mill is an instrument that was originally designed to study the deformation of droplets in 2D pure straining flows [47]. By changing the direction and/or angular velocities of the four rolls, either the magnitude of the vorticity or the straining rates can be selected at will. The geometry of the apparatus is depicted in figure 2.3a and some of the flows that can be created are also shown. This incompressible flow can be characterized by the following velocity gradient tensor $\nabla\mathbf{v}$ expressed in eqn. (2.1), with symmetric **A** and antisymmetric **W** parts (following the convention of [46]):

$$\nabla\mathbf{v} = \frac{E}{2}\begin{pmatrix} 1+\kappa & -(1-\kappa) & 0 \\ 1-\kappa & -(1+\kappa) & 0 \\ 0 & 0 & 0 \end{pmatrix}; \mathbf{A} = \frac{E}{2}\begin{pmatrix} 1+\kappa & 0 & 0 \\ 0 & -(1+\kappa) & 0 \\ 0 & 0 & 0 \end{pmatrix}; \mathbf{W} = \frac{E}{2}\begin{pmatrix} 0 & -(1-\kappa) & 0 \\ 1-\kappa & 0 & 0 \\ 0 & 0 & 0 \end{pmatrix} \qquad (2.1)$$

where E is an effective deformation rate and is associated with the strength of the flow meanwhile κ is associated with the type of flow. The limit cases of this kinematics include pure rotational flow with $\kappa = -1$ characterized for having rigid body rotations but no strain (deformation), simple shear with $\kappa = 0$ characterized for having equal contribution of rigid body rotations and strain, and pure planar elongational flow with $\kappa = 1$ characterized for having pure strain and no rotations. It is worth mentioning the strain rate tensor **A** is diagonal for the chosen (fixed Cartesian) reference system. This implies the principal axis of deformations which are obtained via the calculation of the eigenvectors of **A** coincide with the system of reference and do not change when the flow is changed by the kinematic parameter κ. In terms of the kinematics, there are two deformation axis: i) the "y" axis which is the direction where the fluid particles are compressed and ii) the "x"axis which is the direction where they are elongated at constant volume. What is important to note is that while the direction of the flow might change depending on the particular value of the κ, the axis of deformation do not change and are always collinear with ($\boldsymbol{\delta}_x$, $\boldsymbol{\delta}_y$). This indicates the principal axis of deformation are invariant and the flow aligning nature of mesogens in this generalized 2D flow is more convenient in terms of these invariant directions. The reader is referred to section Appendix A (where we additionally provide the definition of κ in terms of vorticity and strain) for a mathematical proof of the indifference of the principal axis of deformations by considering a fixed coordinate system and a rotating one (see figure A1 in Appendix A).

In a typical film processing method such as [14, 27, 28] with a fixed process coordinates (x, y), the flow kinematics is inhomogeneous, i.e. $\mathbf{A}(x, y)$, $\mathbf{W}(x, y)$, with the flow type changing through space: $\kappa\ (x, y)$. This allows the possibility of having vortex-rich, strain-rich and mixed type of regions. For example if there is a region of recirculation located at (x_r, y_r), then $\mathbf{A}(x_r, y_r) = \mathbf{0}$, $\mathbf{W}(x_r,$

y_r) $\neq$ **0** , with $\kappa(x_r, y_r)$=-1, while next to a solid surface located at (x_s, y_s), we expect **A** (x_s,y_s) $\neq$ **0**, **W**(x_s,y_s) $\neq$ **0**, and the flow type would resemble more the case of $\kappa(x_r, y_r) = 0$, finally, close to the free surface (x_{fs}, y_{fs}) the building blocks strongly align in the extension direction with **A**(x_{fs}, y_{fs}) $\neq$ **0** and **W**(x_{fs},y_{fs}) = **0** with the flow type $\kappa(x_{fs},y_{fs})$=1. Hence, a real flow corresponds to a set of four roll mills where κ changes in space, and by accounting the contributions of the strain over vorticity, as specified in Appendix A, in such processes, specific predictions on how flow affect the collagen orientation and order can be made.

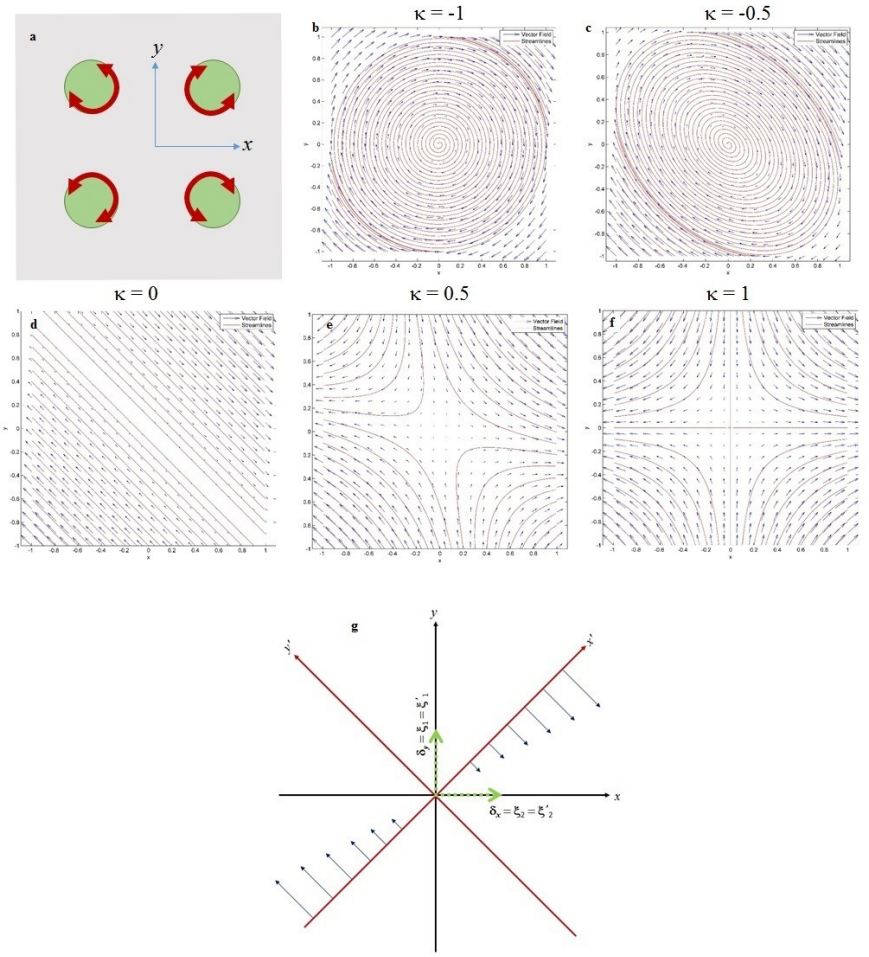

Figure 2.3. Four roll mill schematics (a) and five 2D flows (b-f) that can be created with the velocity vector field and streamlines for the indicated values of κ. Examples include pure rotational (b) simple shear (d), and planar elongation (f). The principal axis of deformation depicted in (g) for the particular case of simple shear flow where both sets of eigenvectors in fixed (x,y) and rotating (x',y') system of reference yields to the same principal axis of deformation of **A**.

2.4 Model and Methods

2.4.1 Model and Scaling

The ordering in collagen solutions is analogous to that of lyotropic liquid crystalline polymers where its dynamic behavior is explored at the mesoscopic level by means of the second moment of the orientation distribution function $\rho(\mathbf{u})$ or **Q**-tensor (symmetric and traceless second order tensor):

$$\mathbf{Q} = \int \left(\mathbf{uu} - \mathbf{I}/3\right)\rho(\mathbf{u})d^2\mathbf{u};\ \ \mathbf{Q} = \mathbf{Q}^T;\ tr(\mathbf{Q}) = 0$$
$$\mathbf{Q} = S\left(\mathbf{nn} - \frac{\mathbf{I}}{3}\right) + \frac{P}{3}\left(\mathbf{mm} - \mathbf{ll}\right) \qquad \text{(2.2 a,b,c,d)}$$

where {**n**, **m** and **l**} correspond to the orthonormal director triad and S and P represent the uniaxial and biaxial scalar order parameter respectively. The order parameters $S = 3/2\mathbf{n}\cdot\mathbf{Q}\cdot\mathbf{n}$; $P = 3/2(\mathbf{m}\cdot\mathbf{Q}\cdot\mathbf{m} - \mathbf{l}\cdot\mathbf{Q}\cdot\mathbf{l})$ are a measure of the molecular alignment with respect to the uniaxial director **n** and biaxial axis **m**. The paradigm used in this work to analyze the microstructure response of chiral mesogens under the influence of flow and the derivations of the equations for the collagen system under analysis can be found in section Appendix B; the reader is referred to [42, 43, 50-59] for liquid crystal rheology and nematodynamics. The dimensionless spatially homogeneous governing equation is:

$$\frac{d\mathbf{Q}}{dt^*} + De\left(\mathbf{W}^*\cdot\mathbf{Q}-\mathbf{Q}\cdot\mathbf{W}^*\right) + \frac{1}{\left[1-3/2\mathbf{Q}:\mathbf{Q}\right]^2}\left[\left(1-\frac{U}{3}-\frac{48\pi^2}{R}\right)\mathbf{Q} - U\left(\mathbf{Q}\cdot\mathbf{Q}\right) + U\left(\mathbf{Q}:\mathbf{Q}\right)\left(\mathbf{Q}+\frac{\mathbf{I}}{3}\right)\right] - De\left\{\frac{2}{3}\beta\mathbf{A}^* + \beta\left[\mathbf{A}^*\cdot\mathbf{Q}+\mathbf{Q}\cdot\mathbf{A}^* - \frac{2}{3}\left(\mathbf{A}^*:\mathbf{Q}\right)\mathbf{I}\right] - \frac{\beta}{2}\left[\left(\mathbf{A}^*:\mathbf{Q}\right)\mathbf{Q} + \mathbf{A}^*\cdot\mathbf{Q}\cdot\mathbf{Q} + \mathbf{Q}\cdot\mathbf{A}^*\cdot\mathbf{Q} + \mathbf{Q}\cdot\mathbf{Q}\cdot\mathbf{A}^* - \left[\left(\mathbf{Q}\cdot\mathbf{Q}\right):\mathbf{A}^*\right]\mathbf{I}\right]\right\} = \mathbf{0} \quad (2.3\ \text{a,b,c,d})$$

$$De = \frac{|\dot{\gamma}}{6D_r}, \quad R = \quad L_1 \quad , \quad Er = De\cdot R = \frac{\dot{\gamma}\ {}_B T}{2L_1 D_r}$$

where $t^* = 6D_r t$, and where starred variables denote dimensionless quantities, the Deborah number (De) is the ratio of molecular time scale $1/6D_r$ to flow time scale $1/|\dot{\gamma}$, R is the ratio of two square length-scales: the macroscopic chiral length-scale (i.e. the cholesteric pitch p_o) and the molecular length-scale $\sqrt{3ck_BT/L_1}$, and Er is the Ericksen number or ratio of macroscopic time scale $p_o^2 ck_BT/2L_1D_r$ to flow time scale $1/|\dot{\gamma}|$. The molecular length scale is associated to short-scale order parameter variations such as in a defect core (O(nm)) whereas the external scale is usually referred to long-scale orientation changes such as the separation between the plates in a simple shear flow, and in such cases R is usually in the order of $10^5 - 10^6$. However, in the particular case of this work such external length-scale is associated to the pitch found in collagenous materials which is O(μm) – O(10μm), thus the energy ratio has an order of magnitude of $10^3 - 10^4$ and should be retained for more accurate parameter estimations. The Ericksen number is the product of De·R and compares the viscous and elastic torques, and even though it does not appear explicitly in the current formulation it is implicit due to the relationship between De and R.

In general terms, the dynamic behavior of the **Q** tensor under certain kinematics depends on thermodynamic conditions such as the concentration of the chiral rods given by the augmented nematic potential U [33] and also on parameters that depend on the hydrodynamic interactions in

the material as the rotational diffusivity D_r, that is a function of the rotational friction coefficient ζ_r, and the shape parameter β that is a function of the aspect ratio $p = L_p/D$. Hence, these crucial parameters are highly sensitive to the geometry of the mesogens and have a great impact on the evolution of the microstructure of the material. The theoretical description (considering a generalized ellipsoid as the effective shape of molecular collagen for the rotational friction factor) for D_r and β are approximated as follows [41-43]:

$$\beta = \frac{p^2 - 1}{p^2 + 1}; p = \frac{L_p}{D}$$

$$\overline{D}_r = \frac{D_r}{\left[1 - \frac{3}{2}\mathbf{Q} : \mathbf{Q}\right]^2} \qquad \text{(2.4 a,b,c,d,e)}$$

$$D_r = \frac{ck_BT}{\zeta_r}; \zeta_r = \frac{16\pi\eta_s L^3}{3\left(2\ln\left(2L/D\right) - 1\right)}$$

For efficient flow processing of collagen we need to obtain a well-aligned para-nematic state via the FIO effect as represented in the left-hand side of figure B1 in Appendix B. From equation (2.3a) we can make the following qualitative observations that lead to FIO: (i) we require a sufficiently large De which can be effected by flow intensity $|\dot{\gamma}$ in relation to D_r ; (ii) β will have to be sufficiently large to translate the strain rate effect into molecular order and (iii) the flow kinematics defined by κ , which is included in $\mathbf{A}^*$, will have to be calibrated with $|\dot{\gamma}$ to effect order and orientation. The numerical simulations below, informed by experimental data [36], provide the required quantitative envelope of these three effects.

2.4.2 Methodology and Simulation Conditions

The simulations were carried out as follows: we apply the four roll mill kinematics to eqn. (2.3-a) and solve the ordinary differential equations using second-order backward differentiation formulation (BDF). The relative error was set to 10^{-6} and convergence, accuracy and stability is established using standard methods and criteria. Additionally, we assume only three non-zero independent components of **Q**: Q_{xx}, Q_{yy} and Q_{xy}. Throughout the simulations we use the isotropic state as initial conditions ($Q_{ij} = 0$) and the simulations are allowed to reach steady-state. To accomplish the objectives, the methodology is carried out in two parts:

a) Parameter Estimation and Model Validation:

In this first section we fix the flow type κ to simple shear flow by imposing $\kappa = 0$ and use reported values of the effective molecular geometry (L_p = 57, 110, 220 nm [36, 40] and D = 1.36, 3.96 nm [36, 38]) to obtain the theoretical estimates of the shape parameter β and the bare rotational diffusivity D_r. These values are used as inputs to eqn. (2.3-a) which is solved numerically by increasing the Ericksen Er number (or De from eqn.(2.3-d)) and the scalar order parameters (S, P) can be extracted using its definition provided in section 2.1 and plotted as a function of the shear rate (calculated according to the definition (2.3-b) of De using the theoretical value of D_r). The experimental scalar order parameter can be estimated from the SAXS profiles reported for increasing shear rates given by [36] according to the method provided in [60]. It will be shown that the crucial fitting parameter is D_r and essentially only one value will accurately reproduce the experimental flow induced alignment. Predictions of the scalar order parameter outside the experimental range are also obtained for infinite De, where the maximum achievable order is obtained in this flow configuration.

b) Microstructure Evolution

Once the material characterization is complete i.e. β and D_r are known and reproduce the dynamic behavior in simple shear simulations, other types of flows are analyzed by scanning the parametric space with the kinematic parameter κ and the Deborah number. The complete state of orientation is obtained by extracting the scalar order parameter S and the director angle θ (using eqn. (2.2-b)) from the steady-state solutions. Under any given flow conditions, the stationary para-nematic PN phase is defined by the director angle θ and the scalar order parameter S:

$$\theta = \theta(D_e, \kappa), S = S(D_e, \kappa) \quad (2.5)$$

The simulation conditions are summarized in Table 1.1. As is typical of LCPs [4, 59], to have significant effect on **Q**, the Ericksen number is significantly larger than one.

Table 2.1. Simulation conditions for four roll mill kinematics (eqn. (2.1)), and Deborah Number (eqn. (2.3-b)).

Parameter	Values
Deborah number De (Er/R)	(0.1, 0.5, 1, 5, 10, 50, 100, 250, 500, 750, $1x10^3$, $2.5x10^3$, $5x10^3$, $7.5x10^3$, $1x10^4$, $2.5x10^4$, $5x10^4$, $7.5x10^4$, $1x10^5$, $2.5x10^5$, $5x10^5$, $7.5x10^5$, $1x10^6$, $2.5x10^6$, $5x10^6$)/R
Flow-type κ	-0.9, -0.8, -0.7, -0.6, -0.5, -0.4, -0.3, -0.2, -0.1, 0, 0.1, 0.2, 0.3, 0.4, 0.5, 0.6, 0.7, 0.8, 0.9, 1

In order to obtain important limiting D_e conditions of S and θ as a function of material properties such as β and the flow type (κ) we apply the uniaxial approach to eqn. (2.3-a) (see Appendix C) and denote:

$$\theta_{\infty}(\kappa) = \lim_{D_e \to \infty} \theta(D_e, \kappa)$$
$$S_{\infty}(\kappa) = \lim_{D_e \to \infty} S(D_e, \kappa) \quad (2.6)$$

2.5 Results and Discussion

2.5.1 Parameter estimation and validation

(i) Molecular Parameters : β and D_r

Figure 2.4a shows the parameter fitting of the model prediction for two selected molecular geometries reported [36, 39] for molecular collagen as examples (L_{p1} = 160 nm and L_{p2} = 220 nm and setting the effective diameter as D = 3.96 nm). Even when changes in the molecular geometry affect both material properties β and D_r, the most sensitive is the latter that leads to changes from about 350 s^{-1} up to 140 s^{-1} for the shown values respectively whereas β changes from 0.9987 to 0.9993 for the shown values and is always close to the unity for the full geometric range. The effective geometric dimensions of the molecule are a strong function of the electrostatic interactions due to the ionic content in the surrounding medium [36, 38] and even when rotational diffusivities for dilute collagenous solutions have been reported around 1100 s^{-1} [39], values within the same order of magnitude as the theoretical estimates have been reported for similar mesogens [43]. Additionally, the theoretical prediction used here corresponds to that of the single-rod approximation as implemented originally in [41] as a closure argument for the mesoscopic description, and the variation of D_r is accounted by the denominator pre-factor shown in eqn. (2.5-c), which has been found to describe successfully the ordering of liquid crystalline phases [41-43, 58]. The molecular geometry that best describes the dynamic behavior of the acidic solutions corresponds to L_p = 220 nm and D = 3.96 nm and yields D_r = 140 s^{-1}, as can be seen in figure 2.4a that reproduce and extend the experimental results from flow birefringence.

(ii) High Deborah Number Limit : $S_\infty = S\left(D_e \to \infty\right)$

Figure 2.4b shows S and θ in terms of De, where the plateau values corresponding to the maximum order and preferred direction with respect to the x-axis are shown. The former is a function of the molecular shape and this plateau value contrasts to previous hypothesis that indicated S should monotonically increase to the unity [36]; however, perfect alignment under simple shear flow is not possible but it will be shown in section (.4.2) the perfect alignment can be achieved when κ increases. The plateau estimation can be obtained from eqn. (2.3-a) by applying a uniaxial approximation to obtain the equations in terms of the scalar order parameter and director angle which leads to the following important relationships:

$$\sin 2\theta = \frac{-6S}{\beta\left(4+2S-S^2\right)} = \frac{-1}{\lambda}$$

$$\cos 2\theta = \frac{8\left(2US^3 - US^2 + (3 - U - 144\pi^2 / R)\right)}{3\beta De\left(4+4S-5S^2\right)\left(-1+S^2\right)^2} \qquad \text{(2.7 a-b)}$$

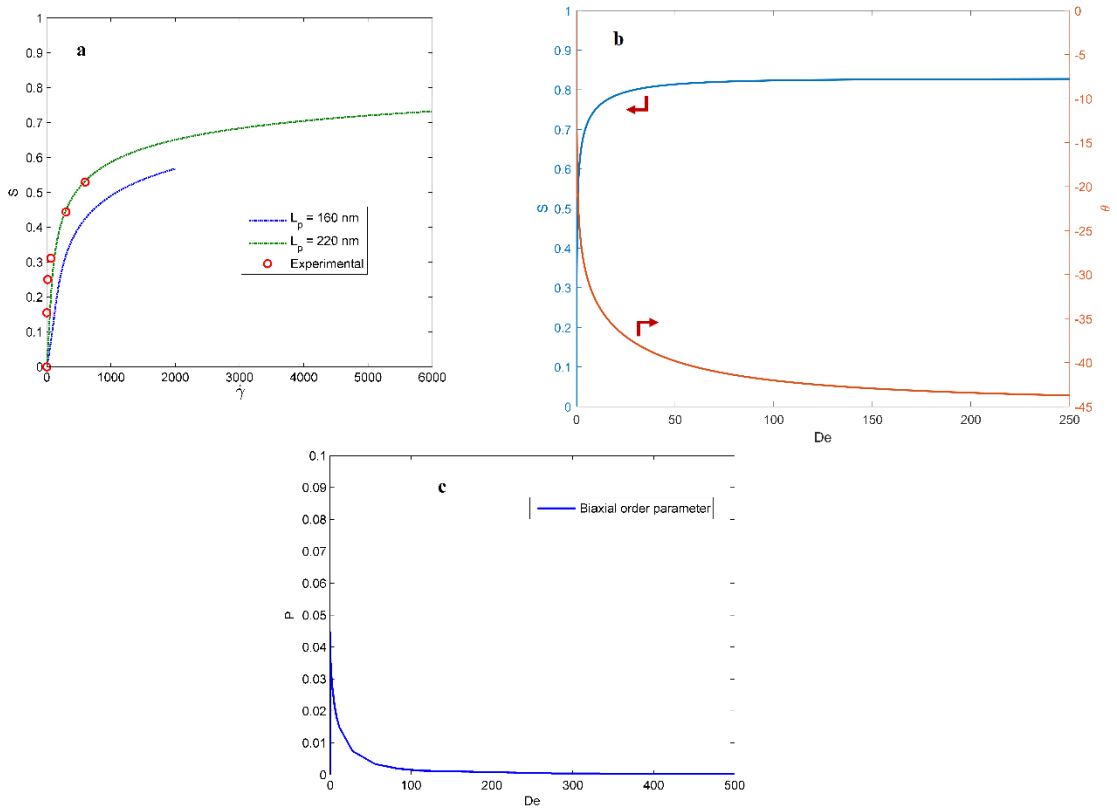

Figure 2.4. (a) Scalar order parameter S as a function of shear rate predictions from this work for two different persistent lengths L_p as indicated in the legend compared with the experimental values extracted from the SAXS profiles from [36], (b) scalar order parameter S (left axis) and director angle θ (right axis) predictions for large shear rate (high De) where the asymptotic values of S and θ can be observed, and (c) the negligible biaxial scalar order parameter as a function of De , showing that the implemented uniaxial approximation is accurate.

The director angle is measured between the direction of the rods and the x-axis, and a relationship between $\sin 2\theta$ and λ (the reactive parameter which is discussed in the following section) is obtained in this particular four roll mill geometry, contrasting to the conventional $\cos 2\theta$ and λ in unidirectional simple shear. Low De implies small S which results in $\theta(\mathrm{De}\to 0) = 0$ from eqn. (2.7-a). On the other hand, when $\mathrm{De}\to\infty$ eqn. 2.7-b implies $\cos 2\theta = 0$ which implies $\sin 2\theta$ is either +1 or -1. The sign is determined by the reactive parameter λ whose large De limit is the unity, hence $\sin 2\theta = -1$ leading to $\theta_\infty = -45^o$. Under this condition, the right-hand side of eqn. (2.7-a) leads to a quadratic eqn. for S that is a function of the shape parameter as established in eqn. (2.8).

For the particular case of the acidic solutions based on the predicted S_∞ plateau value corresponds to 0.83.

$$S_\infty = 1 - \frac{3}{\beta} + \sqrt{\left(1 - \frac{3}{\beta}\right)^2 + 4} \qquad (2.8)$$

Figure 2.4c shows the biaxial order parameter as a function of De that experiences an initial maximum value (~ 0.05) for low De and decays towards zero for larger De, hence any biaxiality is negligible and the uniaxial approximation accurate.

iii) Reactive Parameter Function: $\lambda(S)$

The flow aligning nature under simple shear flow is given by the reactive parameter λ [42] with the flow aligning angle or Leslie angle given by eqn. (2.9):

$$\lambda = \frac{\beta\left(4 + 2S - S^2\right)}{6S} \qquad \theta_L = \frac{1}{2}\sin^{-1}\left(\frac{-1}{\lambda}\right) \qquad (2.9\text{ a, b})$$

whose magnitude determines the shear flow aligning or tumbling behavior; we note that the symbol θ_L refers to the Leslie angle under simple shear flow and that in this chapter we just use θ for the steady director angle under any flow. For the case of rod-like mesogens, $\lambda > 1$ indicates shear flow aligning whereas $\lambda < 1$ indicates a tumbling (non-aligning) regime. For systems whose scalar order parameter is close to the isotropic value, λ is undetermined, as the order in the system increases, λ decreases until it reaches the flow aligning limit. This characteristic value which makes λ the unity is the large shear rate value S_∞, i.e. $S(\lambda = 1) = S_\infty$, any solution with order in the system higher than such value will have tumbling behavior. The collagen λ as a function of S is given in figure 2.5. The figure shows additionally a reference line for the unity and it can be seen

that when $\lambda = 1$, $S = S_\infty = 0.83$. From the Leslie angle relationship $\theta_L = -45^o$, which indicates the collagen molecules are aligned in the direction of the shear flow as shown in figure 2.3-d in the large De limit. Therefore we see that when processing a dilute collagen solution with initially negligible order ($S \approx 0$) will always flow-align in shear. On the other hand, processing under shear conditions an initially highly ordered solution such that $S > S_\infty$ leads to non-aligning behavior, involving defects and texturing [59]. For concentrated synthetic LCPs, typical values of $U = 5$ yielding $S_{eq} = 0.76$ [43] lead to tumbling under low shear. Our estimates predicting flow alignment in dilute solutions capable of achieving an order up to $S = 0.83$ indicate dilute solutions are better suited precursors to obtain uniformly ordered and aligned PN phases without complex shear rate dependent periodic behavior as observed in concentrated LCPs. The uniform alignment and order is then transferred to the final resulting material. This behavior would also be expected of other biomacromolecules where the effective aspect ratio of cellulose and chitin of about $p \approx 10 – 20$ [7] leads to $S_\infty \approx 0.81 – 0.82$ (using eqns. 2.4a and 2.9a). Comparing these results with curves of certain synthetic LCPs where $S_\infty \approx 0.53$ is predicted [44] indicates biomacromolecules' λ vs S curves are shifted to the right and allowing higher order than its synthetic counterparts. Finally we mention that our λ curve is also consistent with the high concentration results of [36], where banded textures after cessation of flow are reported, since these bands are associated with shear flows under $\lambda < 1$ conditions.

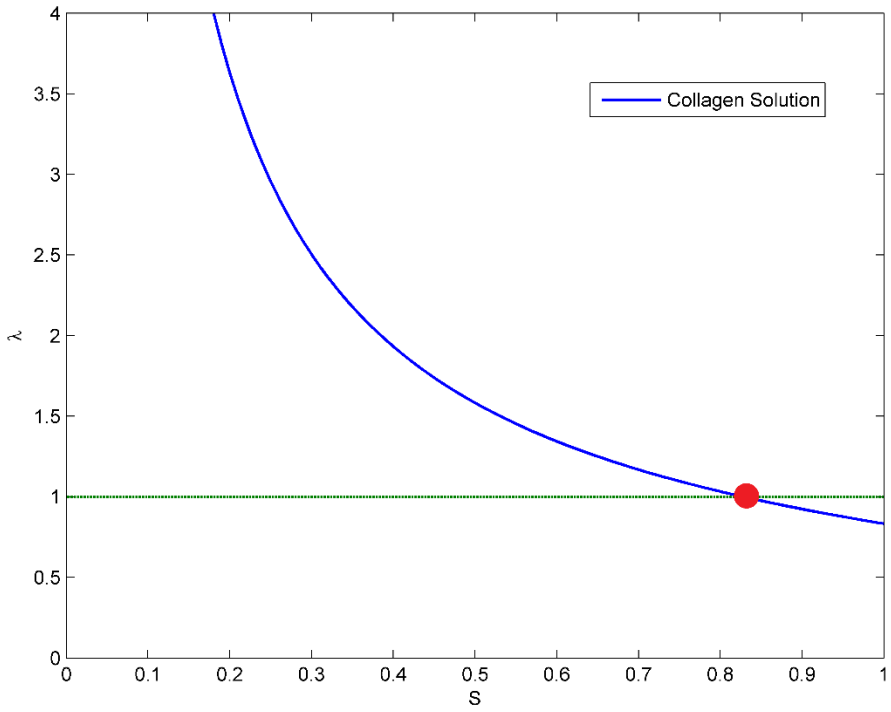

Figure 2.5. Predicted reactive (tumbling) parameter λ of collagen acidic solutions as a function of S, based on nematodynamics [7] and experimental data [36]. The important threshold for flow aligning behavior corresponding to $\lambda = 1$ ($S = S_\infty = 0.83$) is represented by the red dot.

2.5.2 Four roll mill predictions for para-nematic states

Figure 2.6 shows representative results of S (a) and θ (b) as a function of De, for κ = -0.5, 0.5 and 0. Figure 2.6a shows a monotonic increase in the scalar order parameter S that approaches $S_\infty(\kappa)$ whose value increases with κ, until a perfectly ordered phase $S_\infty = 1$ is achieved for a characteristic κ.

The behavior of θ shows an initial monotonic decrease starting from the origin until a high De limit is approached. The precise $\theta_\infty(\kappa)$ is characteristic of each flow type, where flows strong in

vorticity (i.e. $\kappa < 0$) reach their plateau value at lower De compared to flows with $\kappa > 0$. Additionally, $\theta_\infty(\kappa)$ in flows with $\kappa < 0$ is always -45° whereas for $\kappa > 0$ the value of $\theta_\infty(\kappa)$ increases with κ.

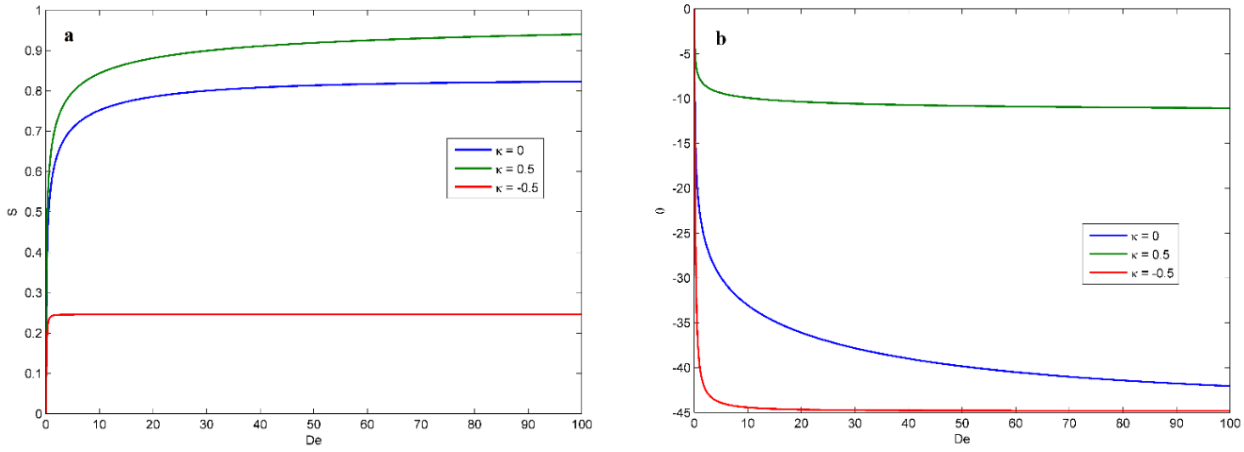

Figure 2.6. (a) Simulated scalar order parameter and (b) simulated director angle as a function of Deborah De number, for different flow types , with $\kappa = 0$ as a reference to the previous section, one with higher straining contribution ($\kappa = 0.5$) and another with higher vorticity contribution ($\kappa = -0.5$), as indicated in the legend

To better understand the effect of changing the flow type for other values of De we present in figure 2.7 the steady-state values of S (a) and θ (b) as a function of κ for three different De (0.1, 1 and $\rightarrow\infty$). For De $\rightarrow \infty$, the scalar order parameter increases exponentially from negative values of κ, with an intercept at the predicted value in the simple shear flow calculations and reaches 1 approximately at $\kappa = 0.1$, which remains constant for higher values of κ. On the other hand, θ remains locked at -45° for $\kappa < 0$, i.e. the system starts to order at constant orientation as the flow changes from a pure rotational to simple shear. Once the system is perfectly aligned ($\kappa \approx 0.1$); as κ increases the orientation increases monotonically until the director angle lies parallel to the x-axis. Even when this limit exists theoretically, it might be unfeasible since it might require extremely large shear rates and other phenomena might appear in such scenarios, nonetheless, the

examination of this limit provides insights of what occurs at other feasible shear rates. In fact, similar behavior is observed for lower De, however the regions of constant orientation and order become narrower and at higher values of θ the former and lower for S. This effect is due to the weakness of the flow in these cases (lower De) and indicates an intimate relationship between the alignment and ordering in the system when the flow time-scale has an order of magnitude comparable to the rotational diffusivity (modest values of De) for any type of flow. The behavior of the curves becomes smoother in the transition region as De decreases.

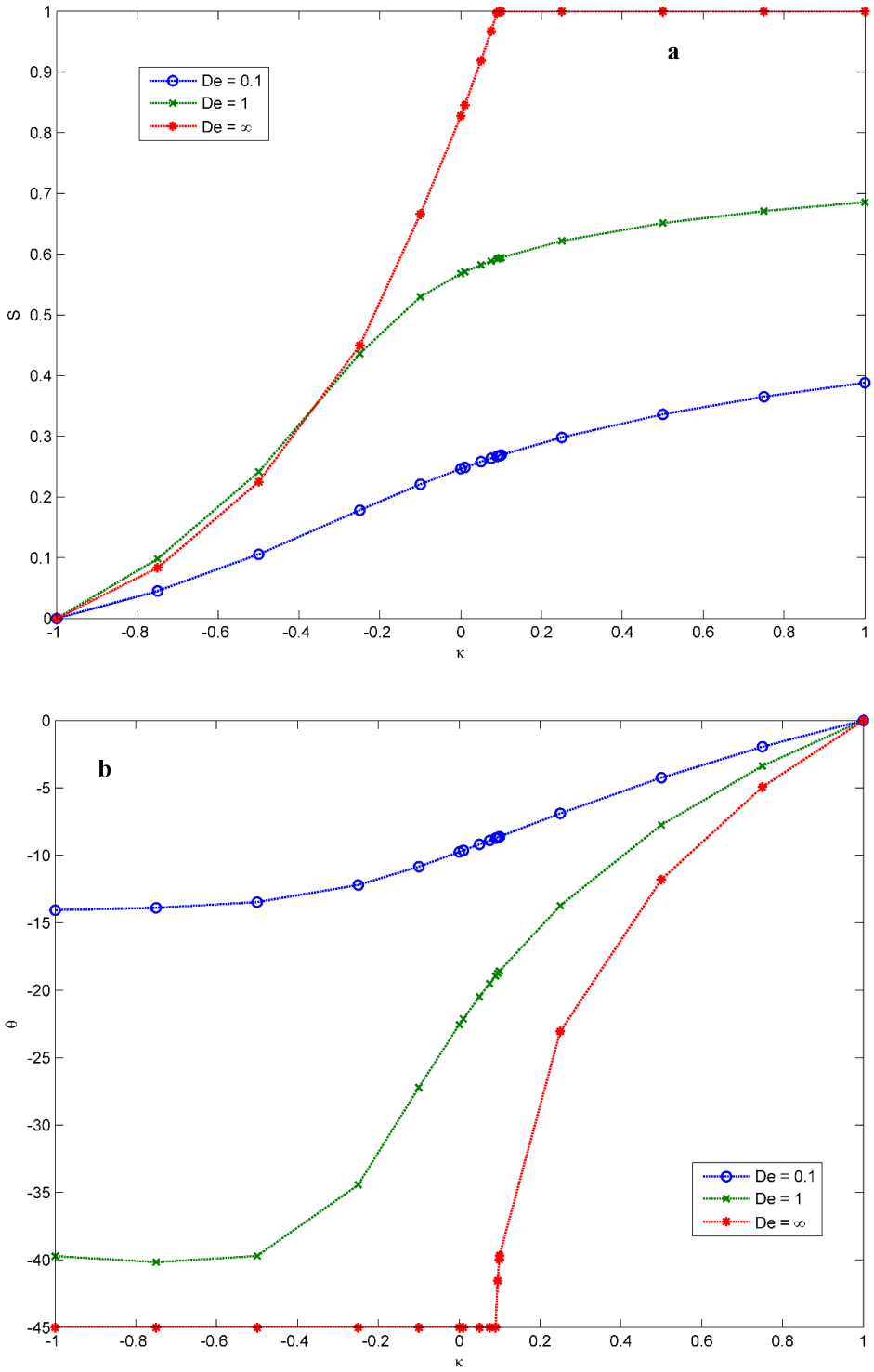

Figure 2.7. Simulated steady-state values of scalar order parameter (a) and director angle (c) as a function of κ for De = 0.1, 1 and De → ∞.

Figure 2.8 shows the master plot of S as a function of θ for different flow types (κ) and intensities De. This plot can be divided into a vorticity dominated region (below the $\kappa = 0$ curve) and a strain rate dominated region (above the $\kappa = 0$ curve). Meanwhile the strength of the flow is given by the Deborah number that increases from right to left according to the color bar. The (**M** = **Q** + **I**/3**)** tensor ellipsoids for large De are also provided to visualize the state of orientation of the mesogens, following [62]. We identify regions where the director angle resembles the value observed in simple shear flow (close to -45^o) however the ellipsoids are sphere-like due to the low S leading to almost horizontal lines close to the bottom of the master plot. As κ increases the ellipsoids become more prolate at an angle of -45^o, and finally for positive values of κ the ellipsoids become more elongated with an orientation that decreases to 0^o at the limit case of $\kappa = 1$. The triangle in Figure 2.8 provides quantitative means to determine the conditions required to create materials with a desired degree of alignment and ordering for flows or well-established processes what is the degree of alignment in the system that is anticipated given the process conditions are known. In particular the (κ_{opt}, De_{opt}) processing triangle is limited by (0.2, 1) for almost simple shear flow and (1, 0.6) for pure extensional flow, which will be further discussed in the subsequent paragraphs.

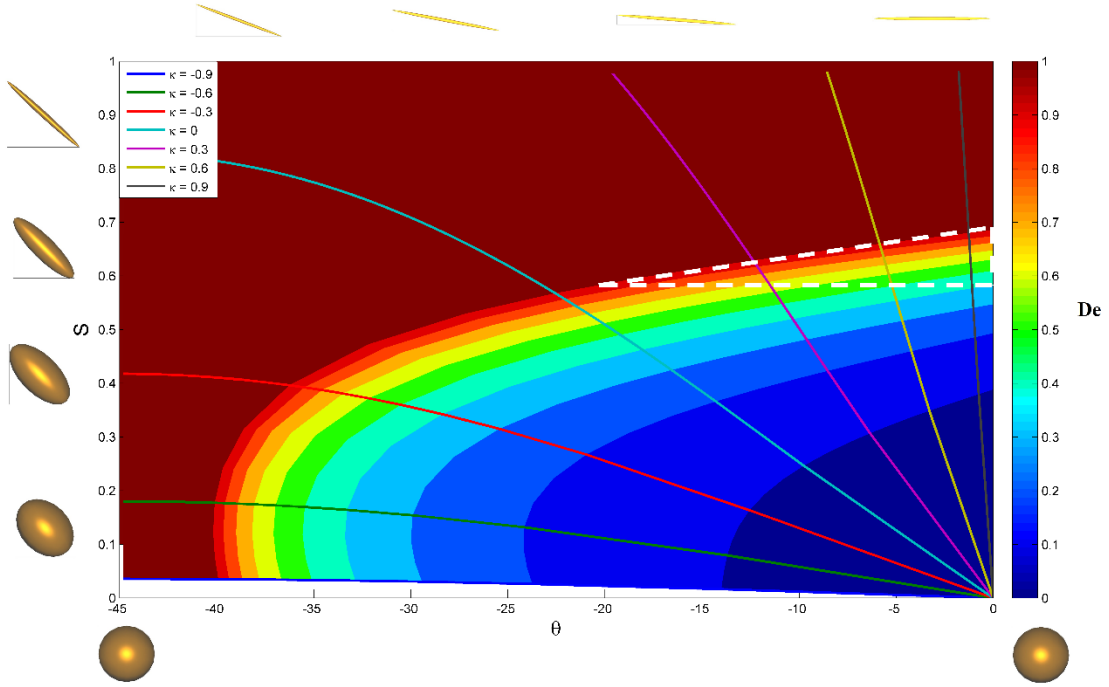

Figure 2.8. Master-plot of the simulated scalar order parameter S and director angle θ for different types of flows (κ curves) and flow strengths as shown in the color map for De, for dilute acidic solutions of collagen. The region surrounded by the white thick triangle on the top right indicates the optimal kinematic conditions required in the pre-alignment stage of defect-free film formation process. The tensor ellipsoids integrate the description of para-nematic state (S, θ).

We carry out the uniaxial analysis as indicated in section 2.6.1 but with the generalized kinematic parameter κ. The generalized expressions are given in eqn. 2.10 (a-c). Only few but useful limiting cases of κ that lead to close form expressions can be analyzed; which are summarized in table II in Appendix C further mathematical details. Equations 2.10 (a, b) reveal how (β, κ, De) affect (θ, S) and eqn. 2.10 (c) encapsulates the processing unit circle where all the variables affecting the order and orientation are considered given that $\sin^2 2\theta + \cos^2 2\theta = 1$ one can easily predict the PN state and depending on the kinematic conditions is the precise location around the circumference that includes the optimal (κ, De) pair (see figure B1 in Appendix B).

$$\sin 2\theta = \frac{-6S(1-\kappa)}{\beta\left(4+2S-S^2\right)(1+\kappa)};\cos 2\theta = \frac{8\left(2US^3-US^2+(3-U-144\pi^2/R)S\right)}{9\beta De(1+\kappa)\left(4+4S-5S^2\right)\left(-1+S^2\right)^2}$$

$$\frac{1}{\lambda^2}\left[\frac{(1-\kappa)}{(1+\kappa)}\right]^2+\frac{64}{9}\left[\frac{\left(2US^3-US^2+(3-U-144\pi^2/R)S\right)}{\beta De(1+\kappa)\left(4+4S-5S^2\right)\left(-1+S^2\right)^2}\right]^2=1 \qquad \text{(2.10 a,b,c)}$$

Table 2.2. Summary of S and θ for the limit cases of pure rotational flow and pure elongational flow (eqns. 2.10).

	κ = -1 (rotational flow)		κ = 1 (elongational flow)	
	Low De	High De	Low De	High De
S	$2US^3-US^2+(3-U-144\pi^2/R)S=0$ $\therefore S=0$	$\frac{6S}{\beta(4+2S-S^2)}=0$ $\therefore S=0$	$2US^3-US^2+(3-U-144\pi^2/R)S-2\beta De(4+4S-5S^2)(-1+S^2)^2=0$ $\therefore S=S(\beta,De,R)$	$(4+4S-5S^2)(-1+S^2)^2=0$ $\therefore S=1$
θ	$\cos 2\theta=0$		$\sin 2\theta=0$	

From Table 2.2, it can be stated that rotational flow for any De is not capable of ordering the mesogens and flows rich in vortex contributions should be avoided or vortex-rich regions should be minimized for producing the collagen films of interest. For strain-rich flows the ordering depends on the intensity of the flow when this is low to moderate and depend on other material properties such as β, D_r and R. When the flow intensity is high, the mesogens present a perfect ordering with S = 1. Other types of flow are capable of creating perfectly ordered PN phases as observed in figure 2.7a, however, the difference between the pure elongational flow (κ = 1) and other flows with a certain degree of vortex contribution (0 < κ < 1) is the direction of the alignment. For the limit case of κ = 1, the mesogens are always aligned in the x-direction, regardless the value of De, which shows the strongly alignment effect of elongational flows.

Finally we use the above results to specify optimal (κ_{opt}, De_{opt}) conditions required in the PN phase that would likely lead to defect-free films. As previously mentioned, the region of interest for processing the dilute collagen solutions is such where the flow-induced PN order resembles the one obtained at equilibrium when the rod concentration is increased after the solvent evaporation. The FIO should produce a PN ordered phase such that:

$$S\left(D_e,\kappa\right)\approx S_{eq}=1/4+3/4\sqrt{1-8/3U-32\pi^2/UR} \quad (2.11)$$

where (De, κ) are some effective averaged values, and S_{eq} is the equilibrium order [33] of collagen in the final dried state. For example when U = 4, $S_{eq}(U=4) = 0.6596$ which is slightly higher than the equilibrium value previously reported for *in vitro* collagenous materials of about 0.55 that corresponds to U ≈ 3.2 [36]. Both values of S define a reasonable range of order and both cases have been reported for collagenous materials to exhibit strong birefringence at rest with well-defined pitch between 0.2 to 8 μm [12, 36]. Besides, in terms of the master plot, both values can be achieved under realistic processing conditions (De~O(10^0)) which leads to deformation rates of approximately 840 s^{-1} that is in the same order of magnitude as the deformation rate inside the depositing device in the process reported by Kirkwood and Fuller [27-29] can be estimated as ; R^3 ~720 s^{-1}.

The most common variable discussed in the literature is S, however the preferred director direction θ plays an important role as it might affect the direction of the formation of the helix which has been reported to occur perpendicular to the flow deposition [27-29]. This might indicate collagen molecules should be oriented at a direction close to the direction of the extension, in terms of the kinematics of the four roll mill would correspond to the principal axis of deformation (i.e. the x -

axis). Pure simple shear flow is not capable of creating these ordered oriented precursor deposited films because the alignment angle is about -30^o when S is within the previously specified range close to S_{eq}. This is a quantitative justification for the inclusion of extensional contributions in processes such as in [14, 27] because of the highly aligning nature of extensional flows. Following the master plot (figure 2.8), for any flow strength the aligning angle is always zero under this limit. However, shear contributions cannot be removed when coating substrates due to the presence of the solid wall and the velocity gradients perpendicular to the substrate that have an order of magnitude of $dv_x/dy = v_r/\delta$, where v_r is the velocity of the substrate and δ is the thickness of the deposited film, such gradient is magnified in thin deposited films. Based on the master plot we can indicate that processes with $\kappa = 0.2$ and higher for De close to the unity are capable of aligning the mesogens to an angle close to -20^o or closer to zero, which produced little to no defects in helix formations induced by light irradiation [32]. Based on the discussed values of order and orientation, the region delimited by the region enclosed by the white triangle on the top right of the master plot with (κ, De) vertices: (0.2, 1), (1, 0.6), (~1, 1) has realistic optimal kinematic conditions to which the precursors must be submitted for likely defect-free collagen film formation processes. The last vertex with an approximate sign (~) is an indication that in real flow situations, as above-mentioned, inhomogeneous kinematics are encountered and pure extensional flow might not be feasible.

Finally, the non-homogeneities could lead to some regions having highly ordered oriented materials and others with little to no order as observed in [14]. In terms of process design, one should analyze the complex kinematics and identify regions where gradients in κ and values of κ close to -1 can be encountered, in order to eliminate such regions if possible or at least minimized to avoid recirculation and produce uniformly oriented PN precursors.

2.6 Conclusions

This chapter presents simulation and scaling of key material properties of dilute isotropic collagen solutions, including the molecular shape parameter β and rotational diffusivity D_r, using an integrated theory-experiment loop. The theory is based on well-established nematodynamics that spans from isotropic dilute solutions to concentrated liquid crystalline solutions and the experimental data [36] provides the flow-birefringence as a function of shear rate. The rotational diffusivity D_r of 140 s^{-1} has an order of magnitude consistent with reported values of other biomacromolecules [61]. The estimated molecular shape parameter β is used to formulate the tumbling parameter function $\lambda(S)$, which is a key quantity in the rheology of liquid crystalline materials. This function is similar to others estimates for synthetic lyotropic liquid crystal polymers, and its key feature for collagen solutions is that it is above one for $0 < S < 0.83$ and below one when $0.83 < S < 1$; the former corresponds to dilute and the latter to concentrated solutions. The formulated $\lambda(S)$ is consistent with experimental data [36] on collagen solutions as it predicts flow-birefringence in the dilute regime and banded texture formation after cessation of flow in the concentrated regime, where the former is a signature of shear-induced orientation ($\lambda > 1$) and the latter of non-aligning or tumbling ($\lambda < 1$) under simple shear.

The nematodynamics model with properties of collagen solutions is explored in terms of flow intensity (Deborah number or ratio of deformation rate to rotational diffusivity) and flow kinematics κ, which is an index of the relative content of strain rate and vorticity rate. The parameter space (κ, De) describes different film processing protocols used to create collagen-based cholesteric layers, which usually contain vorticity rich ($\kappa = -1$), simple shear ($\kappa = 0$) and extensional ($\kappa = 1$) regions. Based on liquid crystal physics and observations from chiral film

formation, we find that the key control variables to convert the precursor para-nematic state into defect free cholesteric films is a sufficiently surface aligned director field and an order parameter S of the same magnitude as that in the stable cholesteric state. These two constraints reduce the parametric processing space into narrow triangle with optimal (κ_{opt}, De_{opt}) (Figure 2.8) limited by (κ=0.2, De=1) for essentially shear flows, and (κ=1, De=0.6) for extensional flows. The estimated region (top right region of figure 2.8) of alignment and order in the deposited film precursors is such that when followed by evaporation they will create defect-free materials as the ones obtained in the work of [27]. These results provide quantitative design parameters for flow-processing collagens into films for tissue engineering and other emerging biomimetic applications.

References (Chapter 2)

[1] Neville, A.C. *Biology of Fibrous Composites*. Cambridge University Press, London, 1993.

[2] Fratzl P.; Giraud-Guille M.M. *Hierarchy in Natural Materials*, Wiley-VCH Verlag GmbH & Co. KGaA, 2011.

[3] Fratzl, P. *Curr. Op. Colloid Interface Sci.*, 2013, ***8***, 32-39.

[4] Fratzl, P; Weinkamer, R. *Prog. Mate. Sci*., 2007, ***52***, 1263 - 1334

[5] Donald, A.; Winder, A; Hanna, S. *Liquid Crystalline Polymers*.2nd Edition, Cambridge University Press, London, 1992.

[6] Blumstein, A. *Liquid Crystalline Order in Polymers*. Academic Press, New York, 1978.

[7] Rey, A.D. *Soft Matter*, 2010, ***6***, 3402-3429.

[8] Rey, A.D. ; Herrera-Valencia E.E.; Murugesan, Y.K. *Liquid Crystals*, 2014, ***41*** 430-451.

[9] Giraud-Guille, M.M.; Besseau, L.; Martin, R. *J Biomech*. 2003, **36**, 1571-1579

[10] Belamie, E.; Mosser, G.; Gobeaux, F.; Giraud-Guille, M.M. *J. Phys.: Condens. Matter*, 2006, **18**, S115-S129

[11] Green, D.W.; Lee, J.M.; Kim, E.J.; Lee, D.J.; Jung, H-S. *Adv. Mater Interface*, 2016, ***3***,1500411

[12] Giraud Guille, M.M.; Mosser, G.; Helary, C.; Eglin, D. *Micron*, 2005, ***36***, 602-608.

[13]Price, J.C.; Roach, P.; El Haj, A.J. *ACS Biomater. Sci. Eng*. 2016 ***2***, 625-633.

[14]Paten, J.A.; Siadat, M.E.; Susilo, S.M.; Ismail, E.N.; Stoner, J.L.; Rothstein, J.P.; Ruberti, J.W. *ACS Nano*, 2016, ***10***, 5027-5040.

[15]Eglin, D.; Mosser, G.; Giraud-Guille, M.M.; Livage, J.; Coradin, T. *Soft Matter*, 2005, **1**, 129-131

[16]Mosser, G.; Anglo, A.; Helary, C.; Bouligand, Y.; Giraud-Guille, M.M. *Matrix Biol.* 2006, **25**, 3-13

[17]Yaari, A.; Posen, Y.; Shoseyov, O. *Tissue Eng. Part A*, 2013, **19**, 1502-1506

[18]Albu, M.A.; Titorencu, I.; Ghica, V. Collagen Based Drug Delivery Systems for Tissue Engineering, in Biomaterials Applications for NanoMedicine. Ed. Pignatello, R. InTech, 2011, 334-358

[19]Giraud-Guille, M.M; Nassif, N.N.; Fernandes, F.M.; Collagen-based materials for tissue repair, from bio-inspired to biomimetic. In: Materials Design Inspires by Nature: Function through Inner Architecture. Ed. Fratzl, P.; Dunlop, J.W.C.; Weinkamer, R. RSC. 2013. 107-127

[20]Giraud-Guille, M.M.; Helary, C.; Vigier, S.; Nassif, N. *Soft Matter*, 2010, **6**, 4963-4967

[21]Cheng, X.; Gurkan, U.A.; Dehen, C.J.; Tate, M.P.; Hillhouse, H.W.; Simpson, G.J.; Akkus, O. *Biomaterials*, 2008, **29**, 3278-3288

[22]Matthews, J.A.; Wnek, G.E.; Simpson, G.L.; Bowlin, D. *Biomacromolecules*, 2002, ***3***, 232-238.

[23]Torbet, J.; Malbouyres,; Builles, N; Justin, V.; Roulet, M.; Damour, O.; Oldberg, A.; Ruggiero, F.; Hulmes, D.J.S. *Biomaterials*, 2007, **28**, 4268-4276

[24]Torbet, J.; Ronziere, M.C. *Biochem. J*. 1984, **219**, 1057-1059

[25]Li, Y.; Huang, G.; Zhang, X.; Li, B.; Chen, Y.; Lu, T.; Lu, T.J.; Xu, F. *Adv. Funct. Mater*. 2013, **23**, 660-672

[26]Antman-Passig, M.; Shefi, O. *Nano Lett*. 2016, **16**, 2567-2573

[27]Kirkwood, J.E.; Fuller, G.G. *Langmuir*, 2009, ***25***, 3200-3206.

[28]Fuller, G.G.; Kirkwood, J.E. Oriented Collagen Gel. U.S. Patent 8,597,717 B2. Dec. 3, 2013.

[29]Paukshto, M.V.; McMurtry, H.; Fuller, G.G.; Bobrov, Y.A.; Kirkwood, J.E. Collagen Materials, Films and Methods of Making Same. U.S. Patent Application Publication. US 2011/0151563 A1. June 23, 2011.

[30]Lee, P.; Lin, R.; Moon, J.; Lee, L.P. *Biomed. Microdevices*, 2006, **8**, 35-41

[31]Saeidi, N.; Sander, E.A.; Ruberti, J.W. 2009, **30**, 6581-6592.

[32]Zheng, Z.; Li, Y.; Bisoyi, H.K.; Wang, L.; Bunning, T.J.; Li, Q. *Nature*, 2016, **531**, 352-356.

[33]de Luca G.; Rey, A. D. *Phys. Rev. E,* 2004*, **69***, 011706

[34]Tanaka, Y.; Baba, K.; Duncan, T.J.; Kubota, A.; Asahi, T.; Quantock, A.J.; Yamato, M.; Okano, T.; Nishida, K. *Biomaterials*, 2011, ***32***, 3358-3366.

[35]De Sa Peixoto, P. ; Deniset-Besseau, A.; Schmutz, M.; Anglo, A.; Illoul, C.; Schanne-Klein, M.C.; Mosser, G. *Soft Matter*, 2013, ***9***, 11241-11248.

[36]Gobeaux, F. ; Belamie, E.; Mosser, G.; Davidson, P.; Panine, P.; Giraud-Guille, M.M. *Langmuir*, 2007, ***23***, 6411-6417.

[37]Hutmacher, D.; Paige-Little, J.; Pettet, G.J.; Loessner, D. J. Mater. Sci: Mater. Med, 2015, **26**, 182-185.

[38]Lovelady, H.H.; Shashidhara, S.; Mattews, W.G. *Biopolymers*, 2013, ***101***, 329-335, 2013.

[39]Claire, K.; Pecora, R. *J. Phys. Chem. B,* 1997, ***101***,746-753.

[40]Gautieri, A.; Russo, A.; Vesentini, S.; Redaelli, A.; Buehler, M.J. *J. Chem. Theory Comput.* 2010, ***6***, 1210-1218.

[41]Doi, M.; Edwards, S.M. *The Theory of Polymer Dynamics*. Oxford University Press, London, 1988.

[42]Grecov, D.; Rey, A.D. *Mol. Cryst. Liq. Cryst.*, 2003, ***391***, 57-94.

[43]Tsuji, T.; Rey, A.D. *J. Non-Newt. Fluid Mech.* 1997, ***73***, 127-152.

[44]Marrucci, G.; Greco, F. *Adv. Chem. Phys.*, 1993, ***86***, 331-404.

[45]Leonov, A.I.; Prokunin, A.N. *Nonlinear phenomena in flow of viscoelastic polymer fluids*. Chapman and Hall, 1994.

[46]Bird. R.B.; Armstrong, R.C.; Hassager, O. *Dynamics of Polymeric Liquids, Volume 1*. John Wiley & Sons, New York, 1987.

[47]Taylor, G.I. *Proc. Royal Soc. London A*, 1934, ***146,*** 501-523.

[48]Higdon J.J.L. *Phys. Fluids A*. 1993, ***5***, 274-276.

[49]Lagnado, R.R.; Leal, L.G. *Exp. Fluids*, 1990, ***9***, 25-32.

[50]de Gennes, P.G.; Prost, J. *The Physics of Liquid Crystals*. 2nd Edition. Oxford University Press, London, 1993.

[51]Chandrasekhar, S. *Liquid Crystals*. 2nd Edition. Cambridge University Press, London, 1992.

[52]Rey, A. D. *J. Rheol*. 2000, ***44***,855-869.

[53]Echeverria, C. ; Almeida, P.L.; Feio, G.; Figueirinhas, J.L.; Rey, A.D.; Godinho, M.H. *Polymer*, 2015, ***65***, 18-25.

[54]Rey, A. D. *Phys. Rev. E*, 1996, ***53***, 4198-4201.

[55]Rey, A. D. *J. Chem. Phys.*, 1996, ***104***, 4343-4346.

[56]Rey, A.D. *Phys. Rev. E*, 2002, ***65***, 022701.

[57]Larson, R.G. *The Structure and Rheology of Complex Fluids*. Oxford University Press, London, 1999.

[58]Forest, M.G.; Wang, Q.; Zhou, R.; Choate, E.P. *J. Non-Newt. Fluid Mech.*, 2004, ***118***, 17-31.

[59]Rey, A.D.; Denn, M.M. *Annual Rev. Fluid Mech.*, 2002, ***34***, 233-266.

[60]Davidson, P.; Petermann, D.; Leveult, A.M. *J. Phys. II*, 1995, *5*, 113-131.

[61]Serdyuk, I.N.; Zaccai, N.R.; Zaccai, G. *Methods in molecular biophysics: structure, dynamics, function*. Cambridge University Press, London, 2007.

[62]Barmpoutis, A.; Vemuri, B.C.; Shepherd, T.M.; Forder, J.R. *IEEE Trans. Med. Imaging*, 2011, ***26***, 1537-1546.

Chapter 3

3 Biological Plywood Film Formation from Para-nematic Liquid Crystalline Organization

3.1 Preface

The previous chapter provided the kinematic conditions to which the dilute collagen solutions should be submitted in order to have the appropriate order and orientation for solvent removal. This chapter analyzes the drying stage of the process and uses the initial order and alignment computed in Chapter 2. A fully coupled model taking into account the mesogen order, the solvent mass transfer and volume reduction is presented. The effect of the internal mass transfer on the resulting microstructure is evaluated. This chapter is reproduced from a manuscript currently in preparation titled: "Biological plywood film formation from para-nematic liquid crystalline organization"

3.2 Summary

In vitro non-equilibrium self-assembly processes of biomacromolecular solutions offer a systematic and reproducible way of generating material architectures found in Nature, such as biological plywoods. Accelerated progress in biomimetic engineering of mesoscopic plywoods and other fibrous structures requires a fundamental understanding of processing and transport principles. In this work we focus on collagen I based materials and structures to find processing conditions that lead to defect-free collagen films displaying the helicoidal plywood (cholesteric or chiral nematic) architecture. Here we report on experimentally-guided theory and simulations of the self-assembly of collagen molecules through water solvent evaporation of pre-aligned dilute

collagen solutions. We develop, implement and qualitatively validate an integrated liquid crystal self-assembly-water transport model that captures the spatio-temporal chiral structure formation in shrinking domains due to water loss. Three microstructural (texture) modes are identified depending on the particular value of the time-scale ratio defined by collagen rotational diffusion to water translational diffusion. The magnitude of the time scale ratio provides the conditions for the synchronization of the helical axis morphogenesis with the increase in the mesogen concentration due to water loss. Slower than critical water removal rates leads to internal multiaxial cellular patterns, reminiscent of the classical columnar-equiaxed metallurgical casting structures. Excessive water removal rates lead to destabilization of the chiral axis and multidomain defected films. The predictions of the integrated model are in qualitative agreement with experimental results and can potentially guide solution processing of other bio-related mesogenic solutions that seek to mimic the architecture of biological fibrous composites.

3.3 Introduction

Natural materials such as collagen, cellulose and chitin are well known for providing support and structure due to its capability to self-assemble into complex multi-scale hierarchical architectures [1-4] usually from liquid crystalline precursor states [1, 2, 5, 6]. Three different analogues to conventional liquid crystals have been identified [7]: i) solid analogues known as biological plywoods (BP) with frozen liquid crystalline order as in plant cell walls [8, 9], insect exoskeletons [10, 11], crustacean cuticles [5], bones [12, 13, 14], fish scales [15], cornea [16]; ii) in vitro, where extracted biomacromolecules in solution can be considered lyotropic liquid crystals, and iii) in vivo biological liquid crystals such as spider silk and biological membranes. One of the most ubiquitous biomesophase is the chiral nematic N* (cholesteric) due to the intrinsic chirality of some of Nature's building blocks as highlighted in [17], however other structural arrangements

are also observed such as nematic and orthogonal [2]. As with synthetic liquid crystals, one distinguishing feature of triple helix collagen and other natural building blocks is a large molecular/particle persistence length to effective diameter aspect ratio : L/D>>1. Frustration during biological self-assembly leads to characteristic topological defects with the same characteristics found in conventional liquid crystals, reinforcing the self-assembly hypothesis in the synthesis and formation of biological plywoods [1, 2]. This modeling and simulation chapter focuses on collagen film formation, but results can be generalized to other biological liquid crystals since the operating mechanisms are expected to be invariant.

The arrangement of the building blocks obtained through the self-assembly process is responsible for multi-functionality [4, 18] and enhanced mechanical properties which has inspired scientists to develop materials through the bottom-up approach [19]. This has been a paradigm changer in materials science and engineering where certain very specific applications require a highly organized mesophases without defects such as security papers [20], sensors [21], contact guidance for cell growth in highly ordered tissue [22]. Therefore, a strategy to control the internal arrangement of the building blocks over several length-scales is required. Strategies involving non-equilibrium self-assembly must take into consideration the rheology and flow-structuring abilities of the precursor state. Chiral nematic precursors are difficult to flow-process given the solid-like behaviour along the helix axis and propensity to uncoil under simple shear, as further discussed below. Hence melting the chirality through dilution, flow processing in the dilute state, and subsequent solvent evaporation has been shown by Kirkwood and Fuller [22, 23] to provide an efficient material processing pathway. Figure 3.1 shows a simplified schematic of key features of this optimal film formation process, where an initial unstable para-nematic phase is converted to a cholesteric phase by solvent removal. Here S is the scalar nematic order parameter of a dilute

collagen solution which is positive (S > 0) due to previous flow-processing, as discussed in the previous chapter [24]. Since there is no chirality in the paranematic phase, the pitch (distance for a 2π rotation) is infinity and the chiral axis **h** is undefined. As the water solvent is removed at an appropriate rate, the order S is retained, but the macroscopic chirality is created, such that we find a well oriented cholesteric helix **h** with a uniform pitch p_o. To characterize and control the film formation process a full integration of the phase ordering process with the solvent mass transfer in a shrinking volume needs to be made. The key challenge and objective of this chapter is to find the process parametric envelop that leads to well-formed defect free uniform cholesteric collagen film, which can only be revealed when the complex interactions between chirality formation rate, dehydration rate, and nematic order relaxation rate in an evolving and shrinking volume are understood and quantified.

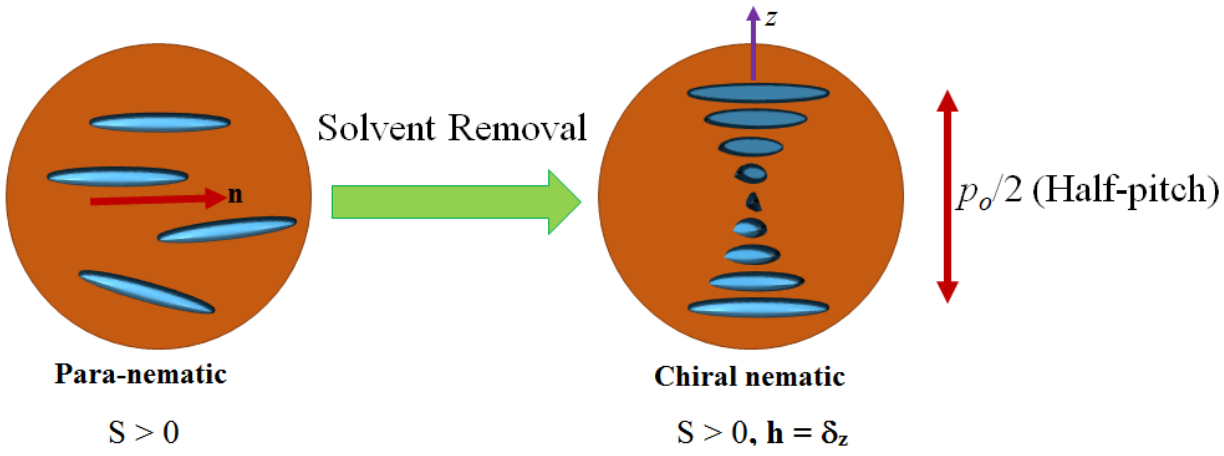

Figure 3.1. Schematic of the process investigated in this chapter. Conversion of a dilute para-nematic phase, characterized by a non-zero scalar order parameter S into a cholesteric N* phase, characterized by a non-zero scalar order parameter and a helical axis **h** (in this case it the "z" direction). The helical axis **h** and the pitch p_o or distance for the average orientation (director) to achieve a 2π rotation define the local chiral nematic state. The initial para-nematic phase is obtained by flow-processing (shear plus extensional flow) a dilute mesogen-containing solution that achieves a sufficiently large scale order parameter S. The goal is to find processing-material conditions that lead to a uniform defect-free N* phase.

The specific objectives of this theory and simulation chapter are: (i) formulate, solve and validate an integrated phase ordering-dehydration model for collagen film formation that includes directed chiral self-assembly, anisotropic diffusion, moving boundaries due to solvent loss and full couplings between liquid crystal formation and solvent mass transfer; (ii) describe and quantify the various mass transfer resistances which might affect the resulting microstructure and (iii) determine the conditions that lead to a homogeneous helical axis and hence defect-free film. The model is spatially 2D, where film geometry is assumed to be rectangular whith a film thickness that decreases with time. Transport process in the surrounding air are not included and the dominant solvent flux directions are validated a posteriori. The initial para-nematic state is assumed to be known from our previous work [24] and passive substrate surfaces are assumed. Convection and surface effects such as Marangoni flow is neglected and isothermal conditions are assumed to prevail. This chapter only considers relatively early times of drying and effects such as gelification are out of the scope of this work. We show that with these restrictions, assumptions, and simplifications, our predictions are consistent with experiments [22, 23] and therefore the dominance of phase ordering-mass transfer coupling is established [22]. When needed we use previously reported [24] rheological properties, molecular aspect ratio, and rotational diffusivity of acidic collagen I solutions.

This chapter is organized as follows: section 3.4.1 provides further information regarding current strategies for obtaining highly aligned materials and describes the experimental process of Kirkwood and Fuller [22] followed by the description of the drying process in section 3.4.2. Directed self-assembly is briefly described in section 3.4.3. The model and simulation conditions are given in section 3.5, which includes the model and scaling in section 3.5.1, the geometry and initial conditions in section 3.5.2 and the methodology and simulation conditions in 3.5.3. The

results and discussion are included in section 3.6 and finally, the main findings are summarized in the Conclusions section. Three appendices are associated with this chapter whose contents are detailed as follows: Appendix D provides the mathematical details of the derivation of the model. Appendix E discusses the free energy and its dependence on the collagen concentration. Appendix F provides additional plots that support the discussion in section 3.6.

3.4 Process Description and Theoretical Background

3.4.1 Film Formation Processes

Various collagen and cellulose solutions have been processed into highly organized materials, films, and fibers. For collagen-based materials the objective is to replicate the organization of matrices as observed in vivo for contact guidance [22], tissue engineering [25, 26], wound healing [27, 28] and others, whereas for cellulosic materials the optical properties of the resulting film are attractive for the design of sensors [9, 29]. This requires the application of an external field or appropriate forces to provide the mesogenic solutions with a given orientation. Hydrodynamic forces are a relatively simple and widely used approach for this purpose [30, 31, 32] where dilute and concentrated solutions have been used for such purpose. Other approaches include electrochemical induced alignment [33], light irradiation [34], and electrospinning [35]. Theoretical studies have been recently developed for biological liquid crystals [7] and also active matter [36]. Dilute solutions display a homogeneous and effective flow-aligning behavior dependent on the deformation rate and flow type [24, 37]. On the other hand, concentrated solutions display inhomogeneous banded textures, indicating tumbling behavior [37]. More generally, cellulosic solutions display a wide variety of regimes [38, 39] with increasing shear rate reflected in the double negative minima exhibited in the first normal stress difference N_1 [39],

where some of the dynamics observed include helix uncoiling modes [40, 41], and the presence of permeation regime [42] which could impact the ease of manipulation [25]. Hence dilute solutions are generally better suited precursors for flow structuring, but unavoidably the use of dilute precursors creates a subsequent solvent evaporation challenge. For the particular case of collagen solutions [22] the water removal process should be isothermal and at an appropriate temperature window since the chemical stability of the triple helix can be compromised with temperature variations.

3.4.2 Drying Process

The film formation process reported in [22] makes use of an external airflow of dry air to evaporate the solvent of the initially deposited dilute para-nematic phase in a laminar flow hood. As drying takes place, a reduction in the volume of the film occurs where the contact area with the substrate remains constant and only a decrease in the vertical height is observed. A schematic representation of the drying process is given in figure 3.2. The width in the "z" direction remains constant as the contact lines (blue crosses) on the lower corners are pinned.

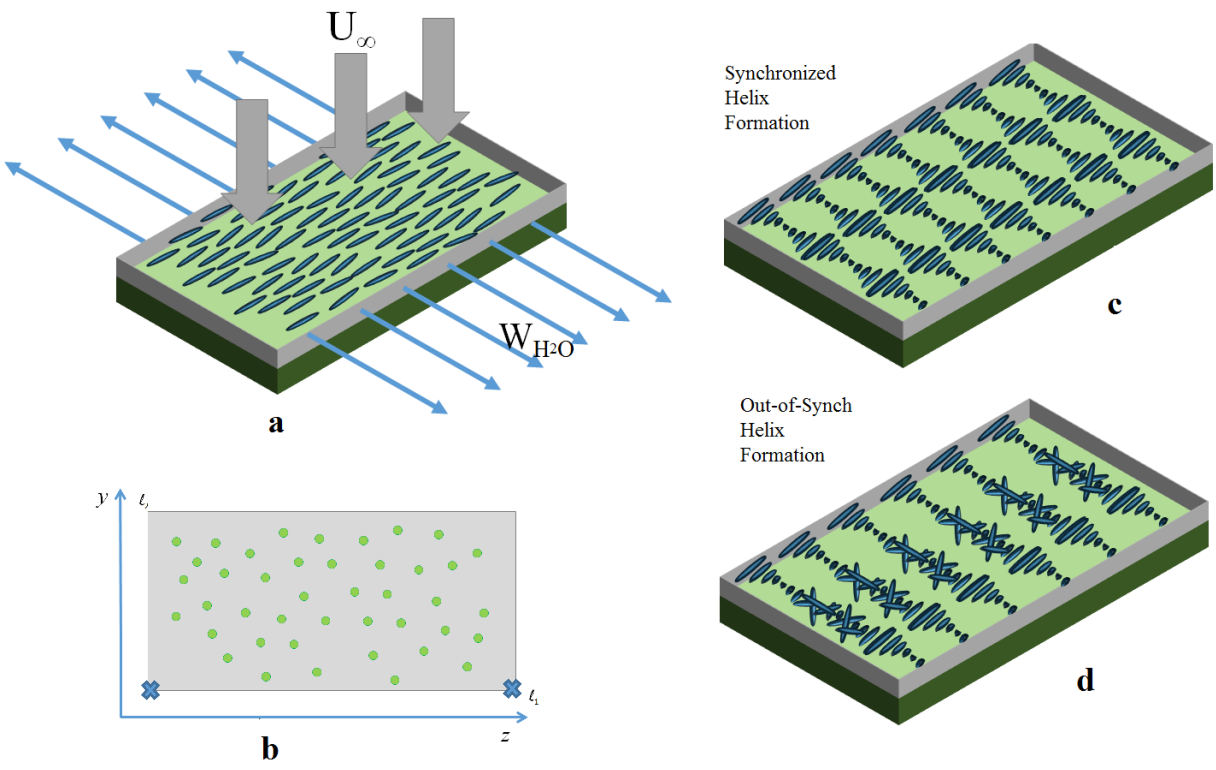

Figure 3.2. Schematic representation of the drying process used in [22] to produce defect-free collagen films with the para-nematic state and a representative cross section (a-b) and a well-aligned cholesteric helix after drying when the process is synchronized (c) and not properly synchronized (d). U_∞ is the characteristic downward air flow velocity, and W_{H_2O} is the horizontal mass rate of water leaving the collagen solution. Initially the collagen is well aligned and well-ordered due to previous flow processing, discussed in [24]. As explained below, the vertical airflow reduces vertical water evaporation.

Experimental evidence [22] indicates the phase transition begins at the vertical edges of the film (contact line regions) and advances towards the center i.e. the diffusion of the solvent within the film is preferentially across the width of the film. This drying behavior has also been reported for water based latex films [43] and cellulosic droplets [29]. Lateral diffusion can be enhanced due to the presence of vertical downwards airflow from a laminar flow hood, as in Fig. 3.2a. Theoretical studies analyzing the mass transfer in stagnation points such as the ones that could be encountered

in the configuration of [22] have demonstrated that the overall mass transfer process is hindered due to the presence of a downstream flow by enlarging the mass boundary layer [44]. This will allow us to assume the water mass flux is horizontal and leaves the system from the edges while the vertical mass transfer from the other boundaries can be considered as negligible.

The dehydration rate is governed mainly by internal and external mass transfer resistances. The internal resistance results from the solvent diffusion within the film whose characteristic time-scale is given by the ratio of L^2/D, where L is the diffusion length scale (film width) and D is the diffusion constant. The external resistance is due to the formation of a boundary layer adjacent to the collagen film. The Sherwood number, discussed in 3.2, defines the relative importance of these two mass transfer resistances. It turns out that given the specifications of laminar flow hoods, physical properties of water based films and the drying process analyzed in this work, the internal resistance is the limiting step. Furthermore, if the water is not removed at an appropriate rate (which will be quantified in the following sections) disordered cholesteric domains are to be expected as shown experimentally when the process is carried out at lower temperatures [22]. Quantification of the mass transfer process and impact on the resulting microstructure are of great importance to better understand the film formation through non-equilibrium processes. We proceed to describe a modeling approach that has been used to describe phase transitions in biological fibrous composites and indicate the modifications of this model to properly describe the drying process.

3.4.3 Theoretical Approaches: Directed Self-Assembly and Water Transport

Theoretical approaches to describe the morphogenesis of the twisted plywood architecture were based on the diffusionless directed self-assembly mechanism which was first described by Neville

[2] and modelled later in [45, 46]. The key feature to produce a monodomain chiral nematic by 1D directed self-assembly is the presence of an aligning supporting layer that promotes strong planar anchoring of the director. The directed self-assembly is described by a one-dimensional propagating front, whose wake is a perfect cholesteric domain and whose growth replaces the unstable isotropic state. The velocity of the front is constant, inversely proportional to the pitch, and proportional to the free energy decrease between the unstable isotropic phase and stable N* phase. The velocity of this front is proportional to the rotational diffusivity and hence very sensitive to the persistence length [45, 46]. On the other hand, the absence of a supporting aligning layers leads to a polydomain textures and the evolution from an unstable state to a polydomain chiral nematic phase follows a nucleation and growth mode [7]. Under more complex confinement such as drops and films with contact lines, directed self-assembly in various biological liquid crystals emerges from existing contact lines [7, 47, 48, 49]. In this case, the aligning torques at the contact line emerge from the anisotropic anchoring of liquid crystals [48, 49].

The diffusionless directed chiral self-assembly [46, 47] is an important contribution of the collagen film formation process studied here but since it assumes a constant driving force for phase ordering (decrease in free energy between unstable isotropic and stable chiral nematic phases) it cannot be applied to the drying process since it has a variable driving force because water is continuously removed from the material. Hence this model [45, 46] should be augmented with the appropriate mass transfer equation to account for a variable mesogen concentration as well as volume reduction of the film due to water solvent loss.

Previous theoretical work regarding mass transfer processes in liquid crystalline materials include the non-Fickian diffusion of gas molecules in a cholesteric films [50] using a coupling of mass

transfer and director rotation. The diffusion of chiral molecules has also been recently explored where the Brownian motion is reported to be affected by collective molecular reorientations [51], effect that might be present in the formation of chiral nematic phases. In general terms evolution of liquid crystal ordering coupled to mass transfer as in our process is known as Model C [52, 53, 54] and its distinguishing feature is the coupling between a conserved (mass concentration) and a non-conserved variable (liquid crystal tensor order parameter **Q**), where the former describes diffusion-driven phase transitions and the latter diffusionless transformations. Since the kinetics of the former decreases with time while that of the latter is constant, couplings between these two phenomena leads to pattern formation and interfacial instabilities, as described below.

3.5 Models and Methodology

3.5.1 Model and Scaling

The model used in this work is based on the Landau – de Gennes (LdG) **Q**-tensor theory [55] and is fully coupled with a mass transfer equation for the solvent where an anisotropic constitutive equation is used [56]. The volume reduction is considered as well following the mesogen mass conservation [57]. The dimensionless set of equations and dimensionless variables are given in eqns. (3.1 – 3.3). Further details regarding the derivation of the equations can be found in Appendix D and additional information regarding the mathematical modeling of liquid crystalline materials is presented in [7, 46, 58, 59] and references therein. The important quantities contained in the tensor order parameter **Q** are the scalar order parameter S (degree of alignment along the average orientation **n**) and the director or average orientation **n**. The evolution of the symmetric traceless **Q**-tensor is given by:

$$\frac{\partial \mathbf{Q}}{\partial t^*} = -\frac{1}{\left[1-\frac{3}{2}\mathbf{Q}:\mathbf{Q}\right]^2}\left\{\left(1-\frac{U(\mathbf{x},t)}{3}\right)\mathbf{Q} - U(\mathbf{x},t)(\mathbf{Q}\cdot\mathbf{Q})^{[s]} + U(\mathbf{x},t)(\mathbf{Q}:\mathbf{Q})\mathbf{Q}\right.$$
$$\left. -\frac{1}{R}\left[\nabla^{*2}\mathbf{Q} - \left[\nabla^*\cdot\left(\nabla^*\mathbf{Q}\right)^T\right]^{[s]} + 8\pi\left(\nabla^*\times\mathbf{Q}\right)^{[s]} + 16\pi^2\mathbf{Q}\right] - \frac{L_2}{L_1}\left[\nabla^*\nabla^*\cdot\mathbf{Q}\right]^{[s]}\right\} \qquad (3.1\text{ a} - \text{f})$$
$$\nabla^* = \ell \qquad z \qquad z \qquad \ldots^* \qquad y \qquad y \qquad \ldots^* \qquad \ell$$
$$\ell \qquad\qquad \ell \qquad\qquad\qquad\qquad \ell$$

where the starred variables indicate a dimensionless quantity with ℓ_c is the characteristic length-scale depending on the coordinate z (ℓ_1) or y (ℓ_2) where N half-pitches are considered in the former and M in the latter and the ratio of both half-pitches define the parameter K. U is the variable nematic potential defined according to Doi [60] as $U = 3\varphi_c/\varphi_c^*$ where φ_c^* is the characteristic phase transition volume fraction and varies according to the assumed binary relationship between the solvent and the mesogens ($\varphi_w+\varphi_c=1$). The particular value of the nematic potential U defines the shape of free energy profile $f(U,S)$ and when U > 3 (U<8/3) the stable state is the ordered (isotropic) state. Intermediate U values lead to meta-stability and are described in Appendix E. The water mass transfer equation is:

$$\frac{\partial c_w}{\partial t} = -\nabla\cdot\mathbf{j}_w\,;\mathbf{j}_w = -\left(D_{iso}\nabla c_w + D_{ani}\mathbf{Q}\cdot\nabla c_w\right)$$
$$D_{iso} = \frac{D_{\|} \quad 2D_{\perp}}{3}\,; D_{ani} = D_{\|} \quad D \qquad (3.2\text{ a} - \text{e})$$
$$\frac{\partial c_w^*}{\partial t^*} = \Pi\nabla\cdot\left(\nabla^* c_w^* + \mathbf{Q}\cdot\nabla^* c_w^*\right)$$

where c_w is the water concentration, $\mathbf{j}_w$ the water solvent flux vector, D_{iso} and D_{ani} are the isotropic and anisotropic diffusion constants; which are assumed to be of the same order of magnitude and denoted hereafter simply as D; and are defined in terms of the parallel ($D_{||}$) and perpendicular ($D_{\perp}$)

components of the diffusion tensor diagonalized in the director coordinate frame [56]. The total water mass balance and film thickness $h(t)$ evolution are:

$$\rho_c \frac{d}{dt}\int_{V(t)} \varphi_c dV = 0$$
$$\frac{dh}{dt} = \frac{2h(t)}{\rho_w L}\left\langle j_z\,|_{z=0}\,(t)\right\rangle \qquad \text{(3.3 a – b)}$$

where ρ_c is the collagen density, L is the length of the film in the z direction and $h(t)$ is the decreasing film thickness (in the vertical direction). The y-averaged flux $\left\langle j_z\,|_{z=0}\,(t)\right\rangle$ depends only on time t. The dimensionless numbers appearing in the model are discussed in section 3.2

3.5.2 Geometry and Initial and Boundary Conditions

The 2D self-assembly model considered in this work corresponds to the $y-z$ plane representing a cross section of the initially deposited dilute collagen film where the prior flow deposition is the x-direction. We consider an initial rectangle where N (M) half pitches are allowed in the z direction (y direction) and the ratio taking into account the geometric anisotropy is defined as $K = M/N$, which is assumed to be less than 1. Figure 3.2-b shows the initial geometry, where the green dots denote that the average collagen orientation of the initial para-nematic phase is in the x-direction.

The initial condition considered in all simulations for **Q** is the para-nematic phase whose degree of alignment is found in the optimal region reported in [24]: $\mathbf{Q} = S^{PN}\left(\boldsymbol{\delta}_x\boldsymbol{\delta}_x - \mathbf{I}/3\right)$, where we use throughout $S^{PN} = 0.68$. We also set the initial mesogen concentration in the isotropic region with $U(z, y, t = 0) = 2$ and its respective value for the mass transfer equation $c_w(z, y, t = 0) = c_o$. We use no anchoring boundary conditions requiring a zero torque to be imposed in all boundaries, representing passive surfaces. In order to maintain the contact area constant and the film shrinking

in the y direction only, we assume the solvent leaves the film through the boundaries whose unit vector points to the "z" direction and a no flux condition is imposed in the rest of the boundaries for the mass transfer based on the description given by [43] and the theoretical analysis in [44]. The external mass transfer can be written in terms of a convective mass transfer coefficient through a boundary layer approach where the rate of removal is given by a concentration difference between the interfacial value and that of the airflow dragging the water from the interface. The summarized dimensionless initial and boundary conditions are given in eqn. (3.4 a-e):

$$\begin{aligned}
&\mathbf{Q}(z,y,t=0) = S^{PN}\left(\mathbf{n}^{PN}\mathbf{n}^{PN} - \mathbf{I}/3\right); c_w^*(z,y,t=0) = 1 \\
&\boldsymbol{\nu}\cdot\frac{\partial f}{\partial\left(\nabla^*\mathbf{Q}\right)} = \mathbf{0} \\
&j_z^*(z^*=0,y^*,t) = j_z^*(z^*=1,y^*,t^*) = -Sh\cdot\Pi\cdot c_w^* \\
&j_y^*(z^*,y^*=0,t^*) = j_y^*(z^*,y^*=1,t^*) = 0
\end{aligned} \tag{3.4 a-e}$$

where $\boldsymbol{\nu}$ is the unit normal vector. Three dimensionless quantities appear: R, Π and Sh which are denominated the energy ratio, the time scale ratio (translational and rotational) and the Sherwood number respectively.

The three dimensionless numbers in these coupled processes are:

$$Energy\ Ratio: R = \frac{\text{Square External Length Scale}}{\text{Square Internal Length Scale}} = \frac{\left(p_o\right)^2}{\left(L_1/3ck_BT\right)}$$

$$Time\ Scale\ Ratio: \Pi = \frac{\text{Collagen Rotational Time}}{\text{Water Translational Time}} = \frac{D}{6D_rL^2} \tag{3.5 a-c}$$

$$Sherwood\ Number: Sh = \frac{\text{External Mass Transfer Resistance}}{\text{InternalMass TransferResistance}} = \frac{kL}{D}$$

The energy ratio R provides a measure to compare the internal length-scale $\xi = (L_1/ck_BT)^{1/2}$ with the external length-scale p_o and is usually a large quantity of the order of 10^4 [24]. Π is the ratio of collagen rotational time scale to the water translational time scale. As per its definition (eqn.3.5b) when Π is too low water removal is relative slow and when Π is too large water removal is fast relative to chirality formation. Finally the Sherwood number compares the external and internal resistances. Using $Sh = Sh(Re,Sc)$ for laminar flow over a flat where $Re \sim O(10^4)$ and $Sc \sim O(10^2)$ we use:

$$Sh = \frac{kL}{D} = 0.664 Re^{1/2} Sc^{1/3} \tag{3.6}$$

3.5.3 Methodology and Simulation Conditions

The set of equations, corresponding to eqns. (3.1a, 3.2e, 3.3b) constrained to ICs and BCs given by eqns. (3.4 a-e), was solved numerically using the finite element method as implemented in the commercial software COMSOL Multiphysics. The discretization was carried out using quadratic Lagrange polynomials and with a maximum of element size of 0.01 dimensionless units. Backward differentiation formulation was used for time integration. Relative error was set to 10^{-4} and convergence, accuracy and stability was established using standard methods and criteria. The final time for the simulations varied depending on the particular value of Π which is varied in the range of 10^3 to 10^5 dimensionless units of time to meet the objectives of this chapter while we use $R \approx 9000$ and $Sh \approx 2000$.

3.6 Results and Discussion

Not surprisingly, when the dimensionless number Π increases across certain critical values we find drastic changes in the resulting film morphology. Using theory and extensive simulations for the collagen-representative parametric values quoted above, three different modes are identified:

$$(i) Monodomain - Polygonal\ Mode : 10^{-6} < \Pi < 10^{-5}$$

$$(ii) Monodomain\ Transition\ Mode : \Pi^* \approx 6\times10^{-5} - 10^{-4}$$

$$(iii) Polydomain\ Mode : \Pi > \Pi^* \approx 6\times10^{-5}$$

We note that, as usual for nonlinear complex systems, unless one performs arc-length continuation and bifurcation studies to directly and exactly compute the stability threshold Π^*, the transition value $\Pi^* \approx 6\times10^{-5} - 10^{-4}$ is necessarily given as a range. The lower value $\Pi^* \approx 6\times10^{-5}$ is found from a theoretical calculation (eqn.3.9) and the upper value $\Pi^* \approx 10^{-4}$ is corroborated by simulations for the time window specified in our simulations and spatial resolution of the adopted finite element mesh. Below we show an exact theoretical calculation for the monodomain stability threshold that gives $\Pi^* \approx 6.2\times10^{-5}$ for $L/p_o = 15$, and generalizes the results for other chiral polymeric mesogen. The specific characteristics of the polygonal and polydomain modes are, as expected strongly evident as one moves farther away from the transition, $\Pi << \Pi^*$ and $\Pi >> \Pi^*$, respectively.

Figure 3.3 shows a summary of the resulting film structures in terms of the long-time $Q_{xx}(y,z)$ visualizations. A vertically periodic layered phase denotes a perfect helix along the z-axis. Low

values of $\Pi\left(\Pi < \Pi^* \approx 6\times10^{-5}\right)$, ranging between [$10^{-6}$, 10^{-5}], lead to three regions in the computational domain where two horizontal (along *z*) homogeneous helices are found close to the edges of the film and an internal region characterized by the presence of a polygonal domain texture with a characteristic width dependent on the particular value of Π. This type of composite microstructure (monodomain-cellular mode) is essentially like the ubiquitous columnar-equiaxed microstructures found in metal casting whose interior lacks directionality due to slow rate of heat removal [61]. Notably, slow heat removal rate in metal casting and slow water removal rate in lyotropic chiral mesophes give analogous structures; a key difference is that in the former heat is evolved at the front and in the latter water resides in the interior. An intermediate value with an order of magnitude of $\Pi = \Pi^* = 10^{-4}$ lead to a horizontal homogeneous helical axis throughout the entire computational domain (monodomain mode). Finally, large values above $\Pi = 10^{-3}$ lead to a polydomain texture in the cross section.

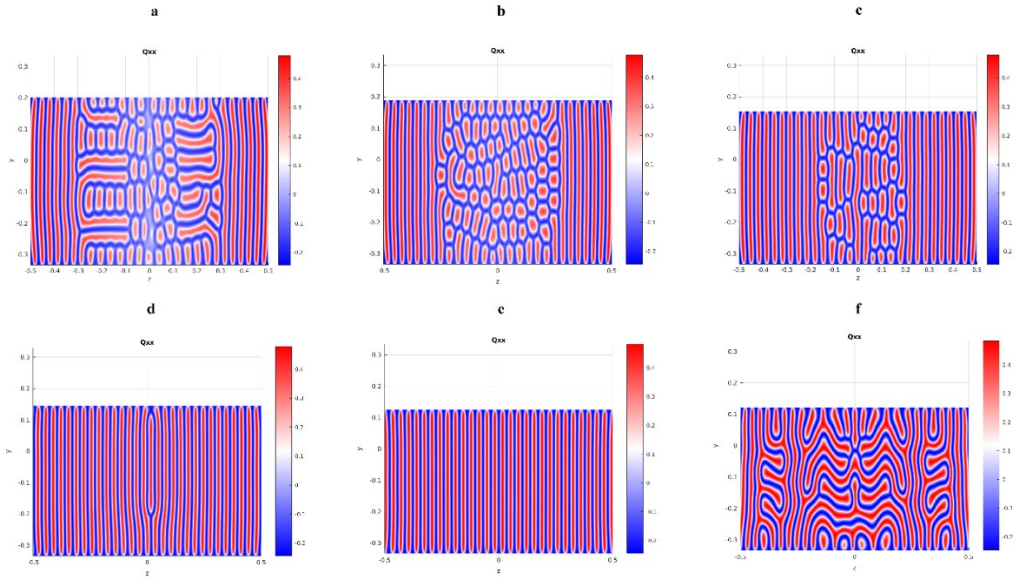

Figure 3.3. Final resulting microstructure in terms of Q_{xx} as a function of (y,z) for $\Pi = 6\text{x}10^{-6}$ (a), $1\text{x}10^{-5}$ (b), $2\text{x}10^{-5}$ (c),$4\text{x}10^{-5}$ (d), $1\text{x}10^{-4}$ (e), and $1\text{x}10^{-3}$ (f). The ideal perfect homogeneous helical axis is obtained for $\Pi \sim O(10^{-4})$.

Figure 3.4 (a-c) shows the evolution of Q_{xx} for the monodomain mode for $\Pi = 1x10^{-4}$. The phase transition to the cholesteric phase is observed from the edge of the cross section and propagates to the central region of the film. The evolution is that of a 1D propagating front and the result is a perfect defect free helix along the z-direction. The figure also shows the change in the height of the initial slightly anisotropic rectangle representing the cross section. A detailed plot of the height h as a function of time for varying Π is found in Appendix F in figure F1. Figure 3.4 (d-e) shows the nematic potential U profile evolution (proportional to the mesogen concentration profile). The rapid increase in the mesogen concentration at the edge of the film is due to the mass transfer boundary conditions with a large Sherwood number. This creates a concentration gradient and the water diffuses from the central region to the edge at a given rate determined by the particular value of Π.

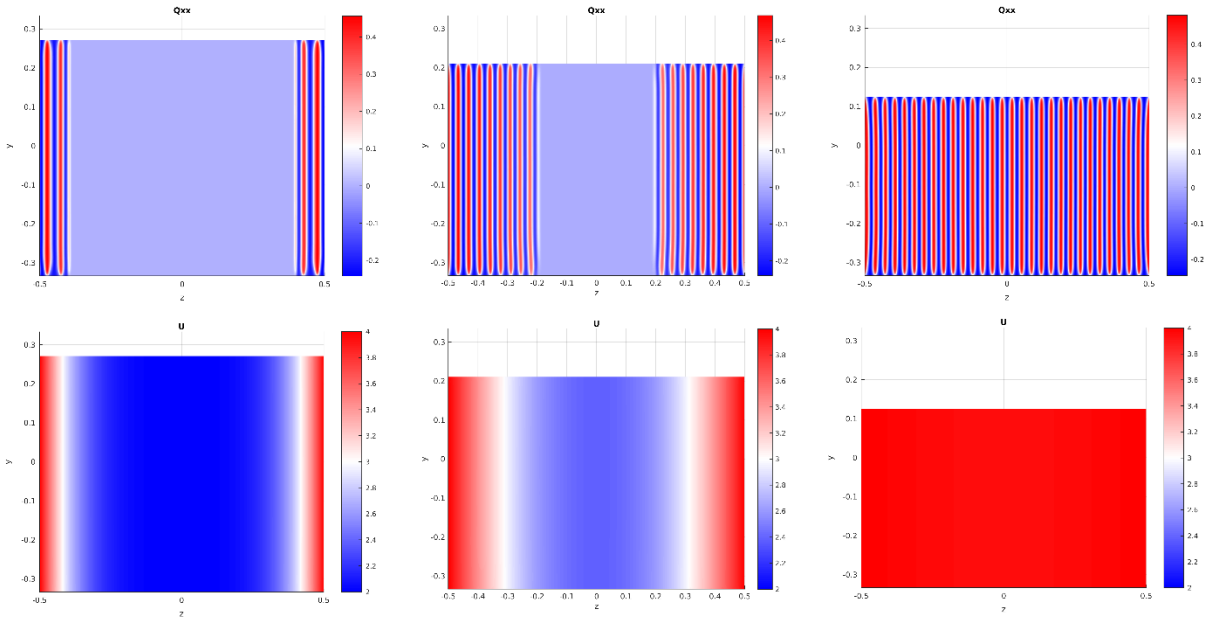

Figure 3.4. Q_{xx} surface plot in terms of the spatial coordinates y-z (a-c) for increasing times ($t^* = 100, 300, 5000$) and the nematic potential U (d-e) for the same times for $\Pi = 1x10^{-4}$ showing a homogeneous helical axis forming from the edge toward the central region of the cross section. For this value of the time scale ratio Π, no defects form.

Figure 3.5 shows the scalar order parameter S, the nematic potential U and the x-component of the director field $|n_x|$ profiles as a function of z for a constant value of y for three increasing times; Appendix F show complementary surface plots of the scalar order parameter S and the out-of-plane director component n_x in figure F2. It can be observed the scalar order parameter S, due to its fast dynamics, relaxes to zero in regions where the concentration has not increased and the nematic potential U is less than the threshold for the ordered phase to be stable, i.e. $U < 3$. A sharp S-front moves from the contact line edges ($z = \pm 1/2$) towards the center ($z = 0$). On the other hand, the alignment given by the previous flow deposition step and captured by the initial conditions $\mathbf{n} = \boldsymbol{\delta}_x$ is more persistent due to the slower dynamics of the director compared to that of S, this is reflected in the central region for early times where the orientation is still out of the plane and $|n_x| = 1$. Once the mesogen concentration is sufficiently large for a phase transition to be observed ($U > 2.7$) where both states, the ordered and disordered are stable, the scalar order parameter increases in such regions where it relaxed and the director begins to exhibit the twisted configuration. The generation of a homogeneous helical axis requires the synchronization of the phase ordering rate (dS/dt) and the drying rate (dc_w/dt). More specifically the propagating helix is moving at the same rate as the location where the metastable state ($U \approx 2.7$) is found:

$$\begin{cases} S = S(z - V_S t) \\ V_w = \dfrac{D}{L} \end{cases} \qquad (3.7a,b)$$

To obtain a monodomain the speed of the 1D traveling waves for S and water removal rate must be equal: $V_S = V_w$. This is summarized in figure 3.5 (a-c) and (d-f) that show the nematic potential U and the scalar order parameter S along with $|n_x|$, respectively.

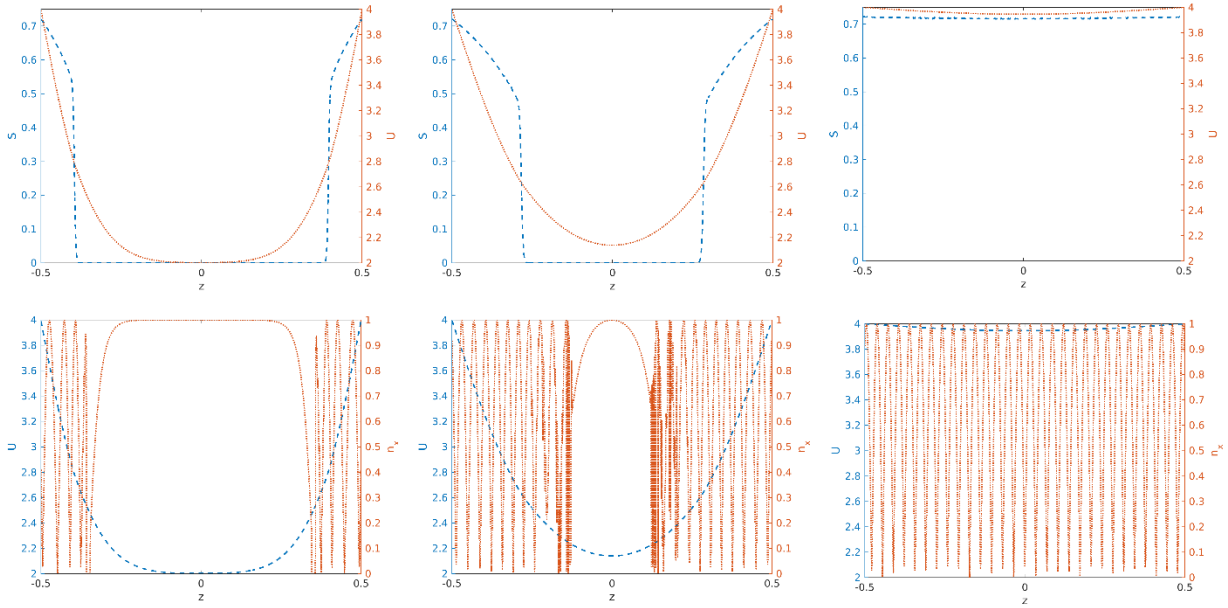

Figure 3.5. *S* and *U* (a-c) fronts moving towards the central region until a homogeneous value is reached throughout the entire domain and *U* and n_x fronts (d-f). Time scale ratio $\Pi = 1\text{x}10^{-4}$. The increasing times are given according to figure 3.4.

According to [7], the velocity V_S of the 1D phase ordering front for U≈3 is

$$V_S = \sqrt{\frac{3}{R}} p_o D_r \left[-\sqrt{\frac{U}{108}} + \sqrt{\frac{3U}{4} - 2 - \frac{24\pi^2}{R}} \right] = 0.3062\left(\mathrm{R}^{-1/2} \mathrm{p}_0 \mathrm{D}_r\right) \tag{3.8}$$

Using eqns. (3.7, 3.8) we find a scaling estimate of the critical time scale ratio:

$$V_S = V_w \rightarrow \Pi^* = \frac{D}{6 D_r L^2} = 0.05 \sqrt{\frac{3}{R}} \frac{p_o}{L} \tag{3.9}$$

which reveals the nature of the stability threshold. Equation (3.9) is a key quantitative finding of this work as it specifically fixes the exact values of geometry (L), properties (*D*, D_r) and structure (p_o) for defect-free films. For $L / p_o = 15$, we find $\Pi^* \approx 6.2 \times 10^{-5}$ which is in the order magnitude of the computed value.

We proceed to describe the system with different mass transfer internal resistances, to evaluate the effect of varying the driving force intensity and to determine how sensitive the system is to changes in Π with respect to Π^*; Appendix F show additional supporting characterizations in terms of Q_{xx} and U for $\Pi << \Pi^*$ and $\Pi >> \Pi^*$ in figures F3 and F4 respectively. Similarly to the previously analyzed monodomain transition mode$\left(\Pi \sim \right.$, in the monodomain-polygonal mode ($\Pi < \Pi^*$) the rapid depletion at the edges produces a rapid increase in the mesogen concentration and a helical axis propagates to the center. The decrease in Π from its critical value Π^* causes a slower water diffusion and consequently a slower increase in the mesogen concentration. The scalar order parameter and out of plane director curves similar to the ones presented in figure 3.5 are presented in figure 3.6 (a-c) and (d-f) respectively. A similar behavior is exhibited by S, however the director presents a twist configuration which indicates the presence of a pre-cholesteric state, defined as a phase presenting a helical orientation (**n**) configuration but low and apparently random order (S<<1). The increase in the mesogen concentration is not synchronized with the scalar order parameter front, hence, the random pre-cholesteric becomes the 2D blue phase [7] (cellular cholesteric phase in two spatial dimensions) that begins to form when both variables are out of phase for approximately half period of the helical structure. Depending on Π, the cellular patterns may distort into polygons. Three regions are clearly separated where two homogeneous helical axes can be found close to the edge and the stabilized defect lattice structure (cellular pattern) is found close to the center where the latter is characterized for having singular and non-singular topological defects at the vertices and at the center of the polygons respectively; see [7]. An amplification to this zone is presented in Appendix F in figure F5.

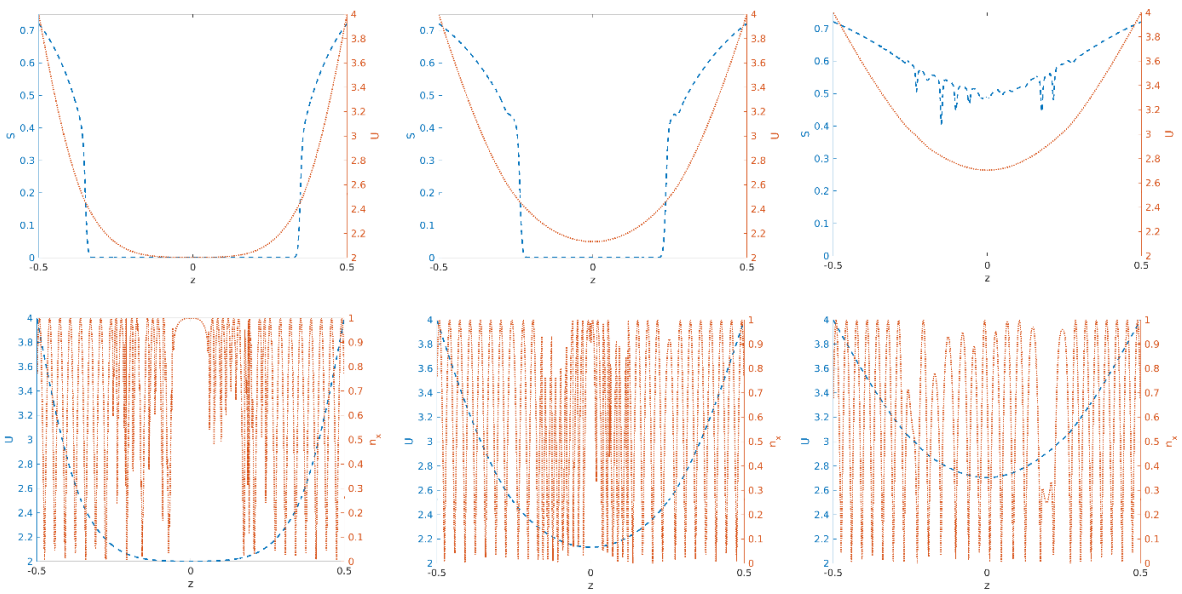

Figure 3.6. *S* and *U* (a-c) fronts moving towards the central region until a homogeneous value is reached throughout the entire domain and *U* and n_x fronts (d-f) for $\Pi = 1\text{x}10^{-5}$. Increasing times are given as $t^* = 1000, 3000, 8000$.

We proceed to analyze the increase in Π (Π > Π*) leading to the polydomain structure. In this case after the fast depletion, the diffusion of the solvent occurs fast causing a rapid increase in the mesogen concentration exceeding the phase transition threshold and S increases everywhere in the cross section non-monotonically, contrasting to the 1D front propagation observed in the previous cases, this causes helices to be formed at any part of the computational domain as observed in figure 3.7 (a-f). Another remarkable difference for this particular case of $\Pi > \Pi^*$ is given in terms of the mass flux. In the previous cases, the flux is unidirectional for early times, as time increases the anisotropy is manifested and regions with non-zero J_y appear and J_z becomes y-dependent, however they appear to be negligible in terms of the mass transfer because by the time they manifest, the mesogen is close to its final and homogeneous concentration. The figures corresponding to these two cases are also presented in Appendix F, in figures F6 and F7. Both components of the flux, J_y and J_z, as shown in figure 3.8 for $\Pi = 10^{-3}$ i.e. for the present case of

$\Pi > \Pi^*$. These anomalies are manifested earlier due to the early onset of the multi-domain helical structure.

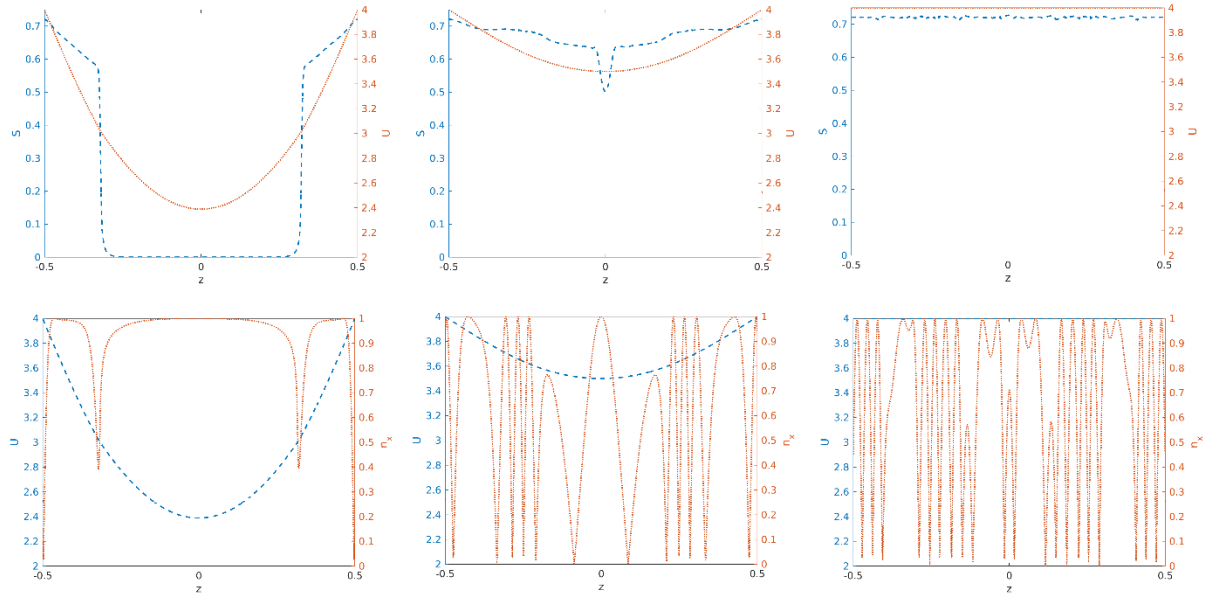

Figure 3.7. *S* and *U* (a-c) fronts moving towards the central region until a homogeneous value is reached throughout the entire domain and *U* and n_x fronts (d-f) for $\Pi = 1\text{x}10^{-3}$. Increasing times are $t^* = 50, 200, 5000$.

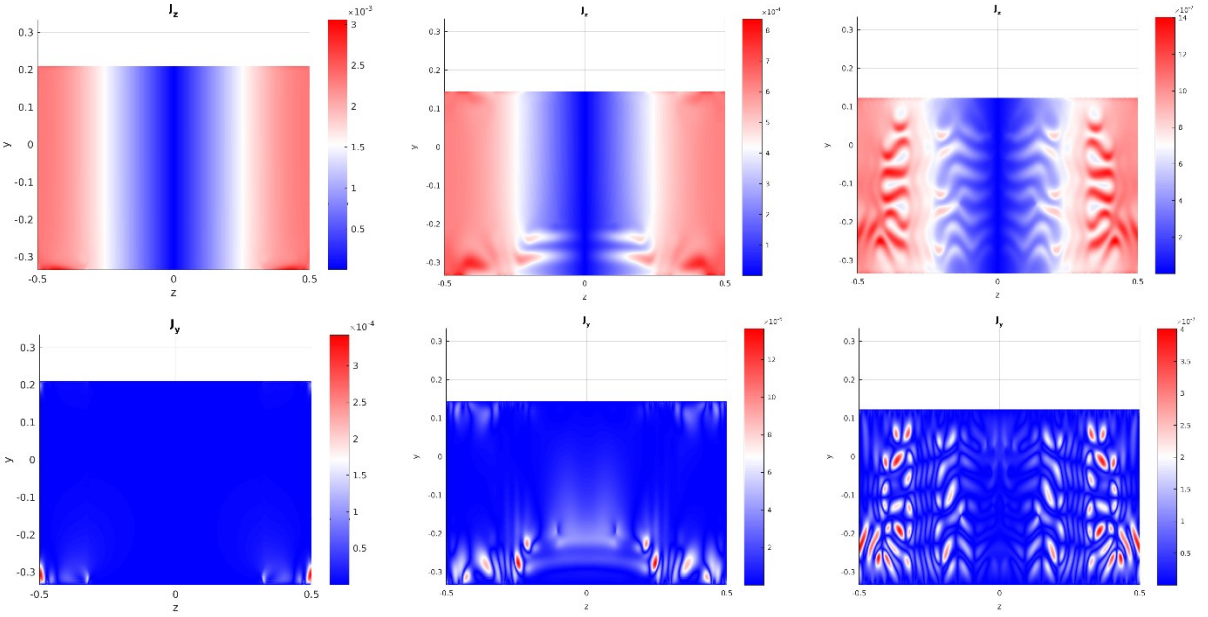

Figure 3.8. Mass flux components profiles in the polydomain mode ; z-component (a-c) and y-component (d-f), showing anomalies and bidirectional arising with increasing times ($t^* = 50, 200, 1000$).

As mentioned above, the time scale ratio Π is a function of solvent (D), and mesogen (D_r) properties , and film geometry (L). To generate defect-free films the material-process geometry should aim at obtaining a ratio of $\Pi^* \sim O(10^{-4})$. Using equation 3.9 we find:

$$\frac{D}{6D_r} = \underset{critical\ curve}{\Pi^* L^2} = \underbrace{0.05.\sqrt{\frac{3}{R}} p_o L}_{operating\ line} \tag{3.10}$$

The critical curve is a parabola whose curvature depends on Π^* and the operating line has a slope that depends on the pitch p_o. Thus the intersection of the critical curve and the operating line provides a unique critical material/process condition that yield a defect free film. Figure 3.9 shows a plot (red curve) of $D/6D_r$ as a function of L for a fixed value of Π^* (eqn. 3.10 middle) and $D/6D_r$ as a function of L for a fixed value of p_o (equation 3.10 right, blue dotted line).

For given material properties ($D/6D_r$) with a pitch p_o in the order of tenths of micrometer as is the case for in vitro acidic collagen I, the ratio ($D/6D_r$) will have one single crossing with a processing curve for the critical Π^*. This is shown in figure 3.9 where eqn. 3.10 is plotted for p_o = 10 μm . Operating with shorter lengths L generates a polydomain texture, and operating with too long L the monodomain – polygonal texture.

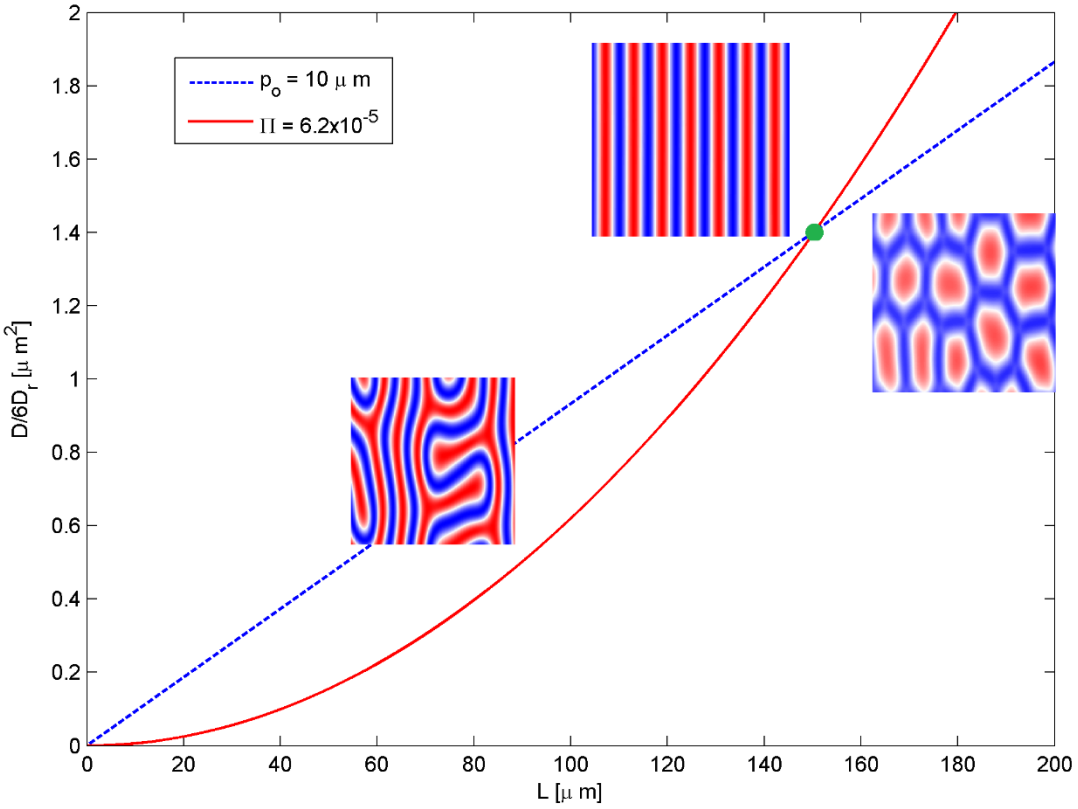

Figure 3.9. Processing curve in terms of the combination of the system properties $D/6D_r$ and the characteristic length-scale L of the system in μm for a material with p_o = 10 μm (blue line) and constant $\Pi = \Pi^*$ (red line). The green dot indicates the intercepting region where a monodomain forms.

The coupling of the solvent diffusion with the mesogen ordering can be interpreted as a positive feedback loop shown in figure 3.10, where changes in the concentration, associated with the solvent diffusivity, produce increases in the scalar order parameter. The figure is inspired by other liquid instabilities associated to heat transfer [55]. This increase induces a torque which is correlated with the mesogen rotational diffusivity constant, and the minimization of energy leads to the formation of a helix. Depending on the actual stage of the drying, the presence of the helical axis can generate changes in other spatial directions, affecting the ordering in the system and

finally impacting in the helical axis. The modulating time-scales are the mass diffusion (L^2/D) and the reciprocal rotational diffusion constant ($1/D_r$) and it was shown that any values of both time-scales lead to a chiral nematic phase, however only by modulating appropriately as the results show lead to a defect-free material.

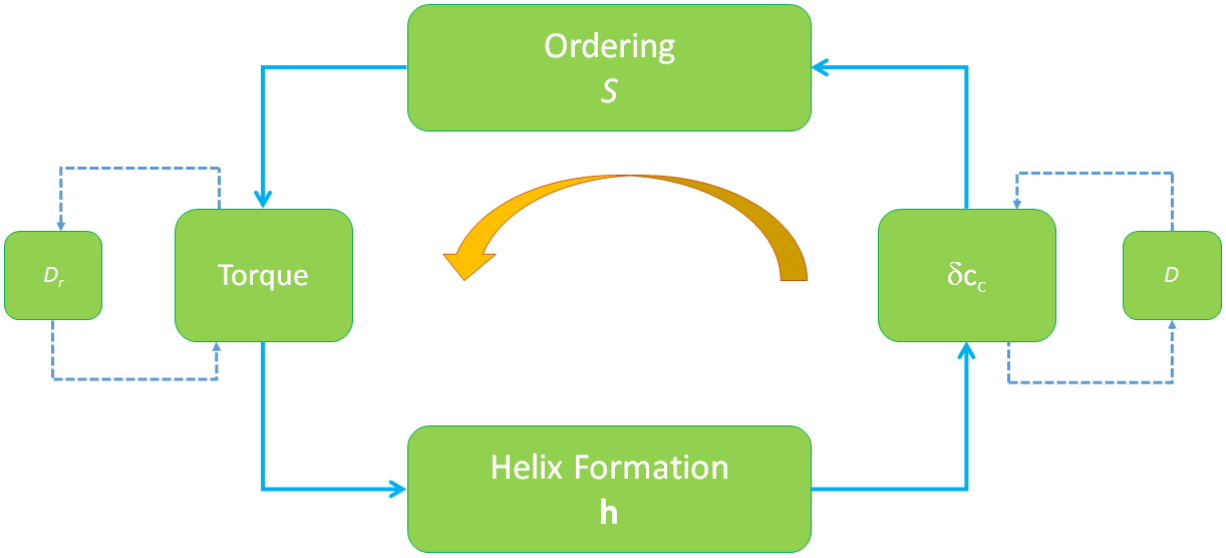

Figure 3.10. Positive feedback loop showing the coupling of the two phenomena explored in this chapter. The drying begins with changes in the concentration (δc_c) that induces ordering in the system followed by its respective torque and helix formation (**h**). The figure is inspired by other orientation-heat transfer couplings in nematic liquid crystals, see fig. B.III.59 in [55]

3.7 Conclusions

We presented a rigorous and fully coupled model that captures the main features in the solvent removal process of defect-free collagen solutions where the initial para-nematic phase, which is obtained in a previous flow deposition process, is converted to a cholesteric phase. The model's main features are the integration of chiral phase ordering and anisotropic mass transfer in a time evolving film geometry of varying thickness but constant substrate contact area due to contact line

pinning. As the integrated model couples conserved (mass) and non-conserved (**Q**-tensor) variables it leads to instabilities since growth by phase ordering and mass diffusion must be synchronized. Three different final microstructure modes were found depending on the mass transfer resistances accounted in the ratio of collagen rotational diffusion time to water translational diffusion time Π. We estimated the critical time scale ratio value that leads to a homogeneous helical axis and showed that the synchronization of the forming helix with the increase in the mesogen concentration is crucial, in qualitative agreement with experiments [22, 23]. A direct analogy with the well-known and ubiquitous columnar-equiaxed metallurgical casting structures is identified [61], where slow heat transfer rate in metal casting corresponds to slow drying rates in collagen plywoods. Finally, we provide a process diagram for the formation of a homogeneous helical axis in terms of the combination of $D/6D_r$ as a function of the characteristic length-scale L (see eqn. 3.10). The simulated biomimetic process for the formation of helicoidal plywoods, consisting in flow-processing dilute mesogenic solutions (collagen, cellulosics), followed by controlled drying can lead to defect free samples when properly fine tuning diffusional properties (D, D_r) , geometry (L), and chirality (p_o).

References (Chapter 3)

[1] Belamie, E.; Mosser, G.; Gobeaux, F.; Giraud-Guille, M. M. *J. Phys: Cond. Matter,* 2006, **18**, S115-S129

[2] A. Neville, *Biology of Fibrous Composites*, Cambridge University Press, 1993.

[3] Eglin, D.; Mosser, G.; Giraud-Guille, M.M.; Livage, J.; Coradin, T. *Soft Matter,* 2005, **1**, 129-131

[4] Messersmith, P. *Science,* 2008, **319**, 1767-1768.

[5] Bouligand, Y. *Tissue and Cell,* 1972, **4**, 189-217.

[6] Donald, A.; Windle, A.; Hanna, S. *Liquid Crystalline Polymers*, Cambridge: Cambridge University Press, 2006.

[7] Rey, A.D. *Soft Matter,* 2010, **6**, 3402-3429.

[8] Roland, J.; Reis, D.; Vian, B.; Satiat-Jeunemaitre, B.; Mosiniak, M. *Protoplasma,* 1987, **140**, 75-91.

[9] Habibi, Y.; Lucia, L.; Rojas, O. *Chem. Rev.,* 2010, **110**, 3479-3500.

[10] Allavherdyan, K.; Galstian, T.; Gevorgyan, A.; Hakobyan, R. *OPJ,* 2013, **3**, 17-22.

[11] Sharma, V.; Crne, M.; Park, J.; Srinivasarao, M. *Science,* 2009, **325**, 449-451.

[12] Giraud-Guille, M.M, *Calc. Tissue Int,* 1988, **42**, 167-180.

[13] Giraud-Guille, M.M.; Mosser, G.; Helary, C.; Eglin, D. *Micron,* 2005, **36**, 602-608.

[14] Risinger, A.; Pahr, D.; Zysset, P. *Proc. J. Scient. Conf,* 2010, **1**, 155-157.

[15] Ikoma, T.; Kobayashi, H.; Tanaka, J.; Walsh, D.; Mann, S. *J. Struct. Bio.,* 2003, **142**, 327-333.

[16] Li, L.; Tighe, B. *J. Struct. Bio.,* 2006, **15**, 223-230.

[17] Mitov, M. *Soft Matter,* 2017, **13**, 4176-4209.

[18] Philp, D.; Stoddart, J. *Angew. Chem Int. Ed. in English,* 1996, **35**, 1154-1196.

[19] Roeder, R. *JOM,* 2010, **62**, 49-55.

[20] Zhang, Y.; Chodavarapu, V.; Kirk, A.; Andrews, M.P. *Proc. SPIE 8258 Org. Phot. Mater Dev. XIV,* 2012, 825808.

[21] Zhang, Y.; Chodavarapu, V.; Kirk, A.; Andrews, M.P. *Sens Actuator B. Chem.,* 2013, **176**, 692-697.

[22] Kirkwood, J. E.; Fuller, G.G. *Langmuir,* 2009, **25**, 3200-3206.

[23] Fuller, G.G.; Kirkwood, J.E. US20100227043 A1, 9 September 2010.

[24] Aguilar Gutierrez, O. F.; Rey, A. D. *Langmuir,* 2016, **32**, 11799-11812.

[25] Giraud-Guille, M.M.; Nassif, N.; Fernandez, F. Collagen based materials for tissue repair, from bio-inspired to biomimetic, in *Materials Design Inspired by Nature: Function through inner architecture*, London, Royal Society of Chemistry, 2013, 107-127.

[26] Price, J.; Roach, P.; El Haj, A. *ACS Biomater. Sci. Eng.* 2016, **2**, 625-633.

[27] Green, D. W.; Lee, J.-M.; Kim, E.-J.; Lee, D.-J.; Jung, H.-S. *Adv. Mater. Inter.,* 2016, **3**, 1500411.

[28] Wilson, S.; Haj, A. E.; Yang, Y. *J. Funct. Biomater.* 2012, **3**, 642-687.

[29] Park, J.; Noh, J.; Salazar-Alvarez, G.; Scalia, G.; Bergrstom, L.; Lagerwall, J. *ChemPhysChem,* 2014, **15**, 1477-1484.

[30] Paten, J.; Siadat,; Susilo, M.; Ismail, E.; Stoner, J.; Rothstein, J.; Ruberti, J. *ACS Nano,* 2016, **10**, 5027-5040.

[31] Tanaka, Y.; Baba, K.; Duncan, T.; Kubota, A.; Asahi, T.; Quantock, A.; Yamato, M.; Okano, T.; Nishida, K. *Biomaterials,* 2011, **32**, 3358-3366.

[32] Besseau, L.; Giraud-Guille, M.M. *J. Mol. Biol,* 1995, **251**, 197-202.

[33] Cheng, X.; Gurkan, U. A.; Dehen, C. J.; Tate, M. P.; Hillhouse, H. W.; Simpson, G. J.; Akkus, O. *Biomaterials,* 2008, **29**, 3278-3288.

[34] Zheng, Z.; Li, Y.; Bisovi, H.; Wang, L.; Bunning, T.; Li, O. *Nature,* 2016*,* **531**, 352.

[35] Mathews, J.; Wnek, G.; Simpson, G.; Bowlin, D. *Biomacromolecules,* 2002**, 3**, 232-238.

[36] Yang, X.; Forest, M.G.; Wang, Q. *Entropy,* 2016, **18**, 202-230.

[37] Gobeaux, F.; Belamie, E.; Mosser, G.; Davidson, P.; Panine, P.; Giraud-Guille, M.M. *Langmuir,* 2007, **23**, 6411-6417.

[38] Echeverria, C.; Marques de Almeida, P.L.; Feio, G.; Figheirinhas, J.; Rey, A.D.; Godinho, M.H. *Polymer,* 2015, **65**, 18-25.

[39] Echeverria, C.; Marques de Almeida, P.; Aguilar Gutierrez, O.F.; Rey, A.D.; Godinho, M.H. *J. Polym. Sci. B,* 2017, **55**, 821-830.

[40] Rey, A. D. *Phys. Rev. E. Stat. Nonlin. Soft Matter Phys,* 1996, **53**, 4198-4201.

[41] Rey, A.D. *J. Chem. Phys.,* 1996, **104**, 4343-4346.

[42] Rey, A.D. *Phys. Rev. E. Stat. Nonlin. Soft Matter Phys,* 2002, **65**, 022701.

[43] Winnik, M. *Curr.Op. Colloid Interface Sci.,*1997, **2**, 192-199.

[44] Fang, T. *J. Fluids Eng.,* 2014, **136**, 0711301-1.

[45] Soulé, E.; Abukhdeir, N.M.; Rey, A.D. *Phys. Rev. E,* 2009, **79**, 021702.

[46] de Luca, G.; Rey, A. D. *Phys. Rev. E. Stat. Nonlin. Soft Matter Phys.* 2004, **69**, 011706.

[47] Rey, A.D.; Herrera-Valencia, E.E. *Langmuir,* 2010, **26**, 13033-13037.

[48] Rey, A.D. *Phys. Rev. E,* 2004, **69**, 041707.

[49] Rey, A.D. *Liq. Cryst.* 2000, **27**, 195-200.

[50] Rey, A.D. *Mol. Cryst. Liq. Cryst,* 1997, **293**, 87-109.

[51] Quémener, M.; Galstian, T. *Phys. Rev. E,* 2017, **95**, 052701.

[52] Gurevich, S.; Soulé, E.; Rey, A.D.; Reven, L.; Provatas, N. *Phys. Rev. E,* 2014, **90**, 020501.

[53] Soulé, E.; Rey, A.D. *Eur. Phys. J. B Cond. Matter Complex Syst.,* 2011, **83**, 357-367.

[54] Provatas, N.; Elder, K. *Phase-Field Methods in Materials Science and Engineering*, John Wiley & Sons, 2010.

[55] Oswald; P.; Pieranski, P. *Nematic and Cholesteric Liquid Crystals*, Boca Raton: CRC Press, 2005.

[56] Khabibullaev, P., Gevorkyan, E.; Lagunov, A. *Rheology of Liquid Crystals*, New York City: Allerton Press Inc, 1994.

[57] Okuzono, T.; Ozawa, K.; Doi, M. *Phys. Rev. Lett.,* 2006, **97**, 136103.

[58] Forest, M.G.; Wang, Q.; Zhou, R. *Rheologica Acta,* 2004, **44**, 80-93.

[59] Forest, M.G.; Wang, Q.; Zhou, R. *Rheologica Acta,* **2004**, 43, 17-37.

[60] Doi, M.; Edwards, S. *The Theory of Polymer Dynamics*, Oxford Science Publication, 1988.

[61] Flemings, M. *Solidification Processing*. Materials Science and Technology, Wiley - VCH, 2006.

Chapter 4

4 Structure Characterisation Method for Ideal and non-Ideal Twisted Plywoods

4.1 Preface

In this chapter, a description of the twisted plywood architecture present in both: man-made plywoods (as the film obtained in the Chapter 3) and in natural plywoods is obtained by means of a geometric model and implemented visualization tools. 2D incisions of the 3D architecture produce periodic arced patterns. The curvature of the arcs is introduced and used to propose a characterization methodology that efficiently removes the inherent solution multiplicities. This chapter is reproduced from a published paper titled: "Structure Characterisation Method for Ideal and non-Ideal Twisted Plywoods" co-authored by Prof. Alejandro D. Rey; Soft Matter, 2014, 10, 9446.

4.2 Summary

The twisted plywood architecture, known as the Bouligand structure, is a ubiquitous biological and synthetic fibrous composite structure, analogous to that of cholesteric liquid crystals. Twisted plywoods can show ideal or non-ideal structures and are formed via equilibrium or non-equilibrium liquid crystal self-assembly processes. A key to the structure characterisation of plywood films is the specification of the local and global helix vector $h(x)$ and pitch $p(x)$ of the cholesteric order. Previous extensive work demonstrated that oblique cuts of the plywood give rise to arc-patterns that depend both on the unknown incision angle α and the unknown pitch $p(x)$, thus making the precise 3D cholesteric reconstruction ambiguous. In this chapter we present an efficient

method based on geometric modelling and new visualization software that determines unambiguously the cholesteric pitch under spatially homogeneous and heterogeneous conditions. The method is applied to films that display two-pitch and spatially non-homogenous structures, as sometimes observed under equilibrium and non-equilibrium self-assembly. The method can be extended to other biological materials such as cornea-like, cylindrical, and various cuticle plywoods.

4.3 Introduction

Nature's ability of assembly of complex multiscale architectures with optimized structural and functional properties provides a source of inspiration for creating and designing new materials. [1–6]. The ubiquitous material multiscale organization is obtained using different precursor building blocks such as collagen (vertebrates), chitin (molluscs and insects), and cellulose (plants). Common precursors' features in many biological materials are the fibrillar shape and rigidity, which turn out to be essential ingredients for mesophase stability and liquid crystal self-assembly. In addition to fibrillar rigidity, chemical, geometric and electrostatic chirality is a common source of macroscopic chirality as observed in many self-assembled biological materials [5]. Collagen extracted from living tissue can self-assemble into complex architectures in vitro without the intervention of any tissue-specific cells [4] establishing deep correspondence between biological materials and liquid crystals.

Biological liquid crystals are generally classified into: (i) solid analogues (plant cell walls, bones, fish scales, cornea) (ii) in vitro biomacromolecular solutions (collagen, DNA), and (iii) in vivo (silk proteins, membranes) [5, 7]. The interaction between liquid crystal physics and biological mesophases is now generating a better understanding of biological self-assembly and biomimetic

principles. In this chapter we focus on the use of in vitro precursors for producing solid chiral liquid crystal analogues, also referred to as biological plywoods. Two types of biological plywoods can be distinguished according to the assembly process. Equilibrium self-assembled plywoods are formed by directed chiral front propagation, where the helix propagates from a supporting layer into the isotropic phase, leaving behind a defect-free cholesteric which can then be cross-linked [8, 9]. Non-equilibrium self-assembled plywoods on the other hand, require a sequence and synchronization of several transport processes to create the plywood. Some stages include fluid flow deposition and subsequent solvent evaporation to induce the liquid crystal phase transition to become a solid analogue [10, 11]. Numerous observations indicate that in both cases the resulting plywoods can display ideal or non-ideal architectures. In the former the helical configuration is spatially homogeneous with a constant pitch and fixed helix axis throughout the entire domain, while non-ideal plywoods display variable pitch and/or helix axis. The equilibrium plywood self-assembly process has been extensively studied [8, 9, 12–14] and the non-equilibrium process remains unexplored from the theoretical point of view [15], given the complexity of cholesteric interfaces and nematodynamics [16]. One research driver for the non-equilibrium self-assembly process is the relatively shorter time required for the synthesis of plywoods for biomedical and biotechnological applications. The characterization methodology developed in this chapter can be used for equilibrium and non-equilibrium processes. The objective of the work presented in this chapter is to generalize the twisted plywood architecture models first formulated by Bouligand [6, 21] and Giraud – Guille and co-workers [17–20, 28–31] and to develop a tool for the 3D reconstruction of ideal and non-ideal plywood architectures from typical experimental 2D cross-sectional micrographs.

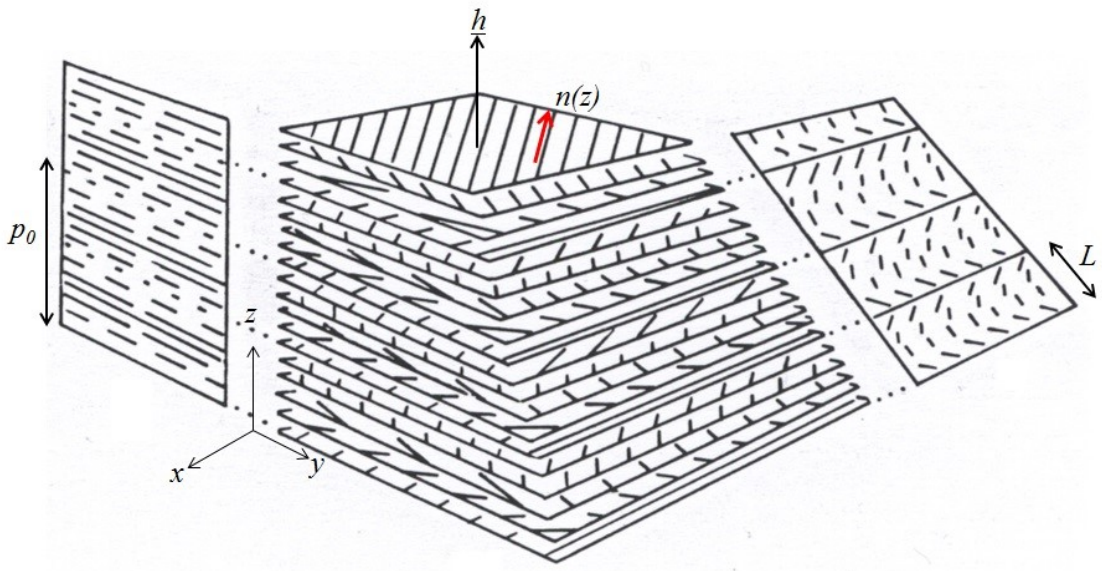

Figure 4.1. Schematic of the twisted plywood architecture, corresponding to a chiral nematic N* phase, rectangular coordinates (x,y,z). The average molecular orientation or fibrillar units are denoted by the director **n**(z). The helix axis $\mathbf{h}=\delta_z$ is normal to the parallel planes, whose distance is half the pitch p_o. A 2D cross-sectional cut of the 3D plywood results in arced patterns whose periodicity is L.

The organization of this chapter is as follows. The twisted plywood architecture model is first briefly reviewed and then the previously presented method of 3D cholesteric reconstruction from 2D arc-patterns is extended by introducing the intrinsic geometry and curvature of the arcs. Applications of the extended method that highlights the critical resolving power of curvature are presented. Finally, materials with pitch heterogeneities and multiple pitches as observed experimentally [22, 23] are analysed to demonstrate the practical utility of the method. Spatial variations of the helix axis *h* (see Fig. 4.1) are beyond the scope of this chapter and are left for future work.

4.3.1 Twisted plywood architecture and structure determination

The plywood model for biological tissues was described by Bouligand [21]. One of the first observations was made in oblique sections of the organic matrix of crab cuticle in which arced structures were observed throughout the entire sample. These arcs were visible under the light microscope but better resolved by classic TEM [4] and it was later observed that it was not exclusive of chitin, but was also observed in plant cell walls and even in the collagenous matrix of hard bone tissue. This gave rise to the twisted plywood architecture model which idealizes the arrangement of the molecules or fibrillar units in a series of planes in which the fibrils are more or less parallel to one another and whose average orientation (director **n**) rotates in going from plane to plane, corresponding to the chiral nematic N* (cholesteric) phase. The cholesteric helix is defined by the pitch or distance for 2π rotations (p_o), the helix orientation axis h, and the sense of rotation (left/right), as shown in Fig. 4.1. The observed arced patterns, [5, 21] shown in the right panel of Fig. 4.1, are a 2D periodic structure of wave-length L, visible when the cutting angle 'α' is between 0º and 90º and each arc corresponds to a 180º rotation in several nematic planes that make up the entire structure. However when $180º < \alpha < 360º$, the arcs reverse to their mirror image, which is why the manifestation of these arcs could be thought as the "fingerprint" of supramolecular chiral structure. Other patterns were identified in bone osteons [17] due to the specific arrangements of collagen fibrils such as the orthogonal plywood architecture and the cylindrical plywood architecture which can be twisted or orthogonal. The resulting arrangement of at least in vitro collagen is a highly pH-dependent process; [24, 25] pH ≈ 2.5 leads to the twisted plywood architecture but an increase to 3.5 results in the orthogonal plywood [24]. Later goniometric studies showed that these arcs changed their periodicity L and when observed at a particular angle these arcs seemed to disappear [22]. This apparent loss of periodicity is an optical

effect that was first observed experimentally [20], highlighting the crucial fact that the 2D periodicity "L" of the arced patterns is a function of the unknown pitch and unknown incision angle α: $L = L(\alpha, p_o)$, revealing the difficulty in reconstructing the 3D fibrillar chiral organisation from 2D observations.

Structural anomalies can be present due to variations in the relative angle of the fibrils [22]. Some characteristic examples presented in Fig. 4.2 have been identified in nature [17, 22]: (a) ideal architecture ($p = p_o$ = const) with a constant periodicity, (b) non-uniform pitch ($p_o = p_o(z)$) and (c) bimodal (two-pitch: p_1 and p_2) twisted plywood patterns; examples of (a) and (c) are shown in Fig. 4.3. In the two latter examples L is not constant since $L(z) = L(\alpha, p(z))$ and $L_i = L_i(\alpha, p_i)$; $\{i = 1,2\}$, respectively. It is worth noting that in the case of the two-pitch plywood, the large arc represents only 180º rotation while with the smaller arcs a full rotation of the microfibrils is observed. In non-equilibrium self-assembly processes such as the solution casting of collagen films [10, 11, 15], these non-idealities (i.e. $p(z), p_i$; $\{i = 1,2\}$) will arise from non-homogenous flow-kinematics and/or from uneven solvent evaporation [10, 15] or even other process conditions such as pH [24, 25], however the mechanisms remain poorly understood. As revealed by Fig. 4.1 and 4.2 and the fact that the 2D periodicity contains complex information (for example, $L(z) = L(\alpha, p(z))$ and $L_i = L_i(\alpha, p_i)$; $\{i = 1,2\}$), the reconstruction of the 3D plywood organization from 2D micrographs is not a trivial task for either ideal or non-ideal plywoods, and as shown below it requires closer examination of the arcs themselves.

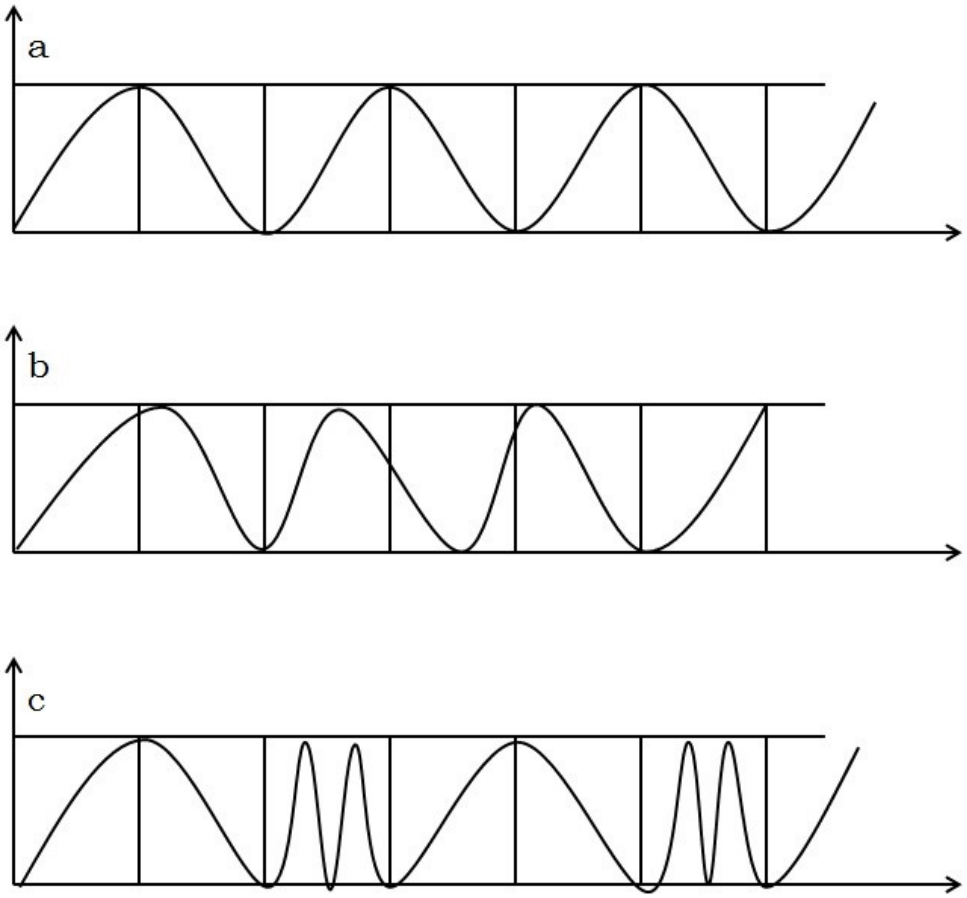

Figure 4.2. Schematic showing a constant periodicity in the microfibril mutual angles (a), non-homogeneous mutual angle leading to a variable periodicity in the arcs (b) and a bimodal pattern that results in a two-pitch plywood (c). Adapted from [22]

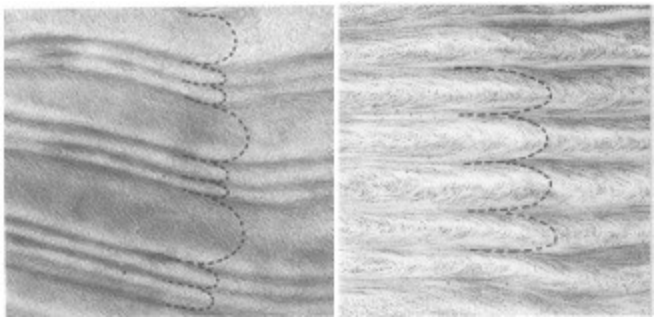

Figure 4.3. Arced pattern for a bimodal (two-pitch) plywood , and (b) arced pattern for ideal single pitch plywood [6]. Copyright permission (3434860436593) from Springer.

4.4 Geometric Model

4.4.1 Ideal plywood model

The geometric model used to describe the twisted plywood is similar to that reported by Bouligand [21, 26], in which a coordinate system is chosen such that the fibrils are parallel to a unit vector n that rotates about the perpendicular coordinate 'z' along the helix vector h, as shown in Fig. 4.4. This director field **n** that describes a cholesteric phase is parameterized by the twist angle $\varphi(z)$:

$$\mathbf{n} = (n_x, n_y, n_z) = (\cos\varphi, \sin\varphi, 0); \varphi = \frac{2\pi z}{p_0} \qquad (4.1\ a,b)$$

in eqn. (4.1) the pitch "p_o" is of the order of 10 μm. As per eqn. (4.1b), for ideal plywoods there is a linear relationship between the spatial coordinate 'z' and the twist angle 'φ'. Taking an oblique cut at an angle α, shown in Fig. 4.4, defines the incision plane (x–s), where s is the in-plane spatial coordinate whose orientation depends on a. The projection of **n**(z) to the (s–x) plane is the planar vector field **u**(α, s):

$$\mathbf{u}(\alpha, s) = \left(\cos\left[\frac{2\pi(\sin\alpha)s}{p_0} \right], \cos(\alpha)\sin\left[\frac{2\pi(\sin\alpha)s}{p_0} \right], 0 \right) \qquad (4.2)$$

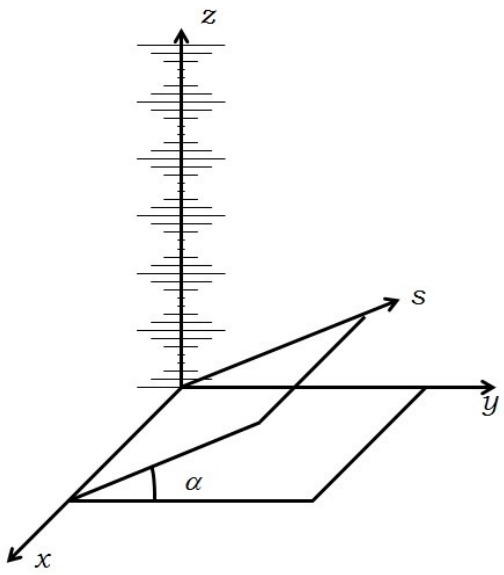

Figure 4.4. Helix-fixed rectangular coordinates (*x,y,z*) , chiral and periodic cholesteric structure, and incision plane (*x*-*s*) with an angle α. The short lines segments normal to the z axis represent the helical rotation of the macromolecules or fibrils about the helix z-axis.

The streamlines $x = x(s)$ of $\mathbf{u}(\alpha,s)$ are the experimentally observed 2D arced patterns given by the solution of:

$$\frac{dx}{ds} = \frac{\cot\left[\dfrac{2\pi(\sin\alpha)s}{p_0}\right]}{\cos\alpha} \tag{4.3}$$

Using the boundary condition $x(0) = x_o$, the space curve $x(s,\{\alpha,p_o\})$, given first by Bouligand, is:

$$x\left(s,\{x_0,\alpha,p_0\}\right) = x_0 + \frac{p_0}{2\pi\sin\alpha\cos\alpha}\ln\left|\sin\left(2\pi(\sin\alpha)\frac{s}{p_0}\right)\right| \tag{4.4}$$

where x_o is a constant that defines the location of each arc in the *x*–*s* plane, and eqn. (4.4) describes the trajectories followed by the arced patterns structure and is a periodic function as anticipated; to obtain the 1D periodicity we equate the argument of the logarithmic term to zero and solve for

the variable s. From the first non-trivial solution to the resulting equation, a linear relationship between the periodicity of the structure L and the pitch p_o can be extracted:

$$L = \frac{p_0}{2\sin\alpha} \tag{4.5}$$

We emphasize that L depends on the pitch p_o and the incision angle α. This relationship of L and p_o can be used for characterisation purposes restricted to knowing p_o or α. To remove this degree of freedom or uncertainty, since neither the pitch nor the incision angle is known a priori, we use the curvature $\kappa(s, \alpha, L)$ of the arced patterns:

$$\kappa(s,\alpha,L) = \frac{-\csc^2\left(\frac{\pi s}{L}\right)}{\cos\alpha\left\{1+\left(\cot\left(\frac{\pi s}{L}\right)/\cos\alpha\right)^2\right\}^{3/2}} \tag{4.6-a}$$

It is worth noting that the maximum curvature depends only on the incision angle:

$$\kappa_{\max} = \frac{1}{\cos\alpha} \tag{4.6-b}$$

Thus, the proposed extended Bouligand model [21, 26] for ideal plywoods is:

$$\textit{Ideal Plywood Structure}: \begin{Bmatrix} x\left(s,\{x_0,\alpha,p_0\}\right) \\ \kappa(s,\alpha,L) \end{Bmatrix} \tag{4.7}$$

The arced patterns given by eqn. (4.4) depend on three parameters: $x = x(s,\{x_o, \alpha, p_o\})$. The two important limiting cases not resolved by the analytical model are: $\alpha = 0, \pi/2$. In the former case no arced patterns emerge because the cut is taken exactly in any of the x–y planes of the cholesteric

structure, and apparently what would be observed is one of the nematic planes of the whole structure, i.e. an infinite arc represents a straight line parallel to the orientation of the fibrils at any of these nematic planes. In the latter case no arced patterns can be identified, however the typical cholesteric representation is observed and the periodicity of the structure is $L = p_o/2$. To overcome these analytical restrictions and to obtain quick 2D patterns and hence 3D reconstructions for any cutting angle α, we developed computational visualization software (see the Appendix G on implementation of the MayaVi visualization software).

4.4.2 Non-ideal plywood model

For non-uniform pitch ($L(x) = L(\alpha, p(z))$) or multiple pitch structures ($L_i = L_i(\alpha, p_i)$; $\{i = 1,2\}$), an extended methodology must be applied. Instead of considering a linear relationship between the 'z' coordinate and the twist angle 'φ' (see eqn. (4.1b)), the following twist angles are introduced for the two-pitch and non-uniform plywoods, respectively:

$$\varphi = \frac{2\pi z}{p_0}\left[H(z) - H\left(z - \frac{p_0}{2}\right)\right] + \left(\frac{4\pi z}{p_0} - \pi\right)\left[H\left(z - \frac{p_0}{2}\right) - H\left(z - p_0\right)\right] + \left(\frac{2\pi z}{p_0} + \pi\right)\left[H\left(z - p_0\right) - H\left(z - \frac{3p_0}{2}\right)\right] + \ldots \tag{4.8}$$

$$\varphi = \frac{2\pi z}{p_0}\left[H(z) - H\left(z - \frac{p_0}{2}\right)\right] + \left(\frac{4\pi z}{p_0} - \pi\right)\left[H\left(z - \frac{p_0}{2}\right) - H\left(z - \frac{3p_0}{4}\right)\right] + \left(\frac{8\pi z}{p_0} - 4\pi\right)\left[H\left(z - \frac{3p_0}{4}\right) - H\left(z - \frac{7p_0}{8}\right)\right] + \ldots \tag{4.9}$$

where $H(z)$ is the Heaviside step function. In both expressions the slope is periodic with regular domain lengths of $p_o/2$ for the two-pitch plywood and irregular domains decreasing periodically

for the latter. By modifying eqn. (4.1) with eqn. (4.8) and (4.9) the following general equation is to be solved for each particular non-ideal case:

$$\frac{dx}{ds} = \frac{\cot\left\{f\left[H\left(z,\alpha\right)\right]\right\}}{\cos\alpha}, x(0) = x_0 \tag{4.10}$$

where $f[H(z, \alpha)]$ corresponds to eqn. (4.8) and (4.9) in terms of 's' and 'α'. The corresponding curvature κ is:

$$\kappa = \frac{-\csc\left\{f\left[H\left(s,\alpha\right)\right]\right\}\dfrac{df\left[H\left(s,\alpha\right)\right]}{ds}}{\left(1+\left\{\dfrac{\cot\left\{f\left[H\left(s,\alpha\right)\right]\right\}}{\cos\alpha}\right\}^2\right)^{3/2}} \tag{4.11}$$

For a given incision angle a the 2D periodicity L is not a constant throughout the entire structure because $p_o = p_o(z)$; such expression is particular to each non-ideal plywood and can be periodic as in the case of the two-pitch plywood, and can be monotonous as in the case of the non-homogeneous pitch plywood. To have a modelling closure for these plywoods, the spatial variations of the periodicity can be obtained experimentally. This leads to a generalized scheme for non-ideal plywoods in terms of space curve ($x(s)$), curvature (κ) and 2D periodicity (L):

$$Non-ideal\ Plywood\ Structure: \begin{Bmatrix} x\left(s,\left\{x_0,\alpha,p_0(s)\right\}\right) \\ \kappa\left(s,\alpha,L\right) \\ L = L\left(s,\alpha,p_0(s)\right) \end{Bmatrix} \tag{4.12}$$

4.5 Results and discussion

4.5.1 Ideal constant pitch plywoods

Fig. 4.5 (a – b) shows two nematic planes corresponding to $\alpha = 0^{o}$ and Fig. 4.5(c) shows the typical cholesteric structure corresponding to $\alpha = 90^{o}$, obtained using the computational visualization software. When α is close to zero, wide arcs start to appear, which narrow as the angle increases and approaches 90º. For a given a, the arcs widen as the pitch increases. This leads to the possibility of having two different 3D cholesteric structures with the same 2D periodic structure, which could lead to a wrong characterisation. This uncertainty is demonstrated in Fig. 4.6. Fig. 4.6 (a, c and d) show the effect on the periodicity L as α increases with a constant pitch and Fig. 4.6 (a – b) when the pitch increases at constant α. Hence it is indeed possible to find:

$$L_1 = L_2 \Leftrightarrow p_{0,1} / \sin\alpha_1 = p_{0,2} / \sin\alpha_2 \tag{4.13}$$

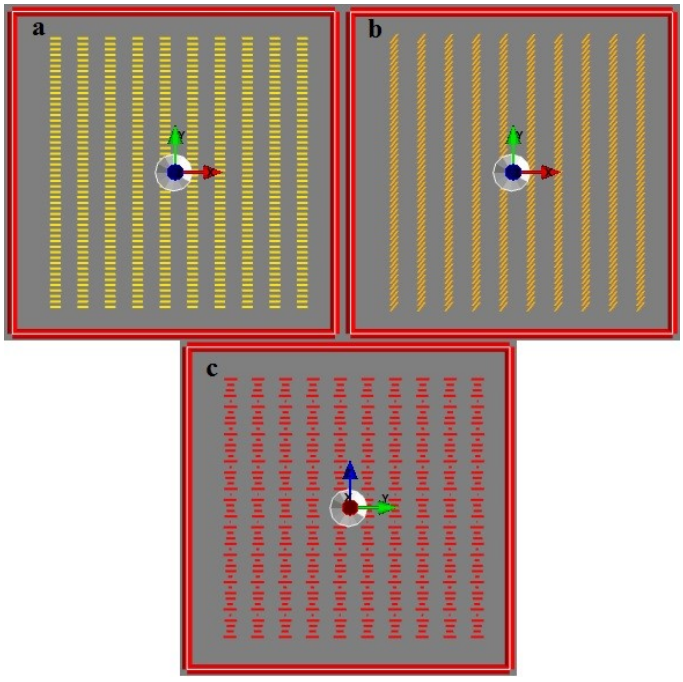

Figure 4.5. Computational visualisations of a twisted plywood architecture with no arc-patterns, for α= 0º (a,b) and α= 90º (c). For more details see Appendix G.

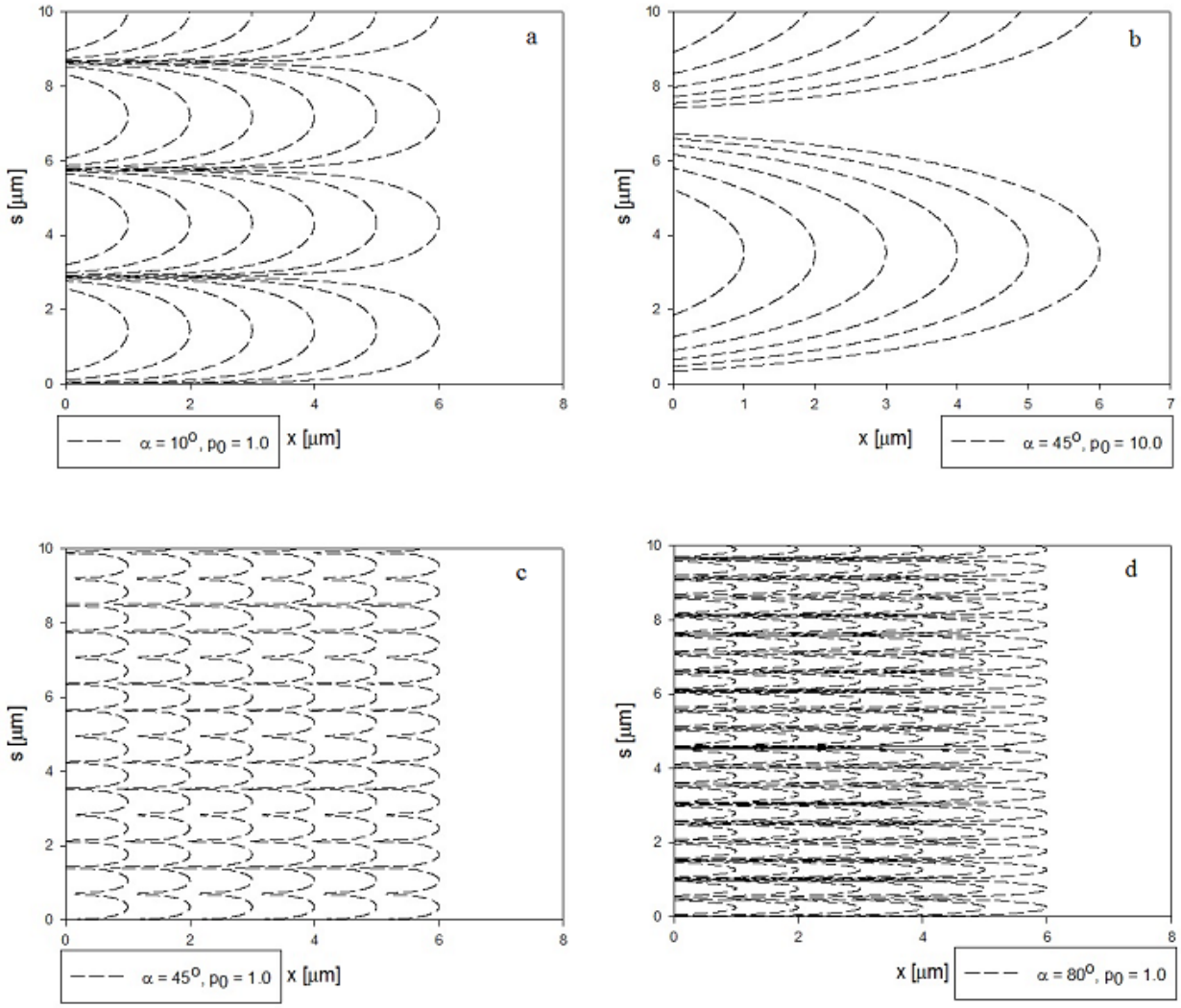

Figure 4.6. Arc patterns of ideal plywoods for increasing incision angle at constant pitch (a, c, and d) and arc patterns for increasing pitch at constant incision angle (b, c).

Fig. 4.7 shows the 2D periodicity L as a function of the pitch p_o for several α's, calculated from eqn. (4.5). Increasing p_o has a stronger effect at smaller α's; a horizontal L-constant line proves eqn. (4.13). Another notable case arises when two different incision planes are taken from the same plywood; the first cut being at an angle $\alpha < 90^o$ and the second at the supplementary angle $\pi - \alpha$. This is shown in Fig. 4.8 where the arcs have the same periodicity L, however the direction of the

arcs are reversed. This orientation behaviour had already been observed experimentally where goniometric observations were carried out on fixed samples (constant incision angle) but when tilting the sample in the goniometric stage the arcs cancelled out at a particular angle and the inverse arcs were obtained by further increase in the tilting angle [22]. In Fig. 4.8 the incision angle is not constant and the image reversal is observed because of the cutting angle's complementarity.

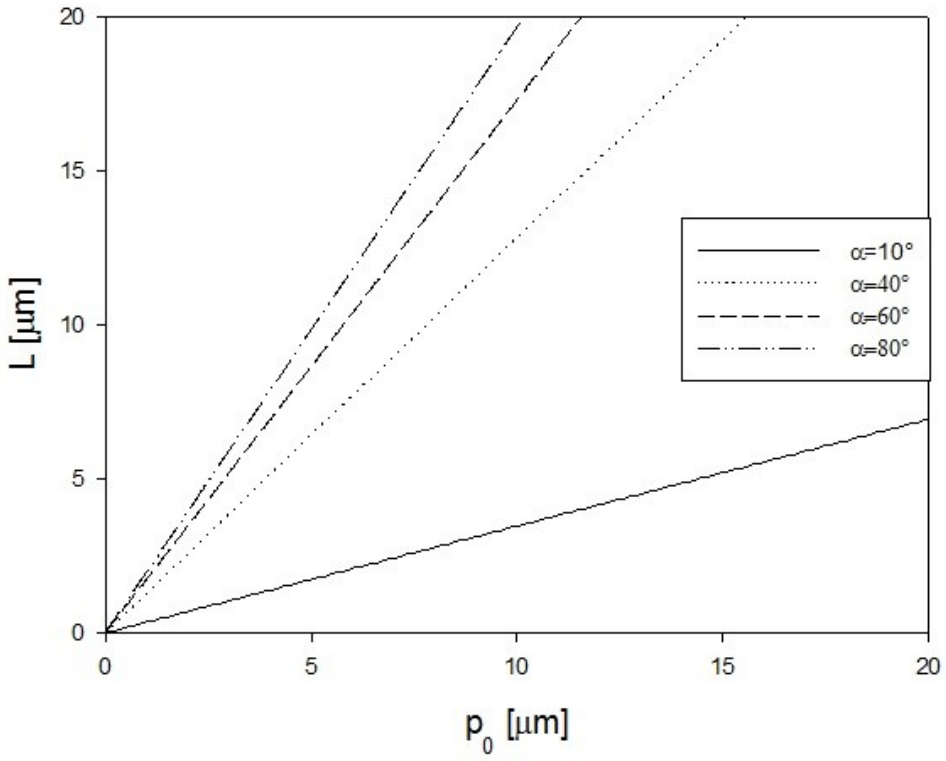

Figure 4.7. Arc periodicity L as a function of the pitch (p_o) for several incision angles (α) for ideal plywoods. The increase of L with p_o increases with α.

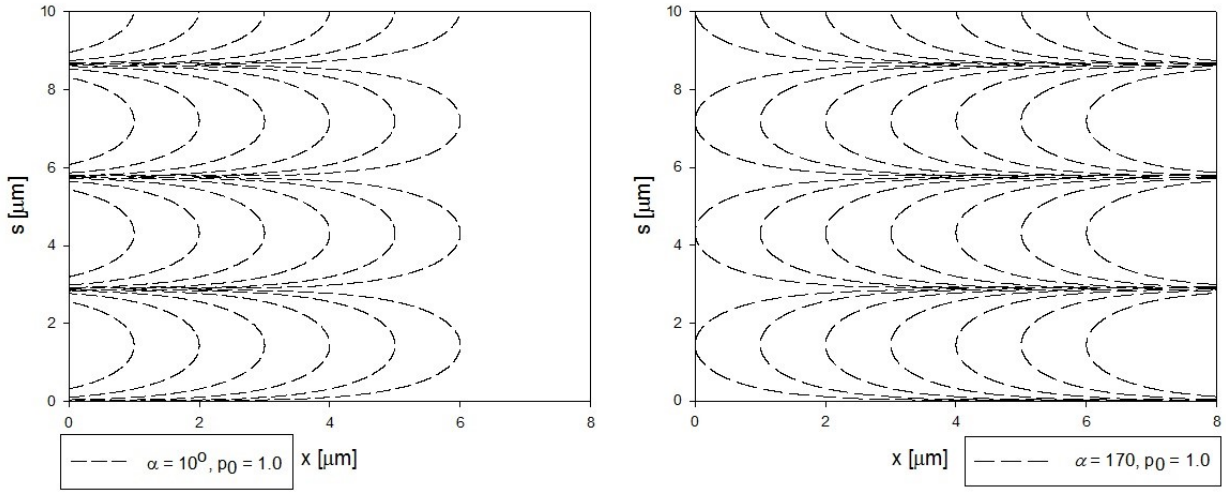

Figure 4.8. Arc patterns of a single ideal plywood obtained from (a) $\alpha = 10^{o}$ and (b) $\alpha = 170^{o}$. The arcs are mirror images because the cutting angle complementarity.

4.5.2 Non-ideal plywoods

(a) Two-pitch plywood (eqn. (4.8–10 and 4.12)). Fig. 4.9 and 4.10 show the twist angle $\varphi(z)$ profile and arced patterns $s(x)$, for a two-pitch plywood. The twist angle $\varphi(z)$ is constant in each domain of length p_o, but it oscillates from domain to domain. The smaller (larger) slope corresponds to wider (narrower) arcs. This result replicates Fig. 4.3(a).

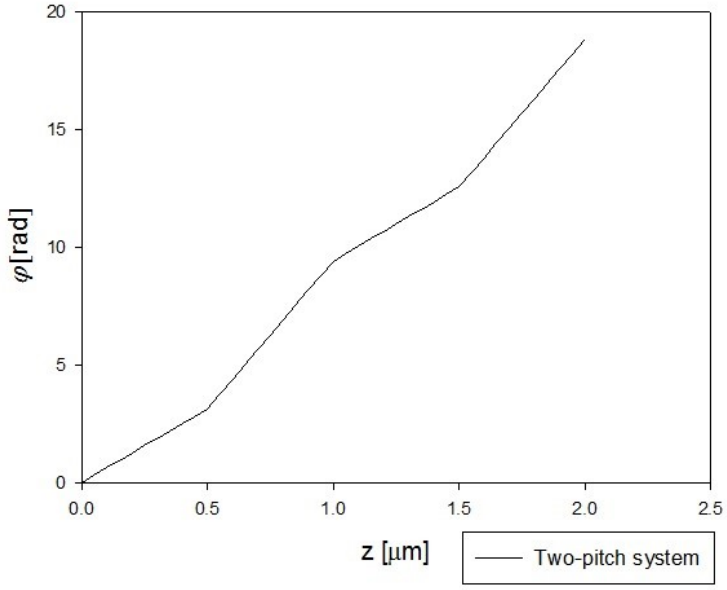

Figure 4.9. Twist angle φ as a function of the spatial coordinate z for a bimodal (two-pitch) plywood. The slope oscillates from domain to domain. The domain length is constant.

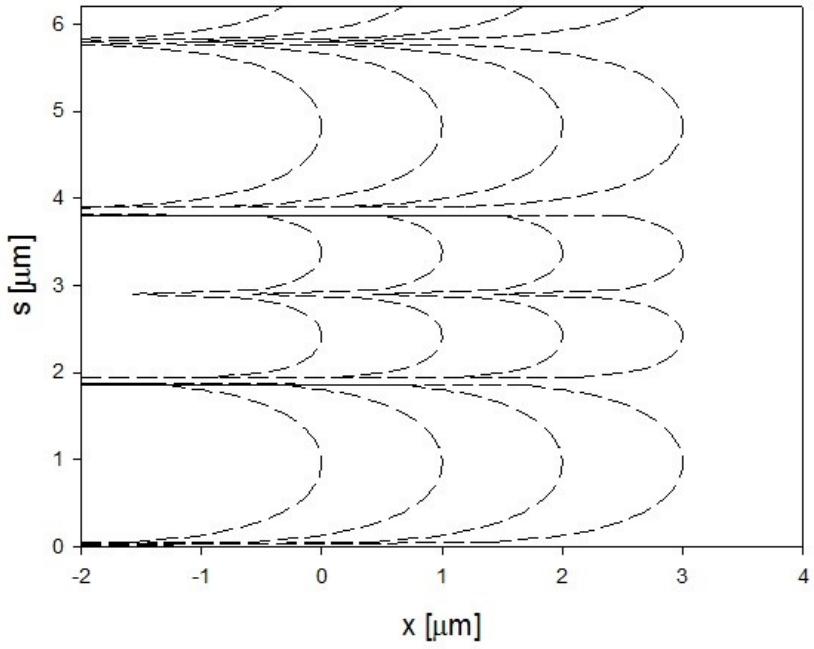

Figure 4.10. Arced patterns for the two-pitch plywood, corresponding to Fig.4.9. The results replicate those of Fig.4.3a.

(b) Non-homogeneous plywood (eqns. (4.9, 4.10 and 4.12)). Fig. 4.11 and 4.12 show the twist angle $\varphi(z)$ profile and arced patterns $s(x)$ for a non-homogeneous plywood. The twist angle has a constant slope in each domain but it increases from domain to domain. In addition, the domain length also decreases. The corresponding arced pattern periodicity L decreases with "s".

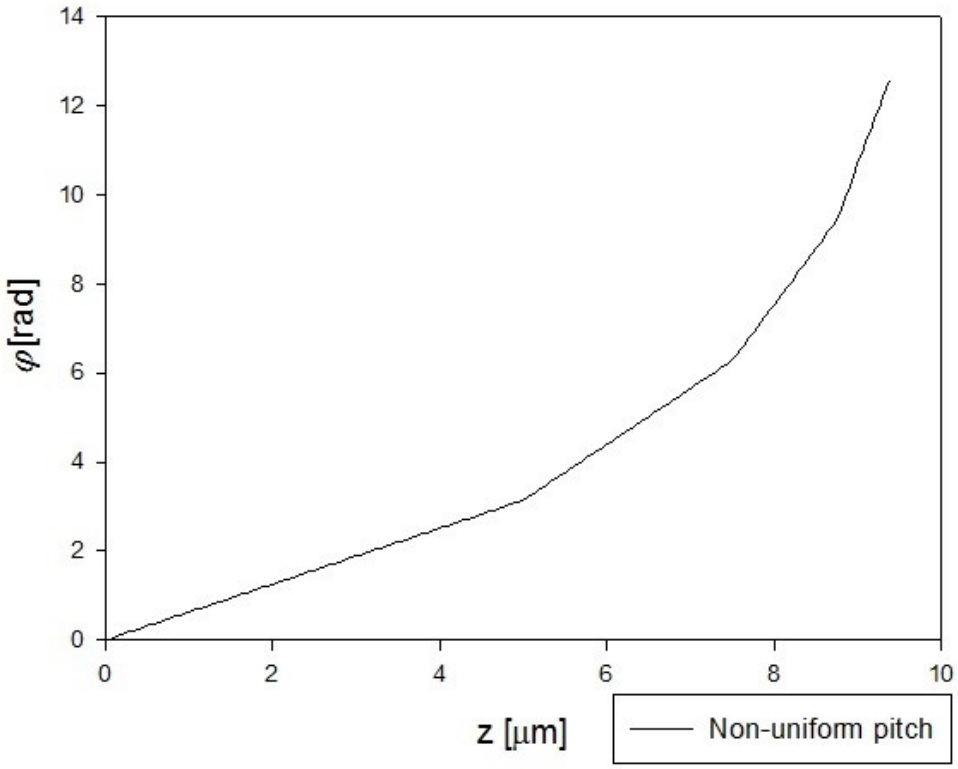

Figure 4.11. Twist angle as a function φ of the spatial coordinate z for a representative non-uniform pitch. The slope increases from domain to domain. The domain length decreases with z.

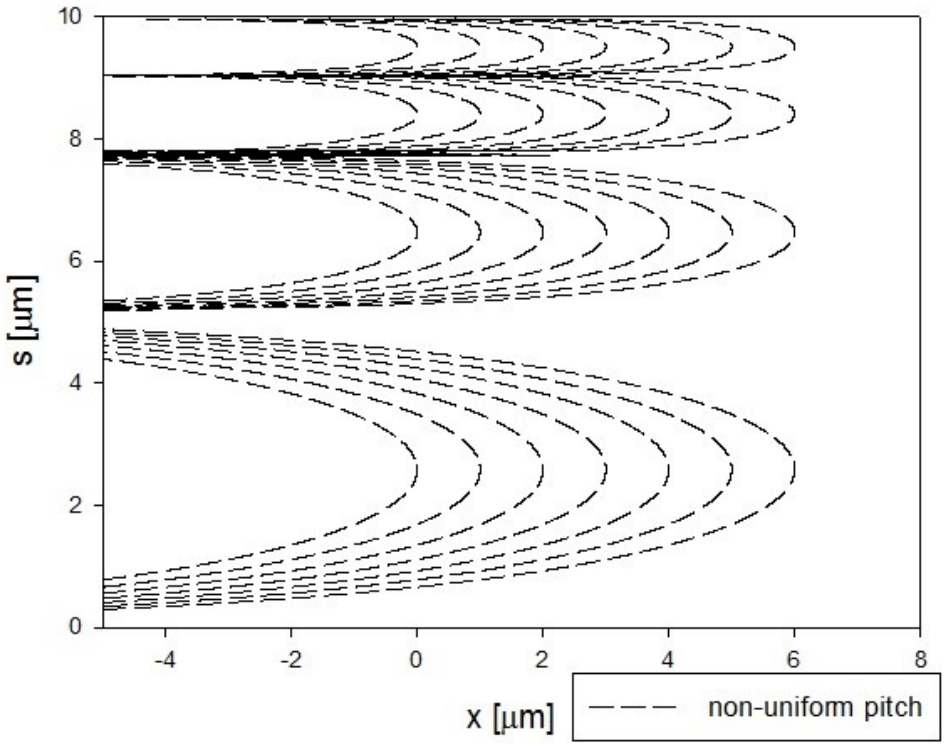

Figure 4.12. Arced patterns s(x) corresponding to a twist angle given in figure 4.11.

4.5.3 3D Structure reconstruction procedure

In order to rebuild the true cholesteric 3D structure by simply using 2D images from experimental micrographs, the curvature $\kappa(s, \alpha, L)$ of the arcs is introduced as per eqn. (4.6-a). The 3D reconstruction procedure consists of:

(a) Fit of the experimental curvature k with the eqn. (4.6-a) and obtain α;

(b) Measure the experimental 2D periodicity L;

(c) Solve eqn. (4.5) to find the pitch p_o.

Next, we show a representative example to demonstrate the reconstruction capacity of the proposed new procedure (eqn. (4.4)–(4.7)) using two plywoods with pitches differing by an order of magnitude ($p_{o,1} = 10p_{o,2}$) but showing the same 2D periodicity ($L1 = L2$). Fig. 4.13 shows one arc for $p_{o,1} = 1.0$, $\alpha = 30º$ and another for $p_{o,2} = 0.1$, $\alpha = 3º$. The arcs are nearly indistinguishable, and correspond to drastically different plywoods, but are made to appear identical by the experimental sectioning. These two plywoods are properly identified when plotting the curvature $\kappa(s)$ computed from eqn. (4.6) as it is shown in Fig. 4.14. The maximum curvature difference is about 15%. It is clear that if the curvature of the arcs is ignored, incorrect predictions can be extracted from the model. This proposed analytical-computational procedure shows significant advantages over the classical pitch determinations which rely on optical measurements that are sometimes restricted to certain pitch ranges [27]. The procedure is applicable to both: equilibrium and non-equilibrium self-assembly plywood formation processes. For plywoods presenting anomalies, as shown with eqn. (4.10)–(4.12), we proceed with the local determination of L_i, as it varies as shown in Fig. (G.5) (see Appendix G); in these cases a is available through any of the visible arcs (eqn. (4.6a) and (b)) and the pitch can be calculated in a piecewise manner in each arc, similar to the ideal case and by appending all the calculated pitches it is possible to know its spatial variations; hence, the gradients of the pitch can be identified by constructing plot like Fig. 4.9 and 4.11, leading to a fuller characterization of the morphology of the twisted plywood.

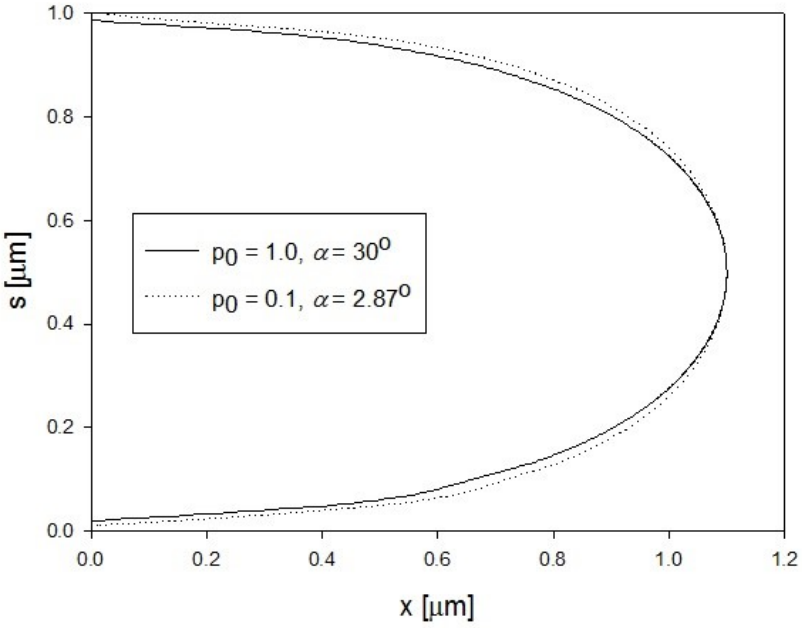

Figure 4.13. Comparison between two arcs with the same periodicity and a pitch difference of one order of magnitude.

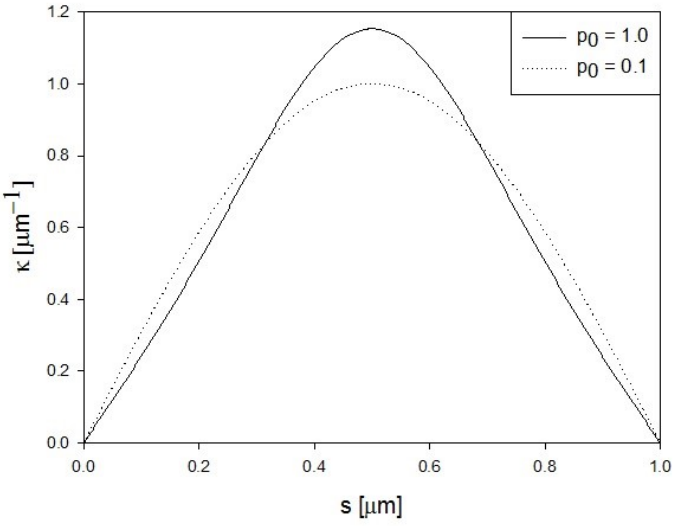

Figure 4.14. Curvature κ as a function of spatial coordinate "s" for the two plywoods shown in Fig. 4.13, with different pitch p_o and with the same periodicity L. The maximum curvature difference between the two cases is about 15% and easily differentiates the two plywoods

4.6 Conclusions

The twisted plywood architecture model originally developed by Bouligand [21, 26] was revisited and extended to describe ideal and non-ideal structures arising from pitch gradients and multiple pitches. A characterisation tool based on analytical results (eqn (4.3)–(4.12) and computational visualization software (see Appendix G) is proposed to reconstruct the 3D cholesteric structure of various plywoods from 2D arc-patterns obtained from experimental oblique cuts, which is an alternative procedure to optical measurements of the pitch which may be restricted to certain values of p_o. A unique and novel feature of our extension is the introduction of curvature and the maximum value of κ (eqn. (4.6a) and (b)) in the observed arcs to eliminate the seldom recognized degree of freedom that exists, since the arc's periodicity depends on both the incision angle and the pitch (eqn. (4.5)).

This characterisation tool can be used in ideal and non-ideal plywoods (Fig. 4.6, 4.10 and 4.12) by taking into account commonly observed pitch variations in a systematic way (eqn. (4.8) and (4.9)). Since there is a wide variety in helical arrangements found experimentally (Fig. 4.3), these effective 3D reconstruction computation and visualization tools can be easily extended and applied to any experimental observation of such biological plywoods including the orthogonal cornea-like plywood, the cylindrical plywood configuration, and those found in various cuticles.

References (Chapter 4)

[1] Eglin, D.; Mosser, G.; Giraud-Guille, M.-M.; Livage, J.; Coradin, T. *Soft Matter*, 2005, **1**, 129.

[2] Fratzl, P. *Curr. Opin. Colloid Interface Sci.,* 2003, **8**, 32.

[3] Giraud-Guille, M. M.; Mosser, G.; Helary, C.; Eglin, D. *Micron*, 2005, **36**, 602.

[4] Belamie, E.; Mosser, G.; Gobeaux, F.; Giraud-Guille, M. M. *J. Phys.: Condens. Matter*, 2006, 18, S115.

[5] Rey, A. D. *Soft Matter*, 2010, **6**, 3402; Rey, A.D.; Herrera- Valencia E. E.; Murugesan, Y. *Liq. Cryst*., 2014, **41**, 430.

[6] Bouligand, Y.; Denefle, J. P.; Lechaire, J. P.; Maillard, M. *Biol. Cell*, 1978, **54**, 143.

[7] Rey, A.D.; Herrera Valencia, E.E. *Biopolymers*, 2012, **97**, 374.

[8] de Luca, G.; Rey, A.D. *Phys. Rev. E: Stat., Nonlinear, Soft Matter Phys*., 2004, **69**, 011706.

[9] de Luca, G.; Rey, A.D. *Eur. Phys. J. E*, 2003, **12**, 291.

[10] Kirkwood, J. E.; Fuller, G. G. *Langmuir*, 2009, **25**, 3200.

[11] Mu, X.; Gray, D. G. *Langmuir*, 2014, **30**, 9256.

[12] Murugesan, Y.; Pasini, D.; Rey, A.D. *Soft Matter*, 2013, **9**, 1054.

[13] Murugesan Y.; Rey, A.D. *Polymers*, 2010, **24**, 766.

[14] Rey, A.D.; Pasini, D.; Murugesan, Y. Natural and Biomimetic Materials, ed. Y. Bar Cohen, CRC Press, 2011, p. 131.

[15] Fuller, G. G.; Kirkwood, J. E. USPAP, US2010/0227043A1, 2010.

[16] Rofouie, P.; Pasini, D.; Rey, A.D. *Colloid Interface Sci. Commun*., 2014, **1**, 23; Rey, A.D. *Phys. Rev. E: Stat. Phys., Plasmas, Fluids, Relat. Interdiscip. Top*., 1996, **534**, 4198; Rey, A.D. *Macromol. Theory Simul*. 1995, **45**, 857.

[17] Giraud-Guille, M. M. *Calcif. Tissue Int*., 1988, **42**, 167.

[18] Besseau, L.; Giraud-Guille, M. M. *J. Mol. Biol*., 1995, **251**, 197.

[19] Livolant, F.; Giraud-Guille, M. M.; Bouligand, Y. *Biol. Cell*, 1972, **31**, 159.

[20] Giraud-Guille, M. M. *Curr. Opin. Solid State Mater. Sci.*, 1998, **3**, 221.

[21] Bouligand, Y. *Tissue Cell*, 1972, **4**, 189.

[22] Roland, J. C.; Reis, D.; Vian, B.; Satiat-Jeunemaitre, B.; Mosiniak, M. *Protoplasma*, 1987, **140**, 75.

[23] Jewell, S. A.; Vukusic, P.; Roberts, N. W. *New J. Phys*., 2007, **9**, 99.

[24] De Sa Peixoto, P.; Desinet-Besseau, A.; Schmutz, M.; Anglo, A.; Illoul, C.; Schanne-Klein, M. C.; Mosser, G. *Soft Matter*, 2013, **9**, 11241.

[25] Gobeaux, F.; Belamie, E.; Mosser, G.; Davidson, P.; Panine, P.; Giraud-Guille, M. M. *Langmuir*, 2007, **23**, 6411.

[26] Blumstein, A. *Liquid Crystalline Order in Polymers*, Academic Press, 1st edn, 1978, p. 261.

[27] Baessler, H. and Labes, M. M. *Mol. Cryst. Liq. Cryst*., 1970, **6**, 419.

[28] Giraud-Guille, M. M. *Tissue Cell*, 1986, **18**, 603.

[29] Giraud-Guille, M. M. *J. Mol. Biol*., 1992, **224**, 861.

[30] Mosser, G.; Anglo, A.; Helary, C.; Bouligand, Y.; Giraud-Guille, M. M. *Matrix Biol*., 2006, **25**, 3.

[31] Fratzl, P.; Giraud-Guille, M. M. *Hierarchically Structured Porous Materials: From Nanoscience to Catalysis, Separation, Optics, Energy, and Life Science*, 1st edn, 2012, p. 29.

Chapter 5

5 Chiral Graded Structures in Biological Plywoods and in the Beetle's Cuticle

5.1 Preface

Following the geometric model presented in the previous chapter devoted to 3D structure reconstruction from periodic patterns from 2D sections, further analysis is provided to reveal and overcome the inherent ill-conditioning for certain incision angles. The proposed methodology from the previous chapter is applied with the aid of in silico cross sections to predict the pitch profile. This chapter is reproduced from a published paper titled: "Chiral Graded Structures in Biological Plywoods and in the Beetle's Cuticle" co-authored with Prof. Alejandro D. Rey, Colloids Interface Sci. Commun., 2014, 3, 18.

5.2 Summary

Biological chiral fibrous composites, known as biological plywoods, found throughout Nature including the exoskeletons of insects and plant cell walls have optimized structural and functional properties, such as the iridescent colors observed beetle cuticles. In many cases the micron-range chirality of the fibrous ordering is usually spatially graded, multi-periodic or layered as opposed to uniform. The challenge to discover structure-property relations in biological plywoods relies on the accuracy of determining the usually space-dependent chiral pitch of the plywoods. Here we use a recently developed geometric model and computational visualization tool to determine the complex spatial gradients present in beetle cuticle which is a canonical example of graded biological plywoods, extensively studied using optical methods. The proposed computational

structural characterization procedure offers a complementary tool to optical and other experimental measurements. The new procedure has wide application in biological materials characterization and in biomimetic engineering of structural and functional materials.

5.3 Introduction

Biological materials are distinguished by hierarchical structures, multi-functionality and self-assembly, which are attributes of liquid crystals and unsurprisingly mesophase organization is then found throughout nature with building blocks like collagen, and chitin [1-4]. Biological Plywoods (BPs) are recognized as solid liquid crystals analogues formed through an efficient entropy-driven self-assembly process [1, 4-6]. Bouligand was the first who successfully described these materials with the Twisted Plywood Architecture model (TPA) [7] in which fibrils are arranged as in a chiral nematic liquid crystal, presenting an average orientation of fibrils that change orthogonally to the fibril orientation; the micron-range distance required for a full (2π) rotation is known as the pitch p_o, whose sign (+ or -) represents the handedness of the helical axis (**h**); see figure 5.1. TPAs include: i) ideal plywoods with constant pitch ($p_0 = const$) and helix axis, and ii) non-ideal TPAs with pitch gradients ($p_0(z)$). Non-idealities are due to specific cellular processes [7] and a response to external stimuli such as the pH dependence of the self-assembly process observed in collagen [8, 9] with structures that range from ideal TPA to orthogonal plywoods, with abrupt changes of 90º in the fibril orientation on adjacent planes [10]. Other ubiquitous non-idealities such as defects and gradients in both **h** and p_o arise during the plywood self-assembly in the presence of secondary phases [11] which result in poly-domain helicoids [12, 13].

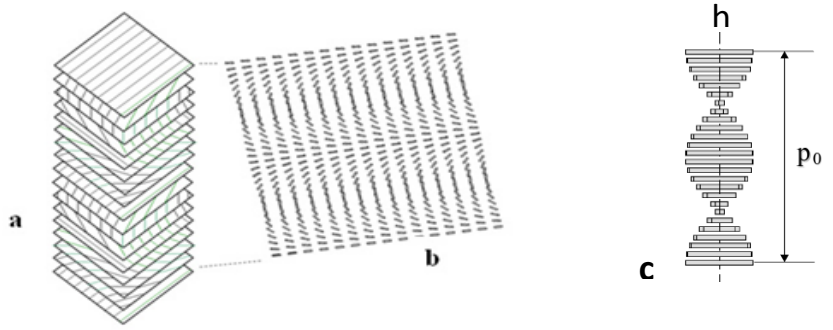

Figure 5.1. (a-b) Schematics of the ideal biological plywoods. Oblique sections (b) give rise to the characteristic arced patterns. (c) Normal view schematic of the helical axis, defined by the helix orientation **h** and the pitch p_o.

In this chapter we focus on non-idealities arising from spatial pitch variations ($dp_0(z)/dz \neq 0$) in beetle cuticles ('aurigans scarab') [14], where the chiral arrangement results in color iridescence [15] and possible thermal regulation [16]; color iridescence due to surface wrinkling is discussed elsewhere [17, 18]. This cuticle can be classified as a graded plywood with pitch gradients in **h** direction. For ideal BPs, oblique incisions lead to the ubiquitous arced patterns with identical arcs throughout the incision plane as a result of the homogeneity in both **h** and p_o observed by Bouligand in crab cuticles [7], whereas for non-ideal plywoods arcs with varying periodicity can be observed in the incision plane due to the pitch variation. The reconstruction of the 3D structure out of 2D observations is a classical inverse problem, and the well-known challenges are due to unavoidable ill-conditioning (small changes in input lead to large changes in output) and solution multiplicity in structure reconstruction.

A method for characterising ideal plywoods that essentially overcomes these challenges has been reported recently [19] for ideal plywoods using geometric modelling and computational tools, which is extended here to a representative graded plywood of the 'aurigans scarab' cuticle. These

new tools do not rely on optics as the Cano-Grandjean defect disclination line method or the Bragg reflection, methods that are known to be limited by its range of applicability and/or its accuracy [20, 21], hence the geometric modelling and computational procedure can complement experimental techniques, leading to a more robust characterisation of the ubiquitous chiral structure.

5.4 Objective and Methodology

The objective of this chapter is to describe a methodology capable of reconstructing the 3D structure of a graded plywood ($p_o(z)$) of 'aurigans scarab' as a canonical example of a complex biological plywood. In this chapter the experimentally determined non-monotonic spatial pitch variations in the beetle cuticle [14] is used to construct arbitrary *in silico* arced patterns, since no experimental arced patterns are accessible, and then each of these sections are used to perform 3D chiral reconstructions. When slicing a plywood at an arbitrary incision angle (α), we obtain a 2D layered arced patterns of period L, and each arc is characterized by a maximum curvature κ_{max}. We introduce a novel geometry-chirality phase diagram and demonstrate that in this diagram a set of (L, κ_{max}) values found experimentally leads to one and only one value of the pitch regardless the incision angle α. The key aspect of our method is that when the 2D patterns are space dependent ($L(z)$, $\kappa_{max}(z)$), the predicted chirality from our model are also space dependent, $p_o(z)$. Finally we prove that the accuracy of the 3D reconstruction methodology decreases with α.

5.5 Results and Discussion

The analytical description of biological plywoods are obtained through the geometric modelling previously published [19] is summarized as follows: the trajectories of the arced patterns are a

function of α and p_o (implicitly a function of the periodicity of the arcs "L"), leading to a system with one degree of freedom with multiple solutions. To eliminate this degree of freedom, the curvature κ of the arcs, which is a function of α and L, is introduced. By measuring the curvature of the experimentally observed arcs and fitting the analytical expression one can obtain the incision angle α and finally the pitch p_o with a straightforward calculation. The equations for the arced patterns and the curvature within each layer are [19]:

$$\frac{dx}{ds} = \frac{\cot\left[\dfrac{2\pi(\sin\alpha)s}{p_0}\right]}{\cos\alpha} \tag{5.1}$$

$$\kappa(s,\alpha,L) = \frac{-\csc^2\left(\dfrac{\pi s}{L}\right)}{\cos\alpha\left\{1+\left(\cot\left(\dfrac{\pi s}{L}\right)/\cos\alpha\right)^2\right\}^{3/2}}, \quad L = \frac{p_0}{2\sin\alpha} \tag{5.2a, b}$$

For graded plywoods as the beetle's plywood, the maximum curvature on a given layer is:

$$\kappa_{\max} = \frac{\pi}{L\cos\alpha} \tag{5.3}$$

Combining the maximum curvature $\kappa_{\max}$ and the 2D periodicity of the arcs L, lead to the following equation that represents the phase diagram in terms of L and $\kappa_{\max}$:

$$\left(\frac{2}{p_0}\right)^2 L^2 - \left(\frac{2\pi}{p_0}\right)^2 \frac{1}{\kappa_{\max}^2} = 1 \tag{5.4}$$

Eqn. (5.4) is a family of hyperbolas for different values of p_o, shown in Figure 5.2. The negative values for curvature indicates a shift in the handedness of the helical axis. Considering one of the hyperbolas for constant pitch, there are an infinite number of combinations of periodicity and

inverse of curvature leading to that precise value of pitch. However, there is one and only one value of the pitch that intercepts both axis of the phase plane for a particular value of α as established in eqns. (5.3, 5.4). The phase diagram (fig 5.2) shows several hyperbolas for different values of p_o, and the straight lines from equation (5.3) show that for a given α there is only one combination of curvature κ_{max} and 2D periodicity L intercepting these lines. The two limiting lines correspond to $\alpha = 0^o$ and $\alpha = 90^o$, corresponding to cuts normal and parallel to the helix. We note that as the helix vector **h** is usually unknown *a priori*, finding α through eqn. (5.3) is a crucial step. Small α angles lead to ill-conditioning as the hyperbolas essentially asymptotes the lines. The practical implementation to determine $p_o(z)$ using the phase diagram (2) is as follows: (1) perform the experimental sectioning of the BP, (2) determine (L, κ_{max}) in a given layer of the 2D arc patterns, (3) use (L, κ_{max}) to determine from the phase diagram (2) $p_o(z)$ and α for the given layer, (4) repeat procedure for all layers, and (5) finally obtain $p_o(z)$ spatial profile. This procedure is schematically depicted in figure 5.3. The stars shown in such figure indicate only one interception of L, κ_{max} per each α leading to only one value of p_o.

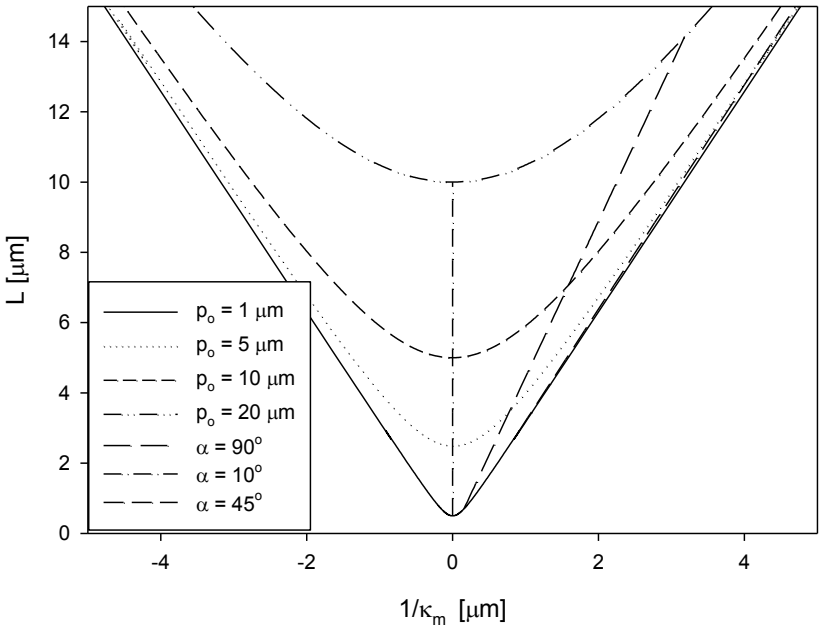

Figure 5.2. Chirality phase diagram in terms of L and arc's reciprocal maximum curvature κ_{max} for several values of pitch . The hyperbolas are from eqn.(5.4) and the lines from (5.3). Performing a section of a real plywoods yield L, κ_{max} and the plot gives p_o, and α.

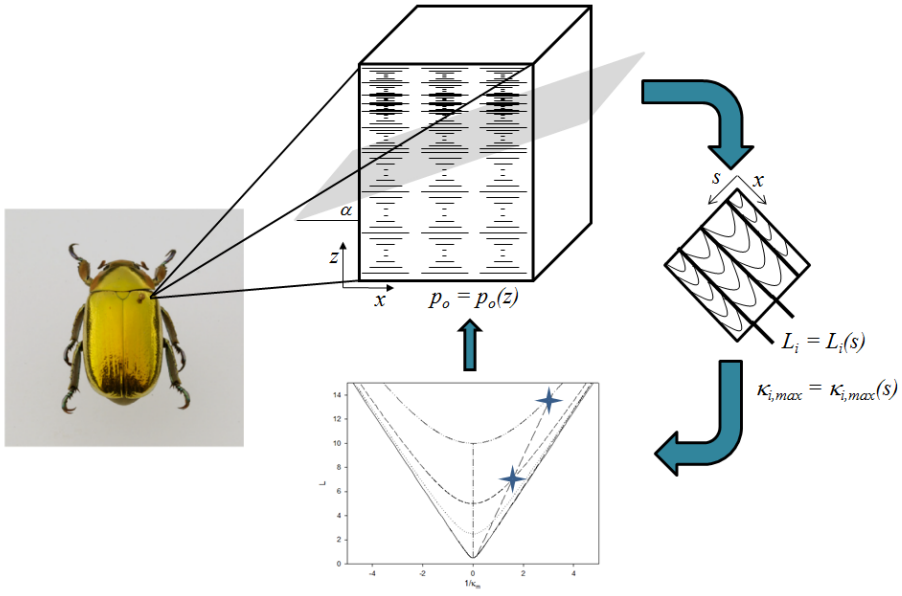

Figure 5.3. Schematic of the characterization procedure to find an arbitrary pitch profile p_o (z): (1) perform the experimental sectioning of the BP (α is unknown), (2) determine (L, κ_{max}) in a given layer of the 2D arc patterns, (3) use (L, κ_{max}) to determine from the phase diagram (Fig.5.2) p_o(z) and α for the given layer (star symbols), (4) repeat procedure for all layers, and (5) finally obtain p_o(z) spatial profile (star symbols) . The scarab photo is adapted from [14]

As mentioned, the arced patterns for the beetle cuticle were created using the 3D visualization tool Mayavi, by first introducing the cholesteric director field and then creating an incision plane with the VectorCutPlane module, and using the experimental information of Libby et al [14] for aurigans scarab, showing the spatial variation of the pitch presented in Figure H.2-H.3 (see Appendix H); we emphasize that although we use the experimental pitch as an input to create the arcs only due to the lack of experimental 2D observations. In reality the procedure would start with the slicing of the biological sample giving the experimental arced patterns. It can be seen (Fig. H.1) that the non-monotonic pitch is initially close to 0.48 μm with a quick increase up to 0.52 μm, followed by a further decrease, then going into a region of essentially constant pitch (approximately 0.37 μm), and finally showing a smooth increase. Characteristic visualizations of sectioning ($\alpha_1 = 15^o$ and $\alpha_2 = 25^o$) this synthetic aurigans scarab plywood and resulting graded arc patterns are shown in Figure 5.4 (a – b for α_1 and c – d for α_2). Technical visualization details for plywoods are can be consulted in Appendix G and H, and for general information about Mayavi the reader is referred [22]. It is observed that initially small arcs appear followed by larger arcs, as expected with pitch variations, regardless the incision angle. The key impact of the incision angle α is the resulting arc periodicity L and the total number of arcs observed, since at a smaller α the incision plane corresponds to a smaller region of the variation of the pitch in the perpendicular coordinate, and hence less information is observed if the size of the sample is kept constant. Three different incision angles were chosen ($\alpha_1 = 15^o$, $\alpha_2 = 25^o$ and $\alpha_2 = 40^o$) to demonstrate the characterisation procedure is accurate regardless the incision angle as shown in figure (5.4) with a sample size constant of 15 μm. To do this, regions in both incision planes were chosen arbitrarily, these arcs were then isolated and the periodicity and maximum curvature were measured, finally the pitch predictions were obtained. The results in Figure (5.5) show good agreement with the

experimental observations, with a low error (under 10%); we note that information regarding the experimental errors in [14] is not accessible. The accuracy in the determination of the curvature has to be high because the calculation of the incision angle is highly sensitive to changes of both L and κ_{max}. Additionally, it is observed that the lowest angle incision plane (15^o) is capable of reconstructing the pitch only up to about 4 μm in the perpendicular direction while the incision at 25^o can predict the pitch variations up to about 8 μm in such direction and that of 40^o up to 12 μm. Hence, the higher the angle the more information can be extracted from the incision plane. It is also worth noting that in the pitch predictions shown in figure (5.5), the error is higher in the 15^o predictions because of the ill-conditioning as stated concerning eqn. (5.2-b); the relationship between L and p_o is highly sensitive to small changes α, when α is small also observed in the phase diagram (fig. 5.2) with the hyperbolas converging to the asymptote for small α. From an experimental point of view, low angles should be avoided because of two reasons: i) the restriction of the sample size, if the sample is small, little information can be extracted from those observations, and ii) the error in the pitch tends to be larger in these cases because of the nature of the model, as noted previously. Hence, when taking a sample if one finds a low value of α it is advised to take another incision at a higher angle in order to improve accuracy and to extract more information out of this 2D observation.

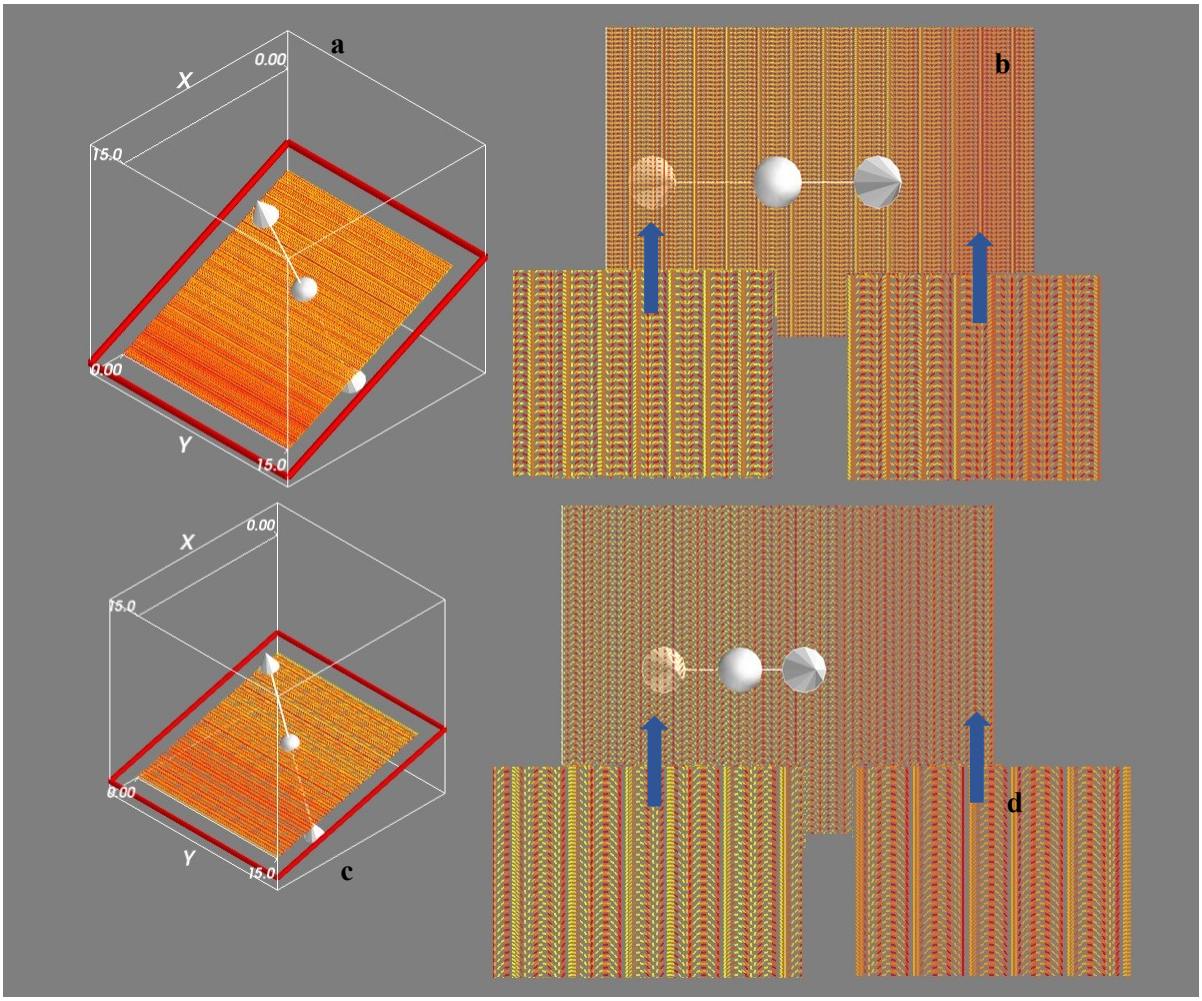

Figure 4. Two in-silico arc patterns, created incision planes (a-b) 25^{o} and (c-d) 15^{o} for the plywood of "aurigans scarab". The arrowed frames show enlarged 2D arcs for clarity. When $p_o(z)$, the 2D periodicity L varies. Smaller specimen regions can be reconstructed in the case of the lower angle. Larger scale images are provided in Appendix H for clarity.

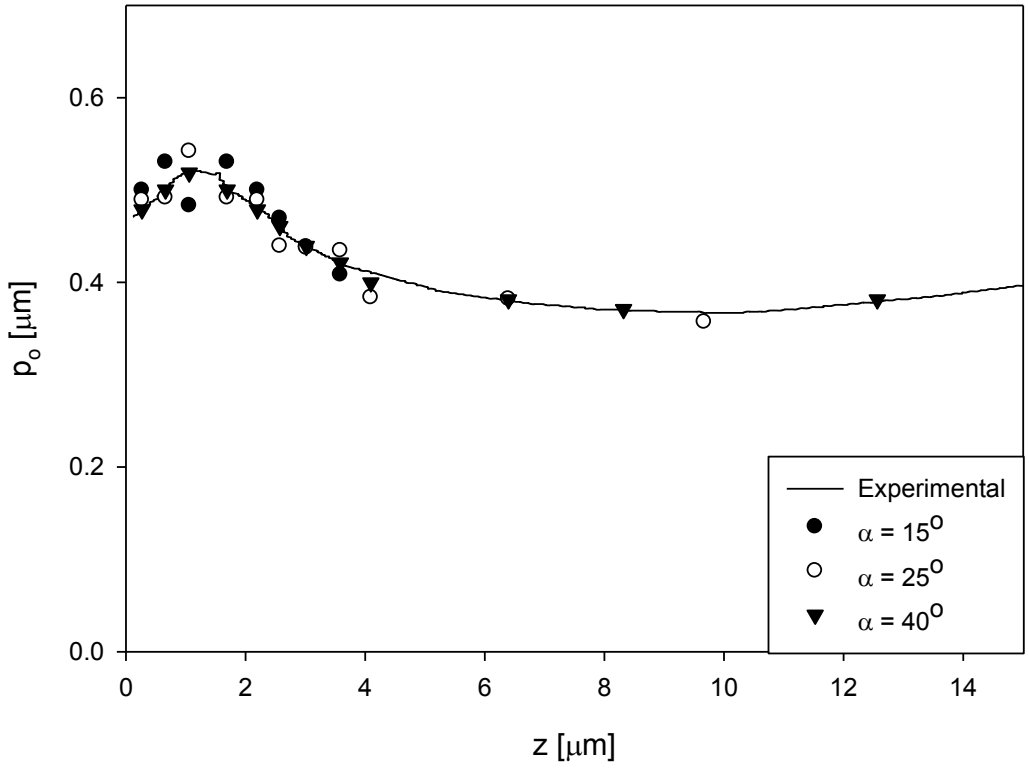

Figure 5. Chirality reconstruction of aurigans scarab from three different incision planes and comparison with experimental data extracted from [14]. Smaller angles cover shorter "z" distances for a given sample size.

5.6 Conclusions

In conclusion, we formulated a structural material characterization procedure for biological plywoods that exhibit non-trivial spatial gradients, using geometric modelling and computational visualization. Determining spatial periodicities and curvatures of 2D arc patterns in conjunction with a theoretically formulated plywood phase diagram yields the sought after cholesteric pitch. The sensitivity of the method to sample sectioning was established and larger sectioning angles

are preferred. We demonstrated the applicability of the 3D chiral reconstruction method for graded plywoods using experimental data for the "aurigans scarab". The proposed computational method complements optical characterization tools that must overcome the difficult challenge of chirality reconstruction. The new procedure has wide applications in biological materials characterization and in biomimetic engineering of structural and functional materials.

References (Chapter 5)

[1] Belamie, E.; Mosser, G.; Gobeaux, F.; Giraud-Guille, M.M. *J. Phys.: Condens. Matter*, 2006, **18**, S115-S129.

[2] Rey, A.D. *Soft Matter*, 2010, **6**, 3402-3429; Rey, A.D.; Herrera-Valencia E. E.; Murugesan, Y., *Liq. Cryst.*, 2014, **41**, 430-451.

[3] Fratzl, P. *Curr. Opin. Colloid Interface Sci.,* 2003, **8**, 32-39.

[4] Neville, A. C. *Biology of Fibrous Composites*, Cambridge University Press, New York, 1993.

[5] A. D. Rey, Herrera-Valencia E. E.; Murugesan, Y. K. *Liq. Cryst*., 2014, **41**, 430–451

[6] Rey A.D.; E. Herrera-Valencia, E.E. *Biopolymers*, 2012, **97**, 374-396.

[7] Bouligand, Y. *Tissue Cell*, 1972, **4**, 189-217.

[8] Roland, J.C.; Reis, D.; Vian, B.; Satiat-Jeunemaitre B.; Mosiniak, M. *Protoplasma*, 1987, **140**, 75-91.

[9] de Sa Peixoto,P.; Desinet-Besseau, A.; Schmutz, M.; Anglo, A.; Illoul, C.; Schanne-Klein, M.C.; Mosser, G. *Soft Matter*, 2013, **9**, 11241-11248.

[10] Lovelady, H.H.; Shashidhara, S.; Matthews, W.G. *Biopolymers*, 2014, **101**, 329-335

[11] Murugesan Y.K.; Rey, A.D., Polymers, 2010, **24**:766-785. Murugesan, Y.K.; Pasini, D.; Rey, A.D. *Soft Matter*, 2013, **9**, 1054-1065

[12] de Luca, G.; Rey, A.D. *Phys. Rev. E*, 2004, **69**, 011706.

[13] de Luca, G.; Rey, A.D. *European Physical Journal E*, 2003, **122**, 291-302

[14] Libby, E.; Azofeifa, D E.; Hernández-Jiménez, M; Barboza-Aguilar, C.; Solís, A.; García-Aguilar, I.; Arce-Marenco, L.; Hernández, A.; Vargas, W E. *J. Opt.* 2014, **16**, 082001

[15] Sharma, V.; Crne, M.; Park, J. O.; Srinivasarao, M. *Science*, 2009, **325**, 449-451.

[16] Allahverdyan, K.; Galstian, T.; Gevorgyan, A.; Hakobyan, R. *Optics and Photonics Journal* 2013, **3**, 17-22

[17] Rofouie, P.; Pasini, D.; Rey A.D. *Colloids and Interface Science Communications*, 2014, **1**, 23-26.

[18] Fernandes, S. N.; Geng, Y.; Vignolini, S.; Glover, B. J.; Trindade, A. C.; Canejo, J. P.; Almeida, P. L.; Brogueira P.; Godinho, M. H. *Macromol. Chem. Phys*. 2013, **214**, 25–32.

[19] Aguilar Gutierrez, O.F.; Rey, A.D. *Soft Matter,* 2014, **10**, 9446-9453

[20] Suh, S.W.; Joseph, K.; Cohen, G.; Patel, J. S.; Lee, S.D. *Applied Physics Letters*, 1997, **70**, 2547-2549

[21] Boudet, A.; Mitov, M.; Bourgerette, C.; Ondarcuhu, T.; Coratger, R. *Ultramicroscopy*, 2001, **88**, 219–229.

[22] Ramachandran, P.; Varoquaux, G. *IEEE Comp. in Sci. Eng*. 2011, **13**, 40-51

Chapter 6

6 Geometric Reconstruction of Biological Orthogonal Plywoods

6.1 Preface

Based on the full description of the arced patterns discussed in the previous two chapters and on the similarity of the perspective of the herringbone patterns arising from oblique incision in orthogonal plywoods with the 2D arced patterns of helical plywoods, this chapter provides the tools to reconstruct the 3D structure of orthogonal plywoods from simple 2D incisions. The characteristic feature of these patterns, the herringbone aperture angle is described in detail. This chapter is reproduced from a published paper titled: "Geometric Reconstruction of Biological Orthogonal Plywoods" co-authored with Prof. Alejandro D. Rey, Soft Matter, 2016, 12, 1184.

6.2 Summary

In this chapter we focus on structure determination of biological orthogonal plywoods, fiber-like composite analogues of liquid crystalline phases, where the fibrils of the building blocks show sharp 90^{o} orientation jumps between fibers in adjacent domains. We present an original geometric and computational modelling that allows to determine the fibrillary orientation in biological plywoods from periodic herringbone patterns commonly observed in cross-sections. Although herringbone patterns were long reported, the specific and quantitative relations between herringbones and the orthogonal plywoods were absent or at best incomplete. Here we provide an efficient and new procedure to perform an inverse problem that connects two specific features of the herringbone patterns (aperture angle and wavelength) with the 3D morphology of the structure, whose accuracy and validity was ascertained through in-silico simulations and also with real

specimens (“Eremosphera viridis”). This contribution extends significantly the better known characterization methods of 2D cross sections, such as the arced patterns observed in biological helicoidal plywoods, and with the present proposed methodology it adds another characterization tool for a variety of biological fibrous composites that form cornea-like tissues.

6.3 Introduction

Ordered structures found throughout Nature show a variety of architectures consisting of fibrillar building blocks such as collagen in vertebrates, cellulose in plants and chitin in insects, and are formed through an efficient entropy-driven self-assembly process [1, 2, 3]. The relationship between the architecture of these fiber-based structures and the functionalities such as mechanical behaviour, optical properties is widely recognized [4, 5], yet poorly understood, and has become a source of inspiration in the last decades which has influenced the development of new materials [2, 6, 7, 8].

Biological liquid crystals are commonly observed in sufficiently stiff fibril-based materials and are classified into: (i) solid analogues, (ii) in-vitro biopolymer solutions, and (iii) in-vivo materials and secretions. This chapter focuses on solid analogues; the reader is referred to [1, 2, 9, 10] for more information regarding in vivo and in vitro liquid crystals. Solid analogues or biological plywoods (referred hereupon as plywoods) are materials that present a frozen-in orientated ordered structure from a previous self-assembly step involving liquid crystal organization [11, 12]. Common types of plywoods are nematic, helical and orthogonal and are described in detail in Figure 6.1 together with key geometric quantities and expected cross-sectional patterns. In nematics, the fibrils show a single preferred orientation (a-c), and cross-sections give line (c) or dot (b) patterns. In helicoids, the fibrils rotate continuously in the normal direction (e-f) to parallel

planes on a periodic distance po known as the pitch and cross-sections display helical (e) or arced patterns (f). In orthogonal plywoods, the fibers display a homogeneous domain structure with a sharp fiber rotation between domains (h-g-i) and cross-section are dot-line (h), line-line (i), or herringbone (g) patterns. The plywoods showing a helicoid (d) display the organization of cholesteric liquid crystals or chiral nematics N*, and its abundance in plants and insects is associated with mechanical property optimization that removes the disadvantages of anisotropy as well as diffraction functionalities, as in beetles [13, 14] and tulips [15, 16]. Given the functional versatility and widespread presence in plants and insects, helicoids have been intensely studied [1, 8, 10, 17].

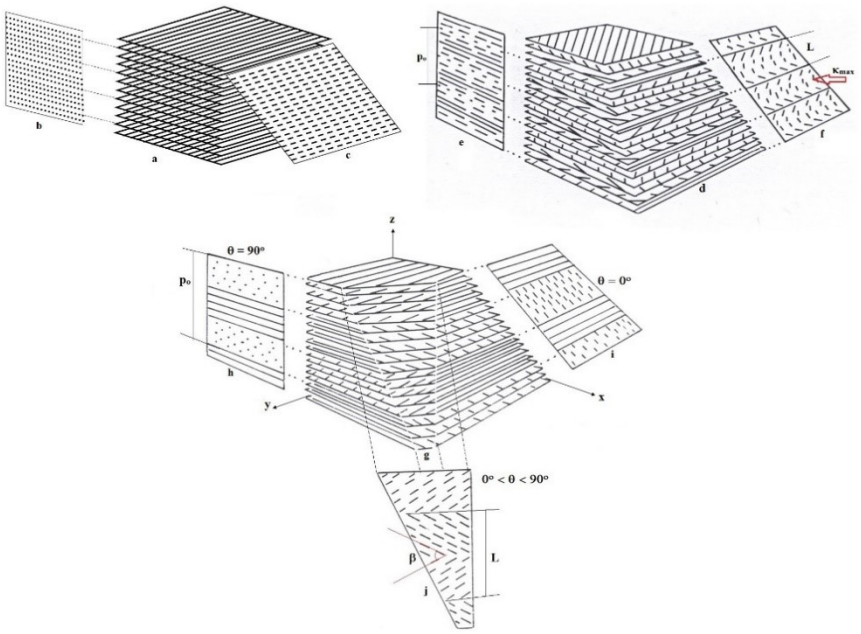

Figure 6.1. Schematic representation of a nematic plywood (a-c) as a series of planes with parallel alignment throughout the entire structure (a) with projections corresponding to dots (b) when the incision is orthogonal to the fibril alignment and a sequence of parallel lines (c) with any other incision angle; helicoidal plywoods (d-f) where the cholesteric arrangement of pitch po is shown (d) and projections corresponding to periodic structures but no arced patterns with periodicity po/2 (e) and the arced patterns with oblique incisions of periodicity L and maximum curvature κ_{max} (f); and the orthogonal plywood (g-j) showing several layers orthogonally arranged and projections without any distinguishable pattern when the incision is aligned with one of the fibril orientation (h-i) and the herringbone patterns of periodicity L and aperture angle β, with a rotation of the oblique incisions.

The structure characterization of biological fibrous composites involves determining the fiber orientation and chiral pitch or domain scales and is a complex inverse problem usually approached using optical methods [18, 19] or by sectioning samples and then performing an analysis based on the resulting 2D cross-sectional patterns shown in Figure 6.1. As mentioned above, cross-sectional patterns of helicoids are usually periodic arced patterns of maximum curvature κ_{max} while cross-sections of orthogonal plywoods are herringbone patterns with an aperture angle β. Figure 6.2 shows a schematic of main geometric features of the arc patterns-helicoids and herringbone patterns-orthogonal plywoods. The reconstruction, indicated by the thick arrows, involves converting the geometric information of these 2D patterns into the full 3D structure. It is crucial to note the 2D patterns are sensitive to the slicing angle α and not all slicing angle produce these distinctive patterns, as further discussed in section 6.3.1. Hence a quantitative understanding of the relation between the pattern and the slicing angle α is crucial. Techniques for ideal and complex arced patterns have been presented [20, 21] and validated [14] but herringbone patterns remain largely unexplored.

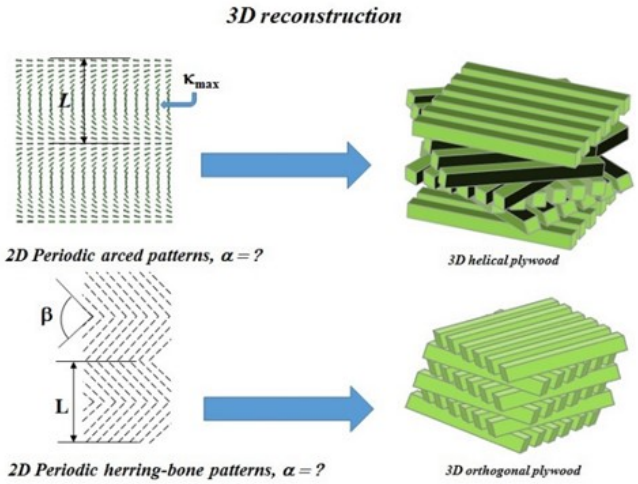

Figure 6.2. Summary of the cross-sectioning characterization procedures, where the full 3D helical and orthogonal structures are reconstructed from 2D observations from the periodic arced patterns [26] and herringbone patterns (this work). The periodic arc-patterns have a 2D periodicity L and maximum curvature κ_{max}. The periodic herringbone patterns have periodicity L and aperture angle β. In both case the slicing angle α is unknown.

The objective of this chapter is to present and validate a methodology for structure characterization of orthogonal plywoods from geometric modelling of 2D herringbone patterns. The ill-conditioning of inverse problems is adequately overcome in this approach by developing an error sensitivity analysis based on in-silico herringbones generated by a versatile 3D visualization method for arbitrary orientation vector fields. This chapter is organized as follows. Section 6.3.1 presents a brief discussion of biological plywoods, fibrillar arrangements, and characteristic 2D patterns on cross-sections. Section 6.4.1 presents the geometric model that forms the basis of converting herringbone patterns into plywood structure. Section 6.5.1 provides the results of the in silico plywood pitch determination followed by section 6.5.2 that evaluates the accuracy of the method and Section 6.5.3 validates the process with the herringbone pattern of i) an algae specimen "Eremosphaera viridis" and ii) in silico created herringbone patterns. Appendix I provides the

algorithmic details used to calculate all the errors introduced from herringbone pattern measurements. The significance of the results are included in the final conclusions.

6.3.1 Plywood Architectures in Nature

In this section we provide a (i) short required background on liquid crystal solid analogues that expands on the key concepts mentioned in the introduction, (ii) define the crucially important sensitivity of arced and herringbone patterns to the slicing angle mentioned in conjunction with Figure 6.1, and (iii) present examples of the diversity of orthogonal plywoods in Nature.

Nematic plywoods have been observed in some insect cuticles through the entire material [22] but also as an intermediate phase sandwiched between two different solid cholesteric-like phases, as in some beetles [23]. The role of this type of architectures in some insect cuticles is hypothesized to serve as the so-called "half wave plate" that changes the helicity of the incident light. When taking incisions of this type of plywood it can be observed (Figure 6.1 a-c) a family of parallel lines showing the preferred orientation which is homogeneous throughout the entire structure when the incision angle lies between 0 and $\pi/2$, as the incision angle approaches the upper limit the length of the projections decrease and when the lower limit is reached dots are observed instead.

Helicoidal plywoods were the first to be studied and explored by Bouligand [20] in crab cuticles made of chitin and is the most widely studied biological plywood and it can show ideal architectures but also non-ideal configurations such as the two-pitch plywood observed in endocarps of some fruits (made of cellulose) [24] and graded structures where the pitch varies longitudinally in the micron range scale as in the cuticle of some scarabs [19]. A characterization procedure based on the projections of the chiral nematic director to an incision plane has been reported [14, 21] which depends on the 2D periodicity of the arcs (L) and the maximum arc

curvature κ_{max} which is found in the middle of the arcs. With these two experimentally measurable quantities (L, κ_{max}) one is capable of reconstructing the entire 3D structure based on 2D observations, thus complementing other optical techniques [18] leading to a more robust characterization of these structures. Depending on the type of plywood (ideal or non-ideal) the observed arced pattern can have constant or variable periodicity. These patterns are indifferent to rotation of the incision plane because of the helical structure shown.

Finally, orthogonal plywoods present abrupt changes in the orientation of 90º in strictly orthogonal architectures, but examples of angles in the range between 45º and 90º can also be found [22]. Other types of orthogonal arrangements have been reported such as the paired orthogonal system where a pair of adjacent layers are orthogonally oriented, but the subsequent set of pairs show a clockwise or anti-clockwise rotation [25] leading to nested arced-patterns. Orthogonal arrangements are known for providing with the necessary strength [26] and one of the functionalities of these plywoods is to preserve or control the shape of the material as in lazy tongs [22]. The arrangement of the fibrils is responsible for a balance in the load as occurs in laminated composites [27] and also of the mechanical failure behavior where the sliding of lamellae prior to the fracture of collagen fibers in mineralized and demineralized samples of fish scales occurs [28]. Reversible texture transitions from orthogonal to randomly oriented fibrils have been observed during the wound healing process in the skin of some amphibians [22]. The orthogonal plywood can be found in certain algae walls, in collagen based materials reinforced with mineral compounds in fish scales [22, 28] and in bone osteons composed of stacks of orthogonal layers of collagen fibers rolled in co-axial cylinders [8, 22, 29, 30]. Cornea is another example in which collagen fibrils are assembled in an orthogonal fashion in the corneal stroma (which composes 90% of the cornea thickness) and besides providing strength and shape control, the stroma is responsible for

nearly 2/3 of the optical power of the eye [26]. Even when the plywood morphology is known to impact the material properties (mechanical, optical, etc.) these relationships are not fully understood [5], but the knowledge of the morphology of the plywoods is crucial to fully characterize these structures in order to make any progress along this line. The structure-property relations in orthogonal plywoods is an evolving area which evidently requires prior structure characterization. A list of natural cellulosic, collagen and chitin materials exhibiting orthogonal plywood organization are given in Table 6.1. It is noteworthy that as in the case of parallel and helical plywoods, a very specific underlying biochemistry does not seem to be necessary. Plywood transitions, such as helicoid ⇄ orthogonal have been reported [31] for acidic collagen I solutions, with higher pH promoting the former. This and other transitions form the basis of Neville's generic classification of biological fibrous composites [22] and highlight the importance of orthogonal arrangements.

Table 6.1 Examples of Biological Orthogonal Plywoods

Cellulose	**Collagen**	**Chitin**
Eremosphaera viridis cell wall (alga) [22, 32]	Paralvinella grasslei cuticle (annelid)[35]	Oryctes rhinoceros eggshell (beetle)[37]
[a] Tilia platyphyllos (larged-leaved linden)[33]	Pagrus major scales (fish)[28]	[a] Aeshna juncea cuticle (odonata)[38]
[a] Picea abies (Norway spruce)[34]	Outer lamellae human long bones [5, 30]	[a] Hydrocyrius colombiae cuticle (hemiptera) [39]
	Bird cornea (several species) [36]	[a] Coleoptera cuticle [39]

[a] Pseudo-orthogonal plywood observed

As in the case of helicoids, a pitch can be defined in orthogonal systems, where the pitch will be built up of 4 domains in strictly orthogonal plywoods if all the domains are of the same thickness. Projections to an oblique plane (oriented by a normal unit vector relative to an orthogonal coordinate system) produce the well-known herringbone patterns with a suitable combination of polar (ϕ) and azimuthal angle (θ), as shown in figure 6.1 [8, 17]. When one of the fibril orientation

lies in any of the coordinate axes (i.e. fixing $\theta = 0^o$ or 90^o) no distinguishable pattern is observed by varying the polar angle in the incision plane but layers with dots and parallel lines are observed whose length depend on the orientation of the plane. On the other hand, the herringbone patterns are observed when rotating the incision plane with the azimuthal angle which avoids any of the orthogonal orientation of the fibrils to coincide with the axes of the incision plane. Perfectly symmetrical herringbones are observed when the azimuthal angle takes the value of 45^o i.e. the two orthogonal sets of fibrils' projection to the incision plane are of the same length because both axes of the incision plane will be shifted equally from any of the two sets of fibrils. As a consequence, any other value of θ will produce asymmetric patterns, creating the effect that any of the two sets of fibrils are longer than the other, however this is only a matter of perspective, the closer to the 45^o value (i.e. the closer the ratio of both projected lengths to one) is preferred as will be shown in subsection 6.4.1. Even when the twist angle is fixed in these plywoods, the perspective created by projecting the fibrils of the plywood on the incision plane creates the perception that the angle between the fibrils is different from 90^o, and generates the herringbone angle β (see figure 6.1) whose value depends on the incision angle for symmetric herringbone patterns.

6.4 Geometric Model

The proposed methodology is based on first sectioning a 3D plywood sample at an unknown angle (α) to obtain a 2D periodic herringbone pattern, and then measuring the pattern observables, which are the 2D periodicity L and herringbone angle β. With (L, β) we next show how to find the domain size p_o. We assume symmetric herringbone patterns unless stated otherwise, since it is always possible to obtain it by proper sectioning and it simplifies the characterization procedure.

Using simple geometry, we find the triangle that connects the plywood characteristic length po and the projected herringbone pattern periodicity L as shown in figure 6.3 leading to the following expression:

$$L = \frac{p_o}{2} \csc \alpha \tag{6.1}$$

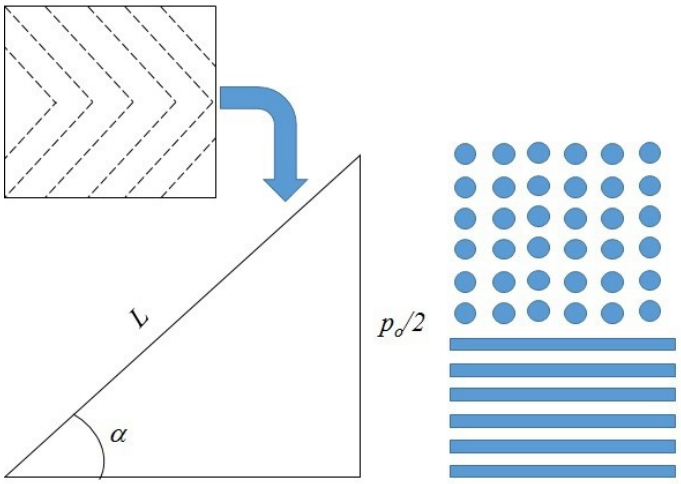

Figure 6.3. Connection between the characteristic length-scale p_o of the orthogonal plywood and the projected periodicity L observed on a cross-section whose magnitude depends on the incision angle α. The upper-left frame are the observed herringbone patterns and the right shows two domains in the actual plywood.

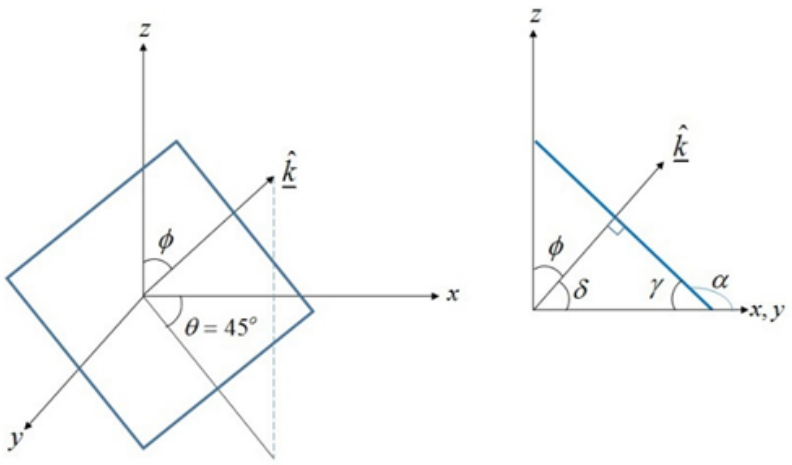

Figure 6.4. (a) Schematic representation of the incision plane and the angles defining the orientation of the normal vector $\hat{k}$ in the laboratory (x,y,z) frame. (b) Side view defining the slicing angle α and the polar angle ϕ.

Equation 6.1 is analogous to the one reported for helicoids [21] and as in that case it cannot be used alone to describe the orthogonal plywoods because the observed periodicity L depends on two unknown parameters α and p_o, hence additional information is required to eliminate the degree of freedom. The maximum curvature κ_{max} in the arced patterns allowed [21] closure in their characterization procedure and the herringbone angle β is expected to be the analogue parameter to the maximum curvature. Based on that hypothesis, the correspondence between the herringbone angle β and the incision angle α is obtained as follows. We set a 3D orthogonal coordinate system with unit vectors $\hat{\underline{\delta}}_x, \hat{\underline{\delta}}_y, \hat{\underline{\delta}}_z$ in which two axes lie parallel to the orientation of the two orthogonal set of parallel families of lines that represent the fibril orientation in the orthogonal plywood. The orientation of the incision plane is given by the normal vector $\hat{\underline{k}}$ pointing outwards from the plane and is a function of both the polar ϕ and the azimuthal θ angles. Figure 6.4 shows schematically

the angles involved and how they are related to the incision plane. The projection to a given incision plane is given by extracting the tangential component of the unit vectors $\hat{\underline{\delta}}_x, \hat{\underline{\delta}}_y$ by using the projection operator defined in eqn. (6.2):

$$\underline{\delta}_i^{\,p} = (\underline{\underline{I}} - \hat{\underline{k}}\,\hat{\underline{k}}) \cdot \hat{\underline{\delta}}_i \tag{6.2}$$

Where the superscript "p" stands for projected and I is the identity second order tensor with $\hat{\underline{k}} = \cos\theta \sin\phi\, \hat{\underline{\delta}}_x + \sin\theta \sin\phi\, \hat{\underline{\delta}}_y + \cos\phi\, \hat{\underline{\delta}}_z = k_x\, \hat{\underline{\delta}}_x + k_y\, \hat{\underline{\delta}}_y + k_z\, \hat{\underline{\delta}}_z$. By taking the dot product of the projected unit vector in the x direction with the one in the y direction (the direction of the layers in the plywood) one obtains:

$$\underline{\delta}_x^{\,p} \cdot \underline{\delta}_y^{\,p} = |\,\underline{\delta}_x^{\,p}\,|\,|\,\underline{\delta}_y^{\,p}\,| \cos\beta = (\hat{\underline{\delta}}_x - k_x\,\hat{\underline{k}}) \cdot (\hat{\underline{\delta}}_y - k_y\,\hat{\underline{k}}) \tag{6.3}$$

In eqn. (6.3), the herringbone angle β appears automatically because it corresponds to the angle created by the projection of the unit vectors in the incision plane. Rearranging eqn. (6.3) in terms of the polar and azimuthal angles and by carrying out the norms of the projected vectors, solving for β leads to:

$$\cos\beta = \frac{-\sin^2\alpha \sin\theta \cos\theta}{\sqrt{1-\cos^2\theta \sin^2\alpha}\,\sqrt{1-\sin^2\theta \sin^2\alpha}} \tag{6.4}$$

Where the relationship $\phi = \pi - \alpha$ in eqn. (6.4) is already taken into account. Equation (6.4) gives an implicit relationship between α and β for a given value of θ. This was done without assuming symmetry in the herringbone patterns and is a general expression for β in terms of α and θ, however α cannot be obtained directly from this expression. One way to overcome this difficulty is to

compare the projected lengths of the fibrils because as one approaches small (large) values for θ, the projected length of the fibrils aligned in the x(y) direction will decrease and the length aligned in the other direction other will increase. This is done by comparing the norm of both projected vectors as follows:

$$| \underline{\delta}^{p}{}_{i} | = \sqrt{\underline{\delta}^{p}{}_{i} \cdot \underline{\delta}^{p}{}_{i}} = \sqrt{1 - k_i k_i} \tag{6.5}$$

The subscript "i" stands for x or y, in the case of k_i indicates the "x" or "y" component of the normal unit vector. We define the projected length ratio $\mathrm{R}(\theta, \alpha)$ as follows:

$$\mathrm{R}(\theta, \alpha) = \sqrt{\frac{1 - k_x{}^2}{1 - k_y{}^2}} = \sqrt{\frac{1 - (\cos\theta \sin\alpha)^2}{1 - (\sin\theta \sin\alpha)^2}} \tag{6.6}$$

Two special limit cases of this expression that do not lead to visible herringbone patterns are: i) θ = 0° and ii) θ = 90°. The ratio in the former case is restricted to the interval $0 \le R(\theta = 0^o, \alpha) \le 1$ with the lower bound R=0 when the incision plane is normal to the fibrils oriented in the "x" direction and the projection of such fibrils are dots (α = 90°) and the higher bound R=1 when the incision plane is parallel to the fibrils, hence the projected length will be the same of the fibril (α = 0°). While in the latter case the ratio is within the interval $0 \le R(\theta = 90^o, \alpha) < \infty$ with the lower bound when the incision plane is parallel to the fibril orientation, similarly to the higher bound of limit case i), and the higher bound when the projected length of the fibrils oriented in the "y" direction decrease to dots resulting in an indeterminate form of eqn. (6.6).

For the intermediate values of θ the ratio R has a finite value within $0 \le R(0 < \theta < 90^o, \alpha) \le 1$ and the upper bound is achieved with θ = 45°. In order to implement the procedure starting with a

real orthogonal plywood specimen, one perform a sequence of cuts, recording R, until an essentially symmetric herringbone pattern is observed, which corresponds to R=1 and $\theta = 45^{o}$. Equation (6.4) now gives:

$$\cos\beta = \frac{-\sin^2\alpha}{1+\cos^2\alpha} \tag{6.7}$$

It is worth noting the herringbone angle β now depends only on α and is not associated with another length-scale from the sample or the incision plane. This is a consequence of the constant twist angle between the plywoods layers and is just a matter of perspective. In partial summary, the proposed methodology relies on eqns. (6.1) and (6.7) when R=1 and consists of the following steps:

1) An oblique incision giving a symmetric herringbone patterns is obtained.

2) Measure L and β from the herringbone pattern on the incision plane.

3) Calculate the incision angle α from eqn. (6.7).

4) Estimate the pitch p_o of the plywood using eqn. (6.1).

5) If the pitch is composed of 4 identical layers the average thickness of each layer can be calculated by dividing $p_o/4$.

Next we evaluate the accuracy and characterize the sensitivity of this structure reconstruction method using synthetic herringbones and then validate the method with a real biological plywood.

6.5 Results and Discussion

6.5.1 Pitch Determination

Firstly, to test the general validity of the procedure we used the Mayavi visualization software 40 where we specified the director field of an orthogonal plywood, performed oblique sections at known incision angles (α) with fixed azimuthal angle of 45^o and measured the 2D periodicity L_m as a function of the known angle α. This was done for several values of p_o. Figure 6.5 shows the linear relationship between L_m and csc(α) extracted from the in silico created herringbone patterns which shows the slope to be essentially po/2 as expressed in eqn. (6.1).

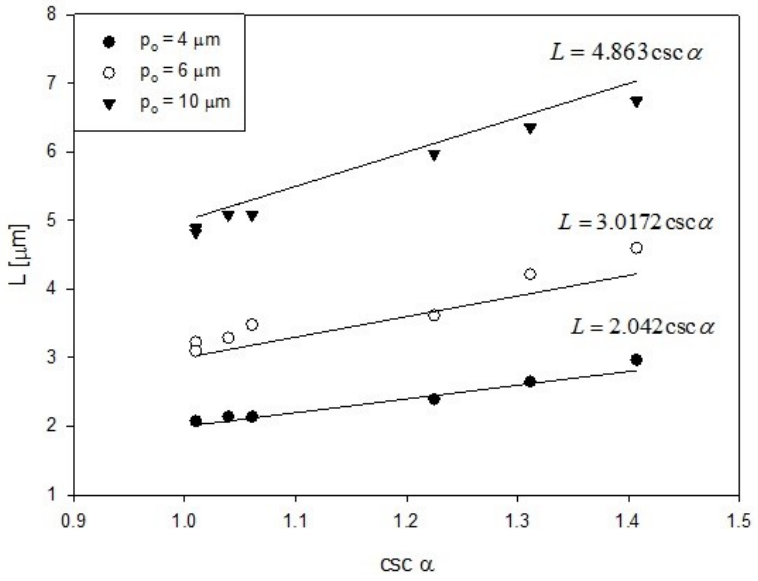

Figure 6.5. Calculated herringbone pattern periodicity L as a function of csc(α) showing a linear relationship with slope $p_o/2$.

Equation 6.1 shows that the pitch is undefined when $\alpha = 0$ and $L \rightarrow \infty$. Physically this means that the incision is made in one of the planes of the parallel oriented layers and no herringbone pattern

is expected which could be equivalent to an infinitely large herringbone pattern since there is no change in the orientation in this layer. This is supported by eqn. (6.7) that predicts $\beta = 0$. As the incision angle increases the periodicity L decreases until it reaches the value $p_o/2$ which occurs when $\alpha = \pi/2$. In this limit case the periodic structure that could be anticipated is one with periodicity $p_o/2$, however $\beta = \pi$ is predicted from eqn. (6.7) and no herringbone pattern is visible and one might incorrectly assume the sample has the structure of a frozen nematic phase. For experimental purposes incision angles close to these limiting values are not recommended since they could lead to wrong conclusions.

It is worth noting that incisions made at the supplementary angle $\pi-\alpha$ lead to the same periodicity and the herringbone patterns appear as their mirror image. This can be observed in figure 6.6 and has also been reported for helicoids [21, 24] and is consistent with goniometric studies.

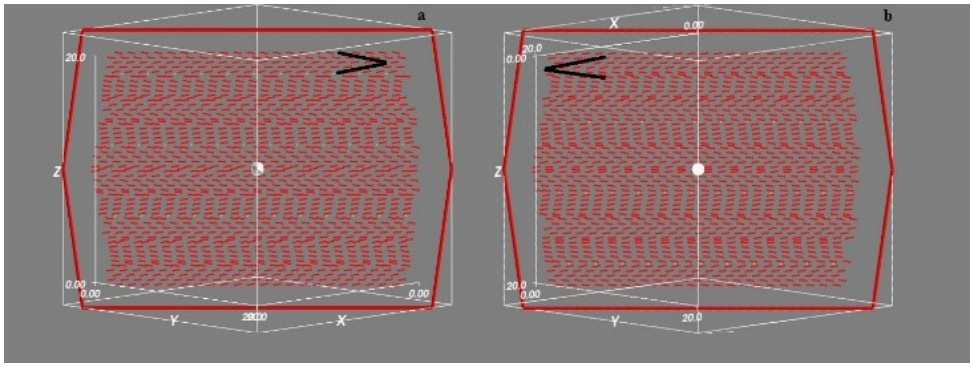

Figure 6.6. Herringbone patterns for a plywood with $p_o = 8$ μm showing the effect of the specular reflection when the incision angle is a fixed angle (α) and another incision is taken at the supplemen-tary incision angle (b).

6.5.2 Error Sensitivity on Structure Determination

In this section we provide guidelines on how to avoid procedures that yield poor predictions on the values of the length scale p_o when working with real orthogonal plywoods. In order to analyze

the predictions and assess the errors of the methodology several incisions of the same plywood would be required, however this information is not easily available. Alternatively the samples showing the 2D periodic herringbone patterns can be created in silico with the 3D visualization tool Mayavi [40] where the director field of an orthogonal plywoods is completely specified along with p_o. Any incision plane can be quickly realized, thus allowing the total control of α. This analysis is independent of θ because R = 1. The algorithmic procedures and mathematical details are given in Appendix I and here we emphasize the significance of the results. In this section we refer to two different sets of variables resulting from the Mayavi visualizations where the inputs for creating the synthetic herringbone patterns are the director fields with different pitch (4, 6 and 10 μm). On the one hand we have the known inputs for Mayavi p_o^M and α_M. These two variables allow the calculation of L_c^M with eqn. (6.1) and β_c^M with eqn. (6.7).

On the other hand we have the variables than can be measured from the 2D synthetic herringbone patterns which will emulate a real experimental application of the methodology: L_m and β_m. using eqn. (6.7) we calculate the incision angle (α_c) and finally by using eqn. (6.1) the pitch can be computed (p_{oc}). The former set of variables will be taken as the predictions from the model as exact values and will be compared with the latter set that simulates the application of the procedure, allowing to calculate the following relative errors since the input is known (see Appendix I):

$$\varepsilon_\beta = \frac{abs(\beta_c^M - \beta_m)}{\beta_c^M} * 100; \quad \varepsilon_L = \frac{abs(L_c^M - L_m)}{L_c^M} * 100; \quad \varepsilon_{p_o} = \frac{abs(p_o^M - p_{oc})}{p_o^M} * 100 \tag{6.8}$$

As shown below, ε_{p_o} is more sensitive to errors in L than errors in β. The in silico herringbone patterns for the plywoods with p_o of 4 and 10 μm are shown in figure 6.7 with two different incision angles α = 130.32° (a & c) and 98.05° (b & d), the third value of the methodology is not

shown for brevity but the predictions are given in tables 6.2 and 6.3. It can be seen that at least qualitatively the herringbone angle β for a given incision angle α does not change with changes in the pitch p_o comparing fig. 6.7 a & b with c & d respectively. This qualitative result is confirmed quantitatively with the measurements of β shown in table 6.2. By moving the incision angle with a constant pitch (fig. 6.7 a & b for p_o = 4 μm and c & d for p_o = 10 μm), it can be observed that an angle closer to 90° leads to smaller values of L, consistent with eqn. (6.1) and confirmed in the measurements shown in table 6.3.

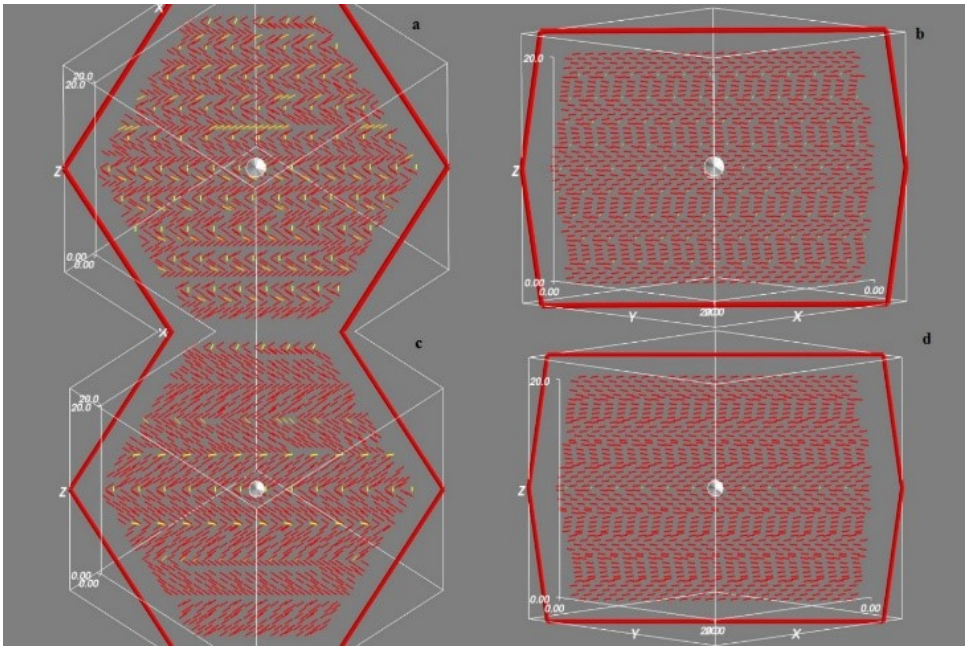

Figure 6.7. In silico created herringbone patterns for a plywood of p_o = 4 (a-b) and 10 (c-d) μm, showing the effect of the periodicity with the incision angle by changing the pitch (a & c with α = 130.32°) and (b & d with α = 98.05°). The herringbone angle obtained from different plywoods at the same incision angle is equal.

Table 6.2 shows the comparison between two sets of data of the herringbone angles, β_c^M and β_m, such values did not change when the pitch was varied, demonstrating these values are pitch-independent. The relative error ε_β is small, having its maximum values when the incision angle is

close to 90º. Intermediate values of the incision angle (or its complement leading to the specular image) lead generally to smaller errors, hence to improve accuracy these angles are preferred, which furnished values of β between 40º and 80º. It is worth mentioning that a similar recommendation was given in the methodology for helicoids [14].

Once β is assessed, the incision angle was calculated (α_c) and compared to the known angle α_M, which led to a negligible error (see Appendix I) meaning that the incision angle calculation is not significantly affected by errors in the measurement of the herringbone angle β. Table 6.3 compares the two sets of data for L and p_o. The errors in the periodicity L are higher with respect to the ones obtained from the herringbone angle comparisons and is propagated to the pitch calculation leading to errors between 2 – 7% for p_o. These values can be attributed mostly to L because the negligible errors found for α, and also it is worth noting that when the error in the herringbone angle β is closest to zero for the values shown in table 6.3 (i.e. $\alpha = 125^o$ with $\varepsilon_\beta = 0.68\%$) the difference between ε_L and ε_{po} is the largest. As mentioned above, the pitch prediction in the methodology has two sources of errors: measurements of (i) β and (ii) L, with the latter being the most sensitive parameter in the methodology (see Appendix I). This indicates L should be carefully measured with high precision instruments in order to have accurate predictions from this characterization procedure.

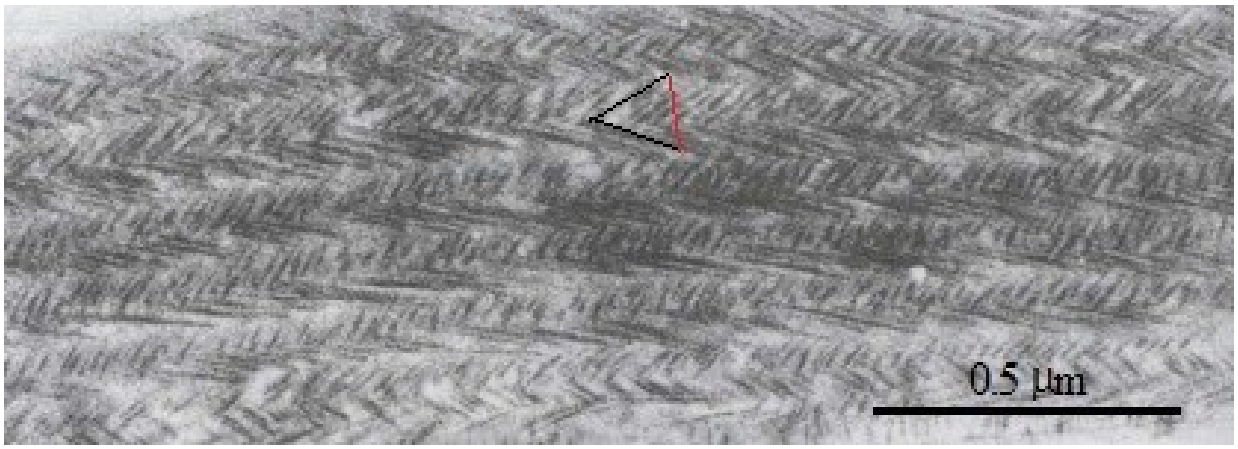

Figure 6.8. Herringbone patterns observed in a sample of the alga "Eremosphaera viridis"with β = 74.3° and L = 0.1146 µm. Copyright permission (3686041171064) from Springer.

Table 6.2 Herringbone pattern measurements

α^M	β_m	β_c^M	ε_β[b]
94.04	7.83	8.07	3.06%
98.05	16.41	15.94	2.85%
112.99	43.15	42.67	1.12%
130.32	65.00	65.81	1.24%
140.24	74.45	75.10	0.88%
151.46	82.63	82.56	0.04%
81.95	16.41	15.94	2.85%
74.21	31.65	30.45	3.79%
54.74	60.41	60.00	0.68%

[b] Error calculated as: $\varepsilon_\beta = \frac{abs(\beta_c^M - \beta_m)}{\beta_c^M} * 100$

Table 6.3 Pitch predictions, periodicities (measured and calculated) and errors

α	p_o = 10 μm				
	L_m	Lc^M	$\varepsilon_L{}^c$	$p_{o\ c}$	$\varepsilon_{po}{}^c$
98.05	4.89	5.05	3.20%	9.67	3.26%
125.26	5.98	6.12	2.40%	9.72	2.81%
81.95	4.82	5.05	4.46%	9.55	4.52%
	p_o = 6 μm				
	L_m	Lc^M	$\varepsilon_L{}^c$	$p_{o\ c}$	$\varepsilon_{po}{}^c$
98.05	3.23	3.03	6.50%	6.39	6.44%
125.26	3.42	3.67	6.96%	5.56	7.35%
81.95	3.09	3.03	2.29%	6.13	2.22%
	p_o = 4 μm				
	L_m	Lc^M	$\varepsilon_L{}^c$	$p_{o\ c}$	$\varepsilon_{po}{}^c$
98.05	2.08	2.02	2.81%	4.11	2.75%
125.26	2.40	2.45	2.17%	3.89	2.58%
81.95	2.08	2.02	2.81%	4.11	2.75%

[c] Errors calculated as: $\varepsilon_L = \frac{abs(L_c{}^M - L_m)}{L_c{}^M} * 100$ $\varepsilon_{p_o} = \frac{abs(p_o{}^M - p_{oc})}{p_o{}^M} * 100$

6.5.3 Biological Validation

The methodology was initially tested on an electron micrograph from the cell wall of the alga "Eremosphaera viridis" by calculating p_o, the average layer thickness and the cell wall thickness which is compared to the one calculated directly from the full sample. Figure 6.8 shows the electron micrograph of the oblique section from the cell wall of "Eremosphaera viridis" and the measured values of the herringbone angle and the periodicity of such patterns which are 74.3º and 0.1146 μm, respectively. The sample size is approximately 0.8125 μm and composed of 14 orthogonally aligned layers. Using eqns. (6.1) and (6.5) leads to the values of $\alpha = 40.74^o$ and p_o = 0.1496μm leading to a layer thickness of 37.4 nm giving a cell wall thickness of 0.5236 μm. The cell wall thickness can also be obtained from the sample size leading to a value of 0.5303 μm which is comparable to the one obtained from the calculation of the proposed methodology (with

relative error of 1.26% calculated as: $\varepsilon = \frac{abs\left(W_{\exp} - W_{calc}\right)}{W_{\exp}}$) thus showing very good agreement with an experimental micrograph.

6.6 Conclusions

Biological plywoods are an important class of fibrous composites found throughout Nature and arise due to the frozen liquid crystal-like organization. Orthogonal plywoods are an important class of these materials, and are found in collagen, cellulose and chitin-based structures. In this paper we develop, apply and validate a reconstruction method for the 3D structure of orthogonal plywoods based on the geometry of 2D herringone patterns obtained by simple sectioning. The reconstruction methodology showed good agreement with experimental observations taken from oblique incisions from the alga "Eremosphaera veridis" and in silico created patterns. It was found that in order to have accurate predictions of domain size, moderate herringbone angles should be considered in the sample to be analyzed. Additionally, incision angles close to 0^o or 90^o should be avoided because incorrect predictions can be obtained. Finally, the precision in the measurement of the 2D periodicity of the herringbone pattern is the most sensitive parameter. The domain structure of orthogonal plywoods, determined from simple sectioning and the four -step algorithm presented here, lies at the core of the structure-properties relations and its determination is crucial in further biological and biomimetic developments, such as in cornea-like tissues.

References (Chapter 6)

[1] Rey, A.D.; Herrera-Valencia, E.E. *Biopolymers*, 2012, **97**, 374.

[2] Rey, A.D. *Soft Matter*, 2010, **6**, 3402.

[3] Belamie, E.; Mosser, G.; Gobeaux, F.; Giraud-Guille, M. M. *Journal of Physics: Condensed Matter*, 2006, **18**, S115

[4] Li, L.Y.; Tighe, B. *Journal of Structural Biology*, 2006, **15**, 223.

[5] Risinger, A.; Pahr, D.; Zysset, P.K. *Proceedings of the Junior Scientist Conference*, 2010, **1**, 155.

[6] Eglin, D.; Mosser, G.; Giraud-Guille, M.M.; Livage, J.; Coradin, T. *Soft Matter*, 2005, **1**, 129.

[7] Giraud Guille, M.M.; Mosser, G.; Helary, C.; Eglin, D. *Micron*, 2005, **36**, 602.

[8] Fratzl, P.; Giraud-Guille, M.M.: *Hierarchy in Natural Materials.* Wiley-VCH Verlag GmbH & Co. KGaA, 2011, 29.

[9] Murugesan, Y.; Rey, A.D. *Polymers*, 2010, **2**, 766.

[10] Habibi, Y.; Lucia, L.A.; Rojas, O.J. *Chemical Reviews*, 2010, **110**, 3479.

[11] Bairati, A.; Garrone, R. *Biology of Invertebrate and Lower Vertebrate Collagen*. NATO ASI Series, 1984.

[12] Gobeaux, F.; Belamie, E.; Mosser, G.; Davidson, P.; Panine, P.; Giraud-Guille, M.M. *Langmuir*, 2007, **11**, 6411

[13] Sharma, V.; Crne, M.; Park, J.O.; Srinivasarao, M. *Science*, 2009, **325**, 449-451.

[14] Aguilar Gutierrez, O.F.; Rey, A.D. *Colloids Interface Sci. Commun*., 2014, **3**, 18-22

[15] Rofouie, P.; Pasini, D.; Rey, A.D. *Colloids Interface Sci. Commun*. 2014, **1**, 23.

[16] Rofouie, P.; Pasini, D.; Rey, A.D. *Chemical Physics*, 2015, **142**, 114701

[17] Philp, D.; Stoddart, J.F. *Angewandte Chemie International Edition in English*, 1996, **35**, 1154.

[18] Baessler, H.; Labes, M.M. *Molecular Crystals and Liquid Crystals*, 1969, **6**, 419.

[19] Libby, E.; Azofeifa, D E.; Hernández-Jiménez, M; Barboza-Aguilar, C.; Solís, A.; García-Aguilar, I.; Arce-Marenco, L.; Hernández, A.; Vargas, W E. *J. Opt.* 2014, **16**, 082001

[20] Bouligand, Y. *Tissue and Cell*, 1972, **4**, 189.

[21] Aguilar Gutierrez, O.F.; Rey, A.D., *Soft Matter*, 2014, **10**, 9446.

[22] Neville, A.C. *Biology of Fibrous Composites*. Cambridge University Press, 1993.

[23] Allahverdyan, K.; Galstian, T.; Gevorgyan, A.; Hakobyan, R. *Optics and Photonics Journal* 2013, **3**, 17-22

[24] Roland, J.C.; Reis, D.; Vian, B.; Satiat-Jeunemaitre B.; Mosiniak, M. *Protoplasma*, 1987, **140**, 75-91.

[25] Giraud-Guille, M.M.; Castanet, J.; Meunier, F.J.; Bouligand, Y. *Tissue and Cell*, 1978, **10**, 671.

[26] Wilson, S.L.; El Haj, A.J.; Yang, Y. *Journal of Functional Biomaterials*, 2012, **3**, 642.

[27] Campbell, F.C. *Structural Composite Materials*. ASM International, 2010.

[28] Ikoma, T.; Kobayashi, H.; Tanaka, J.; Walsh, D.; Mann, S. *Journal of Structural Biology*, 2003, **142**, 327.

[29] Fratzl, P. *Current Opinion in Colloid & Interface Science*, 2003, **8**, 32.

[30] Giraud Guille, M.M. *Calcified Tissue International*, 1988, 42, 167.

[31] De Sa Peixoto, P.; Deniset-Besseau, A.; Schmutz, M.; Anglo, A.; Illoul, C.; Schanne-Klein, M.C.; Mosser, G. *Soft Matter*, 2013, **9**, 11241.

[32] Weidinger, M.; Ruppel, H.G. *Protoplasma*, 1985, **124**, 187.

[33] Roland, J.C.: *Cell Walls '81: Proceedings of the Second Cell Wall Meeting* (D.G. Robinson and H. Quader, ed.). Wissenschaftliche Verlagsgesellschaft, 1981.

[34] Parameswaran, N.; Liese, W. *Holz als Roh und Werkstoff*, 1982, **40**, 144.

[35] Lepecheux, L. *Biology of the Cell*, 1988, **62**, 11.

[36] O'donnell. J.L. MSc. Thesis. University of Bristol, UK, 1992.

[37] Furneaux, P.J.S.; Mackay, A.L.: *The insect Integument* (H.R. Hepburn, ed.). Elsevier, 1976.

[38] Neville, A.C. *Biology of the arthropode cuticle*. Springer-Verlag, 1975.

[39] Simmons, P.H. MSc. Thesis. University of Bristol, UK, 1989.

[40] Ramachandran, P.; Varoquaux, G. *IEEE Computing in Science & Engineering*, 2011, **13**, 40.

7 Conclusions and Original Contributions to Knowledge

7.1 General Conclusions

The objective of this thesis is to contribute to the evolving understanding of non-equilibrium self-assembly processes used in the formation of defect-free collagen based films and the understanding of the morphology of biological and biomimetic plywoods. The understanding and characterization of the underlying processes and resulting material architectures can provide insights to improve current strategies and motivate the development of novel pathways. This thesis explored and revealed the underlying physics of a multi-stage process used to produce defect-free cholesteric collagen based films and the morphology of biological plywoods. A dynamic model based on well-established soft matter theory was developed for the first processing stage to produce new knowledge regarding the ordering and alignment of dilute collagen solutions under a wide variety of kinematic conditions. For the second stage, a fully-coupled order and mass transfer model was developed where the key aspects and parametric envelops for obtaining a defect-free material were identified. Validations of simulations and mechanisms were systematically implemented. By analyzing the morphology of the obtained architecture for this particular flow-drying process as well as others widely found in Nature a comprehensive description of characteristic patterns found in cross sections of the materials was provided using novel computational geometry methods. Taking advantage of such description, a methodology for structural characterization purposes was proposed and tested and its accuracy was demonstrated with actual biological samples. The following subsections highlight the main conclusions of each chapter in this thesis.

7.1.1 Theory and Simulation of Cholesteric Film Formation Flows of Dilute Collagen Solutions.

By using an integrated theory-experiment loop we presented simulations and scaling of key material properties of dilute isotropic collagen solutions, including the molecular shape parameter β and rotational diffusivity D_r. The obtained rotational diffusivity D_r has an order of magnitude consistent with reported values of other biomacromolecules and the estimated molecular shape parameter β was used to formulate the tumbling parameter function λ(S), which is a key quantity in the rheology of liquid crystalline materials. The key feature found for collagen solutions is that it is larger than one for $0 < S < 0.83$ and less than one when $0.83 < S < 1$; the former corresponds to dilute and the latter to concentrated solutions. The formulated λ(S) is consistent with experimental data on collagen solutions as it predicts flow-birefringence in the dilute regime and banded texture formation after cessation of flow in the concentrated regime, where the former is a signature of shear-induced orientation ($\lambda > 1$) and the latter of non-aligning or tumbling ($\lambda < 1$) under simple shear.

The nematodynamics model with the obtained properties was explored in terms of flow intensity (taken into account in the Deborah number) and flow kinematics κ, which is an index of the relative content of strain rate and vorticity rate. The key control variables found to convert the precursor para-nematic state into defect free cholesteric films are a surface alignment of the director field and an order parameter S corresponding to the value of a stable cholesteric state which were based on liquid crystal physics and observations from chiral film formation. This allowed us to enclose the optimal kinematic conditions (κ_{opt}, De_{opt}) to which the dilute solutions should be submitted to be considered as appropriate precursors for the later evaporation stage in the process of defect-free

film formation process. In such enclosed region a key component in the flow type is a larger strain over vorticity contribution. These results provide quantitative design parameters for flow-processing collagens into films for tissue engineering and other emerging biomimetic applications.

7.1.2 Biological Plywood Formation from Dilute Para-nematic Liquid Crystalline Phases

This chapter presented a rigorous and fully coupled model that captures the main features in the solvent removal process of defect-free collagen film formation process where the unstable para-nematic phase, with characteristics obtained in the previous chapter in the flow deposition stage, is converted to the cholesteric phase at constant temperature. The main features of the model are: i) the coupling of the **Q** tensor field with the solvent mass transfer through the variable nematic potential in the equation for **Q** and the anisotropic mass flux in terms of concentration gradients and **Q** and ii) the decrease in volume derived from the mesogen mass conservation. Three different modes in the resulting microstructure were found depending on the mass transfer resistances taken into account in the dimensionless number Π. Homogeneous helical formation occurs when the increase in the mesogen concentration is in synchronization with the initially forming helix from the edges due to the fast initial solvent depletion. Such synchronization is the crucial aspect for obtaining a defect-free material. The two other modes are observed in the resulting microstructure when the two phenomena are out of synchronization. A transition from monodomain to polygonal configuration is observed to happen when the increase in the mesogen concentration is behind the formation of the helix, and the width of the polygonal region is also dependent on the particular value of Π. A polydomain structure is obtained when the mesogen concentration increase is ahead of the forming helix. The particular and narrow range of values of the dimensionless number Π that lead to a homogeneous helical axis was provided. Finally, a process diagram for the formation

of a homogeneous helical axis is provided in terms of the combination of $D/6D_r$ as a function of the characteristic length-scale L and depending on the choice of solvent-mesogen properties of the pair a defect-free structure of length L can be formed.

7.1.3 Structure Characterisation Method for Ideal and non-Ideal Twisted Plywoods.

In this chapter the twisted plywood architecture model was revisited and extended to describe ideal and non-ideal structures arising from pitch gradients and multiple pitches. Based on the analytical description of the TPA (twisted plywood architecture) and with the aid of computational visualization software, a characterization tool is proposed which allows to reconstruct the 3D cholesteric structure of various plywoods from 2D arc-patterns obtained from experimental oblique incisions. This characterization procedure is an alternative characterization tool to optical measurements of the pitch which may be restricted to certain values of the cholesteric pitch p_o. The introduction and use of the curvature and its maximum value is the unique and novel feature of our extension. This characteristic variable of the observed arcs allows to remove the degree of freedom that exists given the fact that the periodicity of the arced patterns depends on both the incision angle and the pitch.

This proposed characterization tool can be implemented in ideal and non-ideal plywoods by taking into account commonly observed pitch variations in a systematic way. Since there is a wide variety in helical arrangements found experimentally, these effective 3D reconstruction computation and visualization tools can be easily extended and applied to any experimental observation of such biological plywoods including the orthogonal cornea-like plywood, the cylindrical plywood configuration, and other more sophisticated arrangements as the ones found in various cuticles.

7.1.4 Chiral Graded Structure in Biological Plywoods and in the Beetle Cuticle.

In this chapter, a structural material characterization procedure for biological plywoods that exhibit non-trivial spatial gradients was formulated by extending the previous geometric modeling and computational visualizations. In materials presenting a complex and sophisticated cholesteric pitch profile, this can be determined through the spatial periodicities and curvatures of 2D arc patterns in conjunction with a theoretically formulated plywood phase diagram given in terms of the periodicity of the arcs and the reciprocal curvature. Key aspects regarding the sensitivity of the method to sample sectioning were established and larger sectioning angles are preferred due to the ill-conditioning introduced when low incision angles are used. We demonstrated the applicability of the 3D chiral reconstruction method for graded plywoods using experimental pitch profile data for the "aurigans scarab" to create the in silico cross sections. The proposed characterization methodology complements optical characterization tools that must overcome the difficult challenge of chirality reconstruction. The new procedure has wide applications in biological materials characterization and in biomimetic engineering of structural and functional materials.

7.1.5 Geometric Reconstruction of Biological Orthogonal Plywoods

In this chapter, the important class of biological plywoods (arising due to frozen liquid crystalline organization) denominated the orthogonal plywoods, widely found throughout nature in collagen, cellulose and chitin-bases structures, were analyzed. Following the geometric model for ideal and non-ideal TPAs, a reconstruction method for the 3D structure of orthogonal plywoods based on the geometry of the 2D herringone patterns obtained by simple sectioning was developed, applied and validated. The reconstruction methodology showed good agreement with experimental observations taken from oblique incisions from the alga "Eremosphaera veridis" and in silico cross

sections with the visible herringbone patterns. It was found that in order to have accurate predictions of domain size, moderate herringbone angles should be considered in the sample to be analyzed. Additionally, incision angles close to 0^o or 90^o should be avoided because incorrect predictions can be obtained. Finally, it was shown the precision in the measurement of the 2D periodicity of the herringbone pattern is the most sensitive parameter. The domain structure of orthogonal plywoods, determined from simple sectioning and the four-step algorithm presented here, lies at the core of the structure-properties relations and its determination is crucial in further biological and biomimetic developments, such as in cornea-like tissues.

7.2 Original Contributions to knowledge.

The original contributions to knowledge resulting from this thesis are:

1. Material properties and effective molecular shape determination for collagenous acidic solutions used in the fabrication of defect-free collagens.

2. Robust methodology to determine the dynamic behavior and flow induced alignment character of dilute collagen solutions using a versatile 2D kinematics that allow to explore a wide variety of strain – vorticity contributions to the flow.

3. Phase plane of scalar order parameter (S) and director angle (θ) in terms of the kinematic parameter (κ) and Deborah number (De), providing the complete state of orientation of the para-nematic phase that precedes the collagen film drying process.

4. Region of kinematic conditions to which the dilute collagen solutions must be submitted to have the appropriate orientation and order to be considered as appropriate precursors to defect-free collagen films.

5. Robust methodology of a 2D self-assembly process taking into account a variable mesogen concentration and film shrinkage.

6. Determination of various modes existing in the drying of the films and the resulting microstructure in terms of the internal mass transfer resistance.

7. Determination of the appropriate conditions for a homogeneous helical axis of cholesteric collagen in the drying of the initially para-nematic phase.

8. Analytical description of the Bouligand structures (ideal and non-ideal) in terms of the 2D sectional periodicity (L) and the curvature of the arcs (κ) observed upon oblique sectioning.

9. Adaptation of the Mayavi visualization tool to produce in silico cross sections of the ideal, non-ideal and orthogonal plywoods.

10. Proposed methodology based on cross sections and the characteristic periodicity and curvature or herringbone aperture angle, depending on the particular case of the plywood, from the projected arced or herringbone patterns and validated through the in silico cross sections of the "aurigans scarab" cuticle and in vivo cross section of the "eremosphera viridis" algae species respectively.

Appendix A. Four Roll Mill Kinematic Analysis

In the work described in chapter 2 it is convenient to use the fixed four roll mill coordinate system denoted by **x** and a rotating system whose orientation depends on κ and is denoted by **x'**. This section contains the detailed derivation of the strain tensor **A'** in the rotating system of reference and the calculation of the eigenvalues and eigenvectors in the **x** and **x**' systems, and will provide a proof of the invariance of the principal axis of deformation direction that is employed in sections 2.5.1 and 2.5.2 to indicate the flow aligning nature of the mesogens. In the second part we derive the relations between the flow type and the invariants of the kinematic tensors in the four roll mill geometry.

A.1. Invariance of Eigenvectors.

From eqn. (2.1) we take the strain tensor **A** in the fixed system of reference **x** and obtain the following eigensystem (i.e. eigenvalues $\{\nu_i\}; i=1,2,3$ and eigenvectors $\{\boldsymbol{\xi}_i\}; i=1,2,3$):

$$\nu_1 = -\frac{E}{2}(1+\kappa); \nu_2 = \frac{E}{2}(1+\kappa); \nu_3 = 0 \qquad \text{(A.1 a, b)}$$
$$\boldsymbol{\xi_1} = \alpha_1(0,1,0); \boldsymbol{\xi_2} = \alpha_2(1,0,0); \boldsymbol{\xi_3} = \alpha_3(0,0,1)$$

where the α_i's are arbitrary constants. It is worth remarking the eigenvectors are constant, which is a consequence of **A** being a diagonal tensor, i.e. it is already written in its principal directions and coincide with the orthonormal triad $\boldsymbol{\delta_x}$, $\boldsymbol{\delta_y}$, $\boldsymbol{\delta_z}$ of the four roll geometry (see Fig. 2.3-g). For brevity we will drop the inessential third eigenvalue and concentrate in the non-zero ones. Let us introduce the rotation matrix $\mathbf{R_z}(\psi)$ that allows the system of reference (x, y) and the tensor **A** be rotated about the "z" axis whose rotation is given according to the flow type, i.e. the particular value of κ:

$$\mathbf{R}_z(\psi(\kappa)) = \begin{pmatrix} \cos\psi & -\sin\psi & 0 \\ \sin\psi & \cos\psi & 0 \\ 0 & 0 & 1 \end{pmatrix} \quad \text{(A.2 a, b)}$$

$$\psi = \tan^{-1}\left(\frac{-(1-\kappa)}{1+\kappa}\right)$$

Rotations are given according to the standard procedure:

$$\mathbf{x}' = \mathbf{R}_z(\kappa)\cdot\mathbf{x}$$

$$\mathbf{v}'(\kappa) = \mathbf{R}_z(\kappa)\cdot\mathbf{v}(\kappa) \qquad \text{(A.3 a, b, c)}$$

$$\mathbf{A}' = \mathbf{R}_z\cdot\mathbf{A}\cdot\mathbf{R}_z{}^T = \mathbf{R}_z\cdot\left(\frac{E}{2}\begin{pmatrix} 1+\kappa & 0 & 0 \\ 0 & -(1+\kappa) & 0 \\ 0 & 0 & 0 \end{pmatrix}\right)\cdot\mathbf{R}_z{}^T$$

leading to the following rotated quantities:

$$x' = x\cos\psi - y\sin\psi = \frac{x(1+\kappa)}{\sqrt{2(1+\kappa^2)}} + \frac{y(1-\kappa)}{\sqrt{2(1+\kappa^2)}}$$

$$y' = x\sin\psi + y\cos\psi = \frac{-x(1-\kappa)}{\sqrt{2(1+\kappa^2)}} + \frac{y(1+\kappa)}{\sqrt{2(1+\kappa^2)}} \quad \text{(A.4 a, b, c)}$$

$$\mathbf{A}' = \frac{E}{\kappa^2+1}\begin{pmatrix} (1+\kappa)\kappa & (1-\kappa)(\kappa+1)^2 & 0 \\ (1-\kappa)(\kappa+1)^2 & -(1+\kappa)\kappa & 0 \\ 0 & 0 & 0 \end{pmatrix}$$

The tensor **A'** is no longer diagonal and hence its eigenvectors are changed, but the eigenvalues remain the same and the relevant eigenvectors of **A'** are:

$$\boldsymbol{\xi}'_1 = \alpha_1'(-(1-\kappa),1+\kappa,0); \boldsymbol{\xi}'_2 = \alpha_2'(1+\kappa,1-\kappa,0) \quad \text{(A.5)}$$

Even though the eigenvectors change with the flow type, these vectors are referred with respect to the rotating system of reference and for any κ, they match with the fixed dyad (δ_x, δ_y) as will be shown in the following examples.

a) Pure elongational flow: The kinematic parameter takes the value of the unity and from eqn. (A.4 a-b) the x', y' remain the original fixed coordinates (x, y) and the eigenvectors from eqn. (A.5) reduce to $\boldsymbol{\xi'_1} = \alpha'_1(0,1,0)$ and $\boldsymbol{\xi'_2} = \alpha'_2(1,0,0)$ which are the eigenvectors in the fixed system or reference. This case is depicted in figure A.1a.

b) Simple shear flow: The kinematic parameter is zero and the x', y' system of reference is rotated counter-clockwise by 45° from eqn. A.2 b. For this case eqn. A.5 reduces to: $\boldsymbol{\xi'_1} = \alpha^{*'}_1(1,-1,0)$ and $\boldsymbol{\xi'_2} = \alpha'_2(1,1,0)$, where the relationship $\alpha^{*'}_1 = -\alpha'_1$ was applied given that the constants are arbitrary. In the rotated system of reference, the coordinates of the two eigenvectors in the rotated system of reference coincide again with the eigenvectors in the fixed system of reference. This case is depicted in figure A.1b.

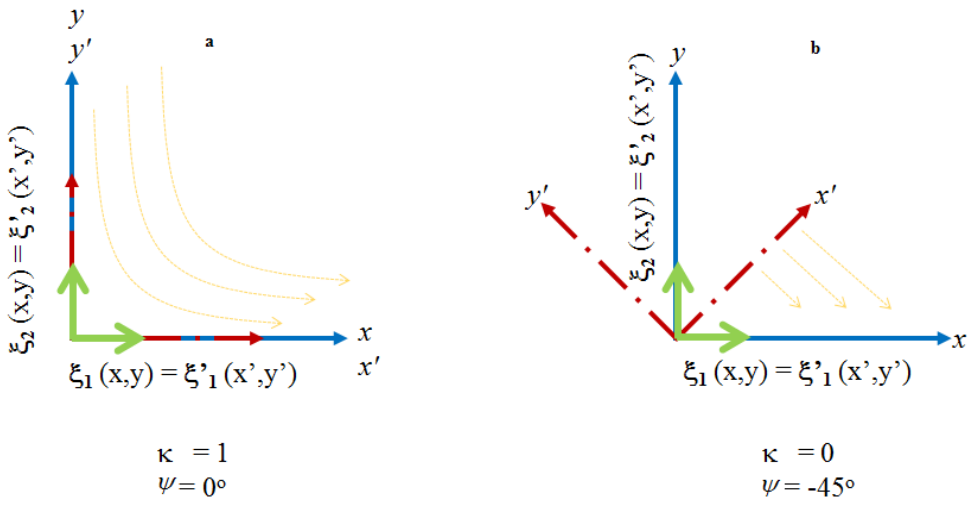

Figure A.1. Schematic of the fixed and rotated system of reference along with the eigenvectors for both systems in pure elongational flow (a) and simple shear flow (b). The blue arrows represent the fixed coordinate system, orange arrows represent the rotating coordinate system, yellow lines the direction of the flow and the green arrows the eigenvectors in either system of reference.

For any intermediate or negative value of κ, the eigenvectors will coincide independently of the system of reference, which indicates the principal axis of deformation are indifferent objects.

The importance of these results is that the flow aligning nature of mesogens in the generalized 2D flows whose direction change according to the kinematic parameter can be discussed with respect to these invariant directions (more specifically the fixed x direction) which is the direction of the extension according to figure 2.3g and as discussed in section 2.4.3. The invariance of the deformation axis explains why the ellipsoids' orientation given in the master plot (figure 2.8) change for different flow types and highlights the orientation angle in this work is given between the particle orientation and this invariant quantity as emphasized in section 2.5.2

A.2. Flow Type κ and Kinematic Tensors' Invariants (A, W).

We now provide a definition of the kinematic parameter in terms of the invariants of the strain **A** and vorticity **W** tensors in the fixed **x** system of reference. Due to the form of **A** and **W** from eqn. 2.1, the only non-zero invariant of these tensors is the second invariant [1]:

$$II_{\mathbf{R}} = tr(\mathbf{R}\cdot\mathbf{R}) = \mathbf{R}:\mathbf{R} \quad \text{(A.6)}$$

According to the definition, the second invariant of **A** and **W** are:

$$II_{\mathbf{A}} = \mathbf{A}:\mathbf{A} = 2\left(\frac{E}{2}(1+\kappa)\right)^2$$
$$II_{\mathbf{W}} = \mathbf{W}:\mathbf{W} = 2\left(\frac{E}{2}(1-\kappa)\right)^2 \quad \text{(A.7 a, b)}$$

Solving for κ in both expressions, allows us to define two special ratios, one which leads to the definition of κ in terms of the invariants of both tensors and another that allows to measure the overall effect of strain and vorticity which will be used in Appendix B during the analysis of the uniaxial approach applied to the **Q**-tensor equations (eqn. 2.3 a in section 2.5.2):

$$\kappa = \frac{2}{E}\sqrt{\frac{\mathbf{A}:\mathbf{A}}{2}} - 1; \kappa = 1 - \frac{2}{E}\sqrt{\frac{\mathbf{W}:\mathbf{W}}{2}}$$

$$\frac{2}{E}\sqrt{\frac{\mathbf{A}:\mathbf{A}}{2}} - 1 = 1 - \frac{2}{E}\sqrt{\frac{\mathbf{W}:\mathbf{W}}{2}}$$

$$\sqrt{2}E = \sqrt{\mathbf{A}:\mathbf{A}} + \sqrt{\mathbf{W}:\mathbf{W}}$$

$$\sqrt{2}E\kappa = \sqrt{\mathbf{A}:\mathbf{A}} - \sqrt{\mathbf{W}:\mathbf{W}}$$

$$\kappa = \frac{strain - vorticity}{strain + vorticity} = \frac{\sqrt{\mathbf{A}:\mathbf{A}} - \sqrt{\mathbf{W}:\mathbf{W}}}{\sqrt{\mathbf{A}:\mathbf{A}} + \sqrt{\mathbf{W}:\mathbf{W}}} = \frac{\sqrt{II_{\mathbf{A}}} - \sqrt{II_{\mathbf{W}}}}{\sqrt{II_{\mathbf{A}}} + \sqrt{II_{\mathbf{W}}}} \text{ (A.8 a – i)}$$

$$(1-\kappa)\frac{E}{2}\sqrt{2} = \sqrt{\mathbf{W}:\mathbf{W}}$$

$$(1+\kappa)\frac{E}{2}\sqrt{2} = \sqrt{\mathbf{A}:\mathbf{A}}$$

$$\Xi = \frac{Strain}{Vorticity} = \frac{\sqrt{\mathbf{A}:\mathbf{A}}}{\sqrt{\mathbf{W}:\mathbf{W}}} = \frac{\sqrt{II_{\mathbf{A}}}}{\sqrt{II_{\mathbf{W}}}} = \frac{(1+\kappa)}{(1-\kappa)}$$

Equation (A.8f) reveals explicitly the nature of the flow type, shown in Fig 2.3 a-f. Equations (A.8h, 12.c) indicate that the formation of the PN phase (Fig. 2-a) is influenced by effective strain to vorticity ratio $\Xi = (1+\kappa)/(1-\kappa)$.

Appendix B. Theoretical Background of Chiral Mesogens' Dynamic Behavior and Derivation of Nematodynamics Equations

B.1. Dynamic Description of Chiral Mesogens under Flow

Similar behavior between collagen solutions and lyotropic liquid crystalline polymers has already been mentioned in chapter 2. It is worth noting that other biomacromolecules used to fabricate highly ordered and structured materials have also been reported to present liquid crystalline polymer-like behavior such as chitin and cellulose [2 – 6], nonetheless these materials are outside the scope of this work. Hence, one may expect from these materials to exhibit similar behavior as LCP; each with its associated dynamic properties such as β and D_r; with the peculiarity that the chiral terms introduce additional phenomena when these are relevant as will be described in this section. In general terms, flow processes in chiral anisotropic materials can be described through the paradigm depicted in figure B.1, adapted from the general nematodynamics scheme provided in [7, 8]. The velocity and microstructure dynamics are coupled in a two-fold closed loop: on the left side, shear and extensional deformation rates create average orientation and molecular order in the system, known as flow-induced orientations and order (FIOO) or simply flow-induced alignment (FIA) and on the other the equally important but less explored orientation-induced flow OIF, which includes phenomena such as back-flow, hydrodynamic interactions present in defect-defect annihilation or in helix uncoiling - recoiling for chiral mesogens. Depending on the concentration of the solution, the behavior in both FIA and OIF can be drastically different. In the former FIA (left side of Figure B.1), when the nematic potential is below the phase transition value (i.e. $U < U^*$, where U is a dimensionless concentration) the stable isotropic state is transformed into a para-nematic phase as in flow birefringence experiments in [9] which is the main focus of

this work, whereas in the opposite scenario (i.e. U > U*) a stable chiral nematic state might undergo additional complex flow-induced phenomena associated to the helix dynamics such as uncoiling, rigid body rotations and/or tumbling behavior [10] depending on the shear rate as studied in [11] using a hybrid Rheo-NMR technique. In OIF (right side of Figure B.1), which is beyond the scope of this chapter, the high concentration regime might exhibit defect-defect hydrodynamics, back-flow, helix recoiling, whilst the low concentration regime may exhibit weak isotropic back-flow in the relaxation of a dynamically aligned para-nematic phase [7, 8].

Two different scales have been used to describe nematodynamics where the first corresponds to a macroscopic scale that takes into account a linear momentum balance coupled with the dynamics of the director **n** field [12 – 14]. At this level, the description of the material is restricted to the interaction between hydrodynamics and the orientation of the material and the scalar order parameter S dynamics are not considered but assumed to remain close to equilibrium value S_{eq}. The characteristic that makes cholesterics different to their achiral counterpart is the presence of the cholesteric helix axis **h** and associated periodicity p_o, with unique phenomena occurring depending on the relative orientation of the helix **h** and the flow direction **v** [10].

Some of these phenomena have been analyzed in the past at this director level such as the flow aligning nature in cholesterics under simple shear when the helix is initially in the vorticity direction [15]. The flow alignment can occur as a travelling wave phenomena when the no anchoring BC is used and as an elastic boundary layer contraction when the orientation is fixed [16], and in addition the tumbling behavior was characterized as a different type of travelling wave phenomenon [15]. When the helix is aligned in the direction of the flow, highly viscous permeation flows are likely to occur which have been described with a unified approach in [17] by including the divergence of the elastic stresses in the linear momentum equation in terms of the viscous

torques allowing a general permeation kinematic description as opposed to the classical flow in a capillary. This director level of description has elucidated some basic principles regarding cholesteric materials [10, 15 – 17]. Nonetheless, producing ordered and oriented collagen materials from isotropic precursors require the description of both orientation and ordering which can be achieved through a mesoscopic model that takes into account the dynamics of a quadrupolar tensor order parameter (**Q**) [12]. This mesoscopic level has been widely used for achiral mesogens [14, 18] to capture complex phenomena such as defect nucleation, shear thinning behavior and sign-changes in the first normal stress difference [19] and analysis under generalized linear flows [20] and has been applied to describe qualitatively biological processes involving chiral building blocks [7 – 8]; however flow processes of chiral systems have not been rigorously and extensively studied nor quantified compared to their achiral counterparts. The specific model used here, able to capture the processes discussed in conjunction with Figure B.1, is detailed in section B.2.

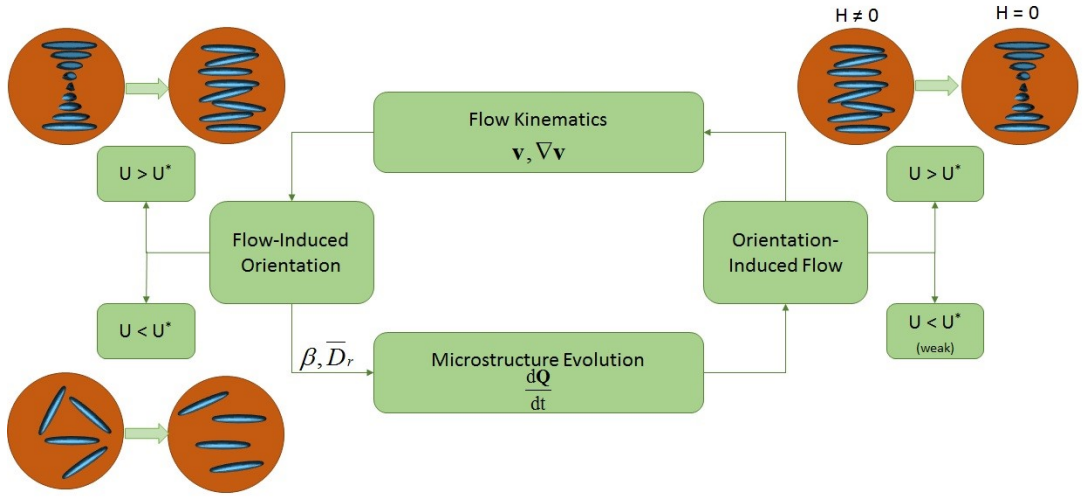

Figure B1. Flow processes' paradigm for chiral mesogens [7], consisting of a coupled loop between flow induced orientation (FIO) on the left and orientation-induced flow (OIF) on the right. The flow kinematics (**v**:velocity) is coupled to the structure velocity d**Q**/dt, where **Q** is the tensor order parameter. The effect of flow on structural changes, and conversely the effect of structure changes on velocity are strongly dependent on concentration U, where U* is the critical phase ordering value. At U>U*, FIO includes helix uncoiling (top left) and at U<U*, we find flow-birefringence. These effects depended on the molecular shape parameter β and rotational diffusivity $\bar{D}_r$ (eqn.(2.4c) shows the difference between $\bar{D}_r$ and D_r). At U>U*, OIF includes flow created by helix re-coiling (top right) after turning off an external field H (in this chapter H is a flow field). At U<U*, OIF will be more weak and isotropic (lower right).

B.2. Mathematical Derivation of the Nematodynamics Equation

The equations of nematodynamics are derived starting with the formulation entropy production function Δ which includes the conventional viscous effects and dissipation due to the rotations of **Q** with respect to the background fluid [19, 21, 22]:

$$\Delta = \mathbf{t}^s : \mathbf{A} + ck_B T\mathbf{H} : \hat{\mathbf{Q}} \quad \text{(B.1)}$$

where **H** is the molecular field, $\mathbf{t}^s$ the symmetric stress tensor with viscous and elastic parts, $\hat{\mathbf{Q}}$ the Jaumann derivative of **Q**, c the number of molecules per unit volume, k_B the Boltzmann constant and T the absolute temperature. The evolution of **Q** is found by expanding the fluxes $\left(\mathbf{t}^s, \hat{\mathbf{Q}}\right)$ in terms of forces $\left(\mathbf{A}, ck_B T\mathbf{H}\right)$ and the result is:

$$\hat{\mathbf{Q}} = -\frac{6\bar{D}r}{ck_B T}\left[\frac{\delta F}{\delta \mathbf{Q}}\right]^{[s]} + \mathbf{F}; \hat{\mathbf{Q}} = \frac{D\hat{\mathbf{Q}}}{Dt} + \mathbf{W}\cdot\mathbf{Q} - \mathbf{Q}\cdot\mathbf{W}$$

$$\mathbf{F} = \frac{2}{3}\beta\mathbf{A} + \beta\left[\mathbf{A}\cdot\mathbf{Q} + \mathbf{Q}\cdot\mathbf{A} - \frac{2}{3}\left(\mathbf{A}:\mathbf{Q}\right)\mathbf{I}\right] -$$

$$\frac{\beta}{2}\left[\left(\mathbf{A}:\mathbf{Q}\right)\mathbf{Q} + \mathbf{A}\cdot\mathbf{Q}\cdot\mathbf{Q} + \mathbf{Q}\cdot\mathbf{A}\cdot\mathbf{Q} + \mathbf{Q}\cdot\mathbf{Q}\cdot\mathbf{A} - \left[\left(\mathbf{Q}\cdot\mathbf{Q}\right):\mathbf{A}\right]\mathbf{I}\right] \quad \text{(B.2 a-c)}$$

$$F = \int f dV; \frac{f}{ck_B T} = \frac{1}{2}\left(1 - \frac{U}{3}\right)\mathbf{Q}:\mathbf{Q} - \frac{U}{3}\mathbf{Q}:\left(\mathbf{Q}\cdot\mathbf{Q}\right) + \frac{U}{4}\left(\mathbf{Q}:\mathbf{Q}\right)^2 +$$

$$\frac{L_1}{2ck_B T}\left[\nabla\times\mathbf{Q} + \frac{4\pi}{p_o}\mathbf{Q}\right]^2 + \frac{L_2}{2ck_B T}\left[\nabla\cdot\mathbf{Q}\right]^2$$

where the superscript [s] represents symmetric traceless tensor, $\bar{D}_r$ is the **Q**-dependent rotational diffusivity, β the above-mentioned rheological shape parameter, $\mathbf{A} = \frac{1}{2}\left(\nabla\mathbf{u} + \nabla\mathbf{u}^T\right)$ and $\mathbf{W} = \frac{1}{2}\left(\nabla\mathbf{u} - \nabla\mathbf{u}^T\right)$ are the symmetric and antisymmetric parts of the velocity gradient tensor

respectively, U the nematic potential, L_1 and L_2 elastic constants associated to the chirality and other modes of deformation, respectively and p_o the cholesteric pitch. Two essential components of this equation are the cholesteric free energy density $f\left(\mathbf{Q},\nabla\mathbf{Q}\right)$ and the applied kinematics appearing in **F**. The former is taken from [23], where equilibrium self-assembly of chiral mesogens is explored. The free energy includes a Landau expansion in terms of even powers of the invariants of **Q** and the elastic energy that penalizes deviations from the cholesteric order (L_1), and splay-bend-twist distortions (L_2). The flow contribution **F** considers the couplings between the symmetric **A** part of the velocity gradient and the **Q** tensor.

Appendix C. Uniaxial Approach Analysis

We now provide the mathematical details of the uniaxial approach used to analyse eqn. 2.6a where the equations are written in terms of the scalar order parameter S and the director angle θ. At the end it also combines the parameter Ξ (eqn. (A8.h)) that encapsulates the effect of strain over vorticity in terms of the invariants of **A** and **W** , and which is a function of κ.

The uniaxial approach consists in assuming the biaxiality is negligible (see Figure 2.4 which supports this assumption where the biaxiality order parameter is plotted as a function of De) which reduces the **Q**-tensor to the following:

$$\mathbf{Q}(t) = S(t)\left(\mathbf{n}(\theta(t))\mathbf{n}(\theta(t)) - \frac{\mathbf{I}}{3}\right); \mathbf{n}(\theta(t)) = (\cos\theta(t), \sin\theta(t), 0) \quad \text{(C.1)}$$

When eqn. C.1 is introduced in eqns. 2.3a and after carrying out the appropriate tensor operations, two coupled scalar nonlinear ordinary differential equations equations can be extracted, one for the scalar order parameter and one for the director angle:

$$\frac{\partial S}{\partial t} = \frac{1}{\left(-1+S^2\right)^2}\left(\frac{2}{3}US^3 - \frac{U}{3}S^2 + \left(1 - \frac{U}{3} - \frac{48\pi^2}{R}\right)S\right) + De\frac{\beta}{8}(\kappa+1)\cos(2\theta)\left(5S^2 - 4S + 4\right)$$
$$\frac{\partial \theta}{\partial t} = -\frac{De}{2}\left((1-\kappa) + \sin(2\theta)\beta\frac{\left(4+2S-S^2\right)}{6S(\kappa+1)}\right) \quad \text{(C.2 a, b)}$$

The steady-state solutions lead to the following relationships:

$$\sin 2\theta = \frac{-6S(1-\kappa)}{\beta\left(4+2S-S^2\right)(1+\kappa)}$$

$$\cos 2\theta = \frac{8\left(2US^3 - US^2 + (3-U-144\pi^2/R)S\right)}{9\beta De(1+\kappa)\left(4+4S-5S^2\right)\left(-1+S^2\right)^2} \qquad \text{(C.3 a, b, c)}$$

$$\frac{1}{\lambda^2}\left[\frac{(1-\kappa)}{(1+\kappa)}\right]^2 + \frac{64}{9}\left[\frac{\left(2US^3 - US^2 + (3-U-144\pi^2/R)S\right)}{\beta De(1+\kappa)\left(4+4S-5S^2\right)\left(-1+S^2\right)^2}\right]^2 = 1$$

By assuming $\kappa = 0$, eqns. (C.3 a – b) reduce to eqns. 2.9 a, b. Let us analyze the particular cases for pure vortex flow ($\kappa = -1$) and pure elongational flow ($\kappa = 1$), that shed light on the results shown in Figures 2.7 a-b and Table 2.2.

a) $\kappa = -1$

In this case, to avoid the singularity, it is convenient to multiply eqn. C.3c by $(1+\kappa)^2$:

$$\frac{4}{\lambda^2} + \frac{64}{9}\left[\frac{\left(2US^3 - US^2 + (3-U-144\pi^2/R)S\right)}{\beta De\left(4+4S-5S^2\right)\left(-1+S^2\right)^2}\right]^2 = 0 \quad \text{(C.4)}$$

For the case of low De, the resulting equation is dominated by the cosine term yielding:

$$\left(2US^3 - US^2 + (3-U-144\pi^2/R)S\right) = 0$$
$$\cos 2\theta = 0 \qquad \text{(C.5)}$$

This indicates the steady-state value of S is given by the stable thermodynamic root of the free energy, which for the case analyzed of dilute collagen solutions is the isotropic value S = 0, meanwhile the angle remains at -45° (see Fig. 2.7b). For the case of high De, the reactive parameter term dominates which yields the following relationship:

$$\frac{6S}{\beta\left(4+2S-1S^2\right)}=0 \quad \text{(C.6)}$$

This indicates the isotropic state (S = 0) is the steady-state solution for high De conditions under pure vortex flow which means the mesogens in dilute solutions do not achieve any order when submitted to these flow conditions and would coincide with the horizontal line from figure 2.8.

b) $\kappa = 1$

For the pure elongational flow, eqn. C.3a leads to the following condition valid for all De:

$$\sin 2\theta = 0 \quad \text{(C.7)}$$

This demonstrates the strong aligning character of elongational flows, where the orientation of the mesogens is parallel to the x-direction of the four roll geometry (Fig.2.3g) for all flow strengths. To analyze the order in such direction, Eqn C.3c reduces to:

$$\left(2US^3-US^2+(3-U-144\pi^2/R)S\right)-\beta De\left(4+4S-5S^2\right)\left(-1+S^2\right)^2=0 \quad \text{(C.8)}$$

Low De shows S tends to its thermodynamic root (i.e. S = 0) (Fig 2.7a). For moderate De the roots of full polynomial (C.6) must be evaluated and the resulting value of the scalar order parameter S depend on β, De and R. Under high De, the second term on the left-hand side of eqn. (C.8) dominates and the only physically significant root of the resulting polynomial is S = 1 as can be seen in fig. 2.7a.

Finally, we can combine eqn. A.8h from appendix A.1 with eqn. C.3c. This eases the analysis allowing to separate the components of flow induced alignment (FIO) into the material properties, flow induced order and the kinematic contribution:

$$\sin 2\theta = -\frac{6S(1-\kappa)}{\beta\left(4+2S-S^2\right)(1+\kappa)} = -\frac{1}{\lambda}\times\frac{1}{\Xi} = \frac{1}{\lambda\times\dfrac{strain}{vorticity}} = -\frac{1}{\beta}\times\frac{6S}{\left(4+2S-S^2\right)}\times\frac{1}{\Xi}$$

$$\underset{FIO}{\sin 2\theta} = \underbrace{-\frac{1}{\beta}}_{\substack{material\\property}} \times \underbrace{\frac{6S}{(4+2S-S^2)}}_{flow-induced\ order} \times \underbrace{\frac{1}{\Xi}}_{kinematic\ ratio} \qquad \text{(C.9 a, b)}$$

The flow induced orientation FIO can be better explored in terms of the kinematic parameter as follows in terms of the director angle θ:

$$FIO = f(\text{material property, flow-induced order, kinematic ratio})$$

$$(i) extension: \Xi \to \infty, \lambda > 1$$

$$\sin 2\theta = \lim_{\Xi\to\infty} \frac{1}{\Xi\lambda} = 0$$

$$(ii) simpleshear: \Xi = 1, \lambda > 1 \qquad \text{(C.10)}$$

$$\sin 2\theta = \frac{1}{\lambda}$$

$$(iii) vortex: \Xi = 0; \lambda \to \infty$$

$$\theta: undefined$$

To summarize the results regarding the state of orientation, eqn. C.3c written in terms of Ξ leads to the equation of a unit circle plotted in figure C.1:

$$\frac{1}{\lambda^2\Xi^2} + \frac{64}{9}\left[\frac{\left(2US^3 - US^2 + (3-U-144\pi^2/R)S\right)}{\beta De(1+\kappa)\left(4+4S-5S^2\right)\left(-1+S^2\right)^2}\right]^2 = 1$$

$$x^2 + y^2 = 1; x = \frac{8\left(2US^3 - US^2 + (3-U-144\pi^2/R)S\right)}{3\beta De(1+\kappa)\left(4+4S-5S^2\right)\left(-1+S^2\right)^2}; y = \frac{1}{\lambda\Xi} \qquad \text{(C.11 a, b)}$$

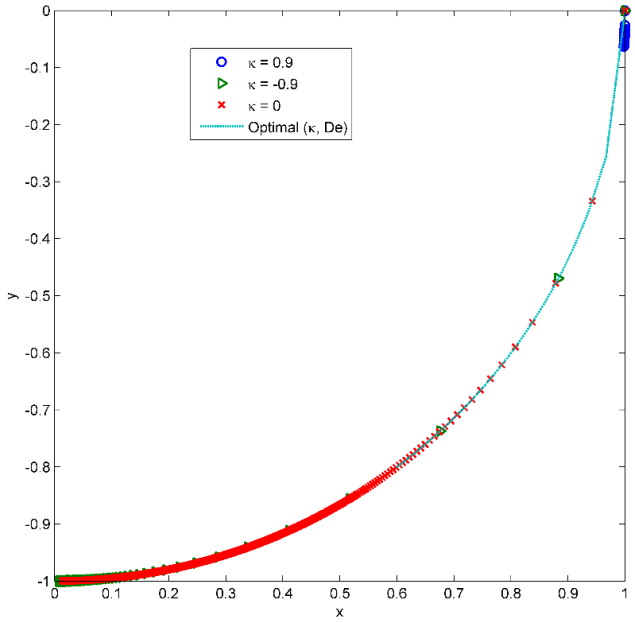

Figure C.1. Unit circle defined by eqn. C.11a where flows with high vorticity contribution are concentrated in the lower part (green markers), flows with high strain are concentrated in the upper part (blue markers) and flows similar to simple shear in the intermediate region (red markers) and optimal processing conditions (cyan line) see section 2.5.2 .

Comparing Figure C.1 with Table 2.2 and Figures 2.7 a-b and 2.8 we see that all flow types and strengths can be summarized and represented around a unitary circumference with all the components affecting the complete state of orientation of the mesogens i.e. λ, Ξ, β, κ, De, U and R. In particular high vorticity tends to minimize $\sin 2\theta$ and maximize $\cos 2\theta$, and high strain tends to maximize $\sin 2\theta$ and minimize $\cos 2\theta$. Shear flow can approximate these limits only by using the flow strength i.e. is close to the region of pure strain with low De, however this implies low order (S) and the region of pure vortex with high De, but in this case it implies high order with orientation of -45º, as shown in Fig. 7 a-b. It is worth mentioning the optimal processing conditions are also included in this circumference and is depicted in figure C.1 as the cyan line which is closer to the maximized region of $\sin 2\theta$.

Appendix D

This appendix presents mathematical details for the derivation of the integrated phase ordering-mass transfer model based on the Landau-de Gennes **Q**-tensor theory and the anisotropic mass diffusion equation in time-dependent geometry. The mathematical description of liquid crystals used in this paper is at the mesoscopic scale and is written in terms of the second moment of an orientation distribution function (ODF) which is the definition of the **Q** tensor as expressed in eqn. (D.1 a-b):

$$\mathbf{Q} = \int \left(\mathbf{uu} - \mathbf{I}/3\right)\rho(\mathbf{u})d^2\mathbf{u}; \mathbf{Q} = \mathbf{Q}^T; tr(\mathbf{Q}) = 0$$
$$\mathbf{Q} = S\left(\mathbf{nn} - \frac{\mathbf{I}}{3}\right) + P\left(\mathbf{mm} - \mathbf{ll}\right) \qquad \text{(D.1 a-b)}$$

This symmetric and traceless tensor can be parameterized in terms of the director triad vectors **n, m, l** and two scalar order parameters (S,P) that result from a linear combination of the eigenvalues **Q**. The unit vector **n** is known as the director or average orientation and S is known as the uniaxial scalar order parameter. From equation (D.1a) we find: $\mathbf{Q}:\mathbf{nn} = 2S/3; \mathbf{Q}\cdot\mathbf{n} = 2S\mathbf{n}/3$. Specific components of **Q** such as Q_{xx} are found from: $Q_{xx} = \mathbf{Q}:\boldsymbol{\delta}_x\boldsymbol{\delta}_x; \boldsymbol{\delta}_x\cdot\boldsymbol{\delta}_x = 1$. Likewise n_x is found from

$n_x = 3\mathbf{Q}:\mathbf{n}\boldsymbol{\delta}_x/2S$.

The total free energy density f can be expressed as the sum of the homogeneous contribution which is a Landau expansion in terms of appropriate invariants of **Q** and proportional to the so-called nematic potential U. This nematic potential U is a dimensionless concentration with respect to the critical phase transition volume fraction. The second contribution to the free energy is known as the elastic free energy from modes of deformation, each associated to an elastic constant L_i. For

chiral mesogens we consider two terms, one related to the twist deformation and intrinsic chirality associated to L_1 and the second encompassing other common modes of deformation and are associated to L_2. The total free energy F is given in eqn. (D.2 b):

$$F = \int_V f dV; \frac{f}{ck_BT} = \frac{1}{2}\left(1-\frac{U}{3}\right)\mathbf{Q}:\mathbf{Q} - \frac{U}{3}(\mathbf{Q}\cdot\mathbf{Q}):\mathbf{Q} + \frac{U}{4}(\mathbf{Q}:\mathbf{Q})^2 + \frac{L_1}{2ck_BT}\left[\nabla\times\mathbf{Q} + \frac{4\pi}{p_o}\mathbf{Q}\right]^2 + \frac{L_2}{2ck_BT}[\nabla\cdot\mathbf{Q}]^2 \quad \text{(D.2 a-b)}$$

where F is the total free energy and f the free energy density. The evolution drives the system to the minimum energy given the initial configuration and a given set of boundary constraints. Given the fact the **Q** tensor is not a conservative field, it follows the Langevin-type dynamics where the time derivative of **Q** is proportional to the so-called molecular field, which is the functional derivative of the total free energy with respect to variations in **Q**: $\left[\delta F/\delta\mathbf{Q}\right]^{[s]}$, where [s] denotes symmetric and traceless. The pre-factor corresponds to the mobility as expressed in eqn. (D.3 a):

$$\frac{\partial\mathbf{Q}}{\partial t} = -\frac{6D_r}{ck_BT\left(1-\frac{3}{2}\mathbf{Q}:\mathbf{Q}\right)^2}\left[\frac{\delta F}{\delta\mathbf{Q}}\right]^{[s]}; [\mathbf{M}]^{[s]} = \frac{1}{2}\left(\mathbf{M}+\mathbf{M}^T-\frac{2}{3}tr(\mathbf{M})\right) \quad \text{(D.3 a-b)}$$

where D_r is the rotational diffusivity (with reciprocal time dimension i.e. [=] 1/time), c the number of molecules per unit volume, k_B the Boltzmann constant, T the absolute temperature. The distinguishing feature of the model derived for this paper is the variable nematic potential $U(\mathbf{x},t)$ which is a function of the solvent volume fraction $\varphi_w(\mathbf{x},t)$. Therefore the information resulting from changes in the mass transfer equation for the solvent φ_w are introduced to the $\mathbf{Q}(\mathbf{x},t)$ tensor dynamics through the nematic potential . On the other hand, the mass transfer equation for the solvent is written in terms of the divergence of the mass flux. We consider here an anisotropic

constitutive equation with an isotropic D_{iso} and anisotropic D_{ani} diffusivity constants. This anisotropic relationship include gradients in the solvent concentration and a bilinear function of **Q** and ∇c_w as expressed in eqn. (D.4 a-b):

$$\frac{\partial c_w}{\partial t} = -\nabla \cdot \mathbf{j}_w ; \mathbf{j}_w = -\left(D_{iso} \nabla c_w + D_{ani} \mathbf{Q} \cdot \nabla c_w \right);$$
$$D_{iso} = \frac{D_{\parallel} + 2D_{\perp}}{3}; D_{ani} = D_{\parallel} - D_{\perp} \qquad \text{(D.4 a-d)}$$

To derive the equation that takes into account the overall total volume reduction due to water loss from the system, we use the mesogen mass conservation within the film.

$$\frac{d}{dt}\int_{V(t)} c_c dV = 0; \rho_c \frac{d}{dt}\int_{V(t)} \varphi_c dV = 0$$
$$\int_{V(t)} \frac{\partial \varphi_c}{\partial t} dV + \int_{S(t)} \varphi_c \mathbf{v} \cdot \mathbf{k} dS = 0 \qquad \text{(D.5 a-c)}$$

where c_c is the mesogen mass concentration, **v** the velocity of the control volume and **k** the unit normal to the corresponding surface. The first term on eqn. (D.5 c) can be expressed in terms of the divergence of the flux of the solvent, which then can be transformed to an integral form by using Gauss' integral transformation. Such integral is then evaluated at the relevant surfaces and by making use of the cross-section average definition $\langle A(t) \rangle = \frac{\int_S A(\mathbf{x},t) dS}{\int_S dS}$ furnishes the equation for the film thickness h(t) (in the vertical direction):

$$\frac{dh}{dt} = \frac{2h(t)}{\rho_w L} \left\langle j_z^{wall}(t) \right\rangle \qquad \text{(D.6)}$$

The physical interpretation of eqn. (D.6) is given as follows: the rate of change of the film thickness is proportional to the flow of water leaving the film through the side boundaries of the geometry, however this flow depends on the order of magnitude of the average surface flux multiplied by its respective cross section which is being modified (it decreases) as the film shrinks vertically. The integrated phase ordering/mass transfer model in an evolving geometry is given by equations D.3-D.6 and is solved numerically using finite element methods as discussed in the paper. The number of differential equations are five partial differential equations for the **Q-**tensor, one partial differential equation for c_w, and one ordinary differential equation for h, for a total of seven differential equations.

Appendix E.

This appendix provides details regarding the particular values of the nematic potential U and its impact on the homogeneous free energy. When the homogeneous free energy is expressed in terms of the scalar order parameter S, the particular value of U provides with the shape to the function and hence indicate the stable thermodynamic state in terms of S. For collagen solution p_o has a small effect on stability thresholds and is not discussed here; see [7]. The isotropic state is stable when U is low and the free energy has only one minimum. Increases in U change the shape of the free energy and a second minimum is obtained yet of higher energy than the isotropic state. The particular value where the second minimum appears is $U^{**} = 8/3$. Further increases in U lead to a stable ordered state when the second minimum is a lower energy state and the range between 8/3 and 2.7 corresponds to local metastable state and the upper bound is denoted as U_{IC} and indicates both minima have the same energy, thus both states: the disordered and ordered are stable. Higher values indicate the ordered state is the stable state and the concentration denominated as U* is the metastable limit. These values are depicted in figure E1.

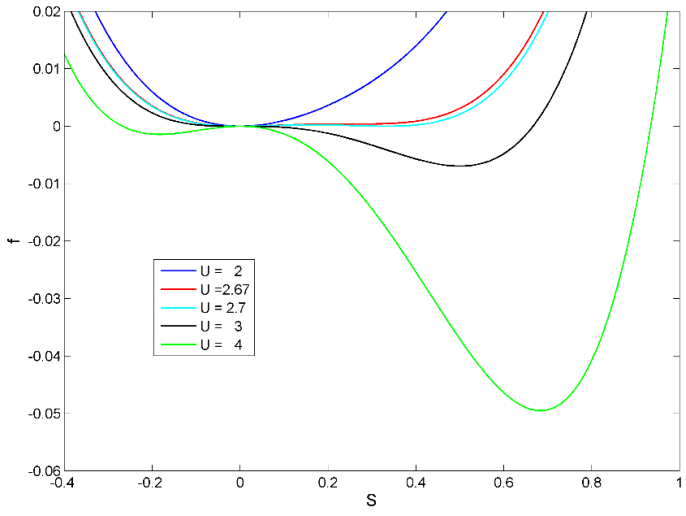

Figure E1. Homogeneous free energy as a function of the scalar order parameter for varying nematic potential U.

Appendix F.

This appendix presents additional plots and surface plots to support the discussion in section 3.6. We first present a detailed figure where the height of the film is plotted as a function of time in figure F1 for varying Π as indicated in the legend.

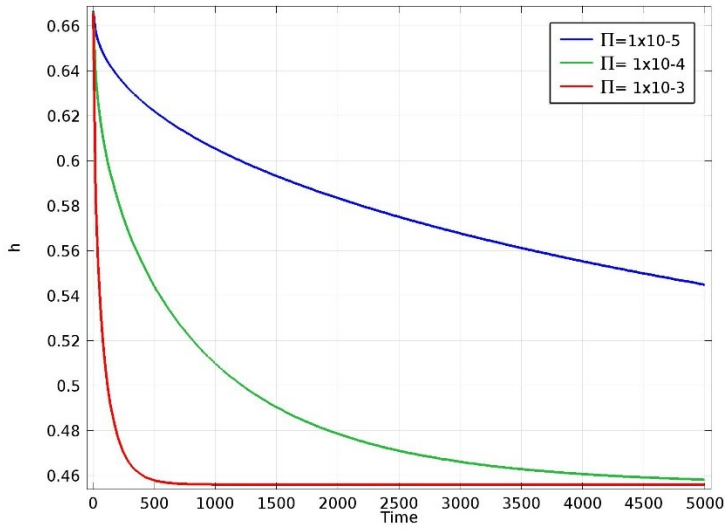

Figure F1. Film height as a function of time as the film dries.

The figure shows that the exponential decay of h(t) increases its rate as the time scale ratio Π increases. The intermediate green curve corresponds to the synchronized phase ordering-water removal mode that yield a defect-free film. The lower (blue curve) and faster (red curve) decays lead to cellular patterns and polydomain patterns, respectively.

Next we discuss the film patterns in the three regimes: monodomain, monodomain-cellular, and polydomain modes. To elucidate the underlying mechanisms it is best to use different quantities related to the **Q**-tensor (phase ordering) and choose the scalar order parameter S(y,z,t), and $Q_{xx}(y,z,t)$, $=\mathbf{Q}:\boldsymbol{\delta}_x\boldsymbol{\delta}_x$. For the water removal rate and thermodynamic transitions we use the mesogen dimensionless concentration U(y,z,t) and the two non-zero components of the mass flux vector

J(y,z,t). We wish to show evidence that when the time scale ratio is lower $\Pi < \Pi^*$ or higher $\Pi > \Pi^*$ than the critical value $\Pi^* \sim O(10^{-4})$, a perfectly aligned helix does not emerge, simply because the water withdrawal rate is either too slow (monodomain-cellular mode) or too fast (polydomain mode), in qualitative agreement with experiments.

(i) Monodomain Transition Mode ($\Pi^*=10^{-4}$)

Figure F2 shows the surface plots of S and $|n_x|$ for increasing times as indicated in figure 3.4 and the curves shown in figure 3.5 are extracted from the presented surfaces at the halved height of the computational domain. The upper figures F2 show a planar stable phase ordering front and a decrease in h. The bottom figures F2 show that the director remains aligned in the interior and that it is compatible with the helical front moving from the edges towards the interior.

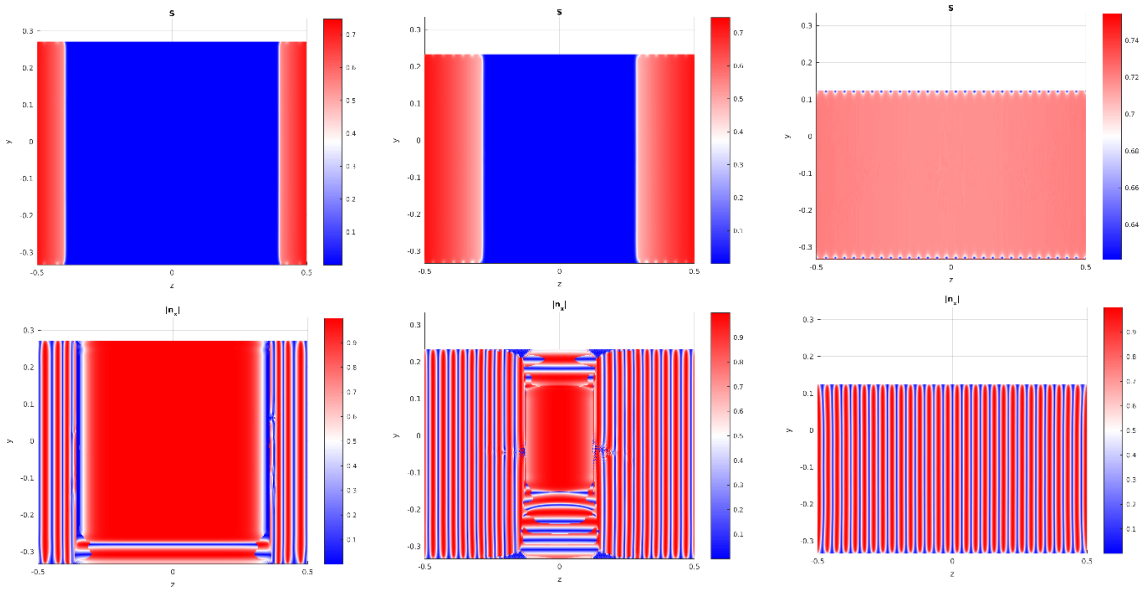

Figure F2. Scalar order parameter S (a-c) and out of plane component of the director n_x (d-f) for increasing times as indicated in figure 3.5, showing a relaxation of S in regions where the stability threshold (U=3) has not been reached but the para-nematic director persists leading to a homogeneous helical axis. Mondomain mode for $\Pi = \Pi^*=10^{-4}$.

(ii) Monodomain-Cellular Mode ($\Pi<\Pi^*=10^{-4}$)

Figure F3 shows the surface plots of the microstructure in terms of Q_{xx} and the change in the mesogen concentration U for increasing times as indicated in figure 3.6. These surface plots show the appearance of the cellular zone due to the presence of a presence of a pre-cholesteric state close to the central region as observed in figure 3.6.

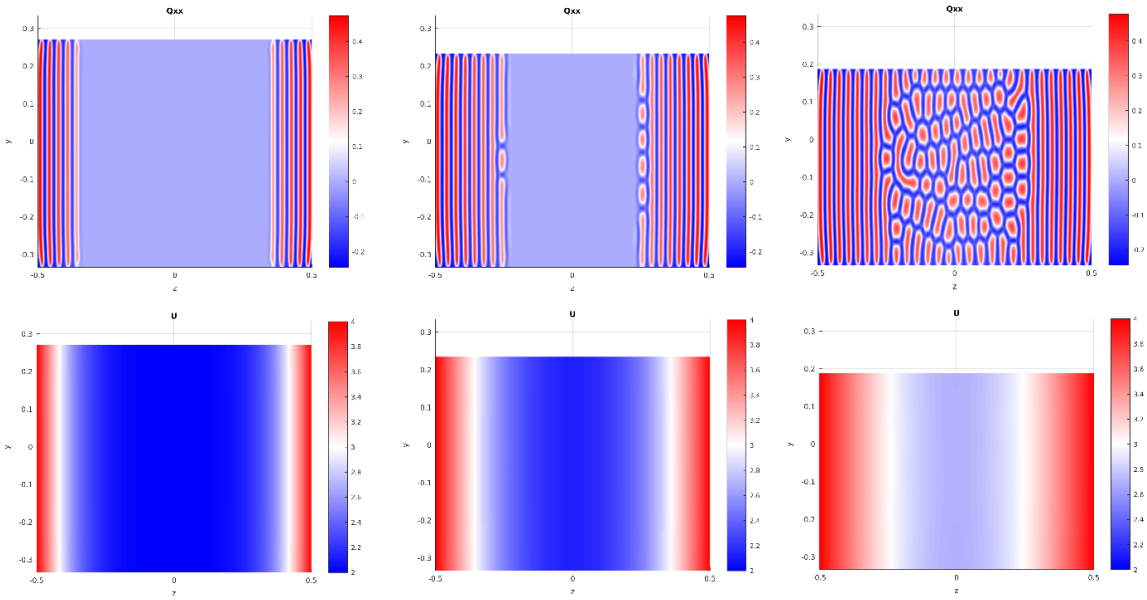

Figure F3. Q_{xx} surface plot in terms of the spatial coordinates y-z (a-c) for increasing times ($t^* = 1000, 3000, 8000$) in the simulations and the nematic potential U (d-e) for the same times for $\Pi = 1\text{x}10^{-5}$ showing a homogeneous helical axis forming from the edge toward the central region of the cross section.

(iii) Polydomain Mode ($\Pi>\Pi^*=10^{-4}$)

Figure F4 are analogue surface plots to figure F3 for $\Pi = 10^{-3}$ and shows the inhomogeneity in the helix formation due to fast diffusion. The curves associated to the presented microstructure and mesogen concentration surfaces are presented in figure 3.7.

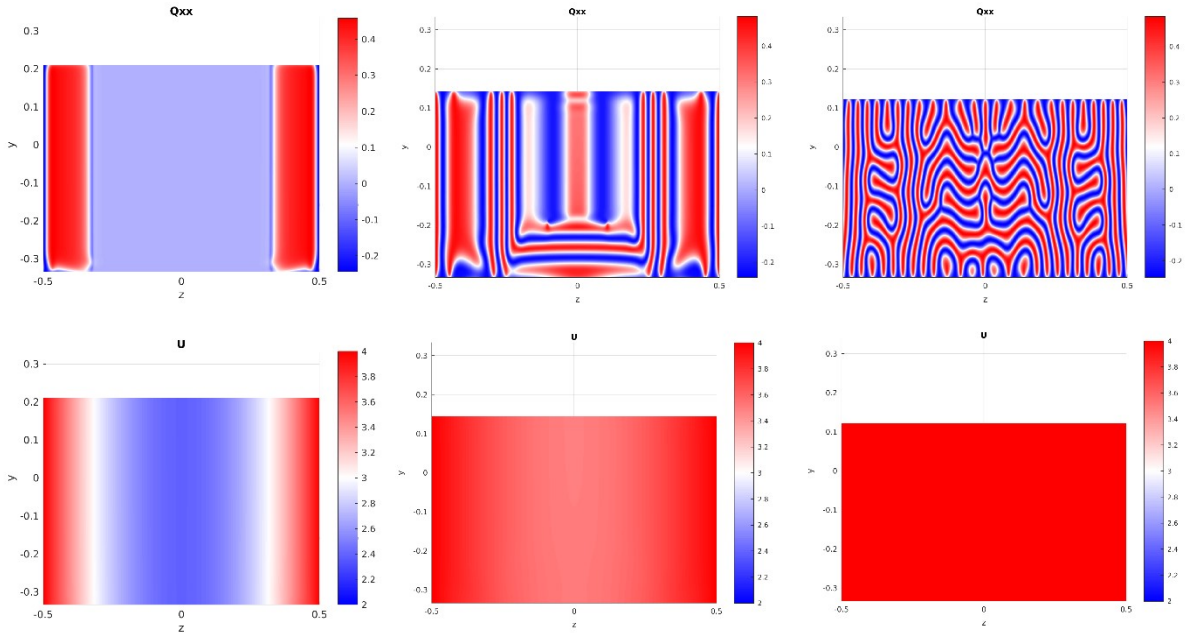

Figure F4. Q_{xx} surface plot in terms of the spatial coordinates y-z (a-c) for increasing times ($t^* = 50, 200, 5000$ and the nematic potential U (d-e) for the same times for $\Pi = 1\text{x}10^{-3}$, showing a homogeneous helical axis forming from the edge toward the central region of the cross section.

Next we focus on the cellular patterns obtained in the central region of the film when water removal rates are slow ($\Pi<\Pi^*$) . These cellular patterns correspond to distorted 2D blue phases and are common in the absence of 1D directed self-assembly [7]. Figure F5 shows and amplification of the polygonal structure obtained for the mono-domain/cellular mode ($\Pi<\Pi^*$) in terms of Q_{xx} (left) and S (right) where it is observed the latter vanishes at the vertices. The hexagonal cellular patterns is clear in the S-plot , which also shows a few penta-hepta defects [7] due to its random origin. The central region of each hexagon is characterized by the presence of non-singular core λ^{2+} disclination and by singular τ^- defects at the N vertices. The total topological defect charge C inside each cell follows Zimmer's rule [7]: $C = (N-2)/2$, which for N=6, yield C=2.

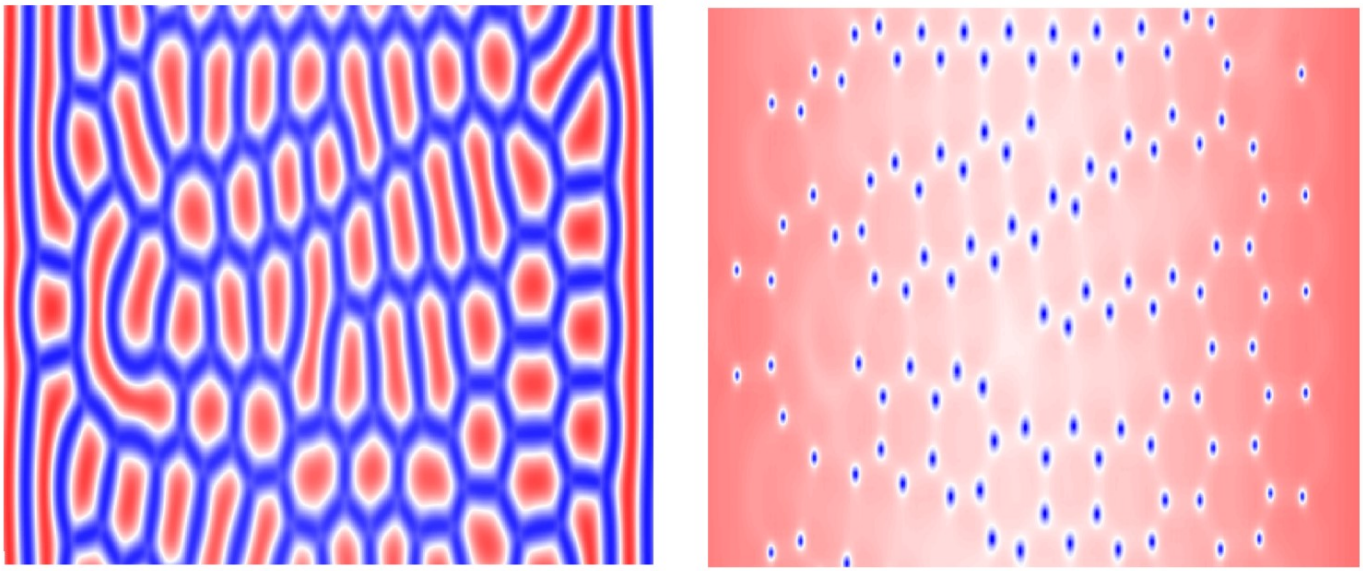

Figure F5. Amplification of the cellular region at the central region of the film for $\Pi = 10^{-5}$, in the monodomain-cellular mode.

Next we focus on the relation of the mass flux vector under synchrony (mondomain mode) and under slow water removal rate(monodomain-cellular mode). Figures F6 and F7 present the flux vector components J_y and J_z for $\Pi = 10^{-4}$ and 10^{-5} respectively for increasing times. The former shows the homogeneity in the mass flux vector components for all times of the simulations and the latter shows homogeneity for early times but inhomogeneity for later time. The non-negligible mass flux J_y in the vertical direction is an indication of the loss of stability of the planar 1D phase ordering front triggered by slow water removal rate.

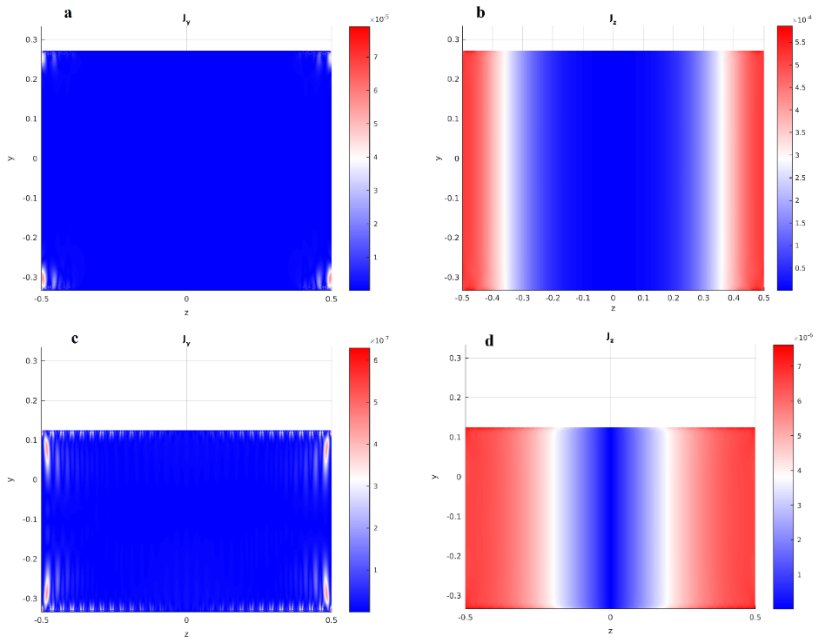

Figure F6. J_y and J_z components of the flux for $\Pi = \Pi^* = 10^{-4}$ (monodomain transition mode; perfectly synchronized water rate removal) at t = 100 (a-b) and t = 5000 (c-d) showing the homogeneity in the "z" component at all times and very weak contributions arising from the microstructure in the "y" component for late times.

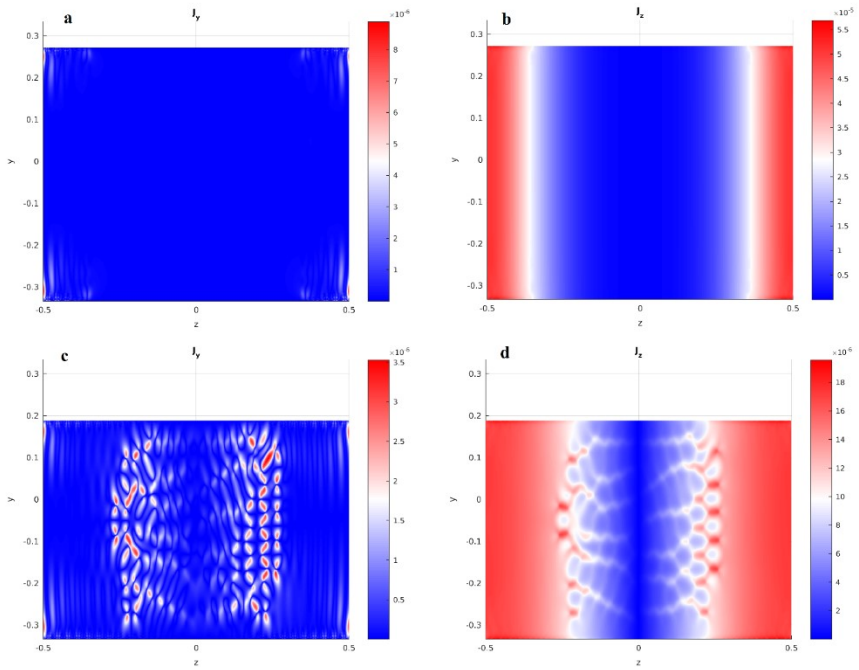

Figure F7. J_y and J_z components of the flux for $\Pi = 10^{-5} < \Pi^*$ (monodomain-cellular mode; slow water rate removal) , at t = 1000 (a-b) and t = 8000 (c-d) showing the homogeneity in the "z" component at early times and contributions arising from the microstructure in the "y" component at later times.

Appendix G. Details on Figure 4.5 and MayaVi Visualization Tool

The following is the supplementary information regarding figure 4.5 and the visualisation tool Mayavi which is a scientific data visualisation in Python available for Windows and MacOSX as part of the Enthought Python Distribution and packaged in other OS such as Ubuntu or Debian. It provides an easy and interactive visualisation for 3D plotting which is why it was used here. This tool was used to provide the visualisation of the limit cases discussed in the article of 0^{o} and 90^{o}, however any case can be visualised as will be shown here. The full documentation regarding Mayavi can be found in the following link: http://docs.enthought.com/mayavi/mayavi/

The visualisation application has a Python command line (figure G.1) where the director field can be defined but as an alternative, one can create a Python script including this information, which can be run in the Mayavi application under the file menu. Figure G.1 shows the start-up screen when launching the software.

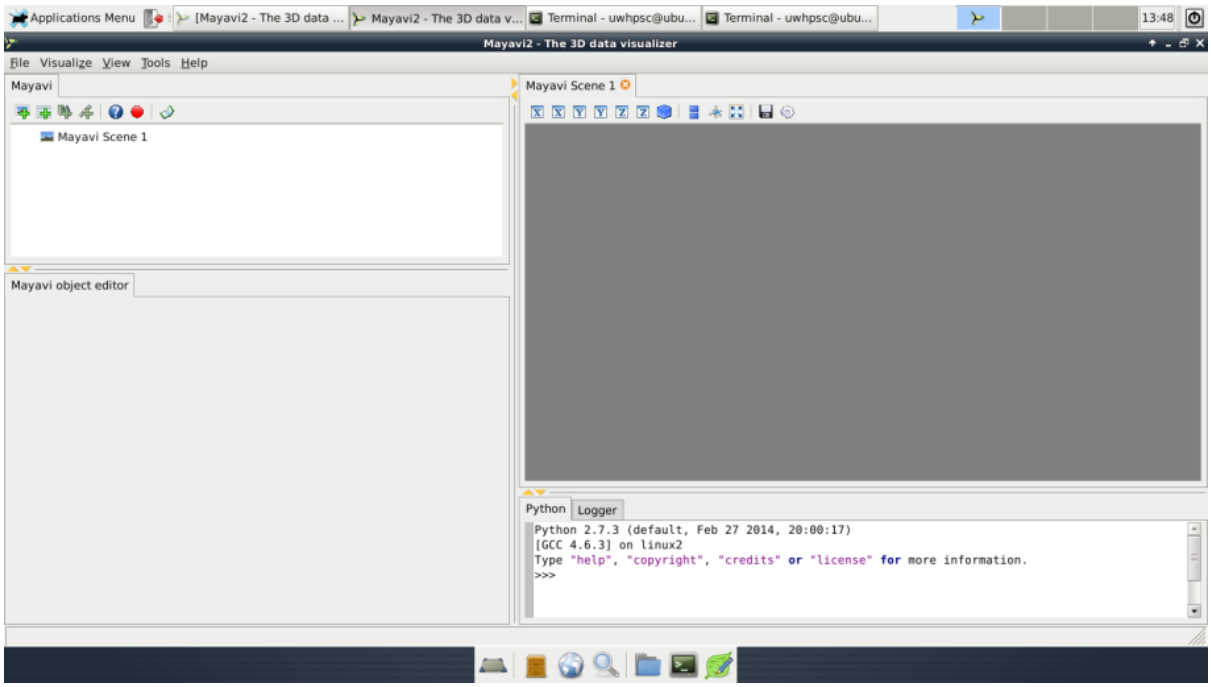

Figure G.1. Start-up screen of the 3D visualisation application Mayavi

Once the director is in the Mayavi, the next step is to hide the vector field and create the incision plane which is achieved by adding a “VectorCutPlane” in the scene. By default this plane will have its origin in the middle of the domain and will have a normal vector which defines its orientation pointing at (i, j, k) = (1, 0, 0) and arrows will displayed in this plane. To create the visualisations showed in the paper, the vector field is hidden because we are only interested in the oblique cuts and the normal vector is adjusted depending on the oblique angle desired. Further options that can be adjusted are the type of glyph shown (e.g. arrow, dash, hooked arrow, etc.), number of points, type of arrangement (random or non-random), and scale factor. The default options are shown in figure G.2 where the incision plane is located in the middle of the domain and the orientation of the normal vector is the x positive direction.

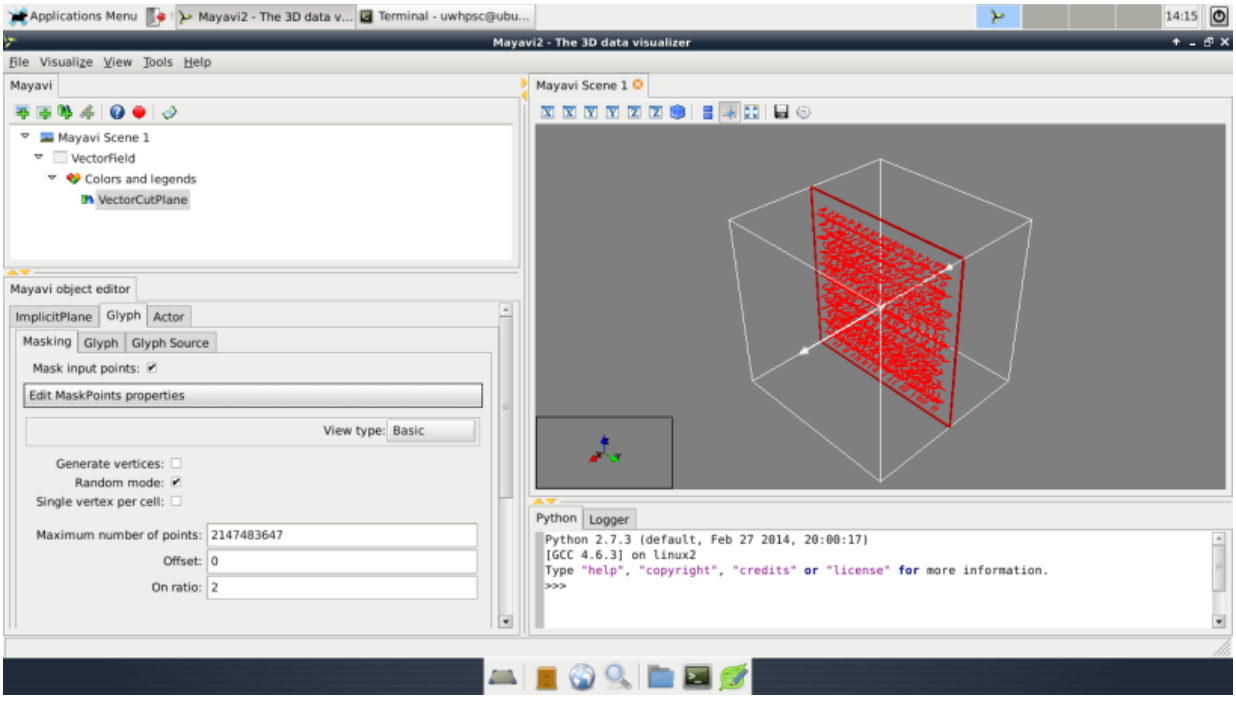

Figure G.2. Default visualisation of the ideal plywood architecture showing arrows with the plane oriented in the positive x direction in with origin in the centre of the computational domain.

Adjusting the type of glyph, number of elements, the orientation and origin of the incision plane the following figures (G.3 and G.4) can be created:

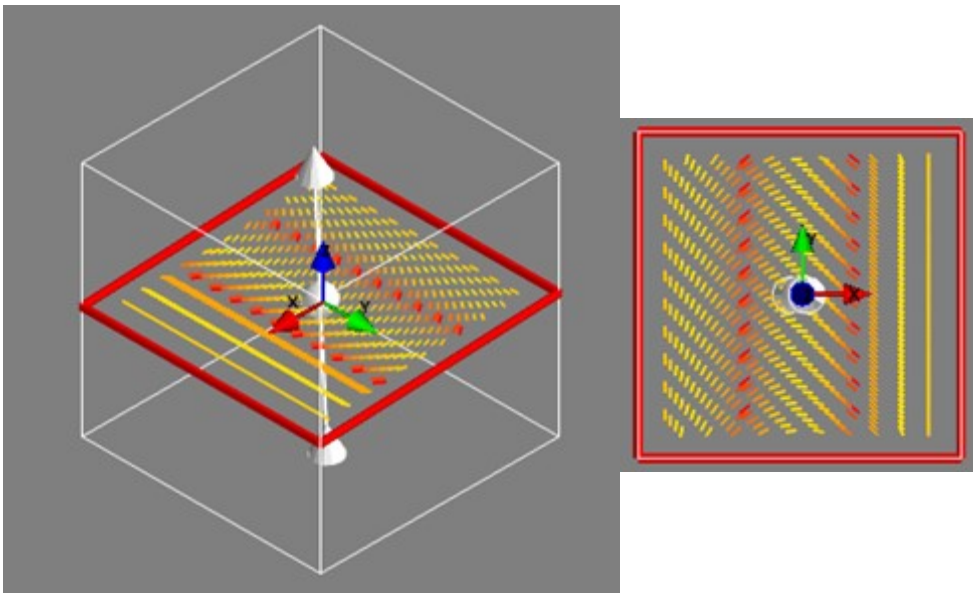

Figure G.3. Oblique cut created in Mayavi with $\alpha = 2.86^{o}$ and $p_0 = 1$ isometric view (a) and incision plane view (b).

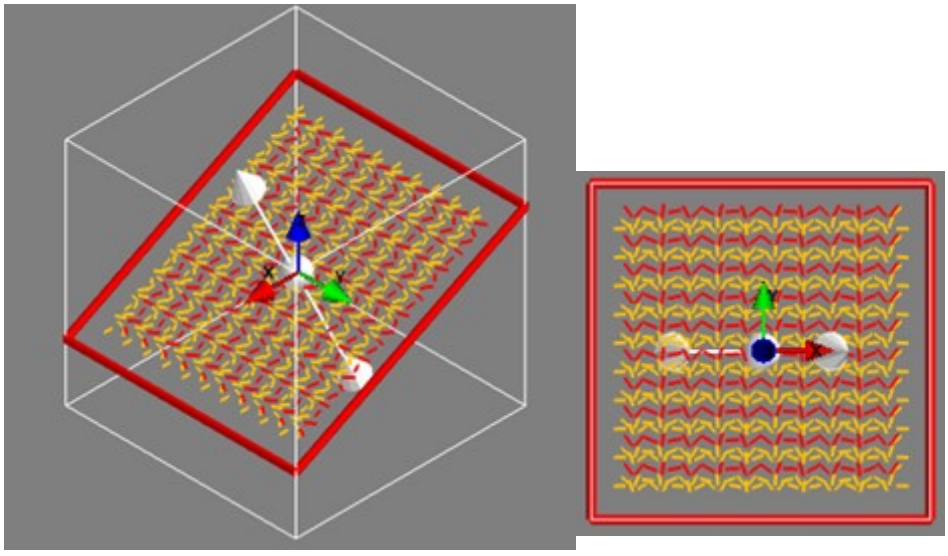

Figure G.4. Oblique cut created in Mayavi with $\alpha = 28.6^{o}$ and $p_0 = 1$ isometric view (a) and incision plane view (b).

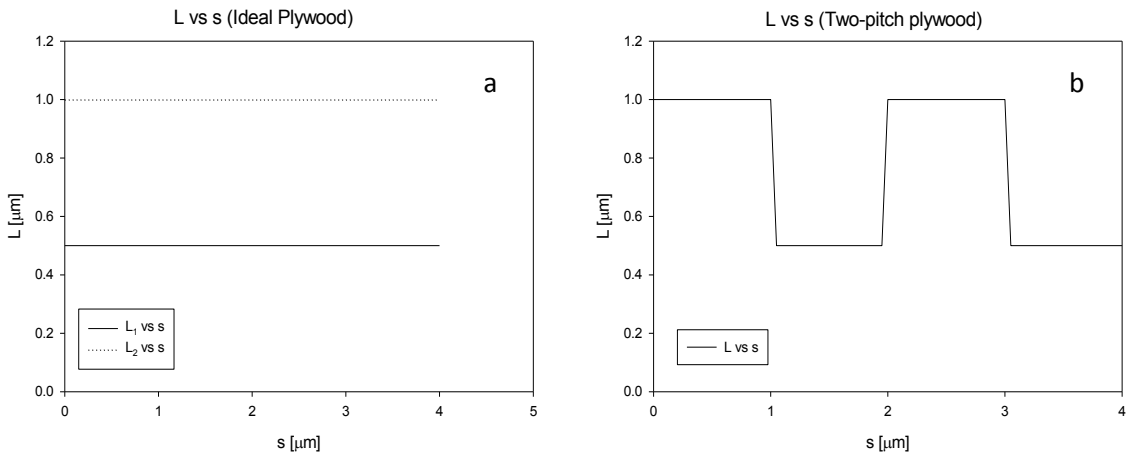

Figure G.5. Periodicity *L* plotted as a function of the spatial coordinate *s* for two ideal plywoods (a) where no variations are observed and for a two-pitch plywood (b) where discrete variations can be identified allowing the system to be treated as ideal in a piecewise fashion.

Appendix H.

The following is the supplementary information presenting the experimental fitting on the data published by Libby et al [24]. Figure H1 shows the polynomial fitting to the data presented by Libby et al regarding the spatial dependence of the pitch in the aurigans scarab.

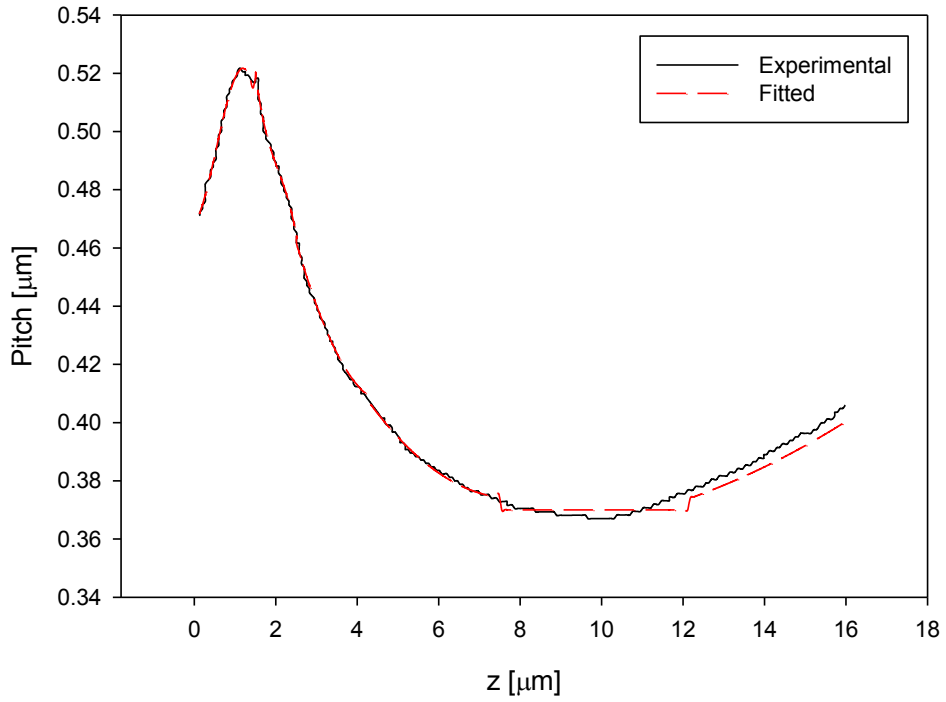

Figure H1. Experimental fitting of the pitch spatial dependence, solid line indicates the experimental values from [24] and the red dash line indicates the fitting.

Figures H2 and H3 present amplifications of the in silico cross sections used in the characterization methodology.

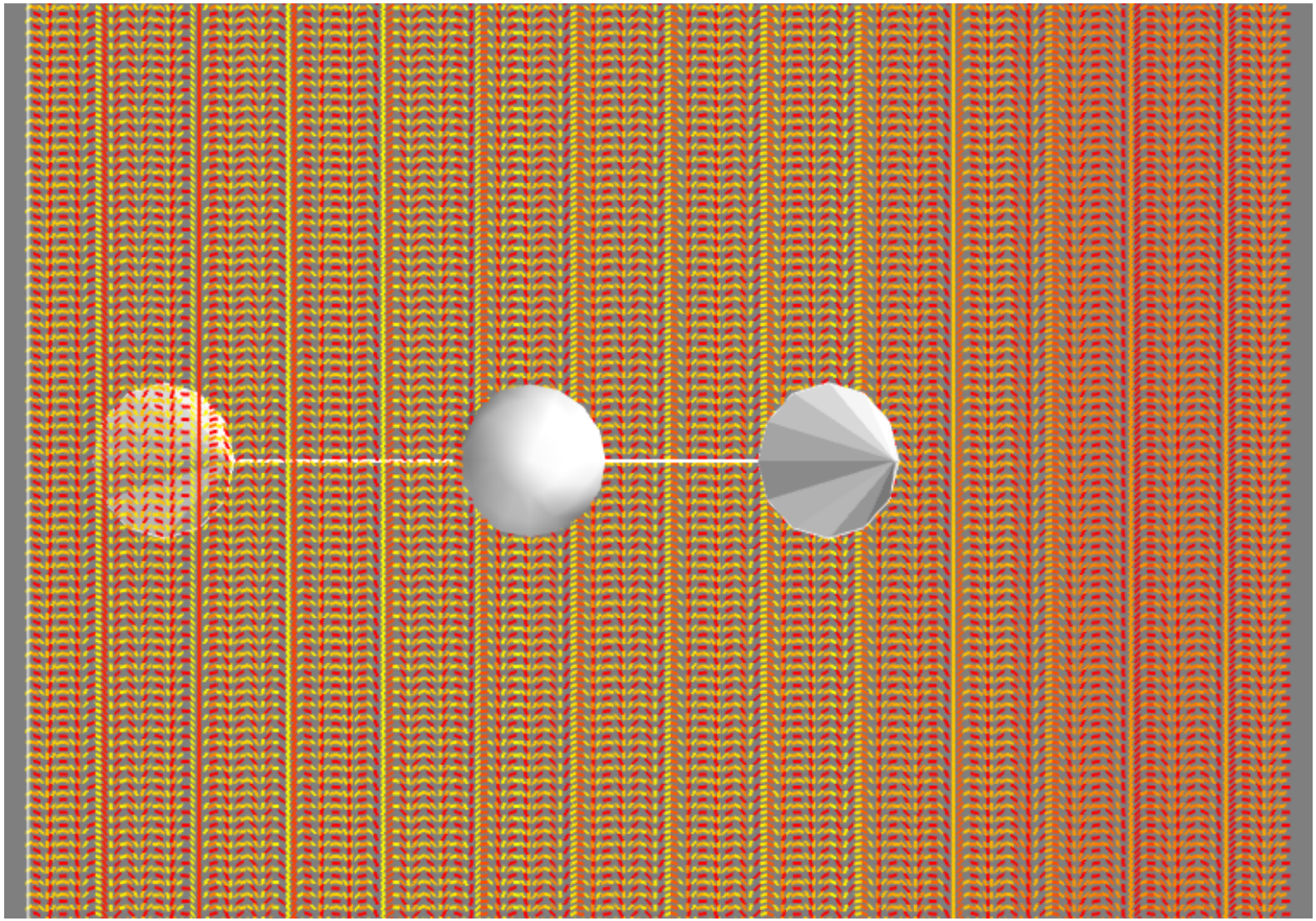

Figure H2. Larger scale image of the incision plane corresponding to $\alpha = 25^{o}$.

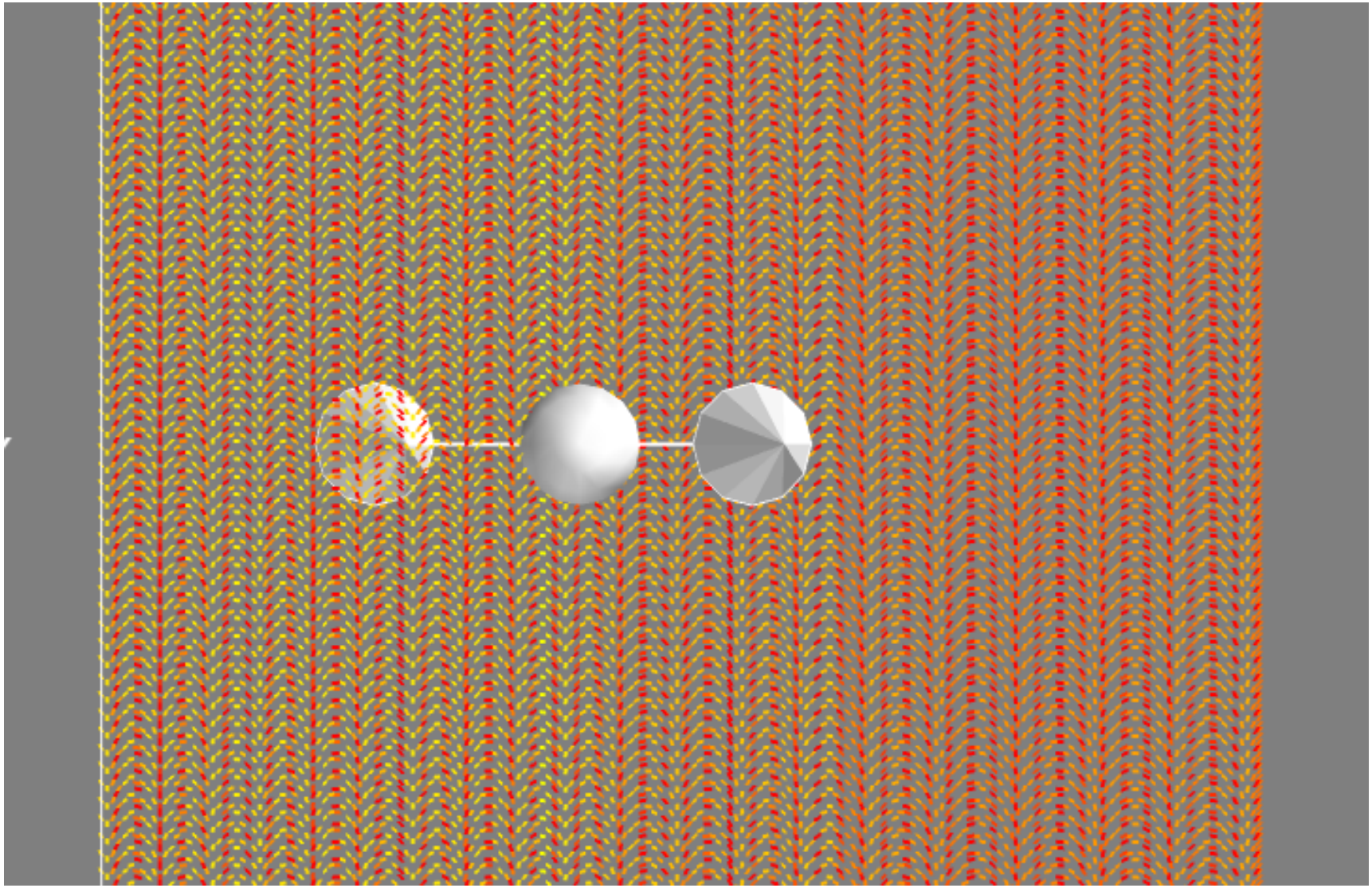

Figure H3. Larger scale image of the incision plane corresponding to $\alpha = 15^{o}$

Appendix I.

This appendix contains information regarding the detailed flowchart in the error assessment procedure, comparison of the incision angles fixed (α^M) in the Mayavi visualizations and calculated from the measurements of the herringbone angle (β_m), a mathematical description of the sensitivity of the pitch in terms of the two sources of errors ε_β and ε_L, discussed in Section 6.5.

The flowchart for the error assessment, described in Section 6.5, is shown in figure I1.

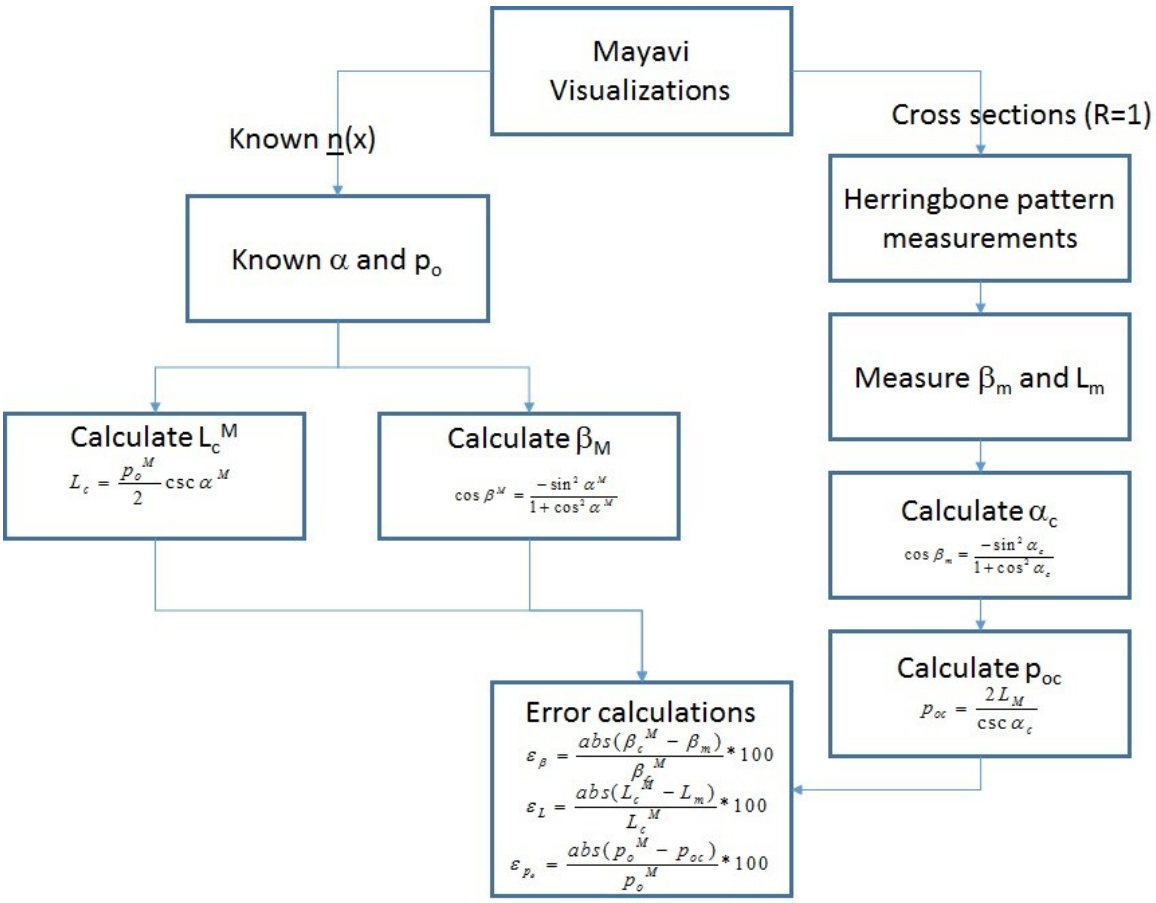

Figure I.1. Flowchart detailing the error assessment procedure.

The left stream is known information (α, p_o) or exactly calculated pattern parameters $\left(L_c^M, \beta_M\right)$ since the plywood was pre-specified and then visualized in the Majavi software. The right column is information measured $\left(L_m, \beta_m\right)$ and calculated $\left(p_{oc}, \alpha_c\right)$ on the in-silico 2D patterns found from slicing a box the plywood also in the Mayavi environment. The last box indicates the error calculations.

Table I.1 shows the negligible errors found for the incision angles found in all cases. Hence this particular quantity will not affect the predictions of the domain size p_o.

Table I.1. Incision Angle Errors $\varepsilon(\alpha)$

α^M	α_{calc}	$\varepsilon(\alpha)$
94.04	93.92	0.13%
98.05	98.29	0.25%
112.99	113.29	0.27%
125.26	125.60	0.27%
140.24	139.44	0.57%
151.46	151.52	0.04%
81.95	81.71	0.29%
74.21	73.53	0.91%
54.74	54.40	0.61%

A mathematical description of the pitch error sensitivity is as follows: the error in the calculation of the pitch is a function of errors emerging from β and L:

$$\varepsilon_{p_o} = \varepsilon_{p_o}(\varepsilon_\beta, \varepsilon_L) \tag{I.1}$$

Given the results in Table I.1, the differential $d\varepsilon_{p_o}$ is:

$$d\varepsilon_{p_o} = \left(\frac{\partial \varepsilon_{p_o}}{\partial \varepsilon_\beta}\right)_L d\varepsilon_\beta + \left(\frac{\partial \varepsilon_{p_o}}{\partial \varepsilon_L}\right)_\beta d\varepsilon_L \tag{I.2}$$

The partial derivatives are expanded as follows:

$$\frac{\partial \varepsilon_{p_o}}{\partial \varepsilon_\beta} = \frac{\partial \varepsilon_{p_o}}{\partial p_o}\frac{\partial p_o}{\partial \beta}\frac{\partial \beta}{\partial \varepsilon_\beta}, \frac{\partial \varepsilon_{p_o}}{\partial \varepsilon_L} = \frac{\partial \varepsilon_{p_o}}{\partial p_o}\frac{\partial p_o}{\partial L}\frac{\partial L}{\partial \varepsilon_L} \tag{I.3}$$

From the definition of the errors, given these are linear functions of their respective variable, the derivatives involving these terms will have order of magnitude of the unity:

$$\frac{\partial \varepsilon_{p_o}}{\partial p_o} \approx O(1); \frac{\partial \beta}{\partial \varepsilon_\beta} \approx O(1); \frac{\partial \varepsilon_{p_o}}{\partial p_o} \approx o(1); \frac{\partial L}{\partial \varepsilon_L} \approx o(1) \tag{I.4}$$

On the other hand the terms with the derivative of the pitch are the ones that determine the order of magnitude of the error. The former leads to a term involving the product of $\sin\beta\cos\beta$ while the latter $\sqrt{\cos\beta}$ being smaller the former.

$$\frac{\partial p_o}{\partial \beta} = f\left(\sin\beta\cos\beta\right); \frac{\partial p_o}{\partial L} = g\left(\sqrt{\cos\beta}\right) \tag{I.5}$$

Since $\frac{\partial p_o}{\partial \beta}\frac{\partial \beta}{\partial \varepsilon_\beta}$ and $\frac{\partial p_o}{\partial L}\frac{\partial L}{\partial \varepsilon_L}$ can also be written as: $\frac{\partial p_o}{\partial \varepsilon_\beta}$ and $\frac{\partial p_o}{\partial \varepsilon_L}$, which can be interpreted as the change of the pitch prediction with respect to errors in the measured variables, from the above

analysis and (I.5) , it can be inferred that the pitch predictions are more sensitive to errors in L than in β:

$$\left|\frac{\partial p_o}{\partial \varepsilon_\beta}\right| < \left|\frac{\partial p_o}{\partial \varepsilon_L}\right| \tag{I.6}$$

In conclusion, for high accuracy in p_o, the error in L should be minimized by careful measurements and high precision instruments.

References (Appendices)

[1] Bird. R.B.; Armstrong, R.C.; Hassager, O. *Dynamics of Polymeric Liquids, Volume 1*. John Wiley & Sons, New York, 1987.

[2] Neville, A.C. *Biology of Fibrous Composites*. Cambridge University Press, London, 1993.

[3] Fratzl P.; Giraud-Guille M.M. *Hierarchy in Natural Materials*, Wiley-VCH Verlag GmbH & Co. KGaA, 2011.

[4] Fratzl, P. *Curr. Op. Colloid Interface Sci.*, 2013, ***8***, 32-39.

[5] Fratzl, P; Weinkamer, R. *Prog. Mate. Sci*., 2007, ***52***, 1263 - 1334

[6] Blumstein, A. *Liquid Crystalline Order in Polymers*. Academic Press, New York, 1978.

[7] Rey, A.D. *Soft Matter*, 2010, ***6***, 3402-3429.

[8] Rey, A.D. ; Herrera-Valencia E.E.; Murugesan, Y.K. *Liquid Crystals*, 2014, ***41*** 430-451.

[9] Gobeaux, F. ; Belamie, E.; Mosser, G.; Davidson, P.; Panine, P.; Giraud-Guille, M.M. *Langmuir*, 2007, ***23***, 6411-6417.

[10] Rey, A. D. *J. Rheol*. 2000, ***44***,855-869.

[11] Echeverria, C. ; Almeida, P.L.; Feio, G.; Figueirinhas, J.L.; Rey, A.D.; Godinho, M.H. *Polymer*, 2015, ***65***, 18-25.

[12] de Gennes, P.G.; Prost, J. *The Physics of Liquid Crystals*. 2nd Edition. Oxford University Press, London, 1993.

[13] Chandrasekhar, S. *Liquid Crystals*. 2nd Edition. Cambridge University Press, London, 1992.

[14] Larson, R.G. *The Structure and Rheology of Complex Fluids*. Oxford University Press, London, 1999.

[15] Rey, A. D. *Phys. Rev. E*, 1996, ***53***, 4198-4201.

[16] Rey, A. D. *J. Chem. Phys.*, 1996, ***104***, 4343-4346.

[17] Rey, A.D. *Phys. Rev. E*, 2002, ***65***, 022701.

[18] Doi, M.; Edwards, S.M. *The Theory of Polymer Dynamics*. Oxford University Press, London, 1988.

[19] Grecov, D.; Rey, A.D. *Mol. Cryst. Liq. Cryst.*, 2003, ***391***, 57-94.

[20] Forest, M.G.; Wang, Q.; Zhou, R.; Choate, E.P. *J. Non-Newt. Fluid Mech.*, 2004, ***118***, 17-31.

[21] Tsuji, T.; Rey, A.D. *J. Non-Newt. Fluid Mech.* 1997, ***73***, 127-152.

[22] Rey, A.D.; Denn, M.M. *Annual Rev. Fluid Mech.*, 2002, ***34***, 233-266.

[23] de Luca G.; Rey, A. D. *Phys. Rev. E,* 2004*,* ***69***, 011706

[24] E Libby, D E Azofeifa, M Hernández-Jiménez, C Barboza-Aguilar, A Solís, I García-Aguilar, L Arce-Marenco, A Hernández and W E Vargas, *J. Opt.*, 2014, **16**, 082001